WC-VC-Co ALLOYS WITH VARIOUS Ru ADDITIONS

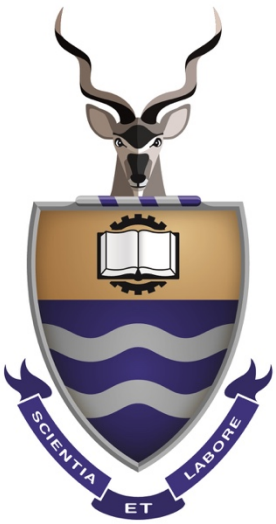

UNIVERSITY OF THE
WITWATERSRAND,
JOHANNESBURG

LIBERTY CHIPISE

A thesis submitted to the Faculty of Engineering and the Built Environment, University of the Witwatersrand, Johannesburg, in fulfilment of the requirements for the degree of Doctor of Philosophy.

March, 2019

DECLARATION

I, Liberty Chipise, do hereby declare that this thesis is my own unaided work. It is being submitted to the Degree of Doctor of Philosophy to the University of the Witwatersrand, Johannesburg. It is has not been submitted before for any degree or examination to any other university.

……

Signature

……day of……..Year……

ABSTRACT

The aim of this work was to establish the effect of Ru additions on the properties of WC-VC-Co alloys. Since previous studies had shown the beneficial effects of having either VC or Ru added to WC-Co alloys, having both VC and Ru in the same alloy system was worth investigating. The following aspects were investigated: magnetic properties, microstructural characteristics, hardness, sliding wear and corrosion properties. Four alloy series: 80WC-10VC-(10-*x*)Co-*x*Ru ($0 \leq x \leq 3$), (89.6-*x*)WC-0.4VC-10Co-*x*Ru ($0 \leq x \leq 2$), (89.2-*x*)WC-0.8VC-10Co-*x*Ru ($0 \leq x \leq 2$) and 89.6WC-0.4VC-(10-*x*)Co-*x*Ru ($0 \leq x \leq 3$) (wt%) alloys were investigated. These compositions allowed establishing the effect of varying Ru at low and high VC contents, and also the effect of Ru partially substituting the Co binder or the WC hard phase. The composition of all alloys in this work is expressed as (wt%) unless stated otherwise.

Magnetic saturation decreased with Ru additions, but did not respond to changes in VC content. Coercivity decreased with Ru additions but was higher for alloys with higher VC content. Generally, the WC mean intercept length decreased with Ru additions and VC content. The binder mean free path generally decreased with Ru and VC contents. Substituting Co with Ru increased the contiguity but the opposite was observed when Ru replaced WC. Higher VC contents corresponded to lower contiguities**.** Ruthenium additions and higher VC contents increased hardness, but decreased fracture toughness. The wear rate decreased with Ru additions and higher VC contents. There was a general improvement in corrosion resistance with Ru additions in all three corrosion environments. The effect of VC content on the corrosion behaviors of the alloys in all corrosion environments was not clear. The alloys corroded most in 1 M H_2SO_4 and were more stable in both 1 M NaCl and synthetic mine water.

Due to the complexity of the alloys, some relationships in literature were not always seen, for example those for WC-Co alloys. Overall, the 80WC-10VC-8.0Co-2.0Ru (wt%) alloy was the optimum, based on performance and Ru content.

DEDICATION

I dedicate this work to my wife, Chido and children, Rudorwashe and Hien, who supported me throughout my studies. To Rudorwashe and Hien, may this be a challenge for you to surpass, through your respective endeavours ahead. I would also like to dedicate this work to the Almighty God who formed me, and is the overall source of the abilities and means by which this work could be achieved. May the Almighty continue to guide me in all my future endeavours.

ACKNOWLEDGEMENTS

Such a project requires hard work, time and commitment. Certainly, I would not have reached this milestone on my own. Therefore, I would like to acknowledge the following people (although I fear leaving out some):

Supervisors, Professor L.A. Cornish (School of Chemical and Metallurgical Engineering, University of the Witwatersrand, Johannesburg, South Africa) and Professor P.K. Jain (Department of Physics, University of Botswana, Gaborone, Botswana) – for their patience and guidance throughout the project. Thank you, a lot!

The African Materials Science and Engineering Network (AMSEN), for funding this work and my upkeep. I am very grateful!

Pilot Tools, for granting access to their equipment and resources. Many thanks to Doctor Chris Freemantle for guiding me through the processes and for freely sharing his knowledge. Many thanks to Joseph, Shumani, Amanda, Tshepo, Boipelo and Solomon for their friendship and support.

Mintek, where I did my corrosion work. Special thanks to Melanie and Dayanda for their assistance.

School of Chemical and Metallurgical Engineering, where I did most of my work.

Colleagues – Kudzai (Civil Engineering Dept.), Jabulani (Striving Mind Projects), Marko (University of Johannesburg), Misheck (Loyalty House International), Michael, Tatenda, Simbarashe and the rest of the postgraduates from the School of Chemical and Metallurgical Engineering. Your presence helped to keep me going.

Manicaland State University of Applied Sciences (MSUAS) - for allowing me to carry on with my studies.

Family - my wife, Chido, for her support and taking care of the kids during my absence. My children, Rudorwashe and Hien, for having to cope without my presence and for cheering me up over the phone. My parents – for their encouragement.

TABLE OF CONTENTS

LIST OF FIGURES

LIST OF TABLES

1. INTRODUCTION

Cemented carbides are very hard, strong, tough and wear resistant sintered composites, and their most basic form is the WC-Co hardmetal [2009Wei, 2005Mac, 2000Lov]. The combination of the hard, strong WC phase and a tough, wear-resistant Co binder phase gives the physical and mechanical properties of the carbides. Due to their unique combination of hardness and toughness, cemented carbides have therefore been the first choice, in most cases, for manufacture of cutting tools, metal forming tools, dies, drill bit inserts, drill head inserts, mechanical seals, blasting nozzles and several other mining tools.

During sintering, the primary concern is the control of WC particle size and grain distribution for desirable hardness and wear resistance [1991McC, 1992Bro, 1995Spr]. Smaller WC particles dissolve in the binder due to their high solubility. After dissolution, there is diffusion of W and C to larger undissolved particles, where growth takes place by Ostwald ripening [1956Gre]. Grain growth has also attributed to grain boundary migration [2001Kis]. The initial carbide particle size distribution was found to be a major influence of grain growth [2011Mah].

To reduce the WC particle size, thus increasing wear resistance due to increased hardnesses, secondary carbides are frequently added. Kim and Accary [1980Kim] deduced that these act as grain growth inhibitors which change the solid/liquid interfacial energy characteristics. Jaroenworaluck *et al*. [1998Jar] attributed grain growth inhibition to the blockage of active growth centers of the carbide grains, and Choi *et al*. [2000Cho] proposed that grain growth inhibition could be related to change in edge energy.

According to Spriggs [1995Spr], the earliest reported secondary carbides to be added to cemented carbides were VC and TaC (in 1938). Other carbide inhibitors which have been studied are Mo_2C [1972Hay, 1979Exn, 1991Bha], Cr_3C_2 [1972Hay, 2000Cho, 1995Sch, 2002Wit], NbC [1972Hay, 2000Cho], TiC [1972Hay, 1979Exn, 1991Bha, 2002Wit] and ZrC [1972Hay, 2002Wit]. When the liquid phase was saturated by the addition of carbides at sintering temperature the order of WC grain growth restriction was found to be VC > Mo_2C >

Cr_3C_2 > NbC > TaC > TiC > ZrC [1972Hay]. When the liquid phase contained about 1.5 at% dissolved carbides, the effectiveness was as follows: VC > NbC > TaC > TiC >Mo_2C > Cr_3C_2 > ZrC [1972Hay]. By considering grain growth inhibition and shapes of precipitated carbides the most suitable carbides were found to be VC > Cr_3C_2 > NbC > TaC [1972Hay]. Another study has reported the most suitable carbides as VC > Cr_3C_2 > NbC > TaC > TiC > ZrC [2002Wit]. Although each grain growth inhibitor has its own advantages and disadvantages, VC is the most attractive due to its low density and high Vickers hardness [1996Luy, 2011Bol].

Due to the effectiveness of VC as a grain growth inhibitor, many investigations on WC-VC-Co alloys have been undertaken, involving different parameters such as composition, particle sizes and temperature [1996Luy, 2000Cho, 2001Are, 2001Zin, 2005Mac, 2005Mor, 2011Bol, 2011 Mah]. Morton *et al*. [2005Mor] also found that VC gave better grain refinement than TiC, TaC, NbC and Cr_3C_2. The addition of V_8C_7 confirmed the possibility of the existence of the mixed carbide, $(V,W)C_x$ in hardmetals [1996Luy, 1997Cho, 2001Obb], and Bolokang *et al*. [2011Bol] found additional phases: V_2O_3 and a τ-type carbide. Luyckx *et al*. [1996Luy] found that WC-VC-Co alloys had good sinterability and better toughness-to-hardness properties than WC-Co alloys. The addition of VC, together with Al, to WC-Co alloys resulted in good wear resistance [2001Are]. Additions of VC to WC-Co coatings improved their abrasion resistance [2005Mac] and the effectiveness of VC as grain growth inhibitor was also confirmed in later studies [2011 Mah]. However, it has been deduced that the VC loses its effectiveness as a grain growth inhibitor with prolonged heat treatment [2000Cho]. Recent work [2018Pot] has shown that grain growth inhibition begins during solid state sintering.

Other efforts to improve the properties of cemented carbides have focused on Co binder modification. The Co binder is preferentially attacked by aggressive media, resulting in significant loss in tensile strength and wear resistance of cemented carbides in such environments [2003Sut]. This lack of corrosion and oxidation resistance, in addition to the high price and deleterious respiratory effects of Co, has thus resulted in investigations for an alternative binder [2001Shi, 2011Pot, 2008Aw, 2012Lin]. Hardmetals of WC-Ni, WC-Co-Ni and WC-Fe-Ni are more corrosion resistant than straight WC-Co composites [2008Aw]. However, compared to hardmetals with Fe or Ni binder, WC-Co still has better mechanical properties and

wear properties due to the superior wettability of carbides and thermo-mechanical properties of Co [1979Exn]. The wettability of WC by the liquid binders, however, decreases with carbon content [2017Kon, 2017Kon1], and high C contents result in contact angles as low as 15° [2017Kon, 2017Kon1]. Upadhyaya *et al*. [1998Upa] also reported deterioration of densification and mechanical properties of submicron WC-10%Co as more Co binder was substituted by Ni. To compensate for the loss of mechanical properties due to binder modifications with Ni, Mo additions were found to improve density, hardness and abrasion resistance [2012Lin].

Previous research has also looked at partial substitution of Co with Ru [2000Shi, 2001Shi, 2011Pot]. Shing *et al*. [2001Shi] compared the effects on hardness of Ru and VC additions to WC-Co alloys. They [2001Shi] found ruthenium additions up to 3 wt% increased the hardness and abrasion resistance of WC-Co alloys, but to a lesser extent than VC.

Potgieter *et al*. [2011Pot] found that Ru additions up to 2 wt% improved the corrosion resistance of WC-Co alloys, and that further increases of Ru content did not increase corrosion resistance substantially. The improvement in corrosion resistance of WC-Co alloys was attributed to the stabilizing effect of Ru on Co [1980Bon, 2011Pot]. Potgieter *et al*. [2011Pot] also found that ruthenium was more effective than VC in increasing corrosion resistance of WC-Co alloys.

To date, WC-Co alloys with both Ru and VC (i.e. WC-VC-Co-Ru alloys) have not been studied. Since the effects of Ru and VC on WC-Co alloys were complementary [2001Shi, 2011Pot], it is worthwhile investigating WC-VC-Co-Ru alloys with varying amounts of Ru and VC.

Therefore, the aim of this research was to investigate the effects of Ru on WC-VC-Co alloys (at both low and high VC contents), and the objectives were as follows:

1. To determine the influence of Ru additions on the magnetic, microstructural and mechanical properties of WC-VC-Co sintered cemented carbides,

2. To conduct a tribological assessment on the effect of Ru additions to WC-VC-Co alloys – sliding wear tests,

3. To determine the influence of Ru on the corrosion behaviour of WC-VC-Co cemented carbide alloys, and

4. To compare the characteristics of high VC and low VC alloys, with Ru.

2. LITERATURE REVIEW

2.1. Cemented Tungsten Carbide Production

Conventional hardmetal production consists of four main steps: powder milling and granulation, pressing and dewaxing, pre-sintering, and sintering.

2.1.1. Powder Milling and Granulation

Milling is the first stage in the production process and is conventionally done in rotational mills [1998Upa], although efficiency-wise vibratory milling was reported to be more efficient [1983Bro]. In the cemented carbide industries, the most common comminution is by ball milling, which is done to ensure blending of carbides with the auxiliary binder metal and the processing aids [1998Upa]. The binder distribution plays an important role in the mechanical properties and porosity of sintered products [1998Upa]. Milling conditions also have a significant influence on the final hardmetal performance related properties such as hardness and transverse rupture strength [1985Goo]. In milling, there are two types of lubricants used to minimize friction between powders and to reduce the tendency to form pressing cracks. These are paraffin wax (in combination with acetone or cyclohexane as the milling medium) or polyethyleneglycole (PEG) in combination with alcohol [1987Aro].

The objectives of milling are two-fold: to promote even distribution of cobalt between the carbide particles and to reduce the tungsten carbide particle size to a desired level [1987Aro]. The most important variables during milling are time and speed of the mill. Hewitt and Kibble [2009Hew] showed that very low rotational speeds needed increased milling periods, and induced large inhomogeneities in the powder due to inadequate kinetic energy input and insufficient localized heat input for alloying. Conversely, very high speeds can lead to excessive heating of the vessel, high wear of the balls, causing increased contamination, and lower powder yields [2009Hew]. The level of contamination was found to increase with milling times, especially for very long milling times, for example, 20 at.% Fe was found in a W-C mixture milled for 310 h, and 33 at.% Fe in pure W milled for 50 h in a SPEX mill [1997Wan].

An optimized mill speed should be 70 – 80% critical speed and the charge should be 30 – 45% of the drum volume, where the critical speed for a mill is given by Equation 2.1 [1998Upa]:

$$n_{crit} = \frac{42.3}{D} \qquad \text{Equation 2.1}$$

where:

n is in rpm, and

D = diameter of cylindrical drum in meters.

Attritor milling has become the most popular milling method for hardmetals, since it gives the same quality of products as conventional milling but with less time. The advantages of attritor milling for hardmetal production are [1998Upa]:

- The attritor mill's action is much faster than conventional equipment, especially when the particle size approaches the micron range. The grinding rate is often much more than 10x that in conventional milling,
- The floor space required is only a fraction of the space than other equipment,
- The attritor mill has a stationary grinding tank (unlike huge rotating drums as in ball mills). The charges can be inspected continuously, and additions can be made at any time during grinding,
- Since the attritor mill circulates chilled water through the jacket, milling can be carried out at lower temperatures, which contributes to the prevention of the oxidation of the milled powder, and
- The product discharged from the attritor mill is in the form of slurry, which reduces health hazards.

Granulation is done to make the dried milled powders free-flowing and of higher apparent density [1998Upa], and therefore makes subsequent pressing easier and faster [1998Upa]. Granulation can be done by pressing powders into billets which are later disintegrated, or by continuously feeding mill powder onto a rotating inclined table, or by spraying a carbide slurry into a stream of preheated inert gas [1998Upa].

2.1.2. Pressing and Dewaxing

The granulated loose powder mass is further compacted and de-waxed. Compaction is done using an external pressure to obtain the desired shape and for dimensional control [1998Upa]. Luyckx *et al*. [1996Luy] successfully compacted their powders both uniaxially and isostatically. Uniaxial compaction can be either single- or double-action [1998Upa]. Single-action compaction involves movement of one punch to achieve compaction, whereas double-action compaction involves movements of both upper and lower punches [1998Upa]. In isostatic compaction, powder is placed in a flexible container which acts as a mould [1998Upa]. The compaction of powder has the following major functions [1998Upa]:

- To consolidate the powders into a desired shape,
- To impart the final dimensions after taking into account dimensional changes resulting from sintering,
- To impart the desired level and type of porosity, and
- To impart adequate strength for handling.

2.1.3. Presintering and Sintering

Wax added during milling to facilitate pressing is later removed by heating the compacts either in hydrogen or in vacuum [1998Upa]. Compacts which require further machining are firstly strengthened by pre-sintering in a vacuum at 650-1250°C [2001Upa], and strengthening is due to local welding of (Co) particles [1998Upa]. Subsequently, sintering is done at temperatures around 1400°C for most hardmetals [1998Upa]. Typically, sintering takes about 15 hours [2001Upa]. Sintering allows for further densification of metal carbides and may be considered as the process by which an assembly of particles chemically bond themselves into a coherent body under the influence of an elevated temperature [1996Ger]. The sintering process involves three steps, schematically represented by a temperature/time cycle (Figure 2.1) [2001All]. The “debinding” stage removes the organic lubricant introduced for compaction and some of the impurities. The heating stage completes the removal of impurities and allows for significant shrinkage. In the final stage, the “sintering plateau” achieves full densification, but with some grain growth.

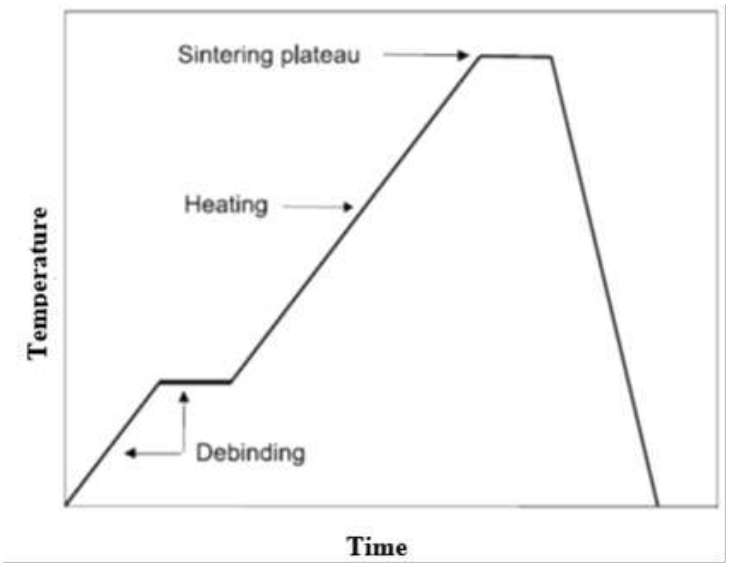

Figure 2.1. Schematic temperature/time cycle showing the classical sintering process [2001All].

2.1.4. Grain Growth During Sintering

During sintering, densification occurs in two distinct stages. The first stage of densification occurs immediately after formation of the liquid phase. This is as a result of wetting of the carbide particles by the binder, thus creating capillary forces that cause the binder to flow between the carbide particles. The WC particles agglomerate due to surface tension forces [1996Ger].

The second stage of densification is the dissolution of smaller particles into the liquid phase. The smaller particles then re-precipitate on the surfaces of larger grains [1996Ger]. This dissolution and re-precipitation mechanism results in a decrease in volume of the solid phase, and hence increases densification [1996Ger]. Since the driving energy for sintering is the tendency of the system to minimize the interface energy, the large surface area of small grains results in their dissolution into the liquid binder. The dissolution, occurring by W solute diffusion in liquid Co, is a rapid step [1954Gur]. The precipitation of W and C onto larger grains results in grain growth, thus a reduced surface area and consequently a decrease in free energy [1996Ger].
The evidence for the solution-reprecipitation grain growth process came from experiments involving the addition of molybdenum carbide to the sintering mixture [1989Ett]. Molybdenum

can substitute for tungsten in WC without significantly changing the lattice structure or its parameters [1988Roe, 1989Ett]. Molybdenum and tungsten have very close atomic radii 0.139 nm (1.39 Å) and 0.141 nm (1.41Å) [1984Ega], thus a MoC-WC solid solution is formed by mixing WC, Mo and C powders or W, Mo and C [1981Kod]. Kodama *et al*. [1981Kod] reported that beyond 70% MoC, a uniform solid solution could not be obtained at high temperature, since MoC became unstable and decomposed. According to Schmitt *et al*. [1983Sch], etching can be used to reveal the zones where molybdenum was incorporated in the WC lattice, under an optical microscope and in a scanning electron microscope [1983Sch]. Murakami etching on samples with MoC was reported [2017Bro].

The kinetics of growth are governed by either transport of the material through the liquid phase (diffusion control) or by the reaction rates of the dissolution or re-precipitation processes at the surface of the carbide grains (reaction control) [1989Ett]. The reaction control phenomenon is generally accepted as the growth mechanism, which accounts for the fact that grain growth in WC-Co is slow compared with other systems, such as W-Ni [1989Ett]. In the WC-Co system, the evaluation of the driving force is difficult [2008Lay], because WC grains generate two types of prismatic $\{1\ 0\ \bar{1}\ 0\}$ surfaces, and two basal (0 0 0 1) surfaces that restrict the flat triangular prism (Figure 2.2) [2008Lay] with truncated corners. This shape of the WC grains is different from what is expected from the hexagonal (type $P\bar{6}m2$) structure of WC with close lattice parameters (a = 0.2906 nm and c = 0.2837 nm) [2008Lay]. Secondly, WC grains are in contact with either other WC grains or with the (Co) binder since the energies of specific WC/WC boundaries and of WC/(Co) boundaries interfaces appear to be of the same order as indicated by the sintered microstructure [1980Hag]. Wang *et al*. [2008Wan] observed that the solution-reprecipitation mechanism that contributes to grain growth during sintering of WC-Co powders also involves coalescence in addition to coarsening.

Grewe *et al*. [1973Gre] stated that grain growth can be further retarded or inhibited by the addition of grain growth inhibitors, such as VC, NbC, TaC, Cr_2C_3, Mo and Ru. The mechanisms by which these grain growth inhibitors interfere with the solution-reprecipitation processes are not completely understood. Earlier studies [1980Kim] concluded that inhibitors change the

solid/liquid interfacial energy characteristics. Almond and Roebuck [1988Alm] favored the hypothesis that inhibitors interfere with the reprecipitation step.

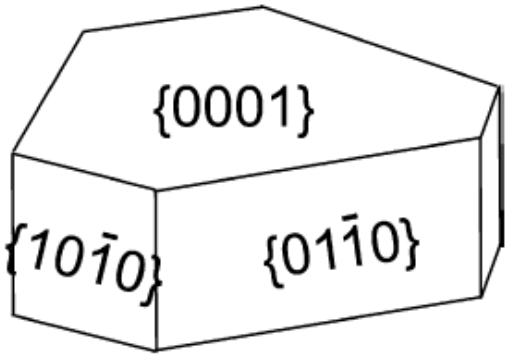

Figure 2.2. Schematic representation of WC grain shape in (Co) binder [2008Lay].

Experimental evidence indicated that the liquid phase played an important role, because the amount of inhibitor needed depends on the amount of the binder phase [1989Ett]. Jaroenworaluck *et al*. [1998Jar] attributed grain growth inhibition to blockage of active growth centers of the carbide grains. Choi *et al*. [2000Cho] proposed that grain growth inhibition could be related to changes in edge energy. Allibert [2001All] found a strong correlation between the C/W ratio in the binder and grain growth inhibition. Allibert [2001All] also found that grain growth can be reduced by using limited amounts of evenly distributed inhibitor, by strict C control and by minimal sintering temperature and time. Enhancement of grain growth occurs during heating and during isothermal holding as the carbon content increases [2003Cha]. For WC-Co alloys doped with VC, Cr_3C_2 or NbC, the inhibitors were effective during the solid state and thus not limited to liquid phase sintering [2007Hua]. Since inhibitors were effective even during solid-state sintering, it is likely that the presence of dispersions on the WC-Co interface interferes with the dissolution and/or precipitation of WC in Co [2007Siv]. Therefore, the mechanism of grain-growth inhibition might not involve alteration of interface energy. Spark plasma sintering (SPS) was found to be more effective in limiting WC grain growth of un-doped WC-Co grades than conventional sintering [2007Hua, 2007Siv]. However, the effect of SPS was less pronounced for 0.9 wt% VC, Cr_3C_2 or NbC grades but still increased hardness and lowered toughness significantly. A two-step sintering process which involves pre-sintering in the solid state at 1250°C and liquid phase sintering (LPS) at 1400°C was found to be effective in limiting

WC grain growth [2009Yan]. Pre-sintering promotes densification prior to LPS, resulting in full densification before excessive grain growth. The two stage sintering technique results in increased hardness and microstructural uniformity.

2.2. Microstructure of Cemented Carbides

In general, microstructures determine the overall physical and mechanical properties of materials. The microstructure of cemented carbides is determined by the following parameters [1998Upa]:

- Basic chemical composition of the hard and binder phases,
- Shape, size and distribution of WC particles, including the contiguity,
- Degree of solubility, in each other, of any different carbides,
- Excess or deficiency of carbon,
- Variation in composition, due to diffusion or segregation,
- Processing technology, e.g., milling, carburizing, and sintering, and
- Coatings, if any, on the cemented carbides.

Tungsten carbide is the major phase and forms two hexagonal carbides, monocarbide WC and subcarbide W_2C [1979Exn]. The monocarbide WC has a highly anisotropic structure [1998Upa] and develops anisotropic crystal shapes which are often described as flat triangular shapes with truncated edges [1979Exn]. Tungsten carbide can be substituted by other carbides, such as TiC, TaC, VC etc. [1996Luy, 2002Wit, 2005Mor, 2008Hua]. Luyckx *et al*. [1996Luy] found that fine grained WC-VC-Co could be possible substitutes for WC-Co alloys, due to their better hardness and toughness properties.

Cobalt is used most extensively as the binder metal in cemented carbides [1998Upa]. The binder phase in WC hardmetals is an alloy containing small amounts of dissolved tungsten and carbon, and may also contain elements to suit the requirements of a particular application [1988Alm]. It is present as a continuous thin film separating the carbide particles [1998Upa]. Tungsten has a high solubility in (Co) (where (Co) is a solid solution based on Co), up to ~40 wt%, whereas Co has negligible dissolution in W [1982Bet].

Precipitates generally observed in the binder phase of cemented carbides are non-metallic impurities, graphite, carbides and intermetallic compounds precipitated during cooling or heat treatment in the solid state [1998Upa]. Pores cannot usually be avoided by normal sintering and are caused by impurities, inhomogeinities, low carbon content, entrapped gases and incorrect sintering temperature [1998Upa].

Microstructural parameters which are measured in quantitative characterization of cemented carbides are [1998Upa]:

1. carbide grain size distribution and mean carbide size,
2. carbide contiguity,
3. binder mean free path, and
4. volume fraction of individual phases.

The size distribution of the tungsten carbide and cobalt phases in sintered alloys is determined mainly by the milling conditions and the initial size distribution of the carbide powder [1965Fis]. In addition to milling and powder properties, the grain size is also affected by sintering conditions [1998Upa]. Contiguity is a quantitative measure of skeleton formation [1970Exn], which is defined as the ratio of particle-boundary surface (WC/WC interface) to total interface surface (WC/WC + WC/(Co) interface) [1959Gur]. The parameters which affect contiguity are cobalt content and sintering time [1959Gur]. Sintering temperature also affects contiguity, but less than cobalt content and sintering time [1959Gur, 1966Fis]. Contiguity, C_β, was measured by Gurland [1958Gur] using Equation 2.2:

$$C_\beta = \frac{2N_{\alpha\alpha}}{2N_{\alpha\alpha} + N_{\alpha\beta}} \qquad \text{Equation 2.2}$$

where:

$N_{\alpha\alpha}$ = the average number of intercepts of a random line of unit length with traces of carbide-carbide interfaces, and

$N_{\alpha\beta}$ = the average number of intercepts of a random line of unit length with traces of carbide-cobalt interfaces.

Luyckx and Love [2006Luy] reduced the expression by Gurland *et al*. [1957Gur] to a relationship between C_β and cobalt volume fraction, V_{Co}:

$$C_\beta \cong \frac{V_{Co}}{(1-V_{Co})(5.975V_{Co}^2-0.691V_{Co}+0.214)} \quad \text{Equation 2.3}$$

Luyckx and Love [2006Luy] confirmed the dependence of contiguity on only cobalt content and not carbide grain size. They also showed that the contiguity of the carbide phase did not appear to tend to zero when the cobalt content tends to one. They explained this in terms of the tendency of the WC grains to coalesce at high cobalt content, due to the formation of WC/WC boundaries of energy lower than twice the energy of WC/(Co) interfaces. Two-atom thick chemically ordered layers (complexions) are formed on straight, faceted WC grain interfaces, resulting in high compatibility stresses across the WC/Co interfaces [2018Kon]. To achieve a good combination of strength and fracture toughness, the complexes are stabilised by quenching, addition of grain growth inhibitors and carbon control [2018Liu].

The mean free path is a measure of the thickness of the cobalt layers and depends on both the cobalt content and the particle size [1970Exn]. Generally, mean free path is used as the most important single parameter in defining microstructure [1955Gur, 1963Gur, 1966Exn]. Gurland and Bardzil [1955Gur] found hardness to be directly related to mean free path. However, a closer analysis on the scatter band for the hardness-mean free path relationship revealed that an additional parameter, such as particle size or composition was necessary to accurately describe the relationship [1966Fis]. The volume fraction of individual phases is easier to measure for straight WC-Co grades than when cubic carbides are added, due to the high solubility of WC into the binder phase [1998Upa].

The variation of the microstructural parameters is shown in Figure 2.3. [1991Bha], which suggests a direct relationship between mean binder free path and average carbide grain size. An inverse relationship between contiguity and mean binder free path or average carbide grain size is also deduced from Figure 2.3.

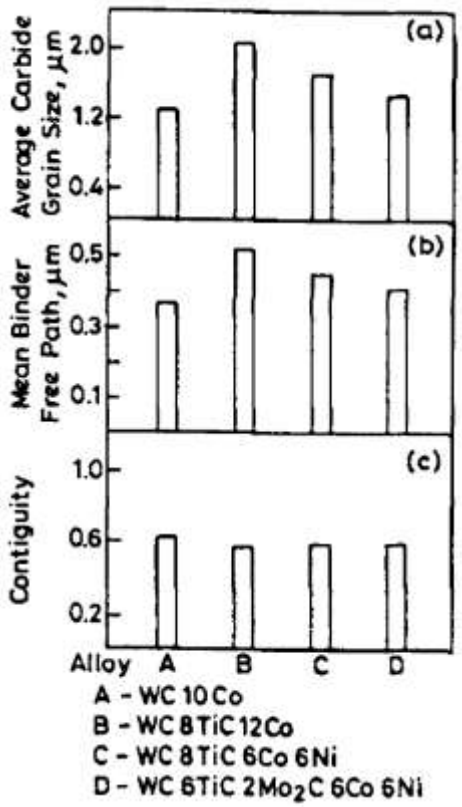

Figure 2.3. Different microstructural parameters of straight and complex tungsten carbide based hardmetals [1991Bha].

2.2.1. The Binder Phase

The binder phase is typically a dilute cobalt alloy containing tungsten and carbon as solutes, and can exist in two allotropic forms – hcp or fcc [1969Gur]. Other iron group metals, such as nickel and iron have been considered [1998Upa]. The use of cobalt in preference to iron and nickel is mainly due to the higher solubility of WC in cobalt, and the super comminution characteristics of Co [1998Upa], since Co exists mainly as hcp up to 450°C, making it very amenable to size reduction. The ease of Co comminution gives it a better distribution during milling, which subsequently, during sintering, leads to desirable microstructures. Even distribution of Co is ensured by sufficient milling [1977Amb], and is also strongly dependent on the carbon content, which controls its redistribution during heating to the sintering temperature [1998Upa]. Tungsten and carbon stabilize the high temperature fcc phase by reducing the transformation temperature [1964Daw]. Carbon is more effective than tungsten in fcc stabilization [1998Upa]. The ratio of

the fcc and hcp phases is determined in bulk alloys by prior processing, treatment and composition [1998Upa].

Although cobalt content is the most important variable in producing cemented tungsten carbides of different qualities [1970Exn], the binder phase is not a pure metal, but rather a cobalt-tungsten-carbon solid solution, Co-W (thus expressed as '(Co)' instead of 'Co', since W is much less than Co). If mixed carbides, such as TiC, TaC and NbC, are present, the binder will have with minor elements of titanium, tantalum, and/or niobium in solid solution [1989Ett]. Rare earth (RE) additions to the binder have been investigated [1991Lis] by studying an alloy of binder composition: 71 Co, 20.5 RE, 8 W (wt%) and the balance C. The RE addition significantly reduced the stacking fault energy of the cobalt and encouraged the $\beta_{(Co)} \rightarrow \varepsilon_{(Co)}$ (fcc $\rightarrow$ hcp) martensitic transformation. The effect of 32.0-43.4 wt% rare earth additions was also studied by Chenguang [1992Che] on WC-8Co and WC-14TiC-8Co cemented carbides. The volume fraction of fcc cobalt (60%) in the plain alloy increased up to 97% (of the binder volume) after RE addition. In addition, the melting point of binder was decreased by about 30°C. The RE had no effect on the cobalt distribution in the WC-TiC-Co cemented carbide.

Upadhyaya [1998Upa] also related the relative ease of interchangeability of the two forms to the low stacking fault energy of dilute cobalt alloys. A typical microstructure of the binder phase showing stacking faults in WC-10Co cemented carbide sintered at 1425°C in hydrogen is shown in Figure 2.4 [1998Upa].

Since the solubility of WC in (Co) increases substantially with temperature, the composition of the binder phase at room temperature can be expected to be determined by many experimental factors, such as sintering temperature and time, rate of cooling, carbide particle size and the mean free path [1971Rud]. The composition of the binder can vary significantly between the boundaries for graphite and η (eta) phase precipitation and is important in determining the mechanical properties of the hardmetal [1988Alm]. This helps industry in obtaining the specific properties of hardmetals as a function of cobalt, nickel and iron binder phases. In practice, these properties are controlled by monitoring total carbon content and maintaining a constant magnetic

saturation to ensure consistence in binder phase carbon and tungsten content among batches [1988Alm].

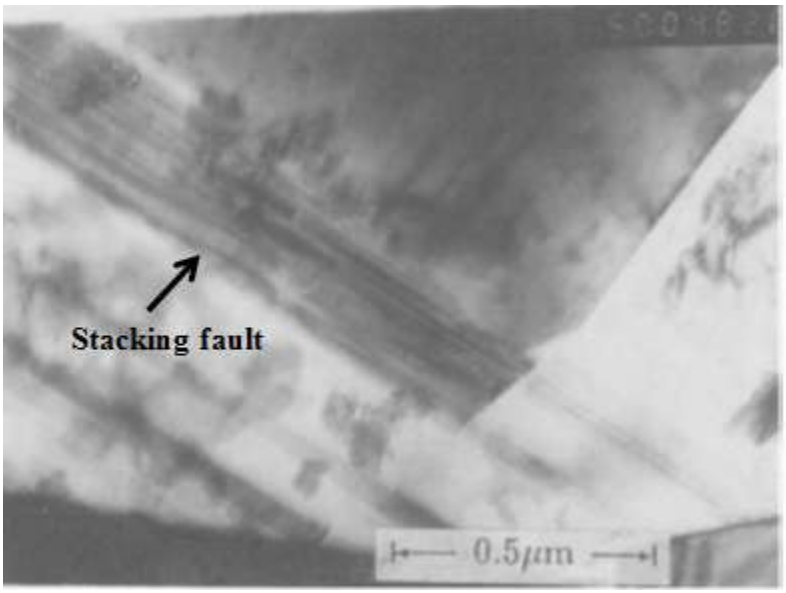

Figure 2.4. TEM bright-field micrograph of WC-10 Co cemented carbide (sintered at 1425°C in H_2) showing stacking faults in the binder phase [1998Upa].

Consistent with the binder phase affecting the mechanical properties of hardmetals, it was demonstrated that the transverse rupture strength exhibited a maximum at a particular carbon content in WC-Co hardmetals [1971Rud]. It was also reported that fracture toughness increases with binder phase volume [1983Bol].

Almond and Roebuck [1988Alm] also confirmed the dependence of mechanical properties on the binder phase composition. They varied the tungsten and carbon contents of the binder phase in WC-Co and WC-(Co-Ni) hardmetals, and the fracture toughness and compressive failure strengths varied by up to 30%. These properties reached maximum values at compositions intermediate between graphite and η phase formation. They also derived expressions which enabled the binder phase compositions of the hardmetals to be calculated. The tungsten content could be up to 5.9 at.% in the binder of a 12 wt% Co hardmetal, whilst it ranged from 0.5 to 2.0 at.% with little dependence on the tungsten content in the binder phases of WC-Co, WC(Co-Ni) and WC-Ni hardmetals.

Compared with WC-Co hardmetals, the hardness and compressive strengths of WC-Ni hardmetals were inferior [1988Alm]. The WC-Ni hardmetals could be strengthened by adding aluminium, or aluminium plus titanium, or tin, or silicon to form precipitates of γ', Ni_3M, where M = Al, Al + Ti, Sn or Si [1988Alm]. Some WC-(Ni-Cr-Mo) hardmetals had comparable hardness and Palmqvist toughness to WC-Co hardmetals. By combining γ' hardening with solid solution strengthening and adding molybdenum to the binder phase of a range of WC-Ni hardmetals, better combinations of hardness and Palmqvist toughness were obtained than for WC-Co hardmetals. The presence of chromium in the binder phase should confer corrosion resistance, while the size and form of the γ' precipitates can be altered by heat treatment to give enhanced strength or creep resistance [1988Alm].

2.2.2. Eta Phase

Eta, η, is a ternary compound of tungsten, cobalt and carbon which results from carbon deficiency in WC-Co alloys [1998Upa]. Isothermal sections of the W-C-Co phase diagram at 1400°C are shown in Figures 2.5 to 2.7 [1952Rau, 1959Gru, 1952Rau1], showing three, one and four η phases. However, later findings (Figure 2.8) [1976Uhr] did not agree with the previous findings [1952Rau, 1959Gru, 1952Rau1] that the η phases have different compositions.

However, it is generally agreed [1978Joh] that the η phase exists in two basic forms, M_6C and $M_{12}C$ [1933Ade, 1943Kis, 1947Met, 1952Rau, 1952Kie, 1970Pol, 1970Ett, 1978Joh, 1998Upa] (Table 2.1). Pollock and Stadelmaier [1970Pol] found that Co_6W_6C retains a narrow homogeneity range down to 1000°C, with lattice parameters between 1.0894 nm (10.894Å) and 1.0902 nm (10.902Å). The compositional range of Co_2W_4C is between Co_3W_3C and Co_2W_4C at 1400°C and narrows to a small range around Co_2W_4C at 1000°C (its lattice constants vary between 1.1066 nm (11.066Å) and 1.1251 nm (11.251Å) [1970Pol]). Graphite or η precipitate in these hardmetals when the C/(V +W) ratio is higher or less than [1 – 0.33 V/(V + W)], where V/(V+W) ≈ 0.72 [2001Obb]. Johansson and Uhrenius [1978Joh] reviewed previous publications of η carbides cell dimensions (Table 2.1).

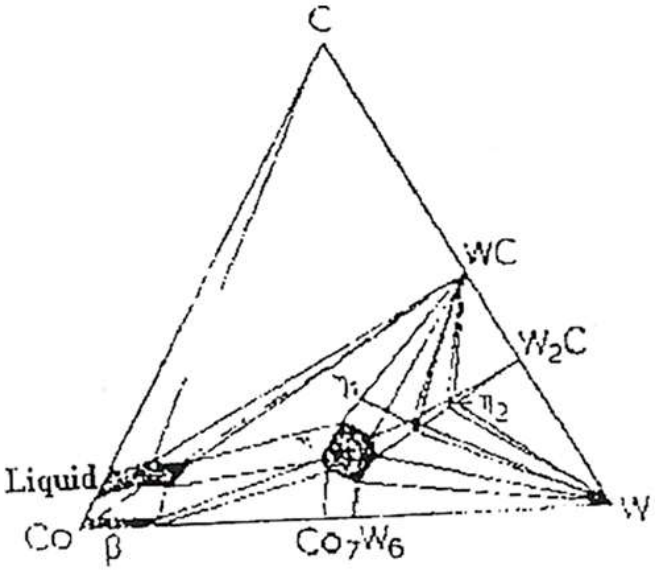

Figure 2.5. Isothermal section of the W-C-Co phase diagram at 1400°C showing three ternary phases [1952Rau].

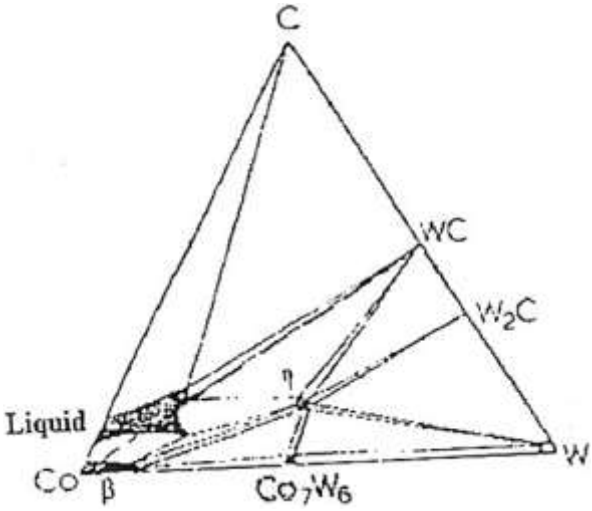

Figure 2.6. Isothermal section of the W-C-Co phase diagram at 1400°C showing one ternary phase [1959Gru].

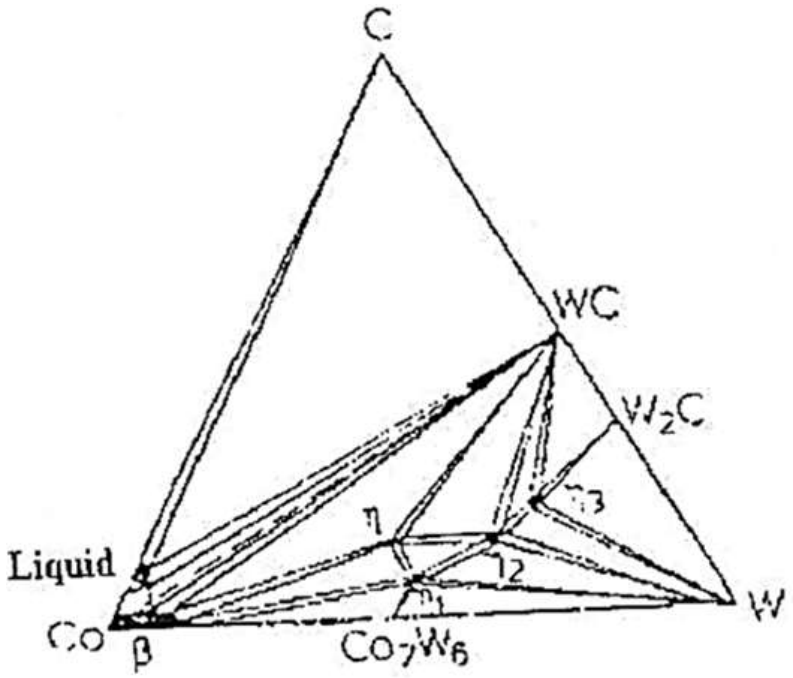

Figure 2.7. Isothermal section of the W-C-Co phase diagram at 1400°C showing four ternary phases [1952Rau1].

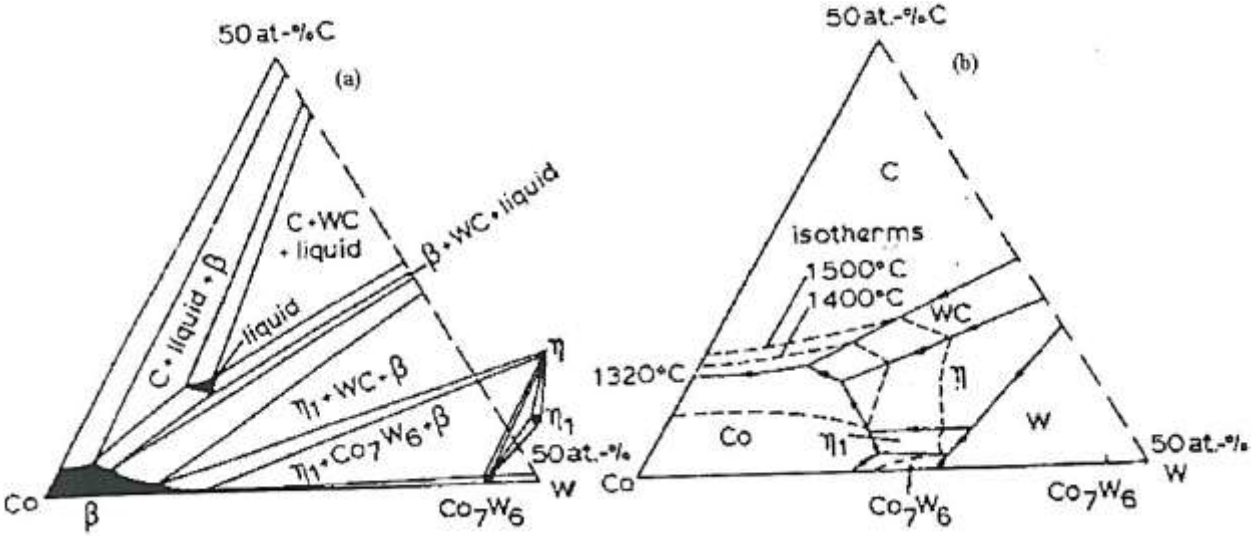

Figure 2.8. Cobalt-rich portion of the W-C-Co phase diagram. a) Isothermal section at 1260°C, and b) projection of the liquidus surface with 1400°C and 1500°C isotherms [1976Uhr].

Table 2.1. Lattice parameters of η carbides (nm) [1978Joh].

Reference	Co_4W_2C	Co_3W_3C	Co_2W_4C	Co_6W_6C
[1933Ade]	1.103	-	-	-
[1943Kis]	-	-	1.1213	1.012
[1947Met]	-	1.1078	-	-
[1952Rau]	-	1.1090	1.125	1.096
[1952Kie]	-	1.1090	1.1218	
[1970Pol]	-	1.1066	1.1251	1.0894-1.0902
[1970Ett]	-	1.108	1.125	1.090
[1978Joh]	-	-	1.1236-1.1250	1.0896-1.0901

Using X-ray and microprobe analysis, Johansson *et al*. [1978Joh] found the lattice parameter homogeneity ranges for M_6C and $M_{12}C$ and found M_6C and $M_{12}C$ to be indistinguishable physically and that M_6C may represent a metastable form which can undergo *in situ* decomposition ($M_6C \rightarrow \beta + M_{12}C + WC$) by a fairly sluggish reaction.

In commercial alloys with fast cooling rates, the presence of M_6C was reported to be more probable than $M_{12}C$ [1983Bol]. Later work [1988Par] reported an M_4C κ-phase, CoW_3C. According to Park *et al*. [1988Par], the Co_2W_4C phase in Table 2.1 is not an η phase, but a θ phase, and thus probably does not have the same deleterious effects as the η phases. The calculated liquidus surface of the Co-W-C system (Figure 2.9) [2005Mar] shows the existence of both the M_6C and $M_{12}C$ η phases, as well as the W-rich phases (M_2C and MC_{1-x}). The three-phase equilibrium (W-Co-η, where η = M_6C) corresponds to a carbon activity of 0.34 at 1430°C (Figure 2.10) [2014Bor]. Therefore, the C activity should be higher than 0.34 at 1430°C to prevent the formation of the η phase.

With minor carbon deficiencies, the η phase formed on cooling after sintering, resulting in isolated concentrated areas in which considerable volumes of WC and cobalt binder phase were locally consumed during its growth [1998Upa]. This was characterized by rounded partially dissolved WC grains [1998Upa]. The η phase undergoes peritectic decomposition with further cooling ($L + \eta \rightarrow WC + (Co)_{fcc}$), and the amount of η retained at room temperature depended on

the cooling rate and carbon content [1977Fre]. Very minor carbon deficiency levels led to the complete depletion of η on cooling, whereas it was retained at higher carbon deficiency levels, irrespective of the cooling rate [1998Upa]. At minor carbon deficiencies, the η phase was characteristically finely dispersed particles (Figure 2.11) [1998Upa].

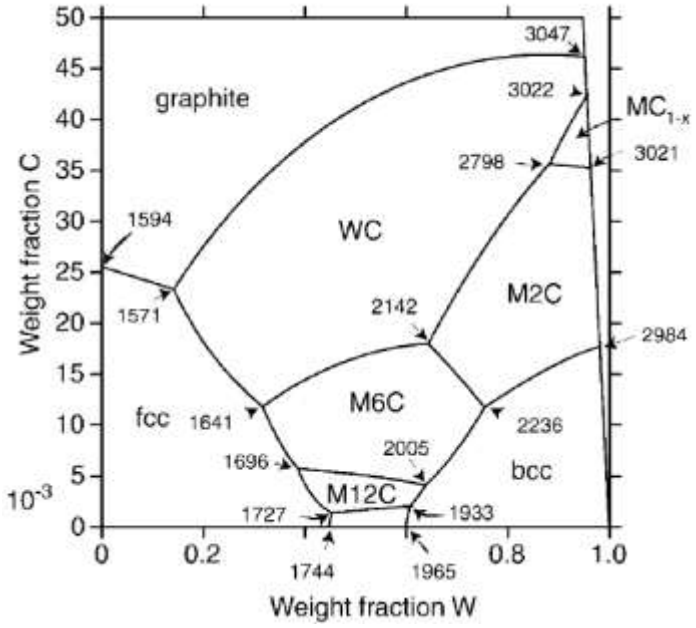

Figure 2.9. Calculated projection of the liquidus surface of the Co-W-C system [2005Mar].

For extreme carbon deficiencies, η is present at the sintering temperature and is retained after cooling [1998Upa]. The morphology of the η phase at extreme carbon deficiencies is characterized by large areas of massive η (Figure 2.12) [1998Upa]. The final η phase distributions and morphologies are controlled by carbon content developed during sintering and cooling. Since η results in poor mechanical properties, carbon control is very important in industrial processes.

Since the η phases have deleterious properties, it is important to determine compositions that do not result in precipitation of η [2001Zin]. The carbon potential mainly affects the WC crystal shape and the microstructure evolution of WC-Co alloys [2002Wan]. The WC crystal shape is completely faceted in C-rich alloys. On the WC/Co and WC/WC interfaces, the WC crystal

shows slightly rounded corners and steps [2002Wan]. Wang *et al*. [2002Wan] also observed a more regular size increase and increase in the number of WC grains with temperature and time.

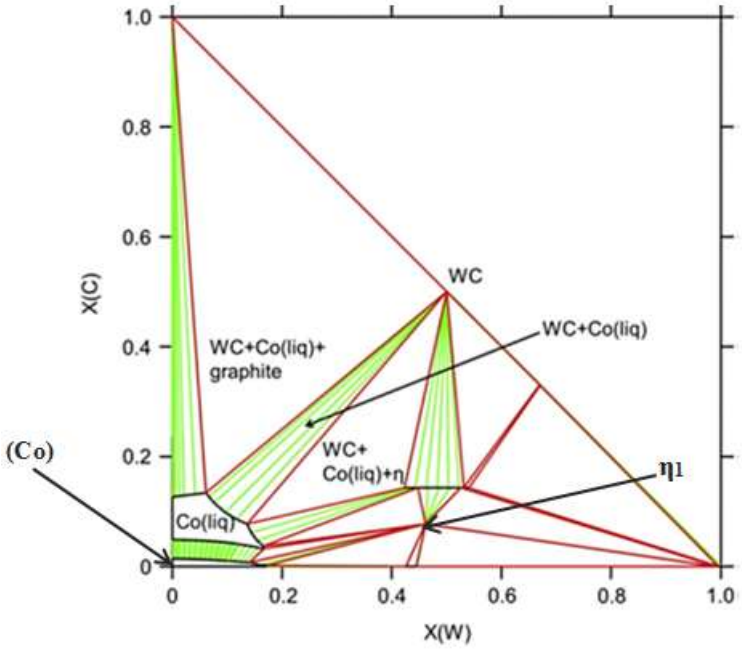

Figure 2.10. Isothermal section at 1430°C for the W-C-Co system [2014Bor] showing two ternary phases η = M_6C and $\eta_1 = M_{12}C$.

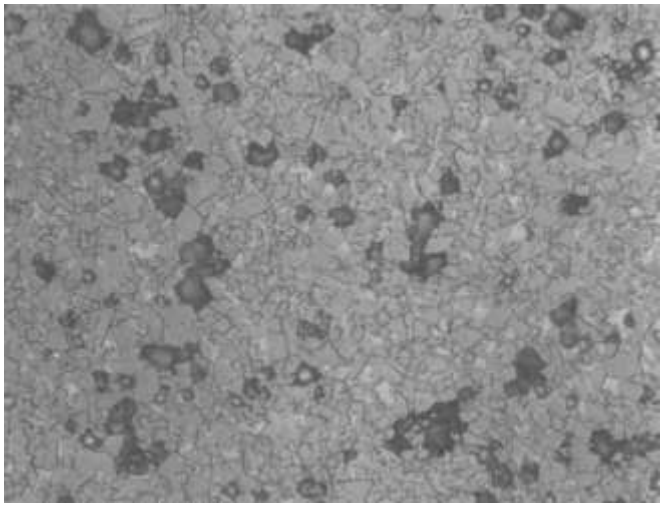

Figure 2.11. Microstructure of a WC-Co-Cr cemented carbide with minor C deficiency showing well dispersed η phase (dark) throughout the WC-(Co) matrix (light), (WC grain size 3µm), Murakami etching (full width ~100µm) (from Dr H. Pastor, CERMeP, Grenoble [1998Upa]).

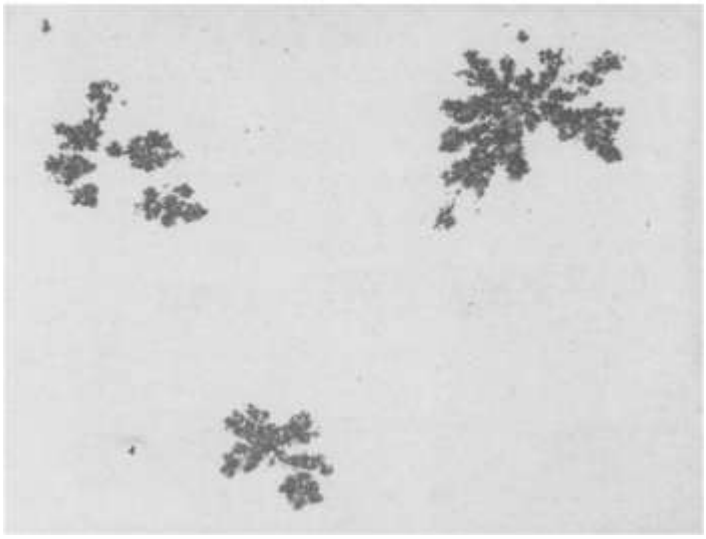

Figure 2.12. Microstructure of cemented carbide with extreme C deficiency showing strong η phase (dark) in the WC-(Co) matrix, light Murakami etching (10 s) (full width ~1500μm) (from Dr H. Pastor, CERMeP, Grenoble [1998Upa]).

2.3. Physical and Mechanical Properties of Cemented Carbides

The common characteristics of the metal matrix composites, such as a tungsten carbide, are superior mechanical properties with increased toughness, stiffness and wear resistance [1999Tru]. Cemented carbides have both the physical properties of ceramics and the electronic properties of metals. They have high melting points, high thermal conductivity, high electrical conductivity and high chemical stability [1998Upa]. The properties of some selected hardmetals (A-E) are shown in Table 2.2.

Upadhyaya [1998Upa] stated that cobalt content is the most important variable in producing cemented carbides of different quality. Vandeput and Mastrantonis [1988Van] reported that transverse rupture strength (TRS) improved with increasing cobalt content, and decreased with increased cubic carbide proportion. Fracture is initiated by (Co) that deforms by plastic flow, causing dislocations to pile up against the carbide crystals [1977Che]. Luyckx and Love [2006Luy] showed that cobalt content is the only variable affecting the contiguity of the carbide

phase. High Co content decreases impingement of carbide grains [1974Gra]. Increasing Co content reduces the hardness of WC-Co alloys [1965Kie].

Carbide particle size has a strong influence on the mechanical properties of cemented carbides [1998Upa]. Hardness and compressive strength decrease with increased grain size, whereas transverse rupture strength increases with increased grain size [1995Pra]. Carbon content also affects the mechanical properties of cemented carbides.

Table 2.2. Properties of selected hardmetals (Krupp-Widia, Essen [2001Upa1]).

Composition, wt %	A	B	C	D	E
WC	94.0	85.3	75	78.5	60.0
Other Carbides (TiC, TaC, NbC)	-	2.7	-	10.0	31.0
Co	6.0	12.0	25.0	11.5	9.0
Properties					
Density ($g.cm^{-3}$)	14.9	14.2	12.9	13.0	10.6
Hardness (HV_{30})	1580	1290	780	1380	1560
Bend Strength (MPa)	2000	2450	2900	2250	1700
Elastic Modulus (GPa)	630	580	470	560	520
Fracture Toughness ($MPa.m^{-1/2}$)	9.6	12.7	14.5	10.9	8.1
Thermal Conductivity ($Wm^{-1}.K^{-1}$)	80	65	50	60	25
Thermal coefficient of expansion (x 10^{-6} K^{-1})	5.5	5.9	7.5	6.4	7.2

2.3.1. Hardness of WC-based Hardmetals

Hardness also increases with volume portion of the hard constituent and contiguity [1978Lee]. Milman *et al*. [1999Mil] also confirmed the inverse relationship between hardness and WC grain size. The Hall-Petch equation [1951Hal, 1953Pet] gave a good approximation of the inverse relationship between WC grain size and hardness for all cobalt contents and temperatures investigated by Milman *et al*. [1999Mil].

Lee and Gurland [1978Lee] developed a relationship that quantitatively correlated hardness values with stoichiometric features of the microstructure. The model incorporates a plastic

analysis into a simplified microstructural analysis. They introduced *in situ* hardness values for the carbide and binder, based on the Hall-Petch relationship [1951Hal, 1953Pet] for bulk materials:

$$H_M = H_{WC} * V_{WC} * k + H_B (1 - V_{WC} * k) \quad \text{Equation 2.4}$$

where:

H_{WC} = 1 382 + 23.1 $d^{-1/2}$ = Vickers hardness of WC (kg/mm^2)

H_B = 304 + 12.7 $\lambda^{-1/2}$ = Vickers hardness of binder (kg/mm^2)

λ = mean free path of the binder phase (mm)

V_{WC} = volume portion of the carbide phase

k = contiguity.

Submicron hardmetal grades (with WC grains smaller than 1μm) have superior hardness and higher compressive strength than coarser grain hardmetals (WC grains greater than 1μm) [1989Ett]. Such materials can be obtained by the sintering of homogenous mixtures of fine or ultrafine powders of WC, Co and growth inhibitors [2001All]. The increased hardness with decreasing carbide grain size does not affect the high values of transverse rupture strength and fracture toughness [1989Ett]. Hardness of WC-Co alloys can be increased by partial replacement of WC with VC. Whitefield *et al*. [1997Whi] reported that WC-VC-Co alloys exhibited a hardness which is equal or superior to that of the hardest WC-Co alloys of equal cobalt content.

Luyckx *et al*. [2001Luy] compared the effects of the WC grain growth inhibitors, V_8C_7 and Cr_3C_2, on the hardness of WC-Co alloys. For the refiner content, V_8C_7 resulted in higher hardness (Figure 2.13). For the same hardness values, Cr_3C_2 content is expected to be higher than V_8C_7 (Figure 2.13). The higher grain refiner content resulted in the finer WC grain size (Figure 2.14). Thus, the higher hardness at equal refiner content is attributed to finer WC grain size (Figure 2.14).

2.3.2. Fracture Toughness of WC-based Hardmetals

Fracture toughness is a measure of the resistance of the material to crack propagation and should be virtually independent of specimen size, geometry and surface finish [1998Upa]. Fracture toughness measurements of cemented carbides are usually done using the Palmqvist method

[1957Pal] and not according to British Standard BS5447 [1977Bri] or American Standard ASTM E 399-78 [1982AST], because it is difficult to pre-crack these materials by fatigue [1998Upa, 2000Shi]. The Palmqvist method [1957Pal], Equation 2.5, gives W_G, the surface crack resistance, a measure of the surface toughness of a brittle material and is often used to measure the toughness of cemented carbides [1978Exn].

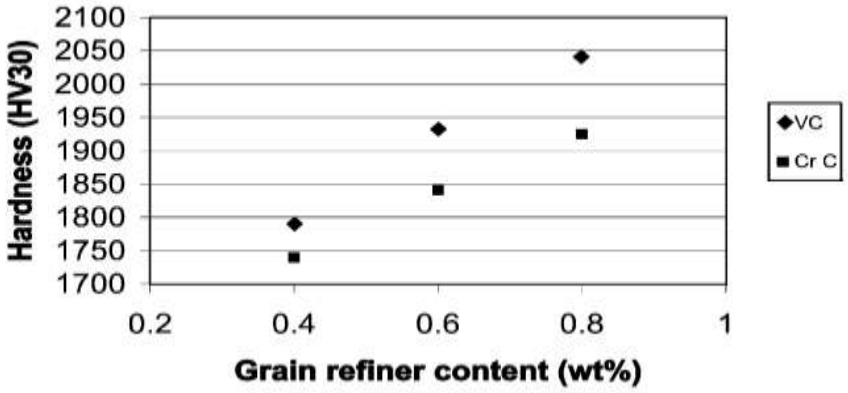

Figure 2.13. Effect of grain refiner content on the hardness of WC-Co (in the legend VC and CrC stand for V_8C_7 and Cr_3C_2, respectively) [2001Luy].

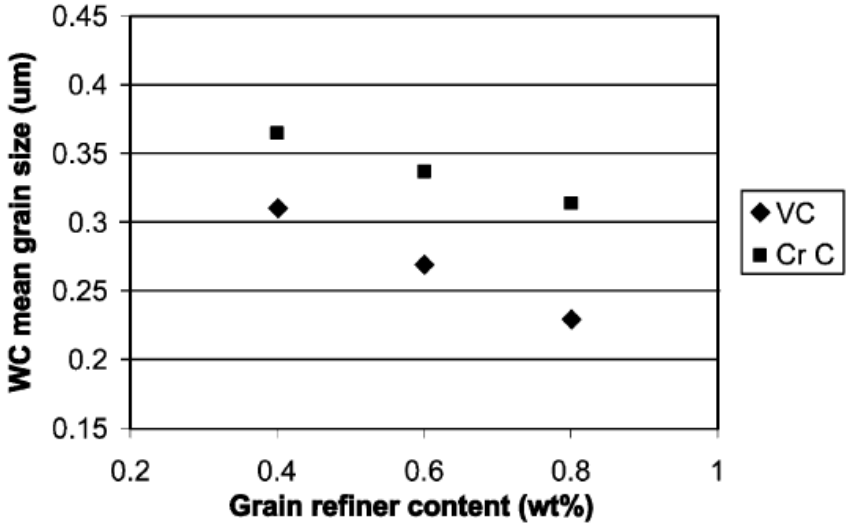

Figure 2.14. Effect of grain refiner content on WC grain size ('VC' stands for V_8C_7 and 'CrC' for Cr_3C_2) [2001Luy].

$$W_G = \frac{P}{L} \qquad \text{Equation 2.5}$$

where:

P = load of the Vickers indenter

L = total length of surface indentations emanating from the corners of the indentation.

The Palmqvist cracks are the first cracks to form during loading, as the indentation is produced, and are the only cracks observed in reasonably tough materials, such as cemented carbides with at least 6% Co [1977Per]. The precision of toughness measurements using Palmqvist indentations is strongly affected by the WC grain size: fine or medium grained alloys exhibit a ~2% standard deviation for fracture toughness, W_G, while the standard deviation approaches 8% for coarse grained alloys [1990Spi]. An important prerequisite for reproducible crack length measurement in Palmqvist testing is the removal of the stressed surfaces from grinding by heat treatment [1998Sch].

Spiegler *et al*. [1990Spi] studied Palmqvist cracks and median cracks (Figure 2.15), which nucleate at the tip of the indenter and propagate into the underlying material. They concluded that median crack models are inappropriate to describe indentation cracking of WC-Co, and that Palmqvist crack models satisfy the criterion of load independent fracture toughness.

Perrott [1977Per] applied elastic-plastic stress functions to indentation deformation and was able to relate W_G and the critical strain energy release, G_{IC} with good results for cemented carbides using empirical estimates of the required plastic and geometrical constraint factors.

Fracture toughness depends on the amount of ductile binder phase present and generally increases with the grain size of the carbide phase [1989Ett]. Luyckx and Allibert [2001Luy] also confirmed the dependence of crack resistance on the WC grain size, and to the mean free path. A "rule of thumb" is that the trends of hardness and toughness are opposed to each other, where increasing hardness usually results in decreased toughness. However, there are deviations from this, such as the hardness and toughness relationship of individual alloys [1998Sch], which vary with changes in composition/microstructure.

According to Ettmayer *et al*. [1989Ett], WC-Co has the highest fracture toughness of all possible combinations of transition metal carbide-iron group binder metals because of the relatively high

fracture resistance of WC compared to other carbides. They also stated that WC does not fracture in an ideal brittle mode, but undergoes some plastic deformation. This was confirmed by the relatively high fracture resistance of WC (50 $J.m^{-2}$) compared to the surface energy of ~ 2-3 $J.m^{-2}$ by Warren [1978War]. On the other hand, cobalt has very low stacking fault energy and consequently a rather high work hardening rate which increases the amount of energy required to fracture the binder ligaments [1989Ett].

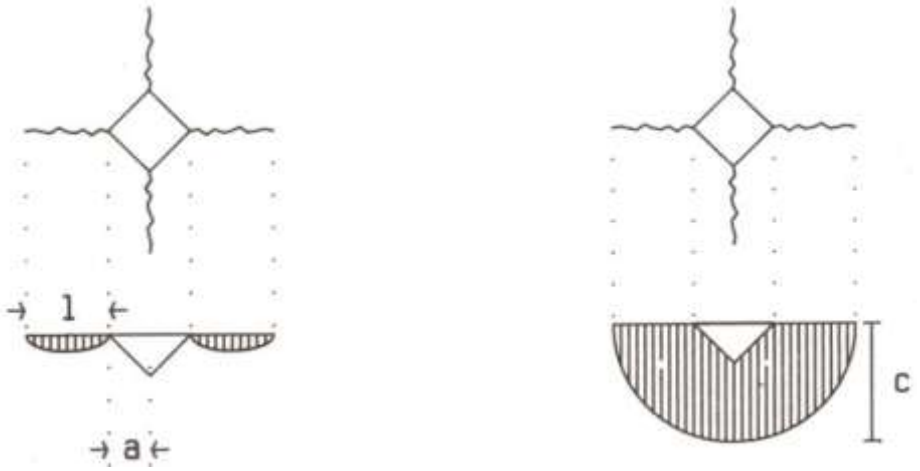

(a) (b)

Figure 2.15. Schematic diagram showing: a) Palmqvist cracks, and b) median cracks [1990Spi].

Luyckx and Allibert [2001Luy] also compared the effects of the WC grain growth inhibitors, V_8C_7 and Cr_3C_2, on the crack resistance of WC-Co alloys. They observed that for the same grain inhibitor content, Cr_3C_2 offered larger crack resistance (Figure 2.16). This was because for the same grain refiner content, V_8C_7 resulted in finer grains (Figure 2.14) and thus narrower binder mean free paths. The narrower the mean free path, the lower is crack resistance [2001Luy]. The lower crack resistance, at similar hardness values, for alloys with V_8C_7 than those with Cr_2C_3 (Figure 2.17) demonstrates the high effectiveness of V_8C_7 as a grain growth inhibitor. This is because crack resistance increases with mean WC grain size (Figure 2.18). At the same hardness values, Cr_2C_3 would be higher (Figure 2.13). Since crack resistance decreases with refiner content, it would be expected that Cr_2C_3 would have a lower crack resistance, but this was not so because lower amounts of V_8C_7 still resulted in finer grain sizes as shown in Figure 2.14.

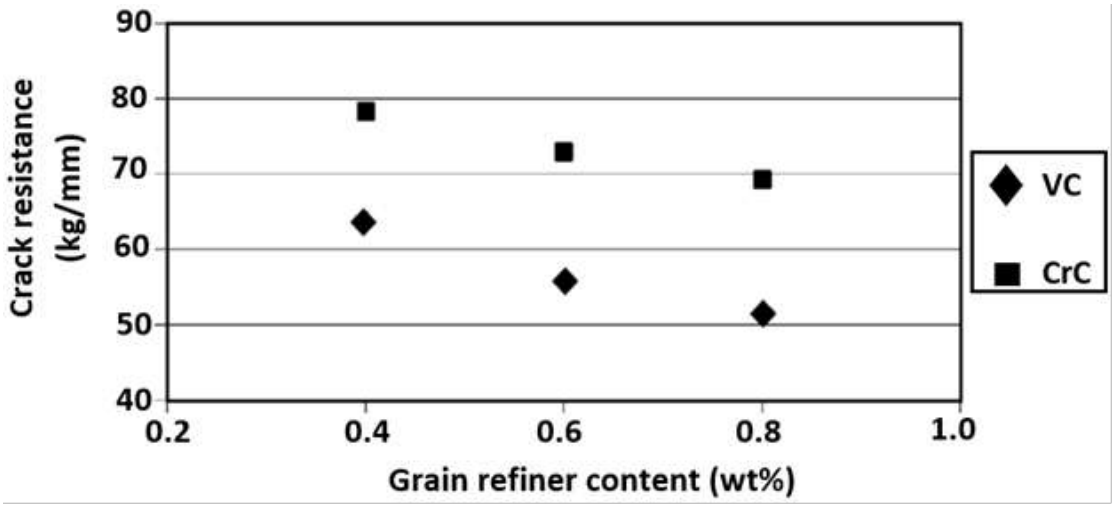

Figure 2.16. Effect of grain refiner content on the crack resistance of WC-Co (in the legend VC and CrC stand for V_8C_7 and Cr_3C_2) [2001Luy].

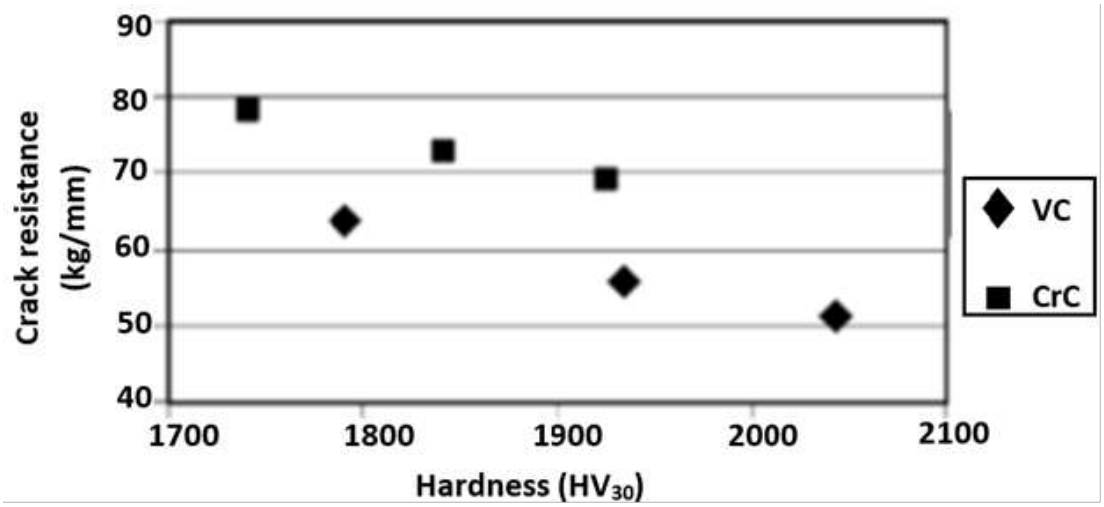

Figure 2.17. Relationship between crack resistance and hardness in WC-Co with the amounts of grain refiners increasing as shown in Figure 2.16 (in the legend VC and CrC stand for V_8C_7 and Cr_3C_2) [2001Luy].

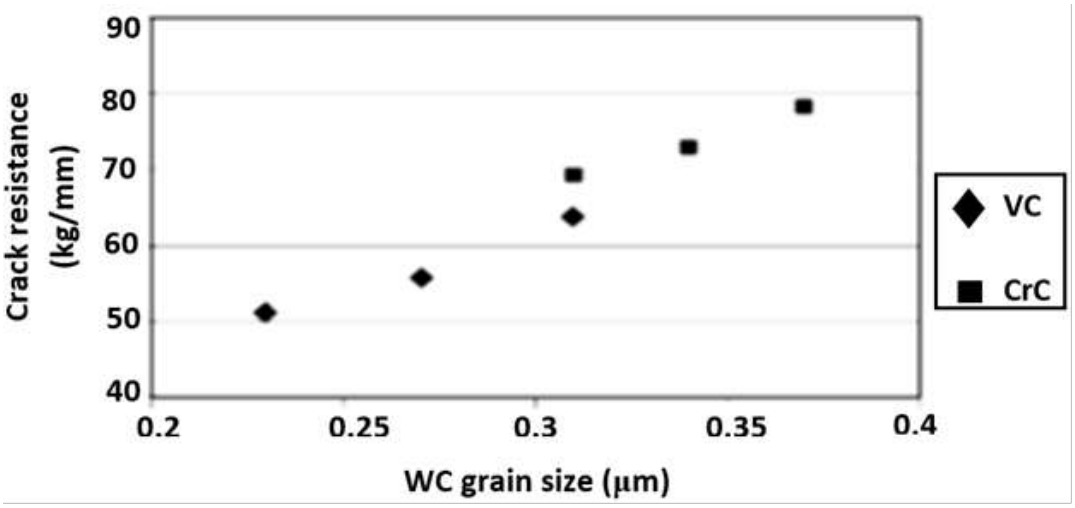

Figure 2.18. Effect of WC grain size on the crack resistance of WC-Co when grain refiners are added (in the legend VC and CrC stand for V_8C_7 and Cr_3C_2) [2001Luy].

2.3.3. Wear Behavior of Cemented Carbides

WC-Co cemented carbides are highly wear-resistant materials, and thus are used for cutting tools [2004Pir], drilling and mining equipment [2002Gil]. In general, friction and wear is believed to result from three components: adhesion, plowing and asperity deformation [2004Pir].

There are three main types of wear: abrasive, erosive and sliding. Sliding wear is the most complex in the way different materials respond to sliding conditions [2004Pir]. Archard [1953Arc] developed an equation for the wear volume, W_v (mm^3):

$W_v = ksF_n.H^{-1}$ Equation 2.6

where:

k = dimensionless wear coefficient

s = sliding distance (m)

F_n = normal force (N)

H = Vickers hardness number of the softer material.

Trent [1963Tre] observed that wear was caused by the diffusion of tungsten and carbon into the workpiece, and that the lower rates of diffusion wear for complex carbides were due to the lower solubility of the mixed carbide phases in the iron-based workpieces. In agreement with Trent [1963Tre], Hedenqvist and Olsson [1991Hed] stated that the wear process involves both

mechanical and chemical interaction between the tool and workpiece, and is mostly governed by the cutting forces, cutting speed and chemical compositions of the tool and workpiece. Larsen-Basse *et al*. [1974Lar] reported that wear of the tools of all cobalt contents appeared to take place by a combination of cobalt erosion and microfracture of the carbide skeleton. They attributed much of the weight loss to the carbide skeleton microfracture. Masuda *et al*. [1993Mas] also attributed wear of WC-Co alloy tools to a loss of WC particles due to brittle fracture. However, too small amounts of wear debris to be compatible with grain fracture were found by Nacrheim and Trent [1977Nae], indicating little abrasive wear during cutting.

The sliding wear resistance depends in a complex manner on cobalt content, grain size and hardness of the composite, and no conventional fracture or plastic deformation of the carbide grains was observed [1997Jia]. Earlier research [1988Gur] also stated that wear resistance and hardness are interrelated. During the machining of carbon and carbon-fibre reinforced plastic composites, Masuda *et al*. [1993Mas] found that smaller carbide grain sizes gave lower wear resistance, despite the increased hardness, and that decreased cobalt content led to decreased wear rates. Thus, although an inverse relationship exists between wear coefficients and bulk hardness of WC-Co alloys [1997Jia, 2004Pir], the most effective way to increase sliding wear resistance is to reduce cobalt content and to increase its grain size [1997Jia]. This relationship is valid typically for 0.5-1.5 μm grain sizes [1997Jia]. However, in terms of abrasion resistance, the wear rate increases with Co content and grain size [1993Mas], in agreement with previous studies [1984Des]. Olsson *et al*. [1988Ols] found that abrasive wear is only significant at low machining speeds. Masuda *et al*. [1993Mas] concluded that abrasive wear is not the primary factor during machining, thus, the contradiction between machining tests and abrasive wear tests.

Fracture resistance of the surface was recognized to be the most important parameter in determining the wear resistance [1974Lar]. Sheikh-Ahmad *et al*. [1999She] found binder removal by plastic deformation and micro-abrasion as the controlling wear mechanism, and that significant improvements in wear resistance were achieved by developing nano-structured cemented carbides with small mean free paths. The latter can be minimized by decreasing the carbide grain size, as well as the Co content [1998Upa]. With increasing binder content, bulk

hardness of composites decreases [1992Bro]. Coarse-grained cermets usually have lower abrasive resistance than fine or medium grain sizes [1984Des].

Wear modes can either be mild or severe. In mild wear, contacting materials polish each other, resulting in a low specific wear rate [1987Lim]. Severe wear produces a surface that is rough and deeply torn, and the wear rate is usually high [1987Lim]. At high temperatures, high speeds and loads, diffusion wear is the main mechanism [1976Nar, 1980Aka]. Other combinations of wear mechanisms also exist in aggressive wear conditions, i.e. surface polishing of WC grains (micro-abrasion), creation of wear debris particles, formation of adhered tribofilms, surface binder removal, grain cracking, grain fracture and/or pull-out [2010Bon]. Plastic deformation of asperities results in micro-abrasion and wear debris particles [1996Wan, 2010Bon]. The compaction of wear debris and/or the smearing and/or oxidation of binder phase results in the formation of adhered tribofilms [2000Eng]. During sliding wear, there are fluctuating forces between the contacting surfaces resulting in the relative oscillating motion of WC grains [2010Bon]. This relative motion of WC grains results in removal of the binder phase, followed by cracks between the grains and finally grain pull-out [2010Bon]. It was also observed that wear of WC–Co alloys was caused by preferential removal of the cobalt binder from between the tungsten carbide grains by plastic deformation and micro-abrasion [2004Pir]. Binder removal was followed by fracture and fragmentation of the carbide grains, which were then dislodged from surface of the grade.

2.3.4. Corrosion of Cemented Carbides

Although cemented carbides have found many engineering applications, their usefulness in chemically aggressive environments has been less successful due to their high susceptibility to corrosion [2010Kon]. The poor corrosion resistance of cemented carbides in aqueous solutions reduces their applications there [2005Sut]. The corrosion behavior of WC-Co hardmetals is controlled by the corrosion resistance of the binder phase [1980Gha, 2003Sut], since the oxidation potential of WC is nobler than Co ions [2004Sch]. The formation of tungsten oxides is a result of high tungsten content, and this in turn leads to a decreased dissolution rate in the pseudopassive region [2005Sut].

Cemented carbides suffer galvanic corrosion since they are heterogeneous materials. The cathodic reaction involves reduction of oxygen or hydrogen at the WC phase [2008Hoc]. Tomilson *et al*. [1988Tom] confirmed the selective dissolution of (Co), after which the remaining carbide skeleton fractures [1974Blo]. Therefore, the life of tools made from cemented carbides is seriously shortened in chemically aggressive environments, since corrosion attack proceeds predominantly at places where WC has fallen out after localized initiation of corrosion [2007Hoc]. However, since the (Co) binder phase contains W and C, it is more resistant to corrosion than pure Co [2003Sut, 2007Hoc]. The dissolved W and C results in the stabilisation of the (Co) fcc phase [1998Hum, 2007Hoc] which has better corrosion resistance than hcp (Co) [2013Seb].

For high-velocity oxygen-fuel (HVOF) sprayed WC-Co cermet coatings [2006Cho], it was shown that chemical composition of the metallic binder and control of micro-cracks are the most important factors influencing the corrosion resistance [2006Cho]. Wet abrasion resistance was found to increase with lower Co content [2007Luy]. The results were attributed to the effect of Co content on the corrosion resistance, since wet abrasion resistance proceeds via corrosion and abrasion.

For WC-VC-Co alloys, it was observed that corrosion resistance decreased with Co of up to 30 wt% [2003Bro]. In WC-Co alloys where corrosion resistance decreases with Co content the trend is to decrease the Co content, but that compromises the toughness of the alloys [2003Bro]. Therefore, VC additions might allow for higher Co contents without compromising both corrosion resistance and toughness.

2.4. VC Additions to Cemented Carbides

The control of grain size is very important during sintering of WC-Co alloys, since the average grain size and the size distribution significantly affect many physical properties [1995Spr, 1991 McC]. The presence of a few substantially larger than average grains from abnormal grain growth (AGG) is detrimental to strength [2000Cho]. Allibert [2001All] stated that abnormal grain growth (AGG) is caused by dissolution-precipitation of WC grains. Only faceted grains

such as WC grains in a (Co) matrix grow abnormally during coarsening [2000Cho]. To inhibit AGG, small concentrations of other metal carbides such as VC, Cr_3C_2, NbC, TaC and their mixtures are usually added to WC-Co to inhibit grain growth during sintering [1995Spr].

Among the grain growth inhibitors, VC is the most attractive due to its physical and mechanical properties, such high Vickers hardness [1996Luy, 2011Bol]. The order of effectiveness of carbides for grain inhibitors was found to be VC > Cr_3C_2 > NbC > TaC > TiC > ZrC [2001Wit]. Therefore, VC addition has received much attention by researchers [1996Luy, 2000Cho, 2001Are, 2001Zin, 2005Mac, 2005Mor, 2009Wei, 2011Bol, 2011Mah]. Additions of VC to WC-Co alloys are usually done in small amounts (about 1 wt%), just to inhibit grain growth during sintering [1977Mad, 1995Spr]. Mader *et al*. [1977Mad] found that the maximum beneficial content of VC that could be accommodated in WC-TaC-TiC without causing embrittlement was 2.5 wt%. When nanocrystalline WC-10Co composite powders doped by 1.0% VC were sintered at 1360°C, ultrafine WC-10Co cemented carbide with an average grain size of <300 nm and better mechanical properties than those obtained from coarser grain grades were achieved [2004Shi]. The mechanism for grain growth inhibition of WC by VC has been attributed to the segregation of V at the WC/(Co) interface [1998Jar]. The grain growth inhibition mechanism was also studied by Cho *et al*. [2000Cho], who observed that when a small amount VC was added, the grain growth process was significantly hindered and AGG suppressed. However, after heat treatments of 16h, the specimens with VC exhibited enhanced AGG behavior. It was suggested that the VC addition is likely to increase the surface energy of a WC crystal, so that the growth controlled by two-dimensional nucleation was retarded. In this case, only a very few exceptionally large grains grew with a reduced rate, so that prolonged heat treatment resulted in enhanced AGG behavior in the WC-VC-10Co specimen.

Randt *et al*. [2000Ran] used V_8C_7, WC and Co as the starting powders for WC-VC-Co alloys. After sintering, the alloys were composed of WC, (W,V)C and (Co) with a mean carbide grain size of 1-2 μm, which is defined as 'fine' [1997Whi]. A comparison between the properties of VC and WC is shown in Table 2.3 [1998Luy]. Table 2.3 [1998Luy] shows that WC has superior properties for the coefficient of thermal expansion, solubility and elastic modulus, but VC has

better hardness and is much lighter than WC. Reasonable properties were also observed for the VC-TaC-TiC hardmetal following the complete substitution of WC with VC [1977Mad].

Table 2.3. Comparison of properties of WC and VC [1998Luy].

Property	VC	WC
Density ($g.cm^{-3}$)	5.7	15.7
Microhardness at 50g ($kg.mm^{-2}$)	2 950	2 080
Elastic Modulus ($kN.mm^{-2}$)	422	696
Coefficient of Thermal Expansion (K^{-1})	7.2×10^{6}	5.0×10^{6}
Solubility in cobalt (wt%)	6	22
Solubility in iron (wt%)	3	7

Luyckx *et al*. [1996Luy] found that up to 10 wt% VC additions to WC-10Co wt% alloys resulted in improved sinterability than expected. They observed higher hardness for WC-VC-Co alloys than WC-Co alloys for equal Co content. The different sintering temperatures of 1330°C and 1390°C used by Luyckx *et al*. [1996Luy] did not affect the mean carbide grain size.

Luyckx *et al*. [1996Luy] attributed the lower toughness of WC-VC-Co to the brittleness of the VC grains, which were of average size ≥10 μm. The large grains offered an easier path of crack propagation [1997Osb]. The use of finer starting powders (<1 μm) prevented the formation and growth of cracks in WC-VC-Co alloys, and also kept the final grain size small during sintering [1997Osb]. Osborne *et al*. [1997Osb] carried out one of the earliest studies on the production of fine grained WC-Co-VC alloys, and prepared fine V_8C_7-WC and V_4C_3-WC powders with the final aim of producing VC-WC-Co hardmetal where the VC grain size was ~1-2 μm. Particular attention was paid to characterisation of the powders at all stages, mixing and milling of the powders and carburization of powders. It was concluded that a V_8C_7-WC powder of mean particle size between 1 and 2 μm could be produced from at least the following two routes:

- Milling a mixture of coarse V_8C_7 and tungsten carbide powders, with a 0.5 wt% Co addition for 48 h, followed by a 3 h heat treatment at 1200°C.
- Milling a mixture of coarse V_2O_5, tungsten carbide and carbon black powders for 48 h, which is then carburized at 1200°C for 3 h.

Osborne *et al*. [1997Osb] identified the second route to be more economical, on the basis that V_2O_5 was cheaper than pre-formed V_8C_7, although the most effective route for the production of V_8C_7-WC powder for VC-WC-Co can be only assessed after sintering. Whitefield [2011Whi] recommended mechanical alloying of the WC and VC starting powders. Mechanical alloying (MA) is a solid-state powder processing technique involving repeated welding, fracturing, and rewelding of powder particles in a high-energy ball mill and produces composite metal powders with controlled microstructures [1974Ben].

Cho *et al*. [1997Cho] observed the formation of solid solutions between WC and VC compounds (V_8C_7 and V_4C_5) in the form of $(W,V)C_x$, and found that up to 18-36 wt% WC can be replaced by VC. However, Whitefield [2011Whi] stated that the mechanical tests of Cho *et al*. [1997Cho] were not representative of the alloys they studied, since the alloys were not fully densified.

Cho *et al*. [1997Cho] showed that VC additions to WC-10Co up to approximately 1:1 WC:VC resulted in higher microhardness and strength in sintered alloys (Figure 2.19). Arenas *et al*. [1998Are] found that VC in WC-10Co alloys inhibited the η phase formation, due to the formation of the cubic phase, γ, with WC in solid solution, i.e. γ-$(W_xV_y)C$, as well as $(W_{0.09}V_{0.24})C$ and $(W_{0.22}V_{0.43})C$, increasing the contiguity of the carbide network up to approximately 50 wt% WC substitution. The VC additions to WC-Co increased hardness [1996Luy, 1997Cho, 1998Are]. The WC-VC-Co alloys had lower toughness than WC-Co alloys of equal cobalt content, but had better toughness than WC-Co alloys of equal hardness [1996Luy]. Similar results were also found in the case of nanograde WC-Co by Whitefield *et al*. [1997Whi] who produced WC-VC-Co hardmetal grades from powders consisting of 10 wt% V_8C_7 and 10 to 15 wt% Co. All WC-VC-Co grades had higher coercivity and hardness than nanograde WC-Co of equal binder content and WC grain size of 0.4 μm. At hardnesses higher than 1700 HV, the toughness of the WC-VC-Co grades was higher than the corresponding WC-Co nanogrades.

Figure 2.19 [1997Cho] shows that the hardness and fracture strength of WC-VC-10Co alloys were related. The toughness was explained by the increase in binder mean free path, L_β, the

decrease in the amount of the brittle η phase and a possible solid solution hardening effect of the γ-phase which might strengthen the sintered body at high temperature [1998Are].

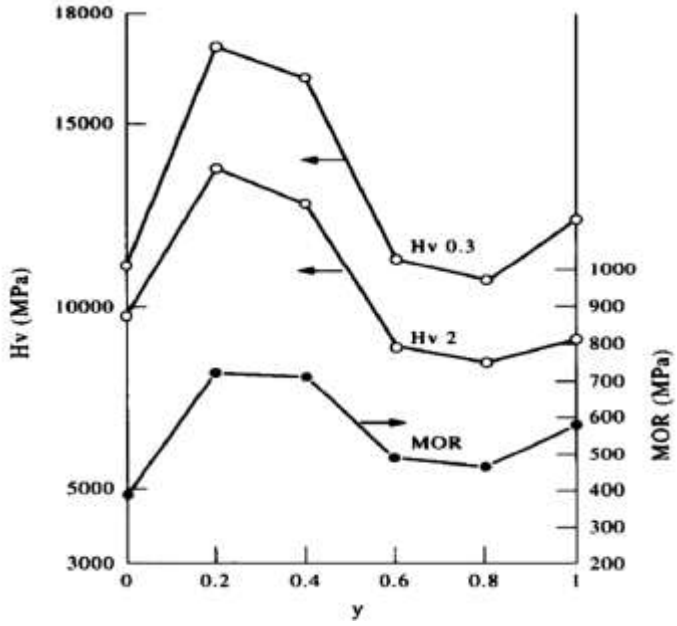

Figure 2.19. Hardness and fracture strength with composition of 90[(1-y)WC-yVC]-10Co cemented carbides where 0.3 and 2 stand for 0.3 and 2 kg, respectively, and 'y' is VC proportion [1997Cho].

The WC-VC-Co alloys with (W,V)C grain sizes of 10-15 μm had better abrasion and erosion resistance than WC-Co [1996Luy, 1998Luy]. Good results [1996Luy, 1998Luy] were obtained, even though WC-VC-Co alloys were not optimized, having the η phase. The results therefore confirmed the suitability of WC-VC-Co as a suitable substitute for WC-Co in some applications. It was also confirmed that finer (W,V)C grain sizes resulted in better mechanical properties. Finer starting powders resulted in smaller mean VC grain sizes, and thus cracks forming in the VC grains would be much shorter than the critical crack size of the material [1996Luy].

Choi *et al*. [2000Cho] produced WC-30Co and WC-1VC-30Co wt% alloys, heat treated at 1500°C for 64h. They observed that VC acted as a grain growth inhibitor only during the early stages of heat treatment, but with prolonged heat treatment, coarse WC grains were observed. They observed that additions of VC resulted in a bimodal WC grain size distribution, instead of

the uniform distribution observed for WC-Co alloys. The bimodal grain size distribution might be due to the high grain growth observed after prolonged heat treatment.

Arenas *et al*. [2001Are], studied the effects VC additions on the sintering behavior, hardness, toughness, elastic properties and wear in 90[(1-*x*)WC-*x*VC]-8Co-2Al wt% alloys, prepared by vacuum sintering in the 1350-1500°C range. Additions of VC up to 13 wt% improved sintered alloy densification. Vickers hardness and toughness varied oppositely, from 12.8-17.5 GPa and 10.5-7.7 $MPa.m^{1/2}$, respectively. Vanadium carbide additions reduced the sliding wear performance of the alloys.

Morton *et al*. [2005Mor] studied the effectiveness of grain growth inhibitors as a function of temperature and carbon content. They observed that in C-saturated WC-Co alloys, the effect of VC as a grain growth inhibitor was not a function of temperature, whereas the other inhibitors (Cr_3C_2, NbC, TaC and TiC) improved with temperature. The TiC and VC inhibitors were strongly affected by C content, but TaC, NbC and Cr_3C_2 were unaffected. Lower C contents favored the dissolution of TiC and VC in the binder, thereby promoting interference with adsorption and desorption processes at the surfaces of WC grains [2005Mor]. Morton *et al*. [2005Mor] also observed that for C deficient WC-Co alloys, all the five inhibitors improved with temperature. They also observed that fluctuations of temperature within the typical sintering range of 1400-1450°C would not cause any variations in hardness or magnetic coercivity of alloys containing Cr_3C_2, NbC, TaC or TiC inhibitors.

Vanadium can be co-added with other grain growth inhibitors e.g. TaC [2011Mah]. Mahmoodan *et al*. [2011Mah] added 0.6 wt% TaC and 0.7 wt% VC to WC-10Co wt% alloys. They found improvement in both hardness and fracture toughness with inhibitor additions. They reported that TaC was responsible for the improved toughness.

Instead of VC, elemental V can be used to form the (V,W)C microstructure of WC-Co alloys [2009Wei, 2011Bol]. Vanadium increased hardness and WC contiguity, and decreased WC grain size [2009Wei]. Both fcc and hcp (Co) binder phases were observed with V additions, contrary to what was observed for Mn, where only the fcc (Co) phase was observed [2009Wei].

According to Weidow *et al*. [2009Wei], the relatively high fcc to hcp transformation temperature for Co with dissolved V is responsible for the existence of both crystal structures. In addition to (V,W)C, fcc $Co_{15}W_8C_6$ and rhombohedral V_2O_3 were formed during sintering [2011Bol]. The fcc $Co_{15}W_8C_6$ phase was formed by the reaction of fcc W, Co and available C [2011Bol]. The rhombohedral V_2O_3 was due to the stabilisation of V by O, and this reaction was the last to occur after all C had reacted; otherwise V_2O_3 could have been reduced [2011Bol].

Lovelock *et al*. [1998Lov1] observed an insignificant effect of spray parameters in high performance/high velocity oxygen fuel (HP/HVOF) process on the wear resistance of WC-Co coatings. However, they observed that the powder type and size significantly affected the wear rate of WC-Co thermal spray coatings. The initial powder composition and its surface/volume ratio affected the WC decomposition, which in turn affected properties like wear resistance [1998Lov2]. Therefore, addition of VC to WC-Co alloys is expected to affect physical and mechanical properties.

The composition range for the formation of WC-(V,W)C_x-Co materials was determined by Obbard *et al*. [2001Obb]. They plotted a partial isothermal section (Figure 2.20) at 1450°C from results deduced from phase compositions and crystal structures in the series at 50 at.% Co with large liquid contents. For V/(V + Co) < 0.06, the constitution was comparable to that of WC-(V,W)C*x*-Co ternary alloys with similar C content. Vanadium dissolved in the Co-based liquid and in the η phase for W/C > 1. These results were in agreement with those from previous studies in WC-Co mixtures with 3 at.% Co substituted for V [1999Lav]. The maximum W content was shown to evolve from 24 to 50 at.% [2001Obb]. Obbard *et al*. [2001Obb] also found that at 1450°C, the (Co) phase was liquid and dissolved approximately 12-8 at.% C and 11-14 at.% (W+V). The limit compositions of (V,W)C_x were found to be 15.4 W, 43.2 C (at.%) and 23 W, 40.5 C (at.%) on the C-rich and W-rich sides.

For V/(V + Co) > 0.06, Obbard *et al*. [2001Obb] reported that the formation of the carbide (V,W)C_x was a function of the carbon content. They found two four-phase fields {L^C + WC + (V,W)C_x^C + C} and {L^W + WC + (V,W)C_x^C + C + η} on the C-rich and W-rich regions, where L^C and (V,W)C_x^C stand for the liquid phase and the V-based carbide in the W-rich side. At 1450°C,

limit phases had fixed compositions that were compared to the limit compositions of the similar W-C-Co regions.

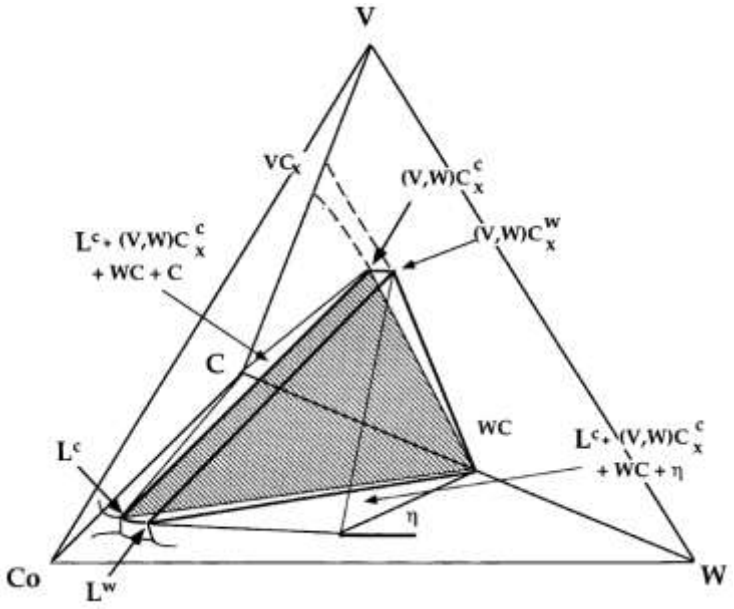

Figure 2.20. Isothermal section at 1450°C of the W-V-C-Co system for phase compositions and crystal structures in the series with 50 at.% Co [2001Obb].

The compositional limits of the liquid, L and η could not be established in the three phase fields: {L + (V,W)C_x + C},{L + WC + (V,W)C_x + η} and {WC + (V,W)C_x + η} [2001Obb], although the results revealed the composition fields with (V,W)C_x and/or η larger than those containing WC. The results were consistent with those of V for W substitution in VC_x.

Obbard *et al*. [2001Obb] confirmed the existence of the three-phase field {Co solution + WC + (V,W)C_x} expected from W-C-Co and W-V-C, which was found between two four-phase domains {Co solution + WC + (V,W)C_x + C} and {Co solution + WC + (V,W)C_x + η}. As mentioned in Section 2.2.2 [2001Obb], the composition range for the formation of WC-(V,W)C_x-Co corresponded to a narrow strip located along the plane defined by the relation (C/ (V+W) = 1 – 0.33 V/ (V+W)) for 0 < V/ (V + W) ≈ 0.72.

It was predicted that precipitates of (V,W)C_x were present in cemented carbides up to 1200°C [2001Obb]. Obbard *et al*. [2001Obb] found that (V,W)C_x dissolved in the (Co) binder from about

1200°C in WC-VC-Co alloys with V/(Co + V) ~ 0.03 and from about 1450°C for V/(Co + V) ~ 0.06 alloys. The features of the interfaces between the various phases at both 1200°C and 1450°C, varied with C/W ratio. The dissolution of WC also resulted in the formation of $(V,W)C_x$.

Zinyana *et al*. [2001Zin] studied fifteen W-V-C-Co alloys of varying compositions sintered at 1450°C for 5 hours, and quenched. They observed $(V,W)C_x$ phases in the (Co) matrices. The microhardness of $(V,W)C_x$ depended on both the V/(V+W) and the C/(V+W) ratios. The highest microhardness was achieved at a V/(V+W) ratio between 0.8 and 0.88. Low C alloys had higher hardness than high C alloys for equal V/(V+W) and C/(V+W) values. Although the alloys had been quenched, the microhardness of $(V,W)C_x$ was nearer to that of ordered VC_x than disordered VC_x. The microhardnesses were attributed to high diffusion rates.

Machio *et al*. [2005Mac] studied the effects of additions of 10 wt% VC to WC-12Co and WC-17Co (wt%) coatings. Commercial WC-12Co and WC-17Co (wt%) coatings were used for comparison. The coatings deposited on stainless steel substrates were tested under identical conditions for abrasion and slurry erosion resistance, using a high pressure high velocity oxy-fuel (HP/HVOF) thermal spraying. The addition of VC improved abrasion resistance, but did not affect slurry erosion. The improved abrasion resistance was attributed to VC which hindered WC grain growth, improved corrosion resistance and the reduction of (Co) volume fraction due to the formation of (V,W)C, with lower density than WC. The similarity in erosion resistance between WC-VC-Co alloys and commercial WC-Co alloys was due to the presence of hard (V,W)C grains with low resistance to impact fracture.

Luyckx and Machio [2007Luy] later studied the compositions and microstructures of the WC-VC-Co and WC-Co coatings in order to understand why WC-VC-Co coatings had superior abrasion resistance. They attributed the superior dry abrasion resistance mainly to the smaller WC grain size of WC-VC-Co coatings. The lower cobalt content of WC-VC-Co alloys was associated with higher wet abrasion resistance. Contrary to previous work [2013Seb], Luyckx *et al*. [2007Luy] found that the fcc (Co)/hcp (Co) ratio was unrelated to the presence of V. According to Sebeya [2013Seb], the fcc/hcp ratio of (Co) was higher in WC-VC-Co alloys and he/she attributed this (Co) stabilisation to the presence of V. Sebeya [2013Seb] studied fully

dense sintered bulk samples, whereas Luyckx *et al*. [2007Luy] investigated powders. Luyckx *et al*. [2007Luy] therefore attributed their different result to the porosity of their powders, and to the different magnitude and distribution of internal stresses that control the (Co) fcc $\rightarrow$ hcp transformation.

Ogunmuyiwa *et al*. [2013Ogu] added 10% VC to WC-Co and produced WC-VC-Co materials of better hardness than WC-Co materials, with comparable toughness and a lower density for weight saving applications, thus confirming VC a good substitute for WC. The additions of VC led to grain refinement of WC in both coatings and sintered materials, with general improvement in the wear performance. Ogunmuyiwa *et al*. [2013Ogu] found WC-12Co (wt%) and WC-10VC-12Co (wt%) coatings (thus unsintered) with the same binder content did not differ significantly in hardness. According to Ogunmuyiwa *et al*. [2013Ogu], VC in large quantities did not seem to affect hardness, thus coatings with WC-12Co (wt%) and WC-10VC-12Co (wt%) had almost similar hardnesses. However, for the sintered alloys, the WC-10VC-12Co (wt%) alloy had a 10% higher hardness than the WC-12Co (wt%) alloy, as a result of the formation of the WV_4C_5 phase.

Sliding wear rates of the 10wt% VC coatings were lower than those of the WC-12Co (wt%) coatings of same Co content [2013Ogu]. The friction results might have been affected by the formation of oxide films which were detected using XRD. These oxide films formed, even though the tests were conducted at room temperature and at low sliding velocity (0.26 m/s). Ogunmuyiwa *et al*. [2013Ogu] suggested that the flash temperatures could have led to the formation of oxides, but they had no equipment to measure the flash temperatures. Similar results were also obtained for sintered alloys where the wear coefficient of the WC-10VC-12Co (wt%) alloy was lower than that of the WC-12Co (wt%) alloy.

Ogunmuyiwa *et al*. [2013Ogu] observed an increase in slurry erosion with VC additions for coatings at all impact angles tested (45° - 90°). They also observed a further improvement in erosion resistance when the Co content of the VC-coatings was increased from 12 wt% to 17 wt% was at impact angles greater than 60°. This was attributed to the optimized processing parameters used for the 17 wt% Co coatings, which resulted in a higher inter-splat strength, which improved erosion resistance [2013Ogu]. As for conventionally sintered alloys, the highest

erosion rates for WC-12Co (wt%) and WC-10VC-12Co (wt%) were at an impact angle of 90°, and the lowest erosion rate at 45°. Below an impact angle of 65°, the erosion rates were similar. Above 65°, the erosion rate of the WC-12wt%Co alloy was higher than that of the WC-10VC-12Co (wt%) alloy, and at 90° it was approximately 50% higher. Wentzel *et al*. [1995Wen] found that erosion-corrosion of carbides decreases with hardness.

2.5. Ruthenium Additions to Cemented Carbides

Studies involving the interaction of different carbides and precious metals at elevated temperatures have shown that in almost all cases, the metal reacts with the carbide to produce free carbon in the form of graphite and undesirable very brittle intermetallic compounds [1968War, 1995Gui], for example:

$WC + Pt \rightarrow (W, Pt)_{(intermetallic\ compound)} + C_{(graphite)}$.

The phase diagram data and *ab initio* results for fcc and bcc Pt-W alloy could be accounted by the CALPHAD method provided an unusually large enthalpy was given to the metastable fcc W [1995Gui].

However, Ru was found not to form intermetallic compounds when reacted with WC, even after prolonged sintering [1968War]. Ruthenium was also found to stabilize the (Co) hcp phase at higher temperatures [1958Han], therefore retaining a phase that imparts less friction on a workpiece than the cubic phase.

Investigations have been done on the effect of Ru and VC additions on the hardness [2001Shi] and corrosion resistance [2011Pot] of WC-Co alloys (Table 2.4).

Ruthenium additions to WC-Co alloys increased hardness (Table 2.4 and Figure 2.21), but concentrations higher than 15 wt% decreased toughness [2001Shi] (Figure 2.22). However, Ru improved hardness less than VC (Figure 2.22), and the decrease in toughness was higher for WC-Co-Ru alloys than WC-VC-Co alloys (Figure 2.22). Shing *et al*. [2001Shi] attributed the decrease in toughness to the hardening of the binder, because Ru remained in solution in the cobalt due to its unlimited solubility [2001Shi] (Figure 2.23). They also attributed the lower decrease in toughness caused by VC than Ru, to lower solubility of VC in (Co), since the

toughness of WC-Co is mainly due to the plasticity of the binder and plasticity decreases with increasing solute concentration. An optimum binder Ru content of about 15 wt% was found [2001Shi].

Shing *et al*. [2001Shi] contradicted claims by Bonjour [1980Bon] who had found up to 1.2 wt% Ru additions to cemented tungsten carbide (WC-6wt%Co) to harden the material without increasing toughness. According to Shing *et al*. [2001Shi], Bonjour *et al*. [1980Bon] compared the properties of WC-Co and WC-Co-Ru alloys of equal binder content, although Shing *et al*. [2001Shi] kept Co constant (Table 2.4).

Table 2.4. The effect of Ru and VC additions to WC-10Co (wt%) alloys on the hardness and corrosion properties [2001Shi, 2011Pot].

Alloy	**Ru**	**VC**	**Hardness (HV_{30}) [2001Shi]**	**Corrosion Rate ($x10^{-2}$ mm/y) [2011Pot]**
1	-	-	1420	14.60
2	0.4	-	1430	10.24
3	1.0	-	1440	7.35
4	1.5	-	1464	7.54
5	2.0	-	1515	2.40
6	3.0	-	1520	2.24
7	-	0.4	1619	16.30
8	-	0.6	1718	-
9	-	0.8	1818	-

Shing *et al*. [2001Shi] also observed that the mean WC grain size decreased with increasing Ru (Figure 2.24). However, they observed that for equal grain refiner content, VC inhibited the grain growth of WC more than Ru (Figure 2.25).

Ruthenium additions were also found to increase the abrasion resistance [2001Shi]. The hardening of the binder phase was reported to be the cause of this, since the binder would be more difficult to remove, causing the WC grains to remain under the residual compressive thermal stresses exerted by the binder longer, thus hindering the formation of cracks in the grains (Figure 2.26). Cobalt has a higher coefficient of thermal expansion than WC and this causes

more stresses to be induced in Co [1952Gur, 1964Daw]. Thus, the presence of residual compressive stresses exerted on WC.

Potgieter *et al*. [2011Pot] found Ru additions to WC-Co alloys beneficial for corrosion resistance. They used the manufacturing procedure for WC-Co-Ru alloys of Bonjour [1980Bon], where the alloys were made by compacting together a layer of Ru powder (~17 μm mean particle size) and a layer of WC-10%Co mixed and milled powder (~1μm mean particle size) at ~1.5 MPa applied in the direction normal to the Ru/WC-Co interface. The samples were then heated to ~1000°C in a tube furnace, and held for 24 h in argon flowing at a rate of $3.33\times10^{-5}m^3.s^{-1}$. The sample was then sintered in vacuum at 1410°C for 1 hour. The sintered samples were then sectioned at the Ru/WC-(Co) interface using a diamond wafer blade.

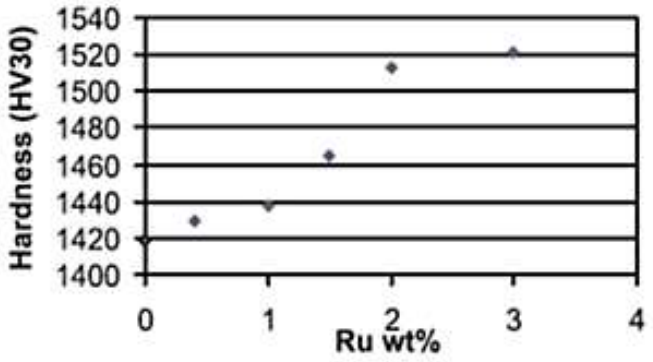

Figure 2.21. Effect of Ru content on the hardness of WC-10Co-Ru (wt%) alloys [2001Shi].

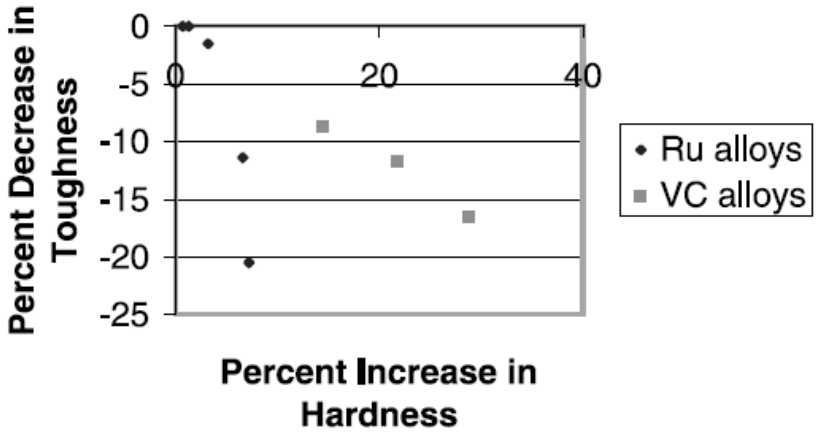

Figure 2.22. Comparison between the rate of decrease in toughness with increasing hardness in

WC-VC-Co and WC-Co-Ru (wt%) alloys [2001Shi].

Potgieter *et al*. [2011Pot] observed the open circuit potentials, OCP, to increase with increasing Ru (Figure 2.27). They attributed the positive shift of potentials to the spontaneous formation of a passive film, which would decrease the dissolution of the samples as the ruthenium increased. The alloy with 0.4 wt% VC had the lowest E_{OC} and the alloy with 3 wt% Ru had the highest E_{OC}. These observations [2011Pot] were confirmed by Konadu *et al*. [2010Kon] who found that high VC contents gave lower corrosion current densities than the base alloy in both HCl and H_2SO_4. The low acid corrosion resistance of WC-VC-Co alloys was also confirmed by Whitefield [2011Whi] who observed significantly higher wear rates for both WC-VC-Co and WC-VC-Co-Ni in acidic mine environments (silica mine) than in non-acidic mining environments (iron ore mine).

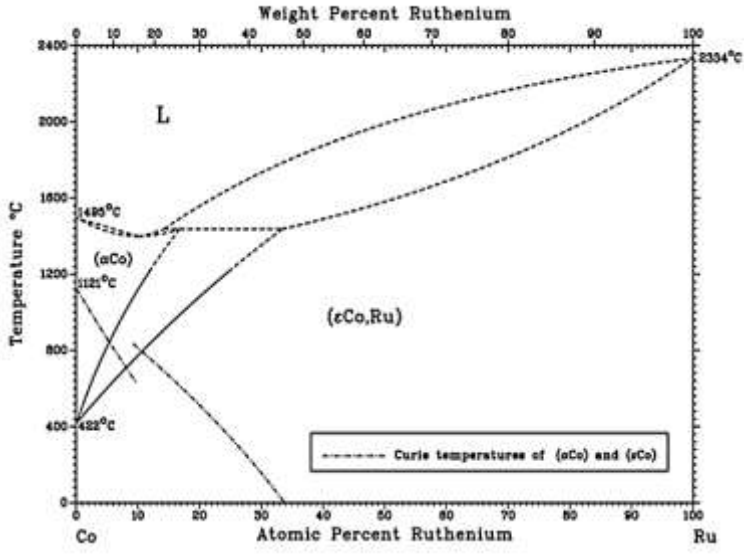

Figure 2.23. Co-Ru phase diagram showing unlimited solubility [1990Mas].

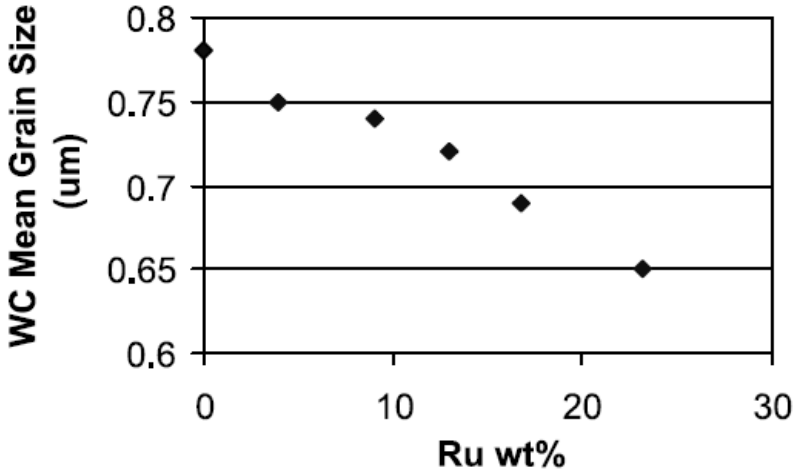

Figure 2.24. Effect of Ru content on the WC grain size in WC-10Co-Ru (wt%) alloys [2001Shi].

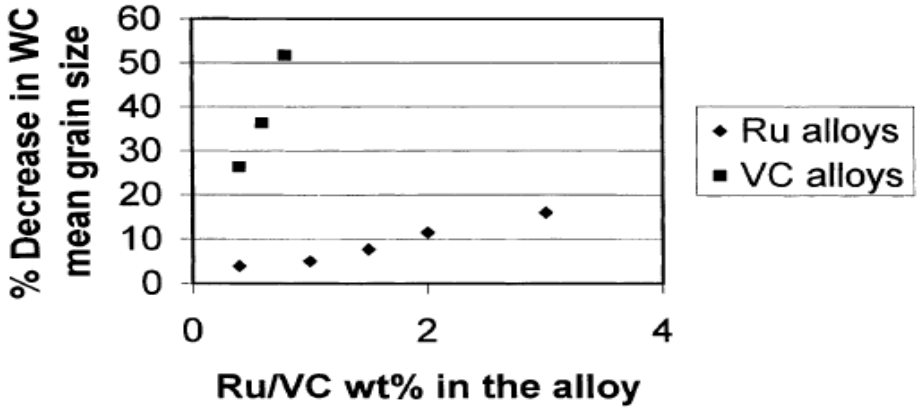

Figure 2.25. Comparison between the decrease in grain size with increasing grain refiner due to Ru or VC additions to WC-Co [2001Shi].

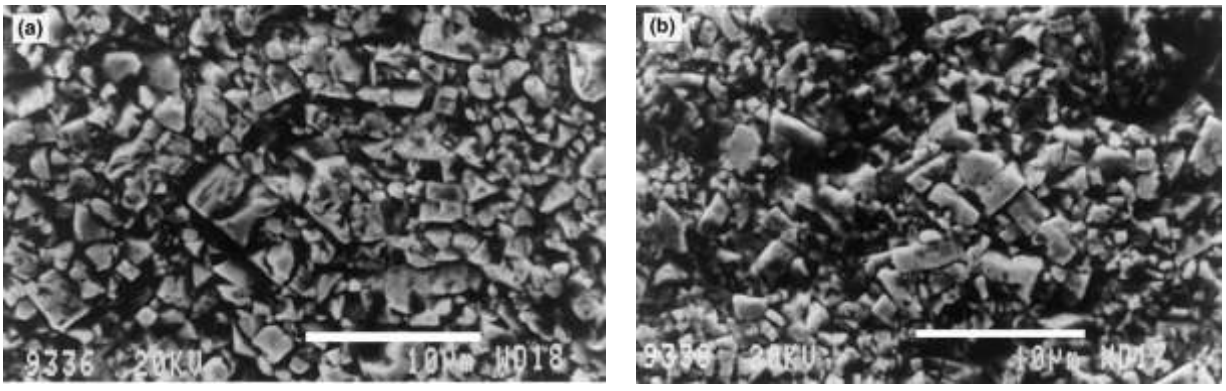

(a) (b)

Figure 2.26. SEM-SE micrographs of worn surfaces after drilling, showing: (a) WC grain micro-cracks in WC-6 wt% Co, (b) no microcracks (an indication good wear resistance) in WC-5.1 wt% Co-0.9 wt% Ru [2001Shi].

All the polarization curves in 1 M H_2SO_4 showed typical active-passive transitions (Figure 2.28) [2011Pot], contrary to previous findings [1996Hum, 1997Hum, 1998Hum] that WC-Co alloys did not undergo any active-passive transition in 1N sulphuric acid, but exhibited direct passivation. Potgieter *et al*. [2011Pot] observed an increase in the corrosion resistance of WC-Co alloys with ruthenium content (Table 2.4 and Figure 2.29) and studied the passivation ranges (Figure 2.30). For the alloy containing 0.4% VC they observed a negative shift in E_{corr}. The current density, i_{crit}, decreased significantly with Ru concentration, from 12.90 $A.m^{-2}$ to 1.42 $A.m^{-2}$.

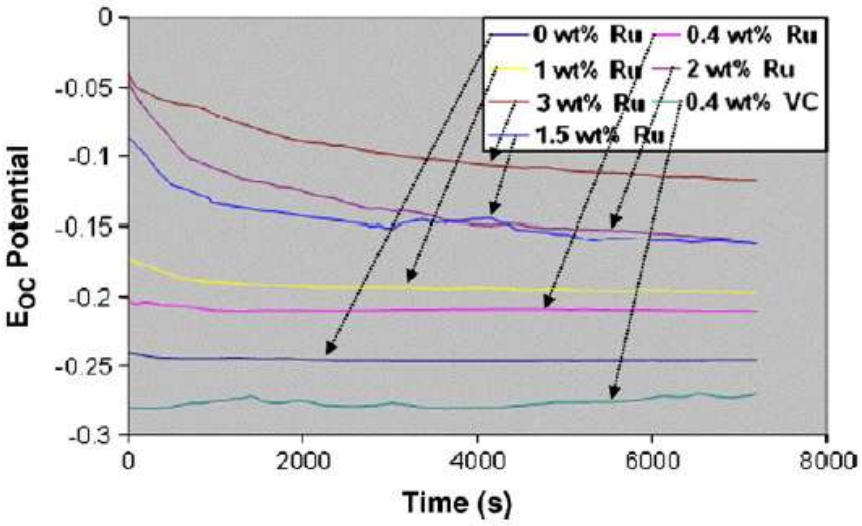

Figure 2.27. Open circuit potentials of samples exposed to 1 M H_2SO_4 [2011Pot].

Potgieter *et al*. [2011Pot] attributed the improvement of corrosion resistance by ruthenium to the stabilising effect of ruthenium on the fcc (Co) phase, β. XRD analyses for WC-Co alloys with different ruthenium additions showed that (Co) phase retained its fcc structure. Sebeya [2013Seb] also reported that the fcc structure had better corrosion resistance than hcp, agreeing with Potgieter *et al*. [2013Pot], as well as other previous researchers [1998Hum, 2006Sri].

WC-Co-Ru alloys containing 1.0 wt% and 1.5 wt% Ru showed almost similar corrosion rates [2011Pot]. The optimum ruthenium addition was 2 wt%, since further additions did not improve corrosion resistance much.

Potgieter *et al*. [2011Pot] explained the increase in corrosion resistance of WC-Co alloys with Ru in terms of a synergistic mechanism of simultaneously decreasing the anodic dissolution and lowering the hydrogen overpotential to influence the cathodic part of corrosion. They also identified surface films consisting of WO_3, $WO_3 \cdot 1/3\ H_2O$, CoO and Co_3O_4 on the corroded WC-Co-Ru alloys after exposure to sulphuric acid. For the 3 wt% Ru alloy, only $CoSO_4$ was detected. Although Potgieter *et al*. [2011Pot] could not identify Ru or VC from SEM, XRD or Raman spectroscopy analyses, the presence of the two elements clearly affected the corrosion properties.

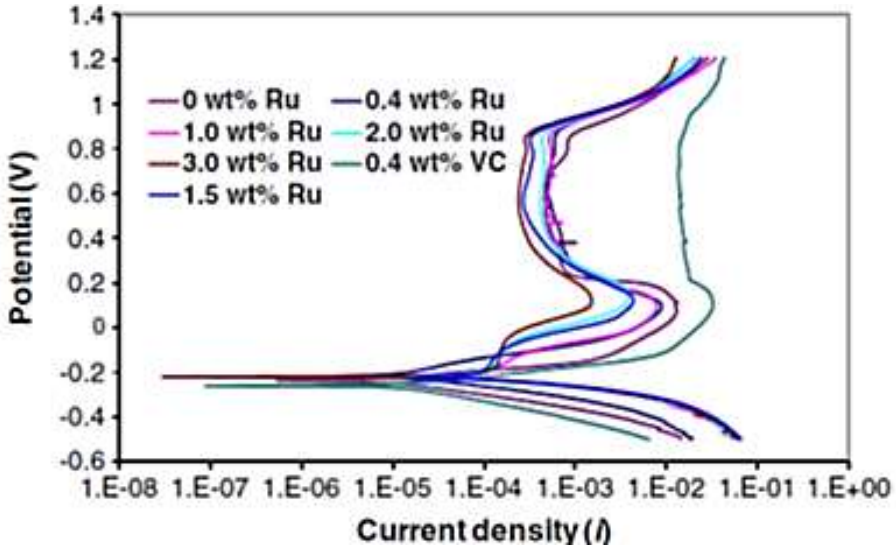

Figure 2.28. Current–potential results of the samples exposed to 1 M H_2SO_4 [2011Pot].

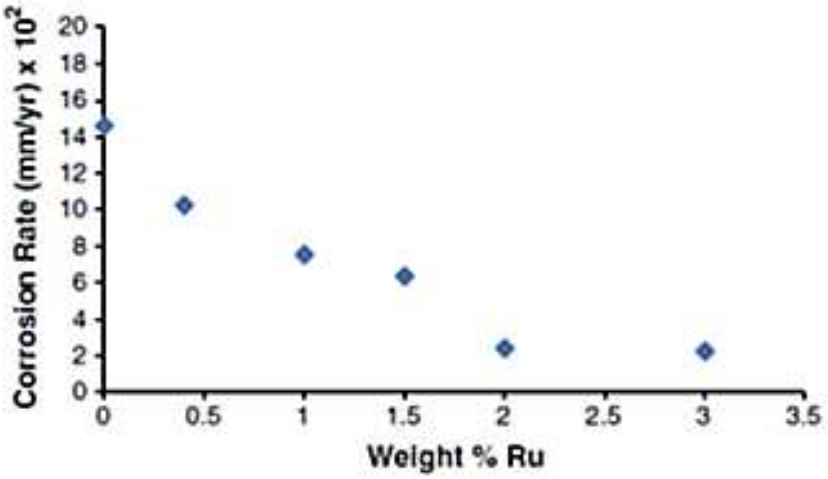

Figure 2.29. Effect of Ru additions on the corrosion rate of (90-x)WC-10Co-xRu alloys [2011Pot].

Both authors [2001Shi, 2011Pot] studied WC-Co-Ru and WC-Co-VC alloys. From their results, it can be postulated that having both Ru and VC in one alloy (i.e. WC-VC-Co-Ru) might result in superior hardness and corrosion properties than in either WC-Co-Ru or WC-Co-VC alloy.

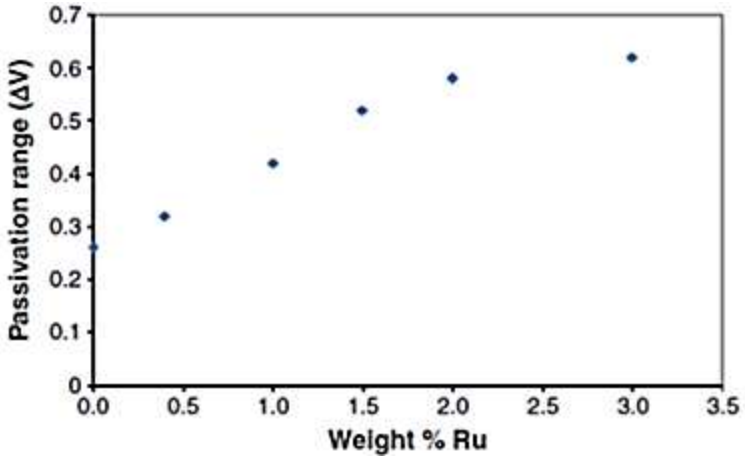

Figure 2.30. Effect of Ru additions on passivation potential range of the alloys in 1 M H_2SO_4 [2011Pot].

3. EXPERIMENTAL PROCEDURE

Powders were milled, compacted and sintered. Particle size analyses were done on raw and milled powders. The WC-VC-Co-Ru hardmetal grades underwent the same tests to establish the effect of ruthenium additions and different VC contents, on microstructure, mechanical properties and corrosion resistance.

3.1. Alloy Production

3.1.1. Starting Powders

Particle size analyses were done using a Microtrac S3500® at Pilot Tools and repeated using a Saturn DigiSizer® II at the South African Nuclear Energy Cooperation (NECSA). The analyses involved adding each of the powders to ethanol, followed by adding a few drops of calgon (1 g of sodium hexametaphosphate dissolved in 1 litre of water) to disperse the powders. A few drops of the alcohol containing dispersed powder were then placed inside the particle size analyser. The particle size analysers had in-built ultrasonic probes for additional powder deagglomeration. For reproducible results, the particle size analysing systems were optimized by adjusting settings of pump speed, ultrasonics and stirrer speeds. Particle size analyses were also done on milled samples.

The alloy contents were varied according to the following relationships:
80WC-10VC-(10-x)Co-xRu ($0 \leq x \leq 3$) (wt%),
(89.6-x)WC-10Co-0.4VC-xRu ($0 \leq x \leq 2$) (wt%),
(89.2-x)WC-10Co-0.8VC-xRu ($0 \leq x \leq 2$) (wt%), and
89.6WC-(10-x)Co-0.4VC-xRu ($0 \leq x \leq 3$) (wt%).

Powders of WC, VC, Co and Ru were mixed by ball milling to give compositions shown in Table 3.1. Compositions 1, 7 and 10 were for control. After milling, a sample was taken from each of the compositions for XRD analyses.

Table 3.1. Compositions of samples (wt%).

Alloy Series	Sample	Ru (wt%)	WC	VC	Co	Ru
80WC-10VC-(10-*x*)Co-*x*Ru	1	0	80.0	10.0	10.0	-
	2	0.4	80.0	10.0	9.6	0.4
	3	1.0	80.0	10.0	9.0	1.0
	4	1.5	80.0	10.0	8.5	1.5
	5	2.0	80.0	10.0	8.0	2.0
	6	3.0	80.0	10.0	7.0	3.0
(89.6-*x*)WC-10Co-0.4VC-*x*Ru	7	0	89.6	0.4	10.0	-
	8	0.4	89.2	0.4	10.0	0.4
	9	2.0	87.6	0.4	10.0	2.0
(89.2-*x*)WC-10Co-0.8VC-*x*Ru	10	0	89.2	0.8	10	-
	11	0.4	88.8	0.8	10	0.4
	12	2.0	87.2	0.8	10	2.0
89.6WC-(10-*x*)Co-0.4VC-*x*Ru (*Includes Alloy 7*)	13	1.5	89.6	0.4	8.5	1.5
	14	3.0	89.6	0.4	7.0	3.0

3.1.2. Milling of Alloy Powders

Milling was done for 8 h in a 1 kg capacity ball mill at a 30:1 ball-to-powder ratio, followed by turbular mixing at a 4:1 ball-to-powder ratio for 4 h. Polyethylene glycol (PEG) (3 wt% of powder weight) and alcohol (20 wt% of powder weight) were added to the raw powders prior to milling. The above parameters were determined after a series of tests involving comparing 100 g and 1 kg ball mills. The parameters and the corresponding results for these tests are given in Section 4.1.2.

3.1.3. Sintering

Green compacts of 10 mm diameter were produced by compaction using uniaxial pressure at 100 kN load. Removal of PEG was done by gradually raising temperature to 450°C. The green compacts were then sintered at a maximum temperature of 1430°C in an ULTRA-TEMP Sinter-HIP furnace. Furnace heating to 1430°C was done in stages using a proprietary process, and the

maximum temperature was maintained for 75 minutes. During the last 20 minutes, the pressure was raised and held at 4.4 MPa to eliminate surface porosity. A cooling rate of 3.5°C/ minute was then administered by switching on the cooling water pump.

3.2. Quality Tests

3.2.1. Density Measurements

A Sartorius ED224S density measuring instrument (Pilot Tools (Pty) Ltd) was used in accordance to the ISO3369 standard, based on the Archimedes' principle. Three samples were used for each composition, and the average values recorded. The specimens were first weighed in air, then weighed again while submerged in water. The sintered samples were submerged in water using a thin copper wire. The temperature of water in beaker was measured to correlate with density according to temperature-density values of Tanaka *et al*. [2001Tan].

The following equation was used to determine the density of the sample, ρ_s:

$$\rho_s = \frac{\rho_w \text{ x } M_a}{M_{wt} - M_w} \qquad \text{Equation 3.1}$$

where:

ρ_w = density of water (g/cm^3)

M_a = dry mass of sintered alloy in air (g)

M_{wt} = mass of wet sample in air (g)

M_w = mass of sintered alloy in water (g).

The densification was determined by considering the ratios between the actual and theoretical densities. The theoretical density is a function of the density and mass proportion of all the constituents of a composition, and is calculated using Equation 3.2.

$$\text{Theoretical density } \text{g/cm}^3 = 100 \left(\frac{x_1 \text{ wt\%}}{\rho_{x_1} \text{ g/cm}^3} + \frac{x_2 \text{ wt\%}}{\rho_{x_2} \text{ g/cm}^3} + \cdots + \frac{x_n \text{ wt\%}}{\rho_{xn} \text{ g/cm}^3} \right)^{-1} \qquad \text{Equation 3.2}$$

where:

x_n wt% = nth constituent mass proportion in the composition ($x_1 + x_2 + \ldots + x_n$) (wt%)

ρ_{x_n} = density of the n^{th} constituent.

3.2.2. Porosity Measurements

Etched and unetched samples were studied at x100 magnification in a light microscope, in accordance to ISO 4505-1978(E) [1978ISO]. A standard chart of porosity in cemented carbides was used (Appendix A).

The Archimedes' principle was also used to determine the porosities of three alloys per composition. This also involved weighing of samples in both air and water after boiling the samples in distilled water for 6 h, to fill pores and to remove bubbles. An oven was used to dry the samples at 85°C. The percentage porosity was calculated according to the following equation:

$$\% \text{ Porosity} = \frac{M_{wt} - M_a}{M_{wt} - M_w} \times 100 \qquad \text{Equation 3.3}$$

3.2.3. Magnetic Tests

Magnetic saturation values were measured using a Setaram Sigmameter Magnetic analyser (Pilot Tools (Pty) Ltd). Each of the alloy samples was first weighed, placed on a sample holder and inserted into the calibrated magnetic analyser. The saturation value, σ, of a sample was determined by comparing the apparent change in weight produced by the field gradient with that produced by 1 wt% Co (i.e. 2.02 $\mu Tm^3/kg$).

Coercivity measurements were done using a Forster-Koerzimeter 1.095 instrument (Pilot Tools (Pty) Ltd) according to ISO3326 standard. Each of the alloy samples was placed between two poles of a magnetizing yoke and the magnitude of the field was increased to maximum. The magnetic field was then decreased to zero. The sample was then removed and placed onto a sample holder and slowly inserted into a measuring coil until a maximum magnetization signal was obtained from the coercivity meter. The anti-polarizing field was increased until its signal dropped to zero.

3.3. Phase Identification and Microstructural Studies

3.3.1. Phase Identification

Phases present in powders and alloys were detected using a Bruker D2 Phaser, X-ray Diffractometer with a Co anode, at 25°C. The 2θ values ranged from 10° to 90°, with a step size of 0.026° and a scan rate of 1 s. A goniometer scanning axis with a radius of 240 mm was used. The specimen and irradiated lengths were both 10 mm. The generator voltage and current were set at 30 kV and 10 mA, respectively. A Phillips Analytical X'Pert HighScore® Software with an in-built database was used for phase identification. XRD patterns of initial powder mixtures, milled powders, as-sintered alloys and corroded alloys were obtained for phase identification. Raman spectroscopy was done to identify corrosion products, at room temperature, using a wavenumber scanning range of 100-2500 cm^{-1}. A light microscope and a laser source of Ar^{+} were used for Raman imaging and capturing the scan patterns.

3.3.2. Sample Preparation

The sintered samples were first mounted in conductive bakelite, then ground and polished using a Struers LaboPol-5 machine (Pilot Tools (Pty) Ltd). For grinding, Piatto 220 and 1200 wheels were used, and AKASEL 9 μm, 3 μm and 1 μm cloths, with Diamaxx diamond slurries, were used for polishing. Alloys for optical microscope studies were etched for 30s using Murakami's reagent [1985Van] to ascertain the presence of the eta (η) phase.

Two sample preparation methods, prior to hardness and fracture toughness measurements, were investigated i.e. extensive polishing and annealing. This was to find the best method for removal of residual stresses induced during grinding. Annealing was done at 800°C for 1 h in accordance to the ISO28079:2009 standard [2009ISO]. The extensive polishing method was done as prescribed by Zhang *et al*. [2008Zha]. Both sample preparation procedures are shown in Table 3.2.

Table 3.2. The two sample polishing procedures investigated.

Polishing stage	Method/ step time (min)	
	Extensive polishing	**Polishing + Anneal**
Polishing (9µm)	30	8
Polishing (3µm)	8	8
Polishing (1µm)	8	8
Annealing (800°C)	-	60

3.3.3. Microstructural Analyses

An AxioCam MRc AV31-KS optical microscope was used at lower magnifications, for example, during hardness measurements and porosity tests. For higher magnifications, a Carl Zeiss Sigma® Field Emission Scanning Electron Microscope (FESEM) was employed to reveal the microstructures of the sintered alloys with energy-dispersive X-ray spectroscopy (EDS) to analyse the overall compositions and the individual phases. A voltage of 15 kV was used at a working distance of 8.5 mm. SEM studies were also done on as-received and milled powders. The overall analyses of the six samples were also determined using SEM-EDS, to verify whether the target alloy compositions were achieved.

The phases identified from XRD were matched to the microstructures using EDS mapping. Since WC was the major component in all alloys, the amount of WC ($wt\%_{wc}$) present in all alloys was estimated from EDS analyses and compared to the target amount. The amount of WC for each alloy was calculated by inserting the wt% W values from EDS analyses into the following equation:

$$wt\%_{WC} = wt\%_{W} \times \frac{RAM_{WC}}{RAM_{W}} \qquad \text{Equation 3.4}$$

where: RAM = Relative Atomic Mass.

3.3.4. Microstructural Quantitative Evaluation

Five enlarged micrographs (x30000) from SEM were used per sample to determine the microstructural parameters of mean carbide grain size (d_{wc}), binder mean free path (λ) and contiguity (C_{β}). At least 500 WC grains were measured per alloy composition. Zeiss Axio

Vision® imaging software was used to determine the average grain size of all samples according to the ASTM E112-96 standard [1997AST]. The appropriate SEM magnification (x30000) was determined by referring to the guideline by Roebuck *et al*. [1986Roe] (Figure 3.1) after preliminary grain size measurements.

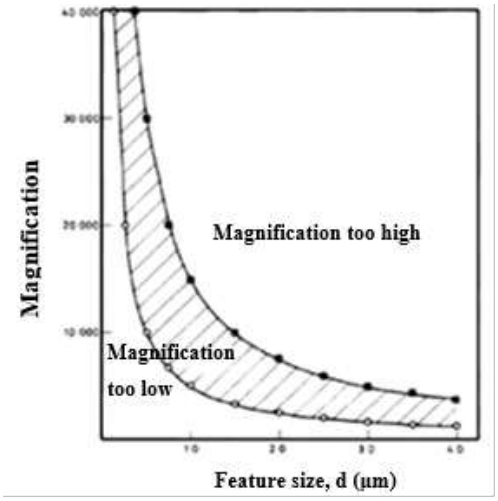

Figure 3.1. Guide to magnification choice for hardmetal feature sizing [1986Roe].

3.3.4.1. Mean Carbide Grain Size and Distribution

Mean grain size measurements were done using the Heyn's linear intercept method [1997AST]. Neighboring lines were separated by at least twice the approximate average intercept length [1968Sch], to minimise the chances of re-measuring the same areas.

The following equation was used to determine the WC mean intercept length, d_{wc}:

$$d_{wc} = L_{wc}/N_{wc} \qquad \text{Equation 3.5}$$

where:

L_{wc} = total length of line across WC grains and N_{wc} = number of WC grains traversed.

3.3.4.2. Binder Mean Free Path

The binder mean free path, λ, was determined using the formula by Exner *et al*. [1966Exn]:

$$\lambda = \frac{2V_\beta}{N_{wc/\beta}} \qquad \text{Equation 3.6}$$

where: V_β = binder volume fraction (here, the Co-Ru binder),

$N_{wc/\beta}$ = number of carbide/binder boundaries.

The presence of Ru in the Co binder was considered in calculating the volume fraction of the binder. The V_β values were derived as follows:

$$V_\beta = \frac{\text{vol.}_\beta}{\text{vol.}_{\text{Alloy}}} \quad \text{Equation 3.7}$$

$$\text{vol.}_\beta = \frac{m_\beta}{\rho_\beta} = \frac{m_{Ru}}{\rho_{Ru}} + \frac{m_{Co}}{\rho_{co}} = \frac{\text{wt\% Ru x } m_{\text{Alloy}}}{\rho_{Ru}} + \frac{\text{wt\% Co x } m_{\text{Alloy}}}{\rho_{Co}} \quad \text{Equation 3.8}$$

$$\Rightarrow \text{vol.}_\beta = m_{\text{Alloy}}\left(\frac{\text{wt\% Ru}}{\rho_{Ru}} + \frac{\text{wt\% Co}}{\rho_{Co}}\right) \quad \text{Equation 3.9}$$

$$\text{vol.}_{Alloy} = \frac{m_{Alloy}}{\rho_{Alloy}} \quad \text{Equation 3.10}$$

$$\text{Therefore, } V_\beta = \rho_{Alloy}\left(\frac{\text{wt\% Ru}}{\rho_{Ru}} + \frac{\text{wt\% Co}}{\rho_{Co}}\right) \quad \text{Equation 3.11}$$

where:

V_x = volume fraction,

vol._x = volume,

ρ_x = density and

m_x = mass, of component *x*.

The volume fraction of the binder phase for each alloy was thus determined using known values of mass fraction and density.

3.3.4.3. Contiguity

Contiguity measurements were done using linear analysis to resolve the binder phases so that carbide/carbide ($N_{wc/wc}$) and carbide/ binder ($N_{wc/\beta}$) boundaries could be counted, where N is the number of boundaries. For the carbide/carbide phase, both WC and (W,V)C were considered. The equation by Gurland [1958Gur] was used to determine experimental contiguity:

$$C_\beta = \frac{2N_{wc/wc}}{2N_{wc/wc} + N_{wc/\beta}} \quad \text{Equation 3.12}$$

where: C_β = binder contiguity.

For comparison with experimental results, theoretical contiguities were determined using Equations 3.13 [1966Exn], 3.14 [1986Roe] and 3.15 [2006Luy]:

$C_\beta = 1.03 \exp(-5V_\beta)$ Equation 3.13

$C_\beta = 0.85 - 1.80V_\beta$, for $0.05 < V_\beta < 0.3$ Equation 3.14

$C_\beta = \exp(-8.4V_\beta)$ Equation 3.15

To determine the best fitting equation to the experimental results, the least mean relative error approach was used [2015Tof], where:

$$\text{Relative error} = \left|\frac{\text{Actual}-\text{Calculated}}{\text{Actual}}\right| \quad \text{Equation 3.16}$$

3.4. Hardness and Fracture Toughness

Vickers indentations were made at 5 kg, 10 kg, 20 kg, 30 kg and 50 kg using a Mitutoyo® Vickers hardness testing machine, to determine the best loads for Palmqvist toughness measurements. Three samples per composition were used for each load. An optical microscope with a graticule was used for hardness and Palmqvist measurements. Measurements were done at x500 magnification in accordance with the ISO28079:2009 standard [2009ISO]. A dwell time of 30 s was used at the selected indenter load. The indentations and crack lengths were measured to evaluate conformity to the Palmqvist method. According to Spiegler *et al*. [1990Spi] the ratio of crack length, l to half the diagonal length, a, of an indentation should be in the range $0.25 \leq l/a \leq 1.25$ for valid Palmqvist results. Thus, l/a values were used to determine the suitable load for Palmqvist measurements.

According to Roebuck and Brewin [2004Roe], residual stresses reduce the total crack length produced by indentations. Thus, the total crack lengths for samples obtained from the two polishing methods shown in Table 3.2 were measured to determine the better method for stress relief, and thus that to be used for fracture toughness tests.

3.4.1. Hardness

The hardness tests were done at 30 kg with reference to the ISO3878 [1983ISO] standard. The following equation was used to determine the hardness of the samples:

$$H_v = \frac{1854.4\ P}{d^2} \qquad \text{Equation 3.17}$$

where:

P = Load (kg)

D = average diameter of diagonals (mm).

3.4.2. Palmqvist Measurements

The Palmqvist toughness (crack resistance), W_G and Palmqvist fracture toughness, W_K, were determined using Equations 3.18 and 3.19 [2009ISO]:

$$W_G = \frac{P}{L} \qquad \text{Equation 3.18}$$

$$W_K = 0.028\sqrt{H_v W_G} \qquad \text{Equation 3.19}$$

where:

L = total crack length.

3.5. Sliding Wear

Samples were subjected to open air dry sliding wear using a CSM ball-on-disk tribometer. The wear balls were made of silicon nitride, and three samples were tested per composition. The test conditions are shown in Table 3.3.

Table 3.3. Parameters for the friction and sliding wear tests.

Test conditions	**Values**
Normal load	10 N
Acquisition radius	2.0 mm
Acquisition rate	30 Hz
Sliding distance	200 m
Linear speed	0.12 m/s
Temperature	~25°C

The worn volumes of the samples and balls were determined according to ASTM G99-95a Standard [2000AST]. The disk volume loss was calculated using Equation 3.20 [2000AST]:

Disk volume loss, $\Delta V_s = 2\pi R\left[r^2 \sin^{-1}\left(\frac{d}{2r}\right) - \left(\frac{d}{4}\right)(4r^2 - d^2)^{\frac{1}{2}}\right]$ Equation 3.20.

where:

R = wear track radius,

d = wear track width, and

r = pin end radius.

The pin volume loss was calculated according to Equation 3.2.1:

$$\Delta V_b = \left(\frac{\pi h}{6}\right)\left[\frac{3d^2}{4} + h^2\right] \quad \text{Equation 3.21}$$

where:

$$h = r - \left[r^2 - \frac{D^2}{4}\right]^{1/2} \quad \text{Equation 3.22}$$

D = wear scar diameter.

The wear rates, W_r, were calculated using the formula [1976Lan]:

$$W_r = \frac{\Delta V}{F_a D_s} \quad \text{Equation 3.23}$$

where: F_a = applied load, D_S = sliding distance and ΔV= volume loss.

The wear track and ball diameter measurements were done using an Olympus BX63 light microscope and a Motic stereo-microscope, as shown in Figures 3.2 and 3.3. Axio-vision software was used to magnify and measure the ball wear scar diameters. Four diameters were averaged per wear scar as shown in Figure 3.3. Three wear scars, corresponding to the different alloys per composition that underwent wear evaluation, were measured and averaged for each ball. Wear mechanisms and wear track elements were identified using SEM-EDS analyses.

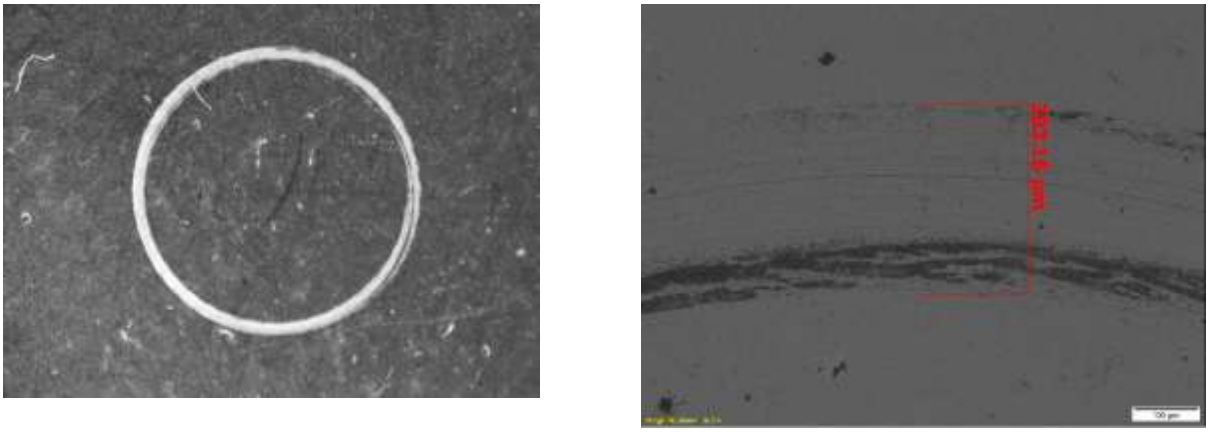

Figure 3.2. An example of a wear track and its measurement (Alloy 14, 89.6WC-0.4VC-7.0Co-3.0Ru (wt%)).

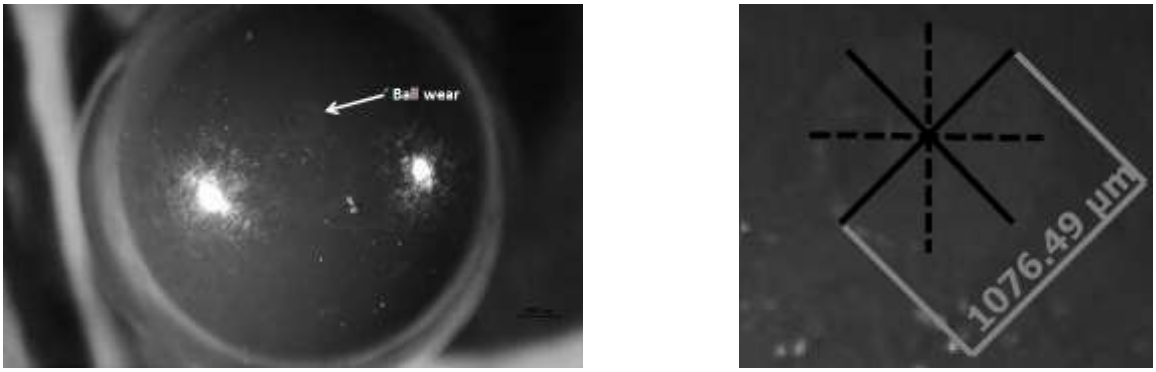

Figure 3.3. An example of ball wear and its measurement (Alloy 7, 89.6WC-0.4VC-10Co (wt%)).

3.6. Corrosion Tests

3.6.1. Electrochemical Tests

Electrochemical tests were conducted according to the ASTM G5-94:2010 standard [2010AST1]. A conventional three-electrode 500 ml Pyrex glass cell was used as the solution chamber. The tests were performed at 25°C in 1 M H_2SO_4, 1 M NaCl and synthetic mine water. The composition of synthetic mine water is shown in Table 3.4. The reference and counter electrodes were made of a saturated calomel electrode (SCE) and graphite. A Lugin probe salt-bridge was used to separate the bulk solution from the reference electrode, and was placed approximately 3 mm from the working electrode. The electrodes were connected to a potentiostat (ACM Instruments – Gill AC). A water bath was used to keep the temperature constant and a thermometer was inserted into the solution chamber to monitor the temperature. Open circuit potentials (OCP) and potentiodyanamic polarisations were measured using ACM software (Version 5).

Table 3.4 Composition of synthetic mine

Compound	Concentration (mg/l)
Na_2SO_4	1237
$CaCl_2$	1038
$MgSO_4$	199
NaCl	1380

An immersion time of 2 h was used for OCP measurements to ensure stability. A scan rate of 2mV/s and a scan width of -250 to 1200 mV were then used for potentiodyanamic polarisations. The polarisation curves were used to measure the corrosion kinetics of the alloys. All calculations of corrosion rate and related information were done in accordance to ASTM G102-89:2010 [2010AST2]. At least two measurements were done for each alloy composition for repeatability.

3.6.2. Immersion Tests

The tests were done according to the ASTM-G31 standard [2012AST] for 90 days at room temperature. The samples were weighed before immersion. For each solution, a 5000 ml beaker was used to accommodate all compositions, each composition having three samples. The beakers were covered with watch glasses to avoid evaporation. All samples were ground to a 120 μm surface finish and their relative positions in the beakers were recorded to cater for any losses of the identification marks. Glass sample holders with minimum contact with the samples were used to minimise crevice corrosion. A 0.4 ml/mm^2 solution-to-test specimen ratio was used for all three set-ups.

After the tests, the samples were cleaned mechanically by scrubbing with a polymeric bristle brush and weighed. The corrosion rates were then calculated according to the following equation [2012AST]:

Corrosion rate (mm/y) = (K x W)/ (A x T x D) Equation 3.24

where:

K = 8.76 x 10^4,

A = area in cm^2 to the nearest 0.01 cm^2,

W = mass loss in g, to the nearest 1 mg, and

D = density in g/cm^3.

3.6.3. Surface Characterization of Corrosion Samples

Elemental analyses of the corroded surfaces were done using SEM-EDS, and the results were compared to those obtained for uncorroded polished samples. Phase identification was done using XRD and a high-resolution Raman spectroscope. Details of SEM-EDS, XRD and Raman tests are given in Section 3.3.1.

4. RESULTS

4.1. Alloy Production

4.1.1. Starting Powders – Analyses and Characterisation

Particle size distributions for the source powders, WC, VC, Co and Ru, are shown in Figures 4.1 to 4.4. The results for WC from the Microtrac following 2 min ultrasonic bath mixing (Figure 4.1a) showed a single particle size distribution curve. A bimodal distribution, and an extra curve, due to agglomeration or bubbles, was seen from the Saturn DigiSizer results (Figure 4.1b). Similar measurement results for VC, Co and Ru powders are shown in Figures 4.2 to 4.4, respectively. The results for 10% undersize (d_{10}), 50% undersize (d_{50}) and 90% undersize (d_{90}) are shown in Table 4.1 for both the Microtrac analyser (MA) and the Saturn DigiSizer analyser (SDA) for all the powders. Only the volume weighted mean (d_{mean}) particle sizes for Microtrac are given in Table 4.1, because the Saturn DigiSizer could not calculate d_{mean}. The average particle sizes d_{supp}, provided by the manufacturer are also shown in Table 4.1, which shows that only Co exceeded the particle size given by the supplier, d_{supp}. The particle sizes for Ru were not specified by the supplier, and were much larger than the other powders.

However, there was some contradiction between MA and SDA results since SDA results for VC, Co and Ru where larger, yet for WC it was the other way round. These differences might have been due to the inherent differences between the two techniques. Although Microtrac and DigiSizer analyses gave d_{50} results which differed by an average of approximately $\pm$38%, a similar size trend was observed, with Ru having the largest particles and similar particle sizes for WC and VC. The shapes of the particle size analyses frequency curves also had similar trends, with Co having the most obvious bimodal distribution. The powders, especially Ru, which had the largest particle sizes, could have remained agglomerated, even after ultrasonic treatment. Therefore, the powders needed to be milled to ensure sufficient particle deagglomeration.

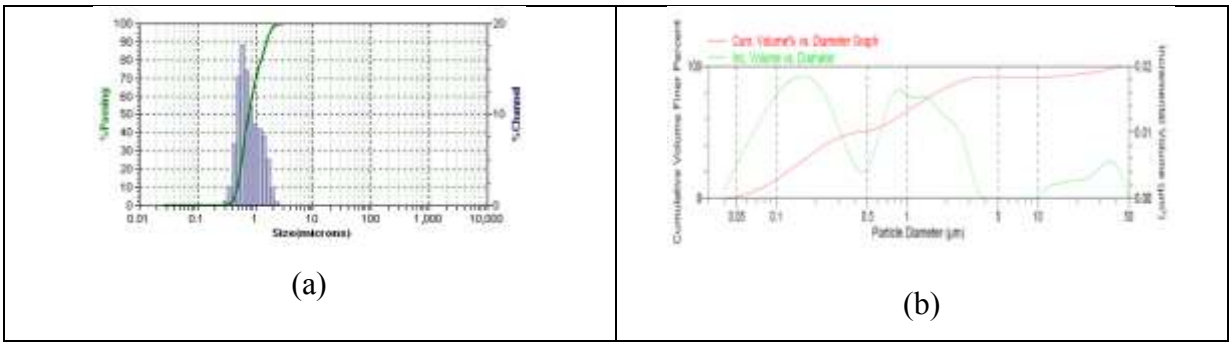

(a) (b)

Figure 4.1. Particle size distribution for WC (2 min ultrasonic bath) measured using: a) Microtrac particle size analyser, and b) Saturn DigiSizer analyser.

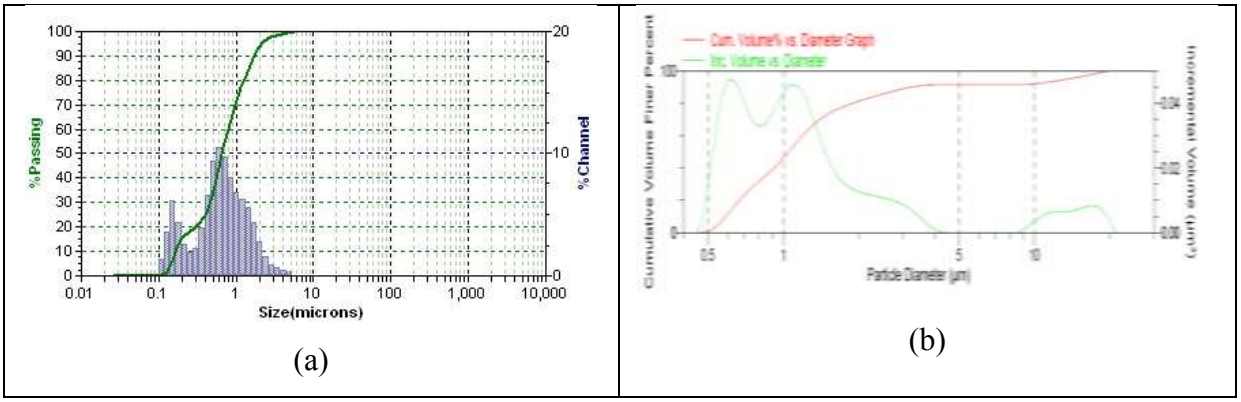

(a) (b)

Figure 4.2. Particle size distribution for VC (2 min ultrasonic bath) measured using a) Microtrac particle size analyser and b) Saturn DigiSizer analyser.

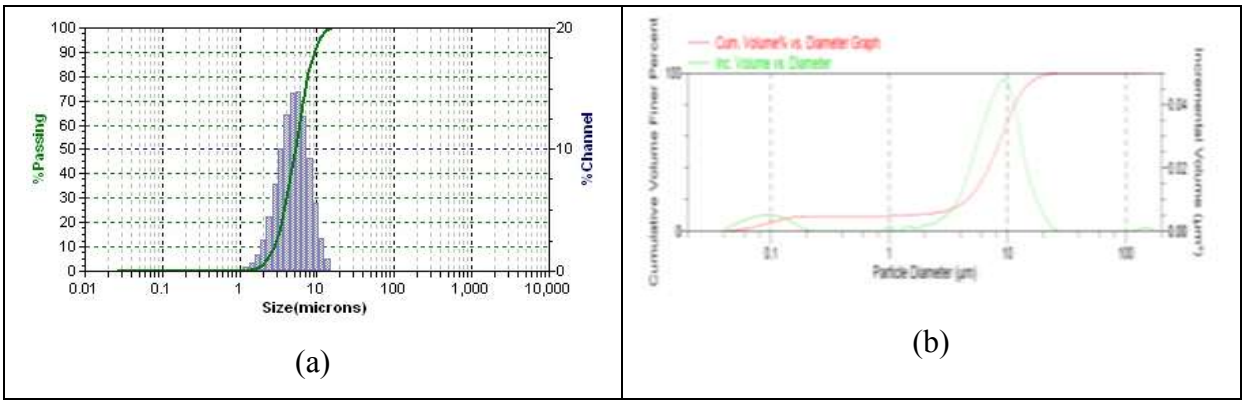

(a) (b)

Figure 4.3. Particle size distribution for Co (2 min ultrasonic bath) measured using a) Microtrac particle size analyser and b) Saturn DigiSizer analyser.

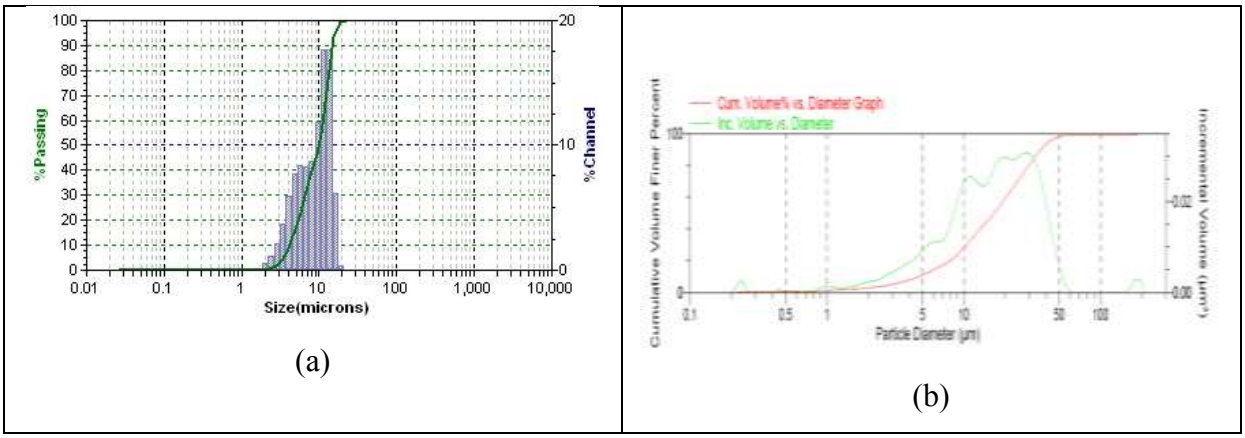

(a) (b)

Figure 4.4. Particle size distribution for Ru (2 min ultrasonic bath) measured using a) Microtrac particle size analyser and b) Saturn DigiSizer analyser.

Table 4.1. Powder particle sizes for WC, VC, Co and Ru (µm) obtained from the Microtrac analyser (MA) and Saturn DigiSizer analyser (SDA).

Powder	d_{10}		d_{50}		d_{90}		d_{mean}		d_{supp}
	MA	SDA	MA	SDA	MA	SDA	MA	SDA	
WC	0.490	0.085	0.756	0.421	1.541	2.851	0.898	-	2.000
VC	0.167	0.589	0.661	1.051	1.707	3.229	0.848	-	<2.000
Co	2.802	1.379	5.26	7.900	9.10	13.858	5.66	-	2.000
Ru	4.06	4.695	9.07	16.706	15.65	36.563	9.51	-	-

4.1.2. Morphology of Starting Powders

SEM micrographs of the starting powders, WC, VC, Co and Ru, are shown in Figures 4.5 to 4.8, respectively. Tungsten carbide particles had a very fine granular morphology with small agglomerates (Figure 4.5), whereas VC exhibited coarser, faceted or round morphologies (Figure 4.6). Both WC and VC had agglomerated particles, whereas Co showed string-like particles (Figure 4.7). The Co manufacturers would not provide their preparation method that resulted in the string-like particles. Ruthenium exhibited two distinct morphologies: densely packed clusters of spherical particles, with large hexagonal crystals (Figure 4.8).

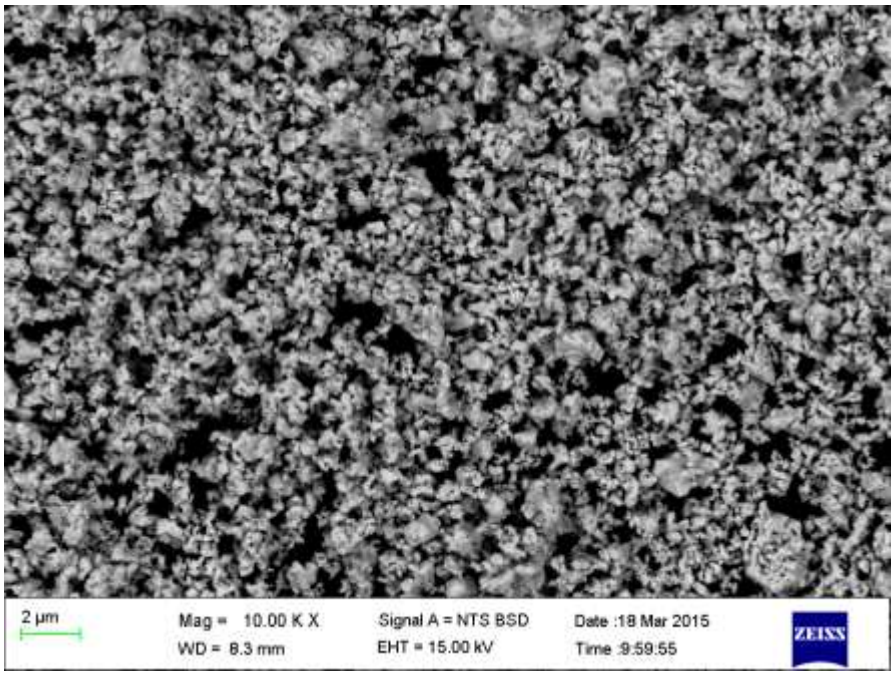

Figure 4.5. SEM-BSE micrograph of WC powder showing a very fine granular morphology.

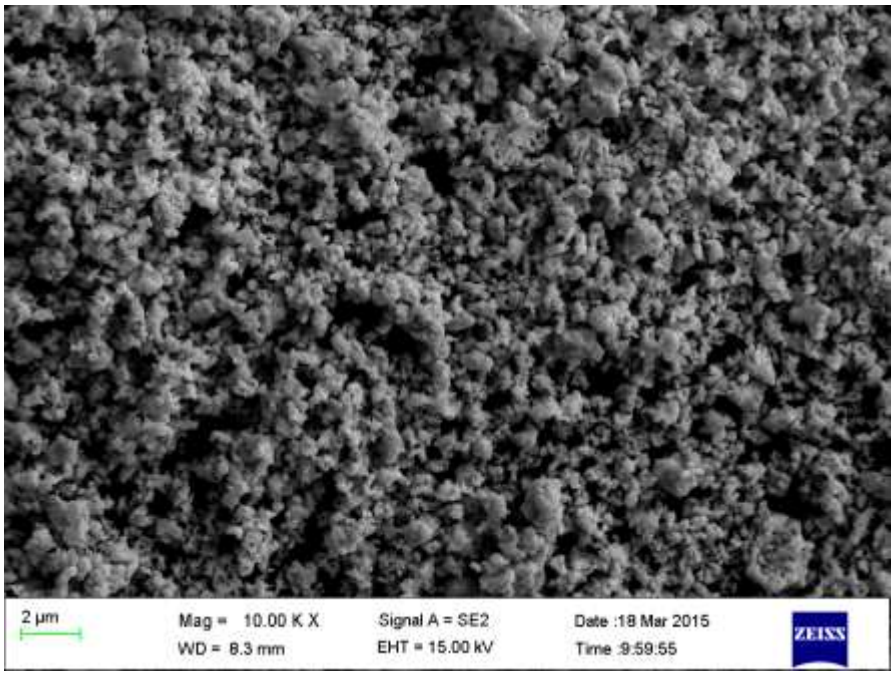

Figure 4.6. SEM-BSE micrograph of VC powder showing coarse, faceted and round grains.

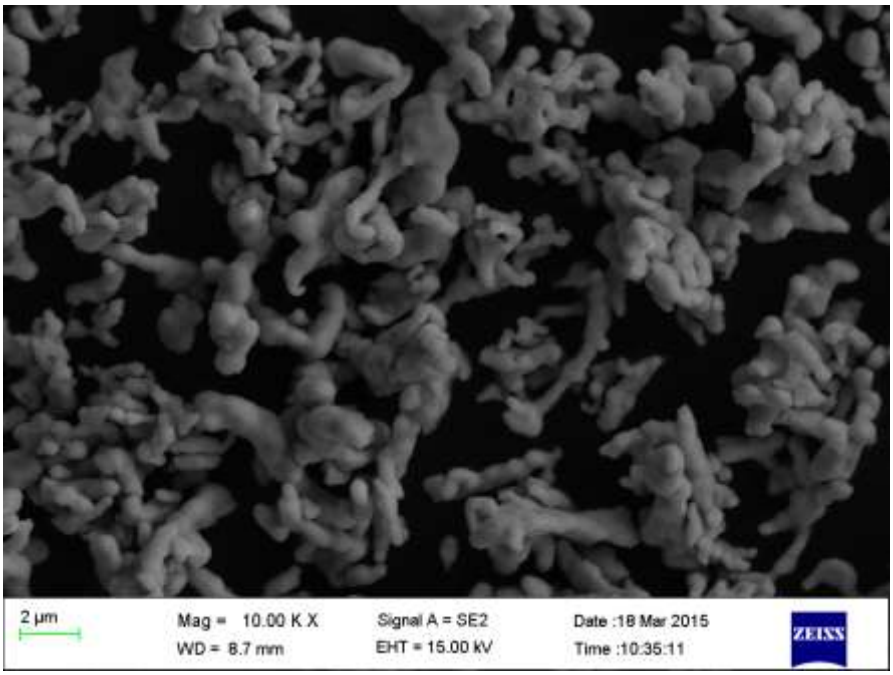

Figure 4.7. SEM-BSE micrograph of Co powder, showing a string-like morphology.

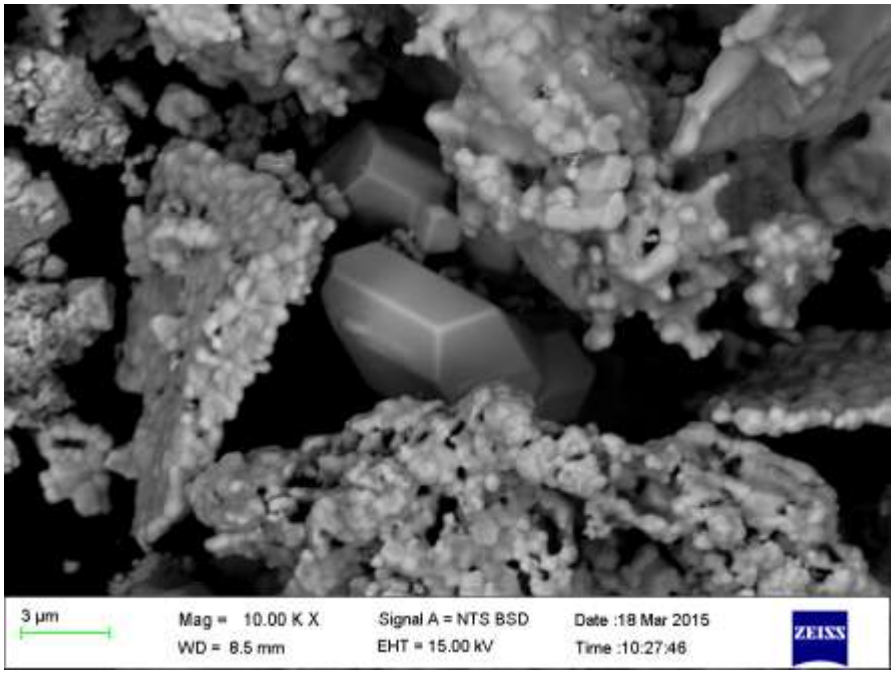

Figure 4.8. SEM-BSE image of Ru powder showing densely packed clusters of near spherical particles and large hexagonal crystals.

4.1.3. EDS and XRD Analyses of the Powders

The EDS analyses of all the powders are shown in Table 4.2. For WC and VC, the composition was approximated as the sum of elemental W or V plus C. However, carbon analyses were not accurate, since some carbon was from the underlying C-tape. The C-tape also resulted in oxygen pick-up, thus, the presence of oxygen in the analysis. The EDS analyses of the C-tape is also shown in Table 4.2. Also, the XRD patterns of the powders (Figures 4.9 to 4.12) did not reveal any oxide peaks. This reaffirms the observation that oxygen content (Table 4.2) is from the underlying C-tape. There was some W_2C and C in the WC powders (Figure 4.9). The two allotropic forms of Co, fcc and hcp, were identified (Figure 4.11).

Table 4.2. EDS analyses of WC, VC, Co and Ru powders, and C-tape.

Element	Source constituents (wt%)	Oxygen (wt%)
W + C	95.4±1.0	4.6±1.0
V + C	99.9±0.1	0.1±0.1
Co	95.9±2.5	4.1±2.5
Ru	89.4±3.6	10.6±3.6
C-tape	72.7±2.3	27.3±2.3

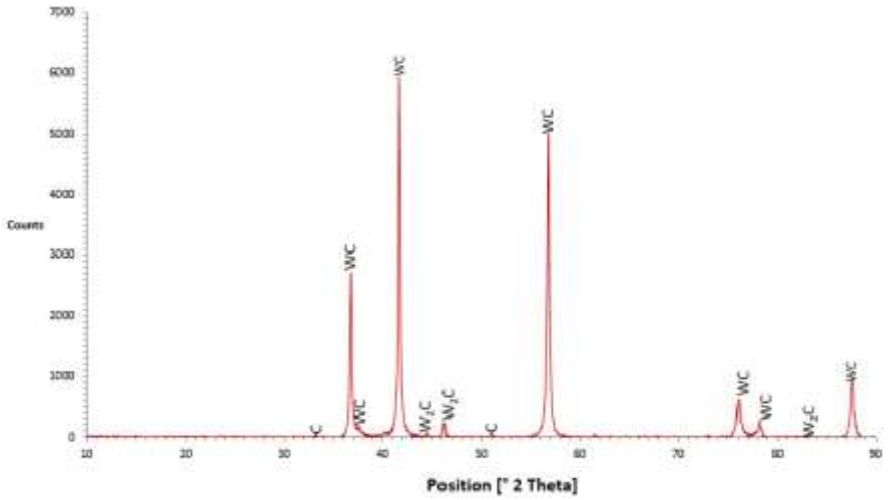

Figure 4.9. XRD pattern for WC source powder

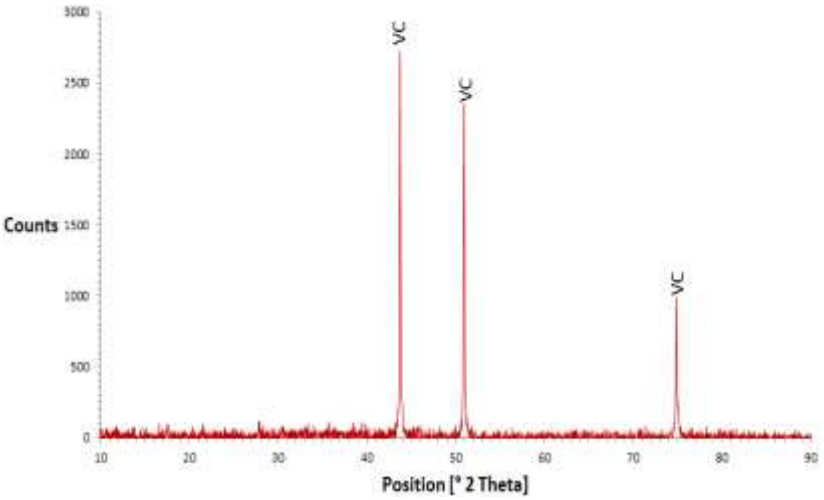

Figure 4.10. XRD pattern for VC source powder.

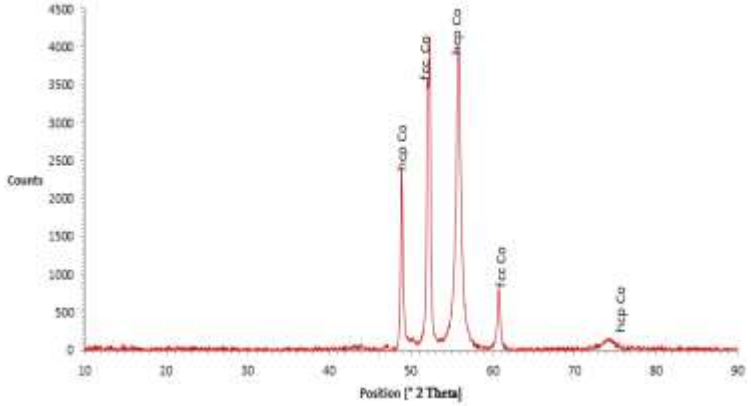

Figure 4.11. XRD pattern for Co source powder, showing both fcc Co and hcp Co.

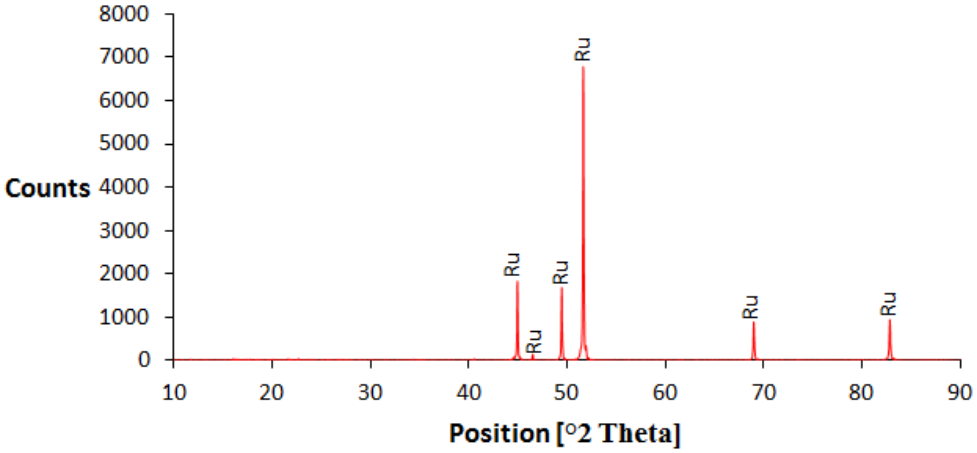

Figure 4.12. XRD pattern for Ru source powder.

4.1.4. Milling of Powders

A 100 g powder mixture of 80WC-10VC-10Co (wt%), corresponding to one of the control alloy composition (Table 3.1), was produced in a 100 g capacity mill at a 3:1 ball to powder ratio. During milling, samples were taken after 1, 3, 4, 5 and 8 hours for particle size analyses. The milling curve (Figure 4.13) shows decreasing particle size with time, resulting in decreased milling rates deduced from the levelling of the curve with time. The initial powder particle size for the mixture was determined as the weighted average mean particle size for the three unmilled powders.

The powder mixture was taken for SEM-EDS analysis, to check for homogeinty prior to sintering. Co retained its string-like morphology, and was more concentrated in some regions, instead of being evenly distributed around the WC and VC particles as can be seen in both low and high magnifications (Figures 4.14 and 4.15).

The particle size distribution for the final 80WC-10VC-10Co (wt%) powder mixture is shown in Figure 4.16, and although the mean particle size for the final powder was 0.761 μm, there were still particles of ~4 μm. According to Figure 4.15, the large particles were coalesced Co particles.

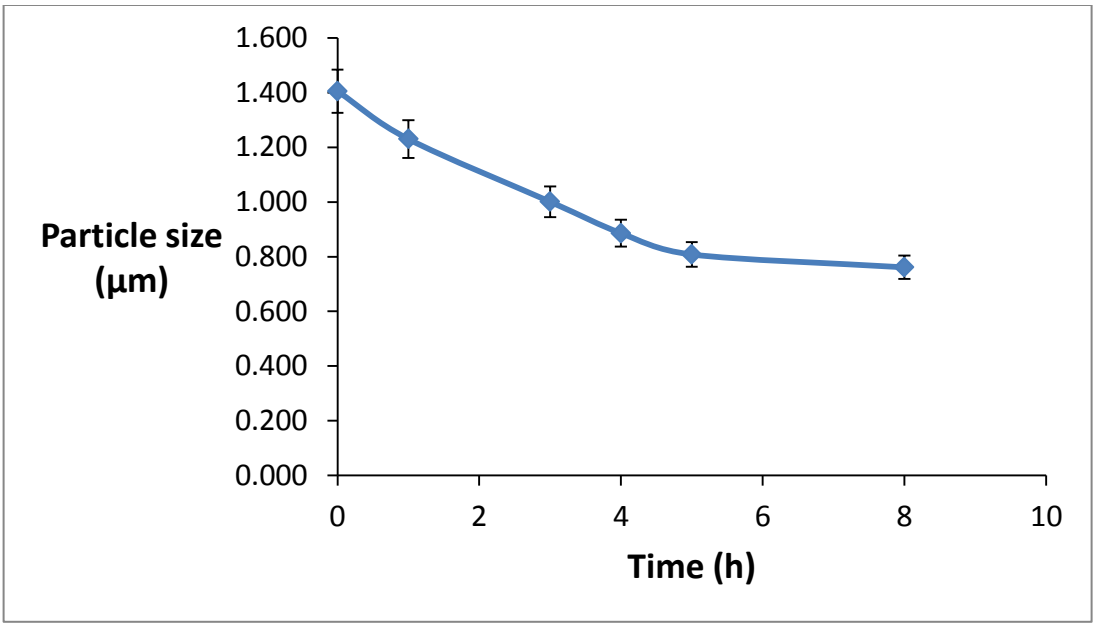

Figure 4.13. Milling curve for 80WC-10VC-10Co (wt%) powder mixture.

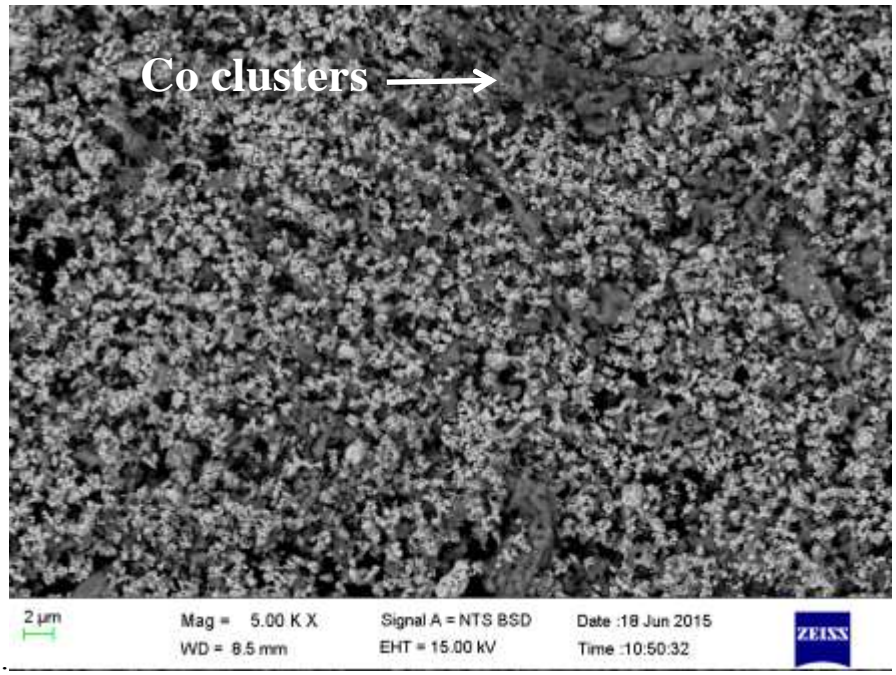

Figure 4.14. SEM-BSE image of milled 80WC-10VC-10Co (wt%) powder showing Co clusters in some regions between WC and VC particles (lighter).

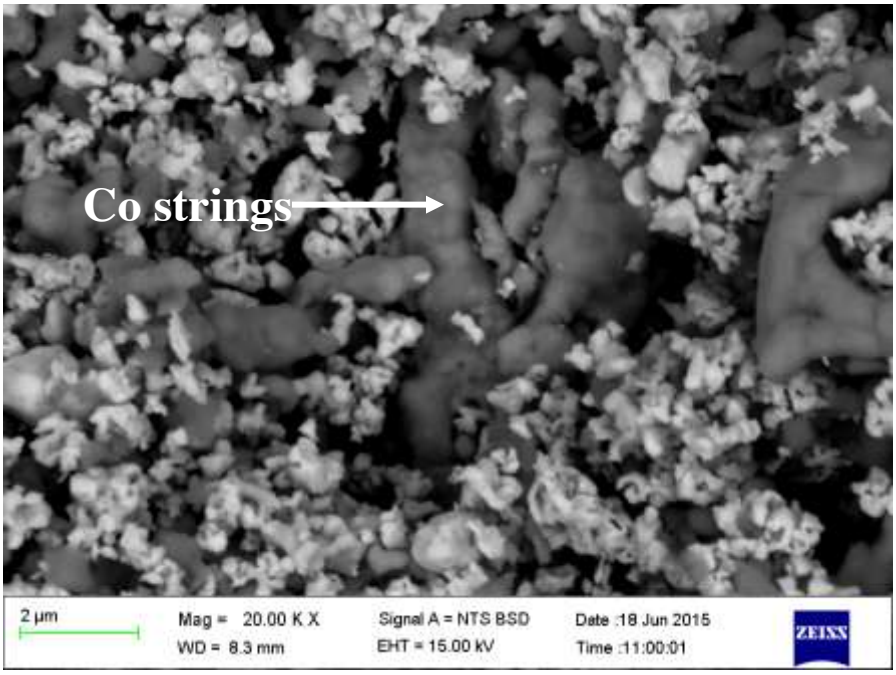

Figure 4.15. SEM-BSE image of milled 80WC-10VC-10Co (wt%) powder showing a Co string-like agglomerate mixed with other powders (light contrast areas).

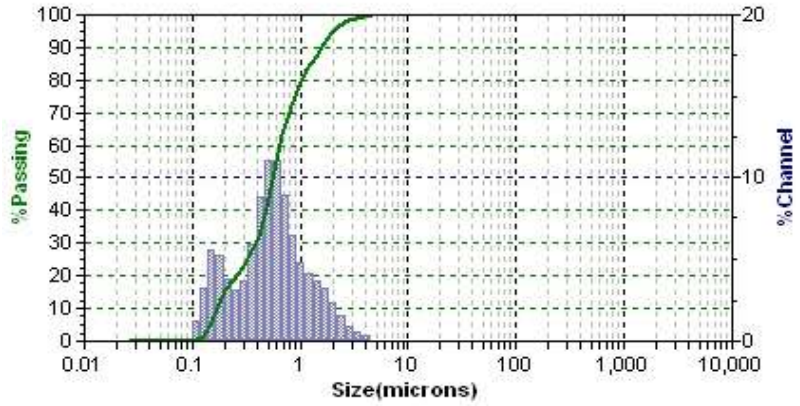

Figure 4.16. Particle size distribution for 80WC-10VC-10Co (wt%) powder mixture after milling for 8 hours (2 min ultrasonic bath).

Since coalescence of Co increases the chances of the final alloys having Co pools, higher porosities and consequently poor mechanical properties, the use of finer Co with mean particle size of 2.9 µm was investigated. The particle size distribution curve for the 2.9 µm Co is shown in Figure 4.17, with a modal particle size of 1.3 µm. The morphology of the finer Co was characterised using the SEM, and the finer Co had a less elongated morphology (Figure 4.18) than coarser Co (Figure 4.7). However, the EDS analyses of the 2.9 µm Co (Table 4.3) showed slightly higher oxidation than coarser Co powder (Table 4.2), but as mentioned earlier, the C-tape contributed to the O analyses. The XRD pattern (Figure 4.19) was similar to that obtained for the larger particle size Co (Figure 4.11), and both fcc and hcp allotropes of Co were also present in the 2.9 µm Co powder. However, the fcc Co peaks were higher in the finer powder.

Another 100 g 80WC-10VC-10Co powder mixture, with the 2.9 µm Co powder, was milled for 24 hours at a 5:1 ball-to-powder ratio. Using a finer starting particle resulted in a mean particle size of 0.495 µm with improved Co distribution (Figure 4.20) compared to using a larger Co mean particle size (Figure 4.14 and 4.15), as expected. Therefore, the 2.9 µm Co was used for the rest of this study.

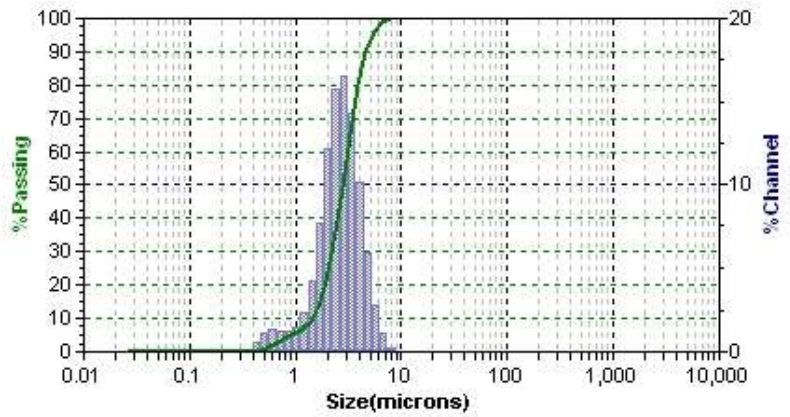

Figure 4.17. Particle size distribution for source fine Co powder (mean particle size – 2.9 µm).

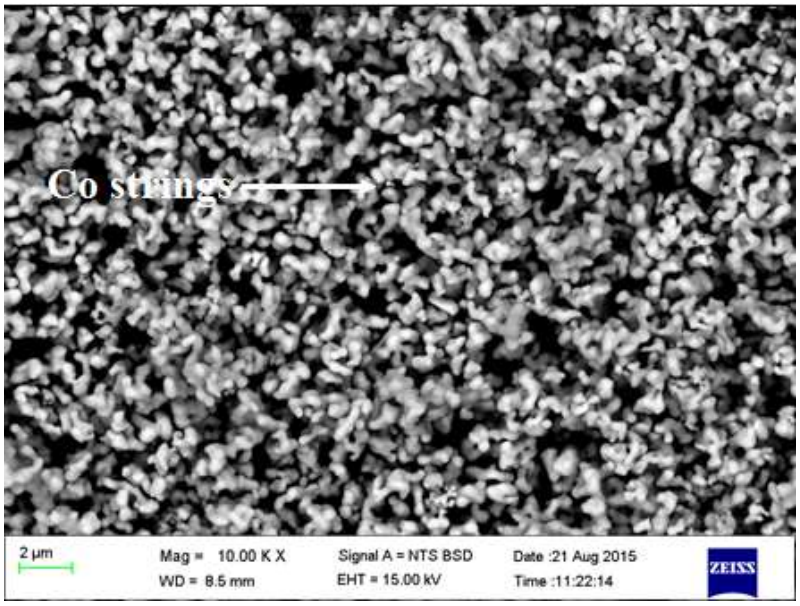

Figure 4.18. SEM-BSE image of the fine Co powder showing a fine string-like morphology prior to mixing.

Table 4.3. EDS analysis of source Co (mean particle size - 2.9 µm).

Element	Amount (wt%)
Co	95.2±0.8
O	4.8±0.8

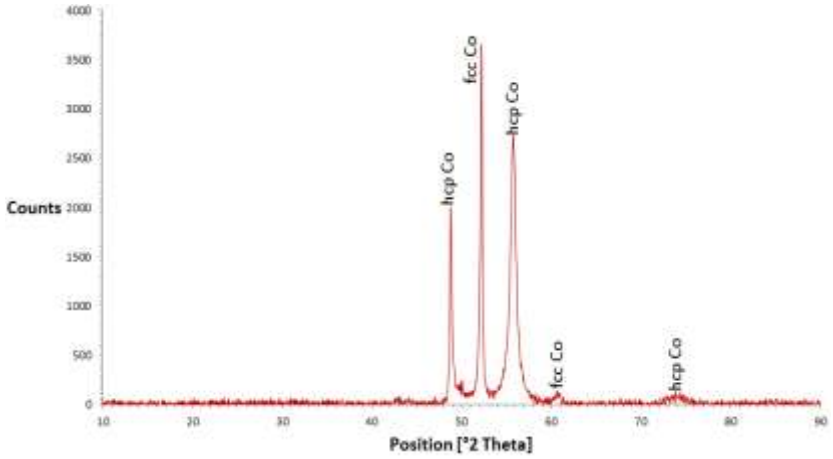

Figure 4.19. XRD pattern of the fine (2.9 µm mean particle size) source Co powder prior to mixing.

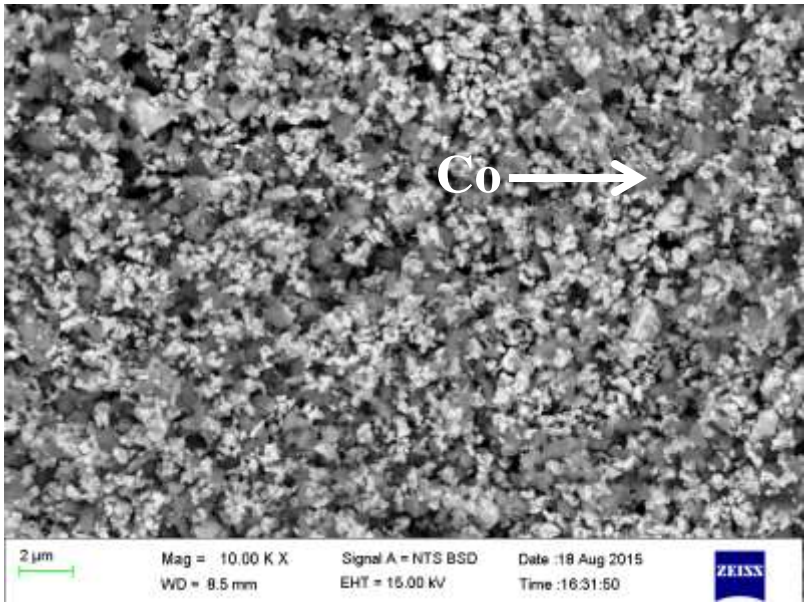

Figure 4.20. SEM-BSE image of 80WC-10VC-10Co powder mixture showing a more even Co distribution as a result of using finer Co powder (medium dark areas).

Table 4.4 shows the results for Ru milling so that 80% of the particles (d_{80}) would be ≤0.898µm, the d_{mean} of WC (Table 4.1). This was because Ru was added in very low amounts, up to a maximum 3 wt% (Table 3.1). It was, therefore, important to ensure that the particles were fine enough to be dispersed around WC particles.

Particle size analyses were done hourly for the first 8 h, then after periods of 12, 15, 48, 72 and 168 h. The time required for each subsequent milling was approximated using the Microsoft Excel SOLVER function on the polynomial equations derived from the plots of particle size against time. Since reduction in particle size with time resulted in decreased comminution rates, the ball-to-powder ratio was increased gradually during milling. The ball-to-powder ratios and the corresponding final particle sizes achieved during milling are shown in Table 4.4.

Table 4.4. Ball-to-powder ratios and mean particle sizes during milling of Ru.

Time Interval (h)	Ball-to-powder ratio	Final mean particle size, d_{mean} (μm)
1-8	3:1	4.59
8-48	4:1	1.27
48-72	6:1	1.00
72-168	8:1	0.524

After milling Ru for 168 hours, d_{mean} was 0.524 μm and d_{80} was 0.811 μm. Therefore, the desired comminution of Ru was attained to allow for better mixing with other powders. A bimodal particle size distribution was observed for milled Ru as shown in Figure 4.21, and the modal particle size (~0.15 μm) was much smaller than the pre-milling modal particle size of ~14 μm (Figure 4.4), confirming significant comminution. The milling curve for Ru at the different ball-to-powder ratios given in Table 4.4 is shown in Figure 4.22.

Milled ruthenium powder was taken for SEM-EDS analysis to determine the morphology, and also to establish if there was any contamination during milling. SEM-BSE images showed significant deagglomeration of Ru from large grains, agglomerations of coarse particles, and agglomerations of fine particles (Figure 4.8) to a morphology of mixed grain sizes (Figure 4.23). The larger hexagonal particles and agglomerates were broken down, and the smallest particles now matched those in the original agglomerates.

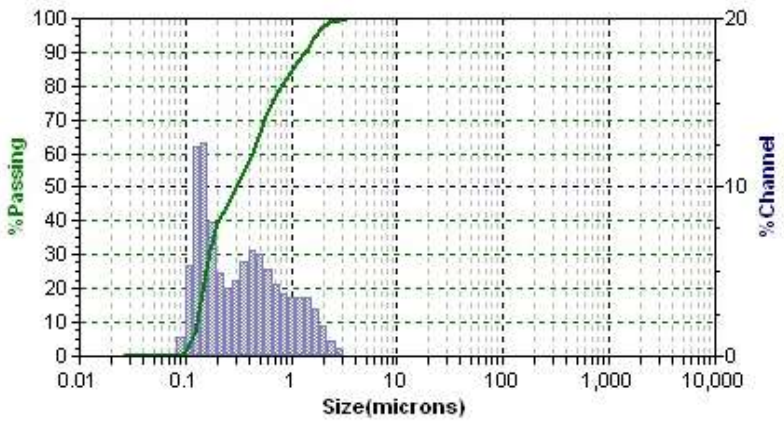

Figure 4.21. Particle size distribution for Ru after milling for 168 hours (2 min ultrasonic bath).

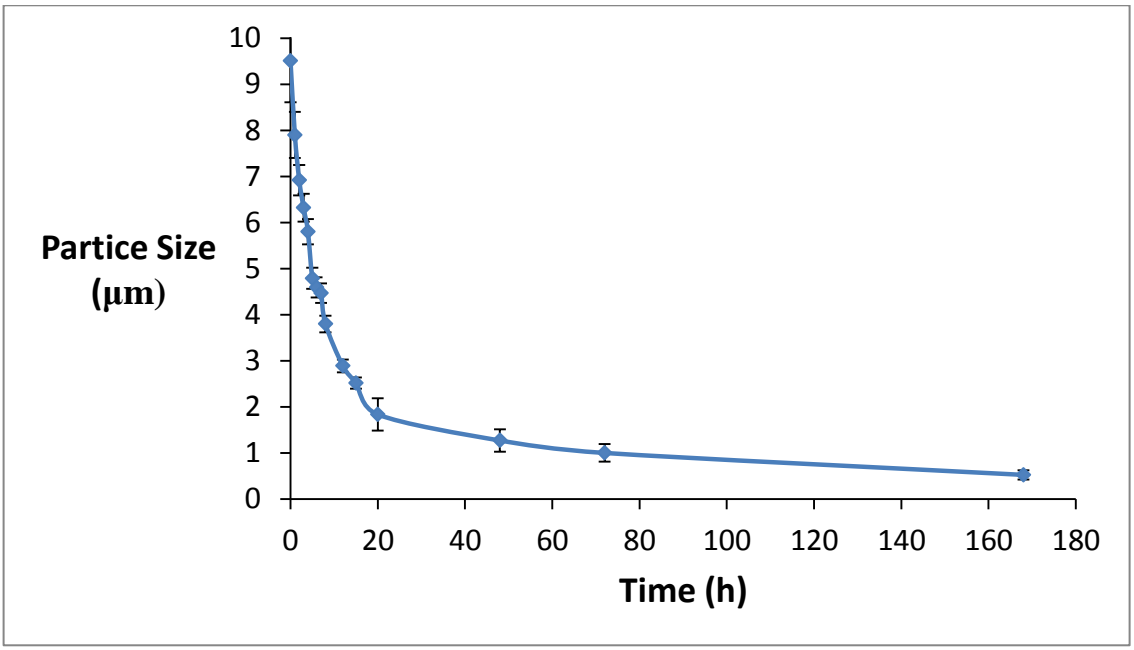

Figure 4.22. Milling curve for Ru with time (at varying ball-to-powder ratios).

Table 4.5 shows there was contamination of Ru with Fe and Cr from the stainless steel mill lining, and with Co from previous runs. The carbon content could not be analysed accurately, since the powders were mounted on a C surface. Thus, for WC, only the W content could be determined. Very high oxygen levels (10.1±3.8 at.%) were also detected, but the analyses were affected by the C-tape.

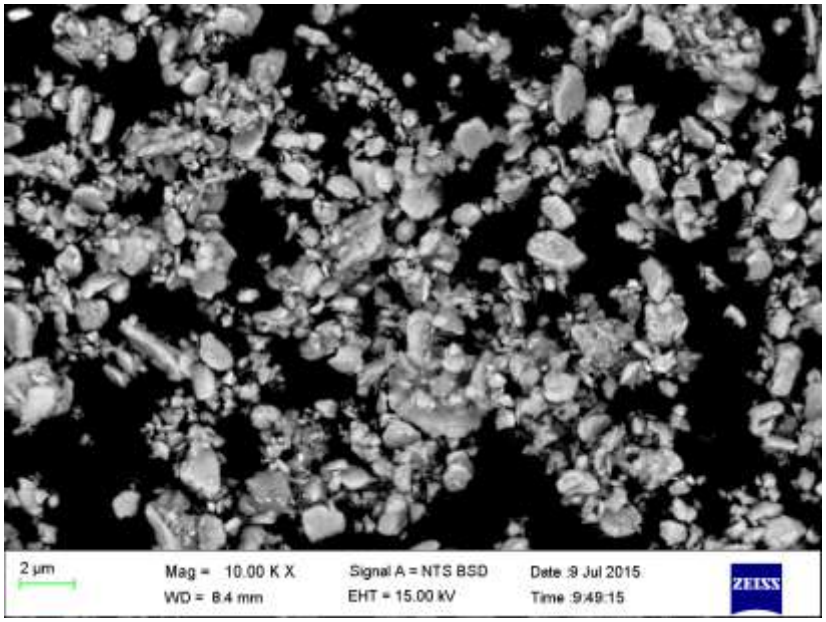

Figure 4.23. SEM-BSE image of Ru milled for 168 hours, showing grains of different sizes.

The XRD pattern for the milled Ru powder (Figure 4.24) was similar to the unmilled powder (Figure 4.12), except that peaks were broader for the milled powders. XRD did not find Cr or Fe since they were in very small quantities (<5 at.%), below the detection limit of XRD (~4 vol.%). However, the oxygen content was too high not to be detected by XRD, but could have resulted in the broader peaks observed for Ru by being dissolved together. Therefore, the oxides could have been due to oxygen pick-up from the C-tape since the EDS analyses of sintered alloys (Section 4.2) also did not reveal oxygen.

Table 4.5. EDS analyses of Ru powder after milling for 168 hours.

Element	**Amount (wt%)**
O	10.1±3.8
Cr	0.7±0.1
Fe	2.7±0.4
Co	0.7±0.1
Ru	85.8±6.3

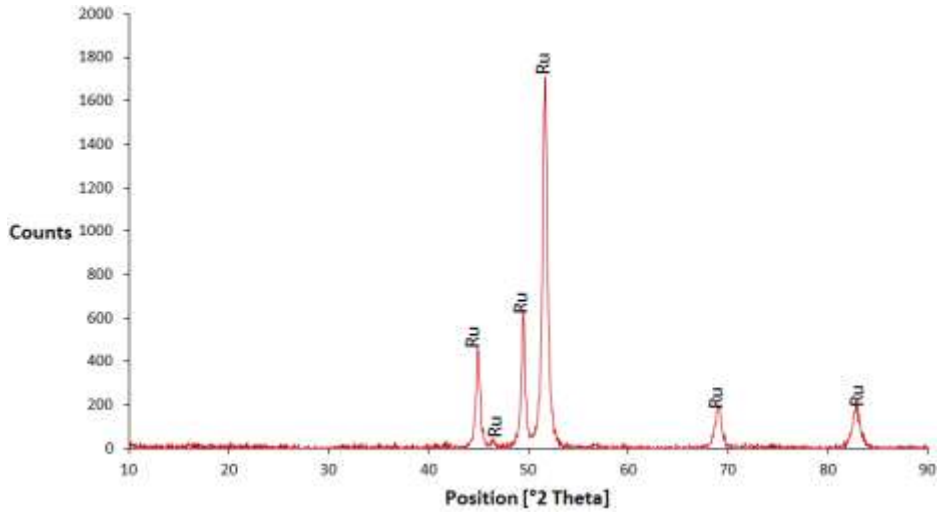

Figure 4.24. XRD pattern for Ru powder milled for 168 hours.

4.1.5. Milling with a 1 kg Capacity Mill

Since the use of a 100 g capacity mill resulted in powder contamination with Cr and Fe (Tables 4.5 and 4.6), the use of 1 kg mill to mix 100 g of powders was investigated. The 1 kg capacity mill had an inherent advantage of having a WC-based lining and milling media, unlike the steel-lined 100g mill, thus reducing chances of Fe and Cr contamination. It was also anticipated that using a bigger mill would result in significantly reduced milling times. Reduced milling times also imply decreased chances of contamination. The particle size reduction and mixing of the products of the two mills were compared. To compensate for a very small amount of powder, a 30:1 ball-to-powder ratio was used. Based on the inverse relationship between the ball-to-powder ratio and milling times, the following intuitive equation was used to estimate the initial milling time for the 1 kg mill:

$$\frac{\text{Ball-to-powder ratio of small mill}}{\text{Ball- to- powder ratio of large mill}} \propto \frac{\text{Milling time in large mill}}{\text{Milling time in small mill}} \qquad \text{Equation 4.1}$$

The SEM-EDS analyses results from the 1 kg mill are also shown in Table 4.6. No Cr and Fe were detected in powders from the large mill. The large errors (Table 4.6) were due to the intereference of the underlying carbon on the analysis. However, powders from both mills had some oxygen, and this was because the unmilled powders already had some oxidation (Table 4.2). Powders from both mills had very similar XRD patterns (Figure 4.25), since the

contaminants from the small mill were below detection level (4 at.%). The XRD results confirmed the phases obtained from the analyses of individual powders, i.e. WC, VC, fcc Co and hcp Co (Figures 4.9-12).

Table 4.6. EDS analyses of 80WC-10VC-10Co milled powders from the 1 kg and 100 g mills.

Element	**Amount (wt%)**	
	1 kg mill	**100 g mill**
C	51.6±6.8	49.0±3.0
O	7.3±1.1	7.0±1.0
Cr	-	1.9±0.3
Fe	-	3.8±0.4
V	11.0±2.1	9.0±1.0
Co	11.1±2.5	10.1±1.0
W	19.0±3.0	19.2±3.0

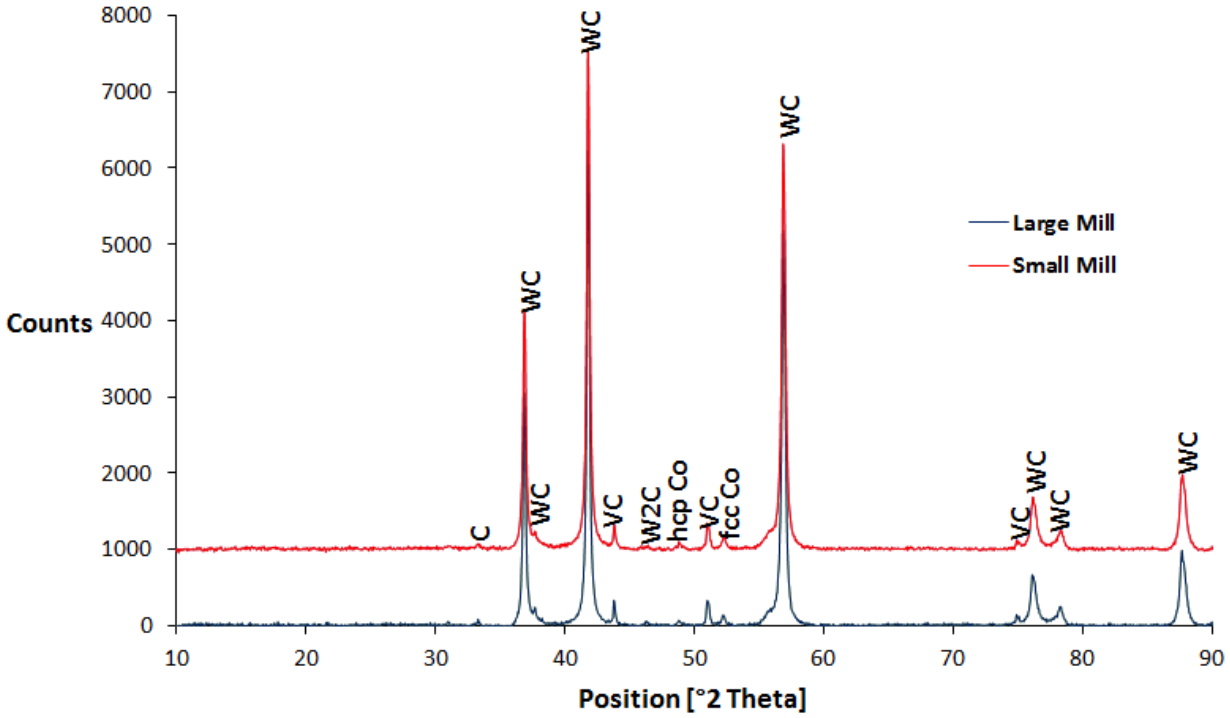

Figure 4.25. XRD pattern obtained for 80WC-10VC-10Co (wt%) powders from 1 kg and 100 g mills.

Particle size analyses revealed a mean powder particle size of 0.618±0.018 µm from the larger mill, coarser than obtained from the smaller mill (0.495±0.019 µm). To compare the mixing capabilities of the two mills, the coercivities of the sintered products from the powders of the two mills were measured (Table 4.7). Unlike alloys from the large mill powders, alloys from the small mill had no variation in coercivity. Also, the higher errors associated with the EDS analyses for the large mill (Table 4.6) could be associated with high powder inhomogeinty. However, since both powders had large errors, there might have been interference of the C surface that held the powders to the sample holder, since the C surface was not fully covered by the powders. The SEM-EDS mapping image of the milled powders (Figure 4.26) showed a more even Co distribution for the small 100 g mill (Figure 4.26a) than obtained from the 1 kg mill (Figure 4.26b), a further indicator of greater milling effectiveness for the small mill. It was therefore concluded that, under the different conditions used, the smaller mill produced a better powder mixture than a larger mill for the same quantities. The use of a much longer milling time (24h) for the small mill compared to that for the large mill (4h), was most likely the main reason for better milling effectiveness.

Table 4.7. Coercivities of alloys from the large mill (4 h milling time) and the small mill (24 h milling time).

Analyses	Coercivity (Oe)	
	1 kg Mill	**100 g Mill**
1	252.0	246.0
2	251.5	246.5
3	250.5	247.0
4	254.0	246.5

Another 100 g mixture of 80WC-10VC-10Co powders was milled for 8 h in the 1 kg mill. After 8 hours, a mean particle size of 0.543±0.005 μm was attained, still higher than that produced from the small mill (0.495±0.018 μm). The powder was taken for EDS mapping (Figure 4.27). A more even Co distribution was observed than obtained after milling for 4 h (Figure 4.26b). However, the distribution was more clumped than observed with the small mill after 24h (Figure 4.26a).

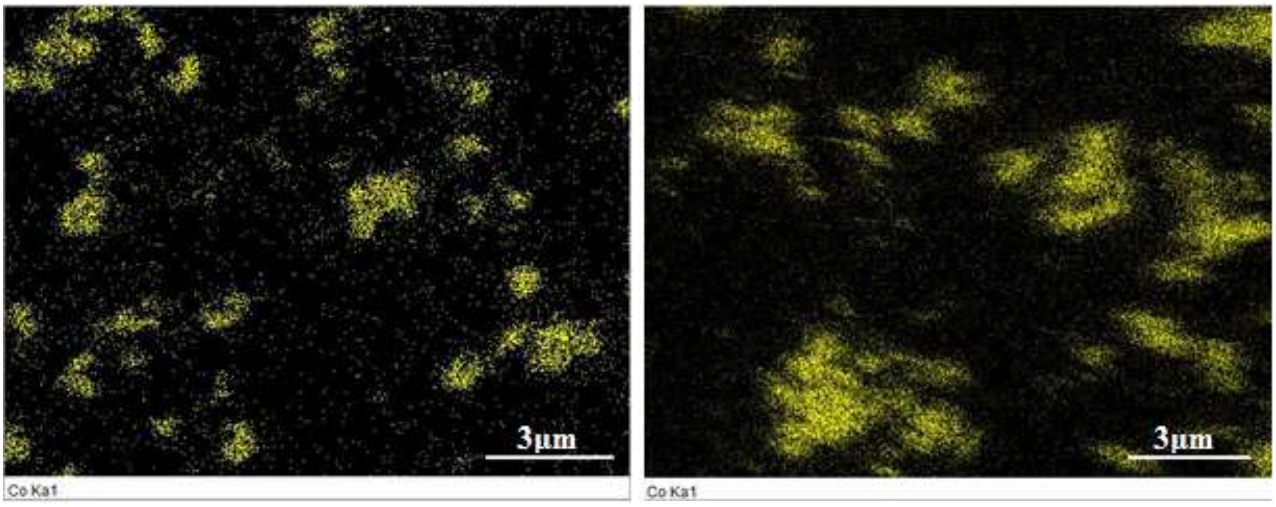

(a) (b)

Figure 4.26. EDS maps of 80WC-10VC-10Co (wt%) powders, showing: (a) better de-agglomeration (more sparse distribution) after milling in the small mill for 24h, than (b) after milling in the large mill for 4h.

Further mixing of the 8 h milled powder mixture was done in a turbular mixture for 4 h at 94 rpm and a 4:1 ball-to-powder ratio. The resulting powder mixture was taken for EDS mapping (Figure 4.28). Cobalt was more dispersed than after mixing in the small mill for 24 h (Figure 4.26a). The SEM-BSE image of the 80WC-10VC-10Co powder (Figure 4.29a) also showed that the Co particles were well distributed throughout the powder mixture. The powders from the 1 kg mill and turbular mixer (Figure 4.29a) had a generally darker contrast than that from the small mill (Figure 4.29b), indicating a more even distribution of Co (dark contrast phase).The powder mixture had a mean particle size of 0.367±0.010 μm, much finer than obtained from the small mill (0.495±0.018 μm). The finer particle size obtained from ball milling followed by turbular mixing resulted in the best homogenous mixing. Furthermore, the 1 kg capacity mill had less potential of powder contamination. The combination of mixing in the 1 kg mill and mixing in a turbular mixer was therefore chosen as the powder mixing method, since it produced better mixing at less time than the small mill.

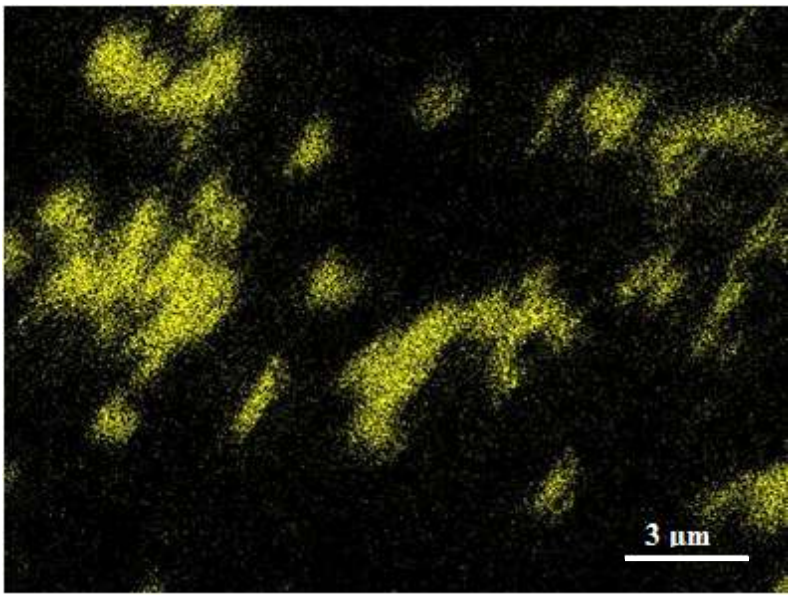

Figure 4.27. EDS map for 80WC-10VC-10Co (wt%) powder after milling in the 1 kg mill for 8 hours, showing a more even Co distribution than after milling for 4 hours (Figure 4.26b).

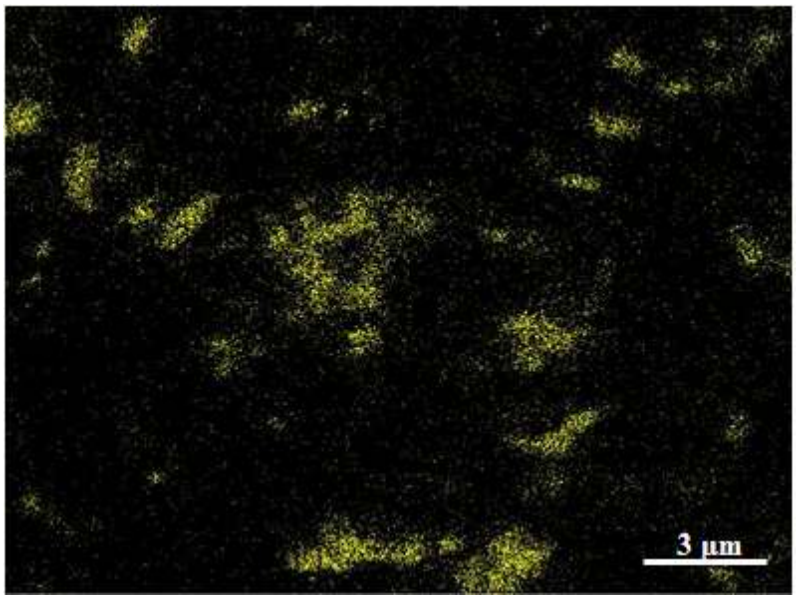

Figure 4.28. EDS map for 80WC-10VC-10Co (wt%) powder showing the Co distribution after milling in the 1 kg mill for 8 hours and mixing in a turbular mixer for 4 hours.

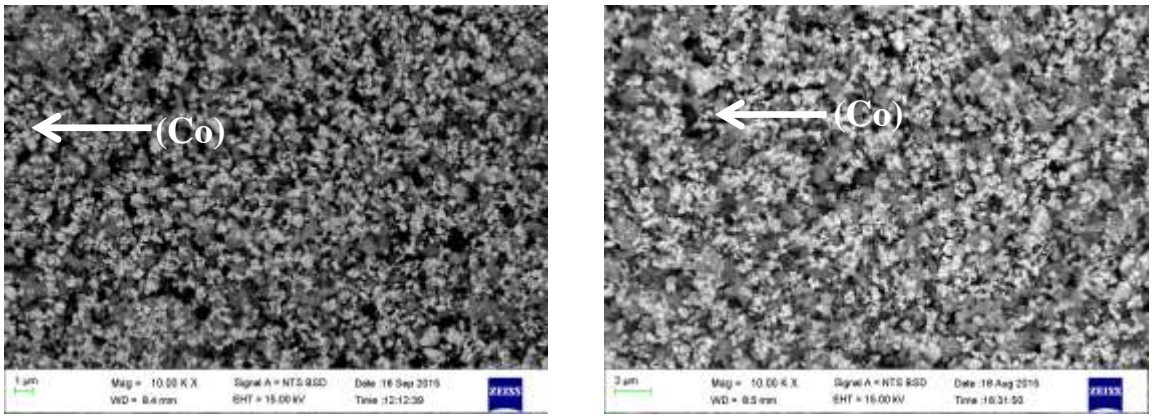

(a) (b)

Figure 4.29. SEM-BSE images of 80WC-10VC-10Co (wt%) powder mixture: a) produced by 1kg ball milling and turbular mixing, resulting in increased dispersion of Co (medium dark contrast phase), than b) obtained from the small mill.

4.2. Quality Tests

The results for density, porosity and magnetic properties of the alloys are reported in this section.

4.2.1. Density

Table 4.8 shows the density results obtained for the sintered alloys. The results for density and the corresponding densification are given in Figures 4.30 and 4.31. For the 80WC-10VC-(10-*x*)Co-*x*Ru (Figure 4.30) and 89.6WC-0.4VC-(10-*x*)Co-*x*Ru (Figure 4.30) alloys, Ru additions increased density. The increase in density was due to Ru replacing less dense Co. Since WC is denser than Ru, the alloy density decreased with Ru additions (WC replacement) in (89.6-*x*)WC-0.4VC-10Co-*x*Ru and (89.2-*x*)WC-0.8VC-10Co-*x*Ru (wt%) alloys (Figure 4.30). As to be expected, due to the low density of VC, alloys with higher VC contents had lower density, with the 80WC-10VC-(10-*x*)Co-*x*Ru alloys (Figure 4.30) having the lowest density.

Apart from the density of the constituting elements, alloy density also depends on the effectiveness of the sintering process. Thus, densification (actual/theoretical) of the alloys was determined. The effect of Ru or VC on densification was not clear, since opposite trends were seen between the 80WC-10VC-(10-*x*)Co-*x*Ru (Figure 4.31) and 89.6WC-0.4VC-(10-*x*)Co-*x*Ru (Figure 4.31) alloys, both of which involved Ru replacing Co. Also, there there were no distinct trends between composition and the densification for the (89.6-*x*)WC-0.4VC-10Co-*x*Ru and (89.2-*x*)WC-0.8VC-10Co-*x*Ru (wt%) alloys (Figure 4.31). All fourteen alloys had greater than 99% densification, an indication of good sinterability.

4.2.2. Porosity

The A porosity was the only type present in all alloys (Figures 4.32a to 4.45a), except for the 80WC-10VC-8.5Co-1.5Ru (wt%) alloy (Alloy 4), that also had B-type porosity. After etching for 15 s to potentially expose the "eta" phase, the latter was not found in any of the fourteen alloys (Figures 4.32b to 4.45b). The appearance of the eta phase in hardmetals is shown in Figure A4 of Appendix A. All micrographs were at x100 magnification.

Table 4.8. Density results of 80WC-10VC-(10-x)Co-xRu, (89.6-x)WC-0.4VC-10Co-xRu, (89.2-x)WC-0.8VC-10Co-xRu and 89.6WC-0.4VC-(10-x)Co-xRu (wt%) alloys.

Series (wt%)	Alloy Number	Ru content (wt%)	Density	Densification (%)
80WC-10VC-(10-*x*)Co-*x*Ru	1	0.0	12.50±0.00	99.7±0.0
	2	0.4	12.51±0.00	99.6±0.0
	3	1.0	12.54±0.01	99.6±0.1
	4	1.5	12.54±0.01	99.4±0.1
	5	2.0	12.56±0.00	99.4±0.0
	6	3.0	12.57±0.01	99.0±0.0
(89.6-*x*)WC-0.4VC-10Co-*x*Ru	7	0.0	14.46±0.03	99.8±0.2
	8	0.4	14.42±0.02	99.6±0.1
	9	2.0	14.38±0.01	99.7±0.1
(89.2-*x*)WC-0.8VC-10Co-*x*Ru	10	0.0	14.37±0.02	99.8±0.1
	11	0.4	14.35±0.02	99.7±0.1
	12	2.0	14.31±0.01	99.8±0.1
89.6WC-0.4VC-(10-*x*)Co-*x*Ru *(Includes Alloy 7)*	13	1.5	14.62±0.01	99.9±0.1
	14	3.0	14.69±0.01	100±0.1

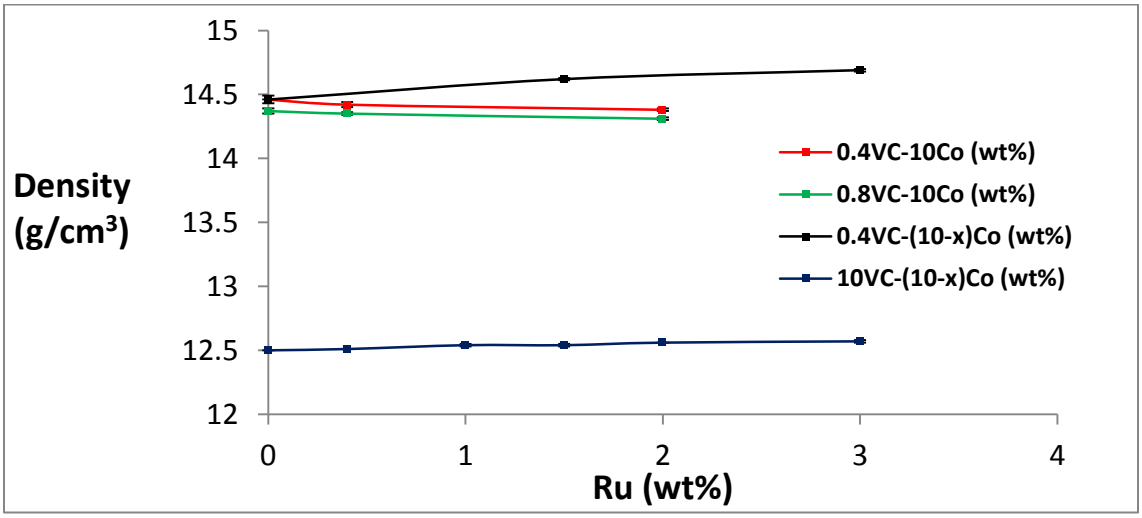

Figure 4.30. Variation of density with Ru additions in 80WC-10VC-(10-x)Co-xRu, (89.6-x)WC-0.4VC-10Co-xRu, (89.2-x)WC-0.8VC-10Co-xRu and 89.6WC-0.4VC-(10-x)Co-xRu (wt%) alloys.

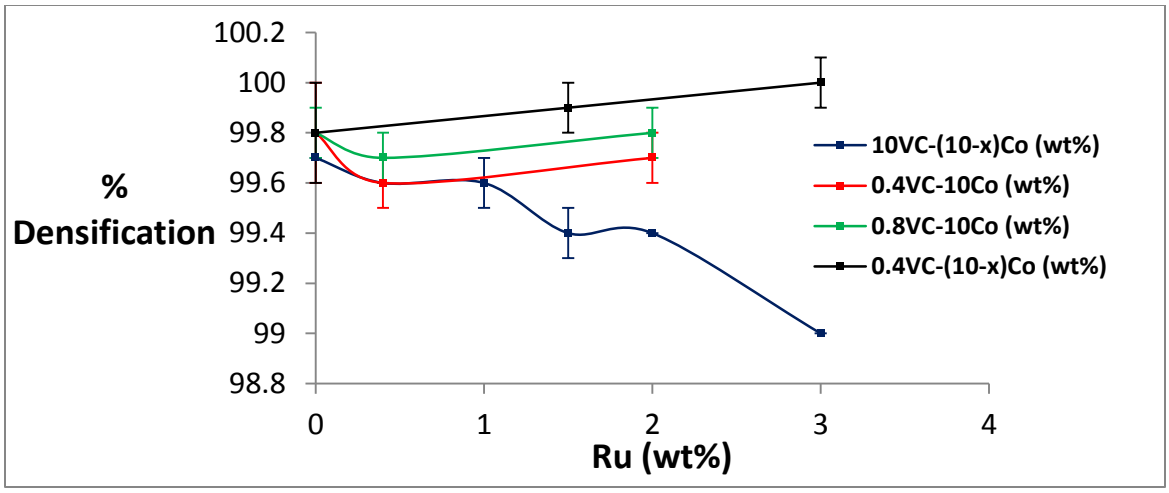

Figure 4.31. Variation of densification with Ru additions in 80WC-10VC-(10-x)Co-xRu, (89.6-x)WC-0.4VC-10Co-xRu, (89.2-x)WC-0.8VC-10Co-xRu and 89.6WC-0.4VC-(10-x)Co-xRu (wt%) alloys.

The porosity ratings for all the alloys are shown in Table 4.9. Standard porosity charts are shown in Appendix A. Porosity results determined using the Archimedes' Principle are also shown in Table 4.9. The volume percentage porosity values from the Archimedes' method were lower than those determined using the standard porosity charts, especially for the (89.6-*x*)WC-0.4VC-10Co-*x*Ru and (89.2-*x*)WC-0.8VC-10Co-*x*Ru (wt%) series (Table 4.9), but more consistent with densification results (Table 4.8 and Figure 4.31).

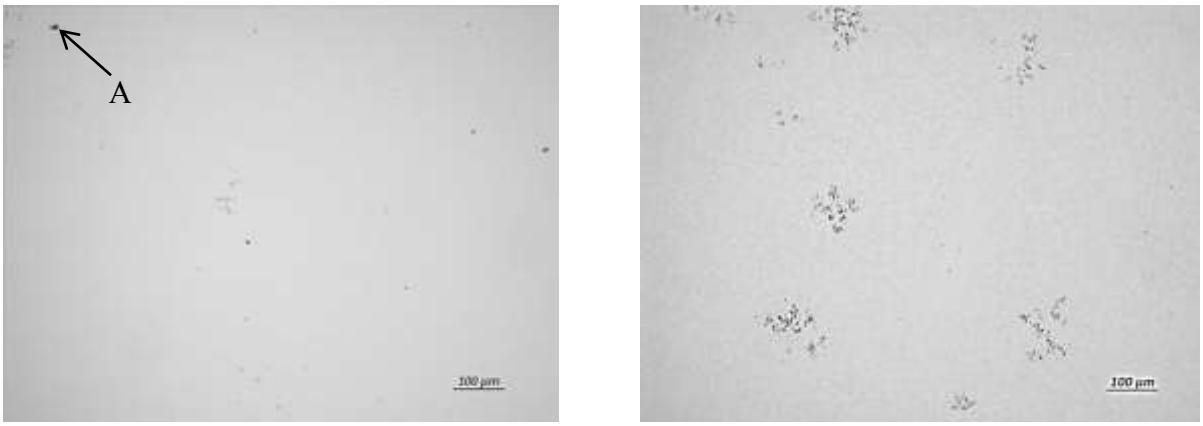

(a) (b)

Figure 4.32. Optical micrographs of sintered Alloy 1 (80WC-10VC-10Co (wt%)): a) showing A-type of porosity, and b) etched for 15 s, showing no eta phase.

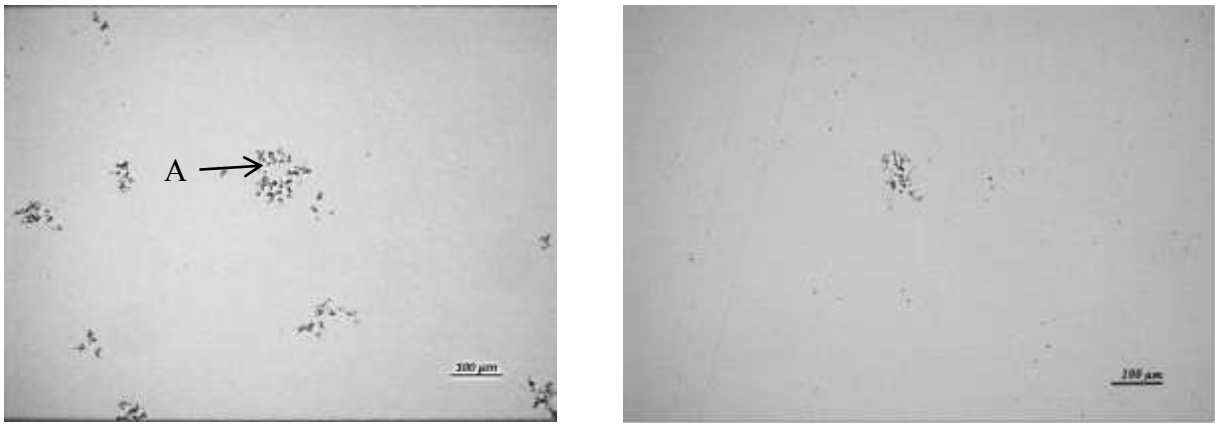

(a) (b)

Figure 4.33. Optical micrographs of sintered Alloy 2 (80WC-10VC-9.6Co-0.4Ru (wt%)): a) showing A type of porosity, and b) etched for 15 s, showing A type porosity and no eta phase.

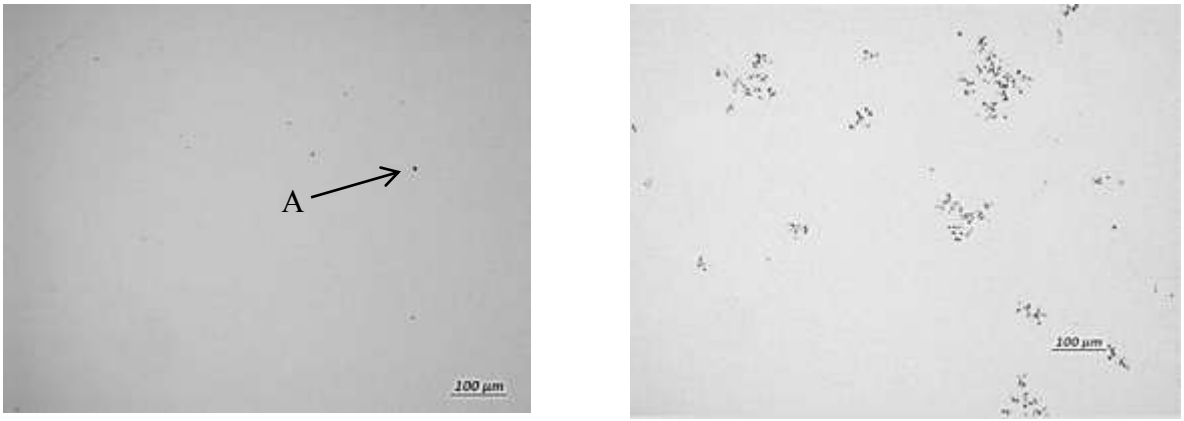

(a) (b)

Figure 4.34. Optical micrographs of sintered Alloy 3 (80WC-10VC-9.0Co-1.0Ru (wt%)): a) showing A-type porosity, and b) etched for 15 s, showing no eta phase.

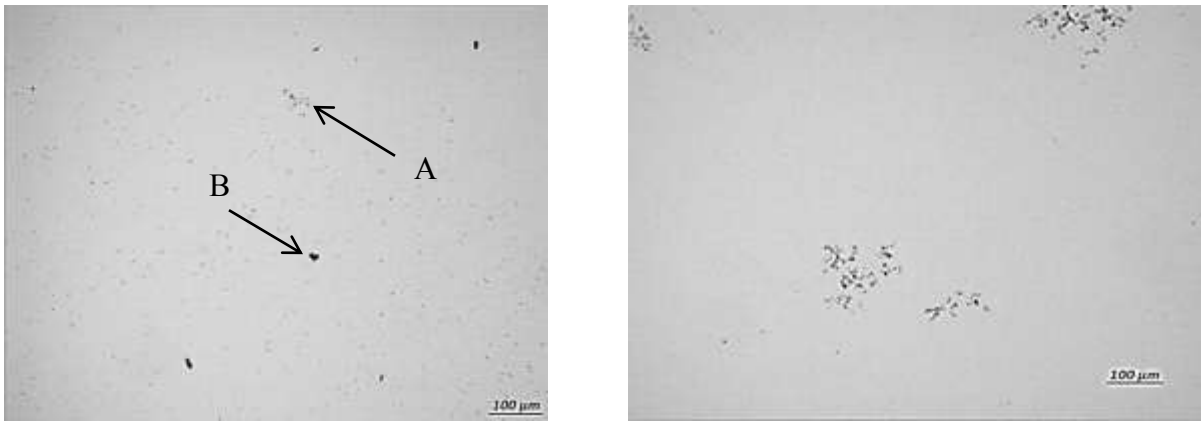

(a) (b)

Figure 4.35. Optical micrographs of sintered Alloy 4 (80WC-10VC-8.5Co-1.5Ru (wt%)): a) showing A and B types of porosity, and b) etched for 15 s, showing no eta phase.

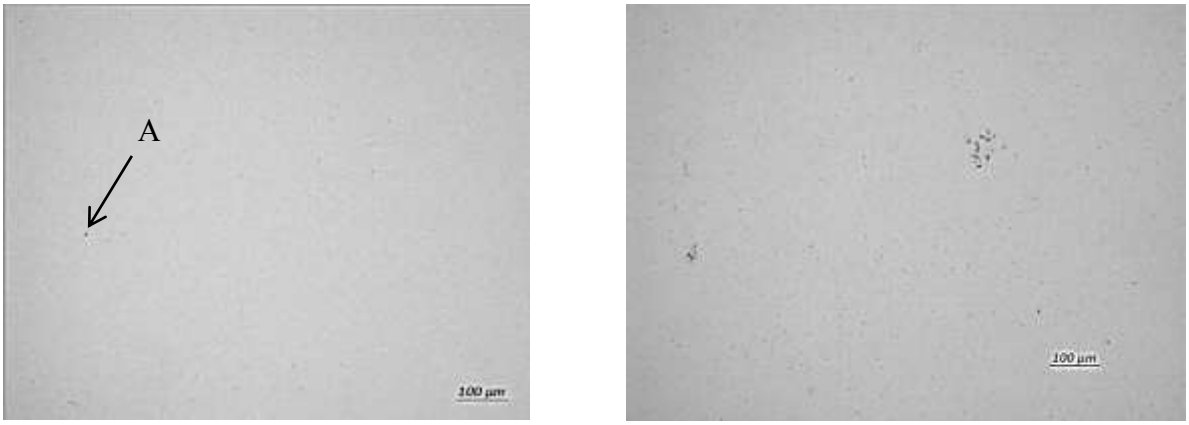

(a) (b)

Figure 4.36. Optical micrographs of sintered Alloy 5 (80WC-10VC-8.0Co-2.0Ru (wt%)): a) showing A-type of porosity, and b) etched for 15 s, showing no eta phase.

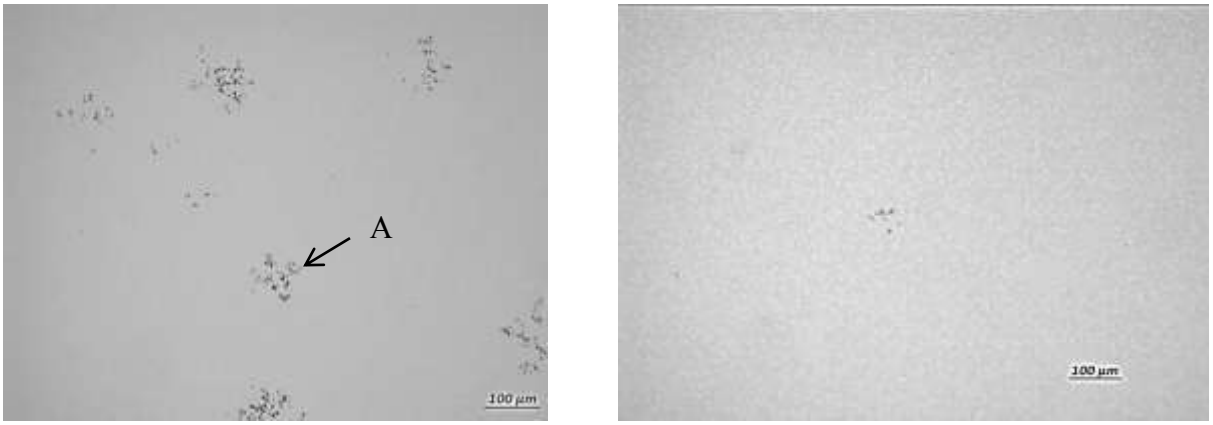

(a) (b)

Figure 4.37. Optical micrographs of sintered Alloy 6 (80WC-10VC-8.0Co-2.0Ru (wt%)): a) showing A type of porosity, and b) etched for 15 s, showing no eta phase.

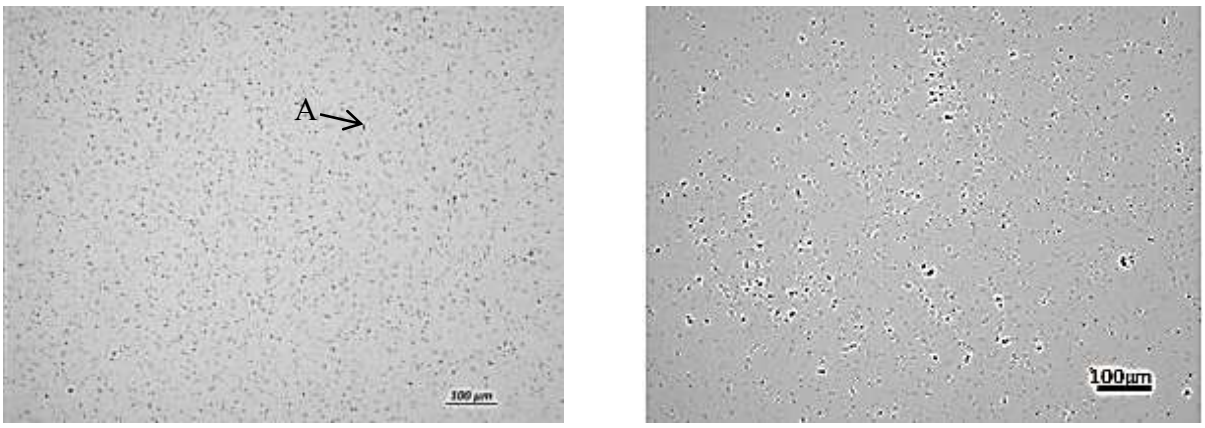

(a) (b)

Figure 4.38. Optical micrographs of sintered Alloy 7 (89.6WC-10Co-0.4VC (wt%)): a) showing A-type of porosity, and b) etched for 15 s, showing no eta phase.

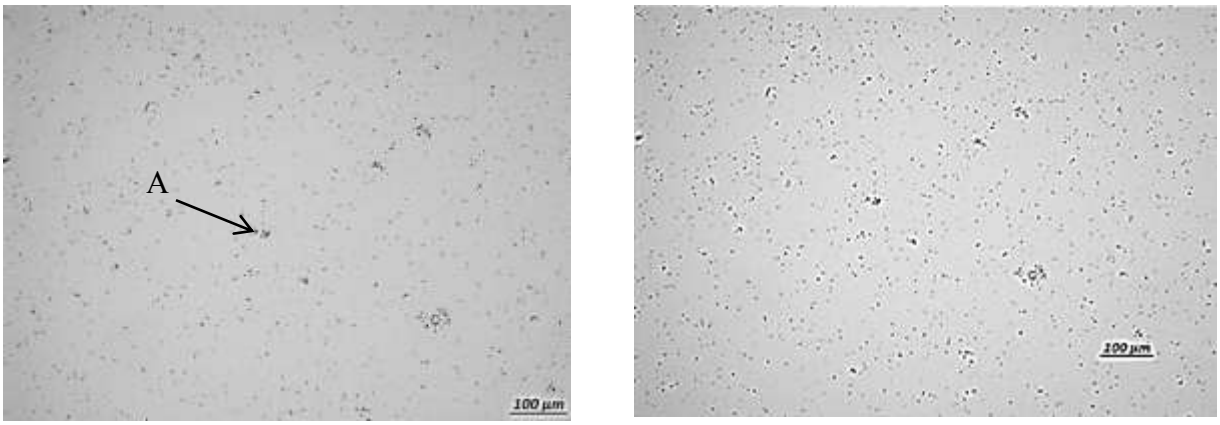

(a) (b)

Figure 4.39. Optical micrographs of sintered Alloy 8 (89.2WC-10Co-0.4VC-0.4Ru (wt%)): a) showing A type of porosity, and b) etched for 15 s, showing no eta phase.

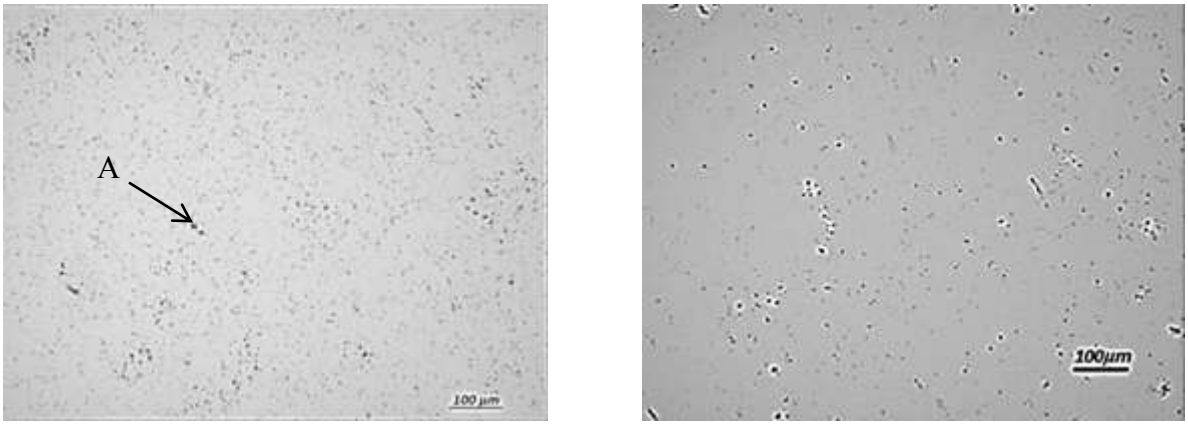

(a) (b)

Figure 4.40. Optical micrographs of sintered Alloy 9 (87.6WC-10Co-0.4VC-2.0Ru (wt%)): a) showing A type of porosity, and b) etched for 15 s, showing no eta phase.

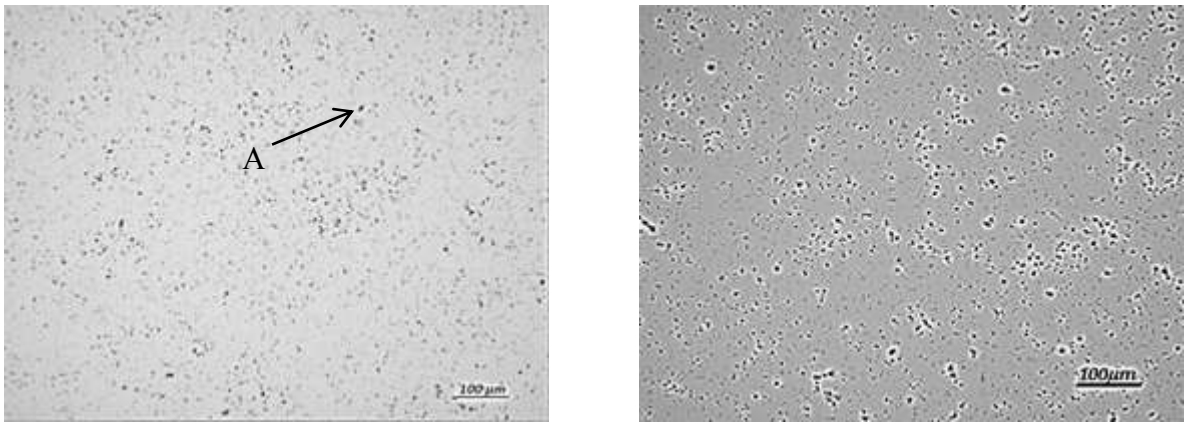

(a) (b)

Figure 4.41. Optical micrographs of sintered Alloy 10 (89.2WC-10Co-0.8VC (wt%)): a) showing A type of porosity, and b) etched for 15 s, showing no eta phase.

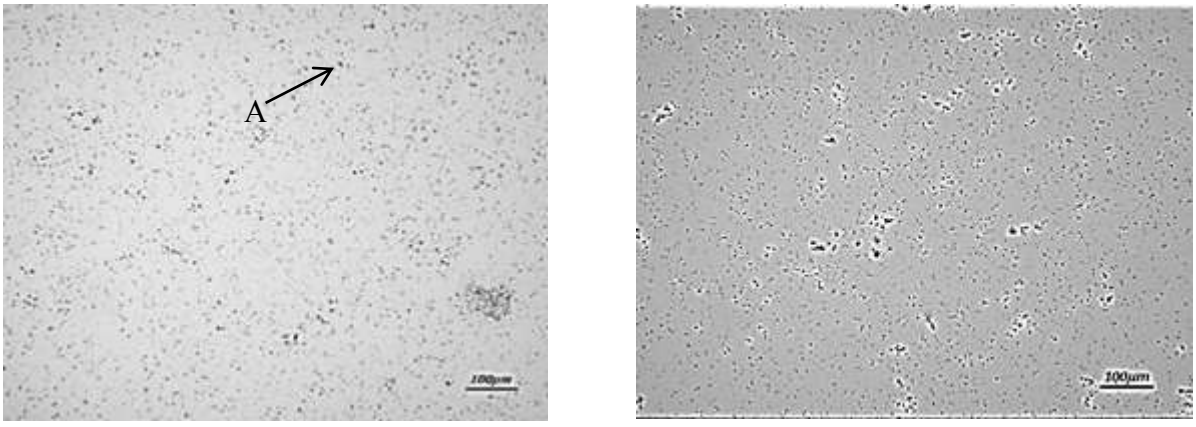

(a) (b)

Figure 4.42. Optical micrographs of sintered Alloy 11 (88.8WC-10Co-0.8VC-0.4Ru (wt%)): a) showing A-type of porosity, and b) etched for 15 s, showing no eta phase.

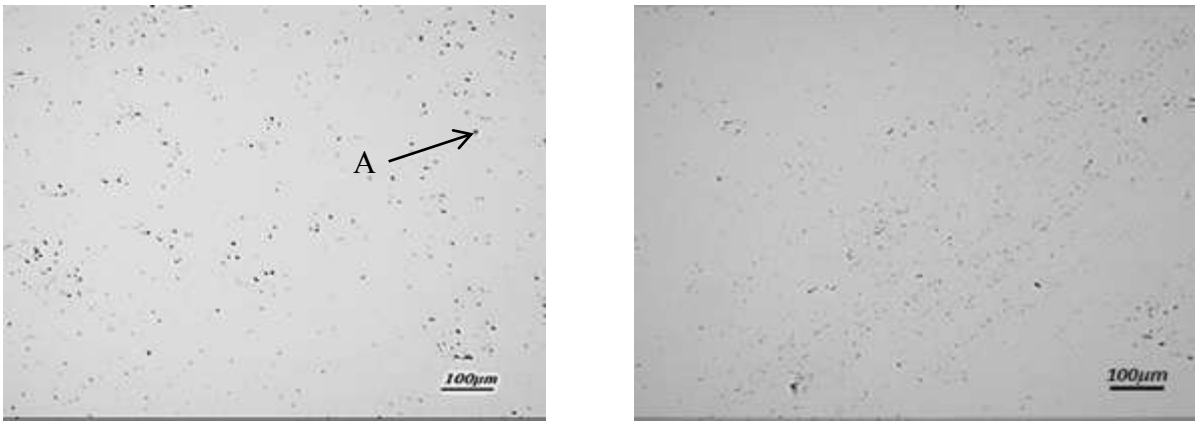

(a) (b)

Figure 4. 43. Optical micrographs of sintered Alloy 12 (87.2WC-10Co-0.8VC-2.0Ru (wt%)): a) showing A-type of porosity, and b) etched for 15 s, showing no eta phase.

There was no distinct trend between both comparative and measured porosities with either VC or Ru content. For all alloy series, the effect of Ru on the comparative porosities was not very definite, and the 89.6WC-0.4VC-(10-*x*)Co-*x*Ru alloys had the same comparative amount. The highest estimated porosities were seen in the (89.6-*x*)WC-0.4VC-10Co-*x*Ru and (89.2-*x*)WC-0.8VC-10Co-*x*Ru alloys that had 0.4 and 0.8 wt% VC.

However, the 89.6WC-0.4VC-(10-*x*)Co-*x*Ru alloys that had 0.4 wt% VC had the lowest porosities. There was also no correlation between the comparative and measured porosities. For examples, Alloy 3 had one of the lowest comparative porosities, but one of the highest measured porosities.

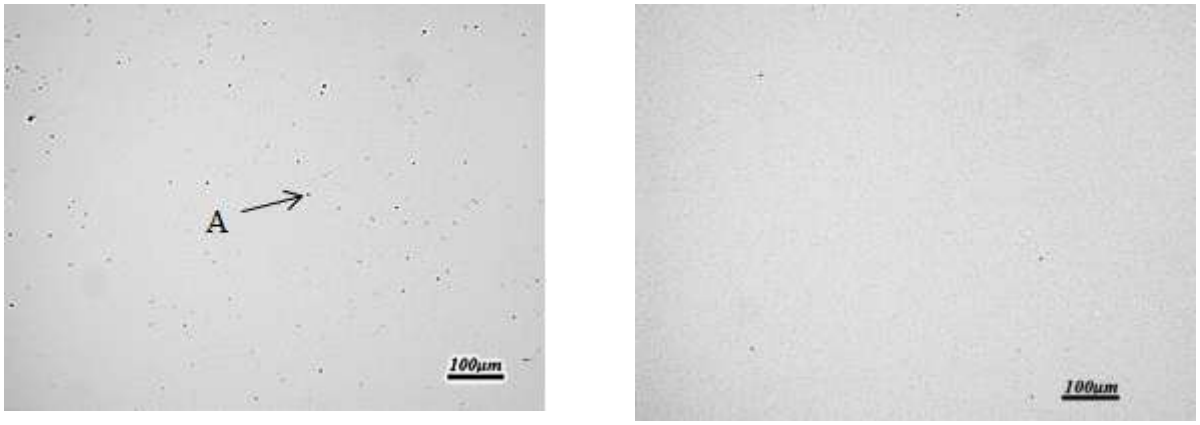

(a) (b)

Figure 4.44.Optical micrographs of sintered Alloy 13 (87.6WC-10Co-0.4VC-1.5Ru (wt%)): a) showing A-type of porosity, and b) etched for 15 s, showing no eta phase.

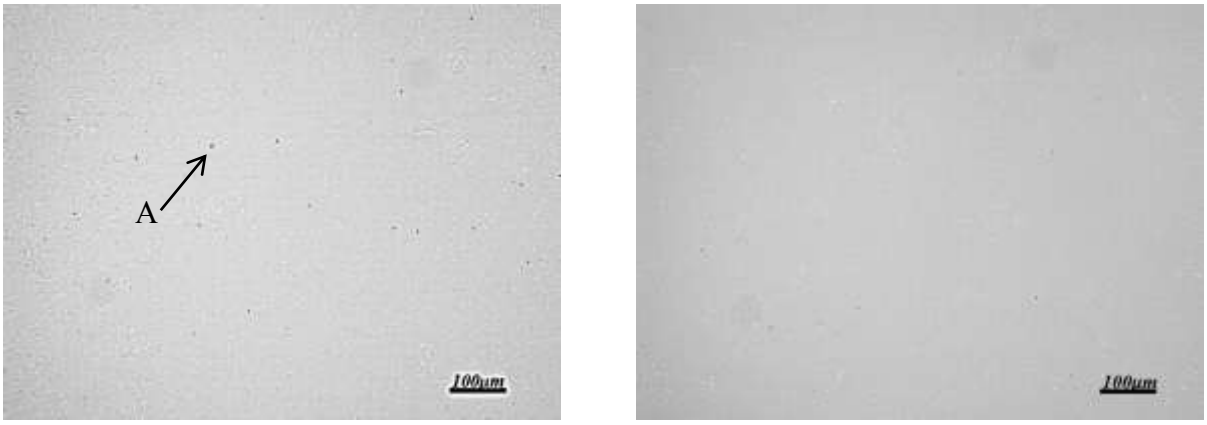

(a) (b)

Figure 4.45. Optical micrographs of sintered Alloy 14 (86.6WC-10Co-0.4VC-3.0Ru (wt%)): a) showing A-type of porosity, and b) etched for 15 s, showing no eta phase.

The comparative porosities were generally higher than the measured porosities. The measured porosities were more consistent with the densification results (Table 4.8 and Figure 4.31).

Table 4.9. Porosity ratings for Alloys 7 to 12 according to standard porosity charts (Appendix A, Figure A4) and Archimedes' method.

Series (wt%)	**Comparative Porosity in Accordance to ISO4505 Standard [1978ISO]**					**Measured Porosity In Accordance to**
	Alloy Number	**Ru content (wt%)**	**Porosity rating**	**Approx. volume porosity**	**Industrial Rating**	**Approx. volume porosity (%)**
80WC-10VC-(10-*x*)Co-*x*Ru	1	0.0	A02B00C00	0.02	Low	0.02±0.01
	2	0.4	A06B00C00	0.20	High	0.03±0.01
	3	1.0	A02B00C00	0.02	Low	0.03±.001
	4	1.5	A02B02C00	0.04	Low	0.01±0.01
	5	2.0	A02B00C00	0.02	Low	0.02±0.01
	6	3.0	A04B02C00	0.08	Moderate	0.03±0.01
(89.6-*x*)WC-0.4VC-10Co-*x*Ru	7	0.0	A08B00C00	0.20	High	0.01±0.01
	8	0.4	A06B00C00	0.20	High	0.02±0.01
	9	2.0	A06B00C00	0.06	Moderate	0.03±.001
(89.2-*x*)WC-0.8VC-10Co-*x*Ru	10	0.0	A08B00C00	0.40	High	0.02±0.01
	11	0.4	A06B00C00	0.20	High	0.03±0.01
	12	2.0	A08B00C00	0.40	High	0.02±0.01
89.6WC-0.4VC-(10-*x*)Co-*x*Ru (*Includes Alloy 7*)	13	1.5	A02B00C00	0.02	Low	0.02±0.01
	14	3.0	A02B00C00	0.02	Low	0.01±0.01

4.2.3. Magnetic Measurements

Table 4.10 shows the magnetic properties for all alloys. The errors were too small to show (Figure 4.46). The magnetic saturation decreased with increased Ru additions in all alloy series (Figure 4.46). As to be expected, cobalt substitution had greater effect on magnetic saturation than when Co content was fixed, since the 89.6WC-0.4VC-(10-*x*)Co-*x*Ru and 80WC-10VC-(10-*x*)Co-*x*Ru alloy series had lower magnetic saturations than the (89.6-*x*)WC-0.4VC-10Co-*x*Ru and (89.2-*x*)WC-0.8VC-10Co-*x*Ru alloy series. It is clear that VC content did not have any effect on magnetic saturations, since the control alloys for all alloy series had close results.

For the 80WC-10VC-(10-*x*)Co-*x*Ru series, Ru additions of 0.4 wt% resulted in increased coercivity, but further Ru additions had the opposite effect (Figure 4.47). Coercivity increased with Ru content for (89.6-*x*)WC-0.4VC-10Co-*x*Ru (wt%) alloys (Figure 4.47), but there was the opposite trend for (89.2-*x*)WC-0.8VC-10Co-*x*Ru (wt%) alloys (Figure 4.47). For the 89.6WC-0.4VC-(10-*x*)Co-*x*Ru alloy series, coercivity increased with 1.5 wt% Ru additions, but decreased with up to 3 wt% Ru. Generally, higher coercivities were observed for alloy series with higher VC content, such that the 80WC-10VC-(10-*x*)Co-*x*Ru series had the highest values for all Ru additions (Table 4.10).

The relationship between coercivity and magnetic saturation for the 80WC-10VC-(10-*x*)Co-*x*Ru and 89.6WC-0.4VC-(10-*x*)Co-*x*Ru alloys (Figure 4.48) followed the same trend as for coercivity with Ru content (Figure 4.48). For (89.6-*x*)WC-0.4VC-10Co-*x*Ru alloys, there was a direct relationship between coercivity and magnetic saturation (Figure 4.48), whereas an inverse relationship was observed for (89.2-*x*)WC-0.8VC-10Co-*x*Ru alloys (Figure 4.48). However, two of these series had more narrow Ru contents, so it was difficult to derive the relationship.

Table 4.10. Magnetic saturation and coercivity values for sintered 80WC-10VC-(10-x)Co-xRu, (89.6-x)WC-0.4VC-10Co-xRu, (89.2-x)WC-0.8VC-10Co-xRu and 89.6WC-0.4VC-(10-x)Co-xRu (wt%) alloys.

Series (wt%)	**Alloy number**	**Ru content (wt%)**	**Magnetic saturation ($\mu Tm^3/kg$)**	**Coercivity (Oe)**
80WC-10VC-(10-*x*)Co-*x*Ru	1	0.0	19.9±0.2	276±1
	2	0.4	18.2±0.1	286±2
	3	1.0	16.3±0.1	274±1
	4	1.5	14.2±0.2	264±1
	5	2.0	12.3±0.2	233±2
	6	3.0	7.9±0.1	223±1
(89.6-*x*)WC-0.4VC-10Co-*x*Ru	7	0.0	20.0±0.1	144±1
	8	0.4	19.6±0.0	147±1
	9	2.0	15.8±0.1	164±2
(89.2-*x*)WC-0.8VC-10Co-*x*Ru	10	0.0	19.9±0.1	200±1
	11	0.4	19.5±0.1	197±1
	12	2.0	16.0±0.0	181±1
89.6WC-0.4VC-(10-*x*)Co-*x*Ru (*Includes Alloy 7*)	13	2.0	12.9±0.0	184±2
	14	3.0	6.1±0.1	165±1

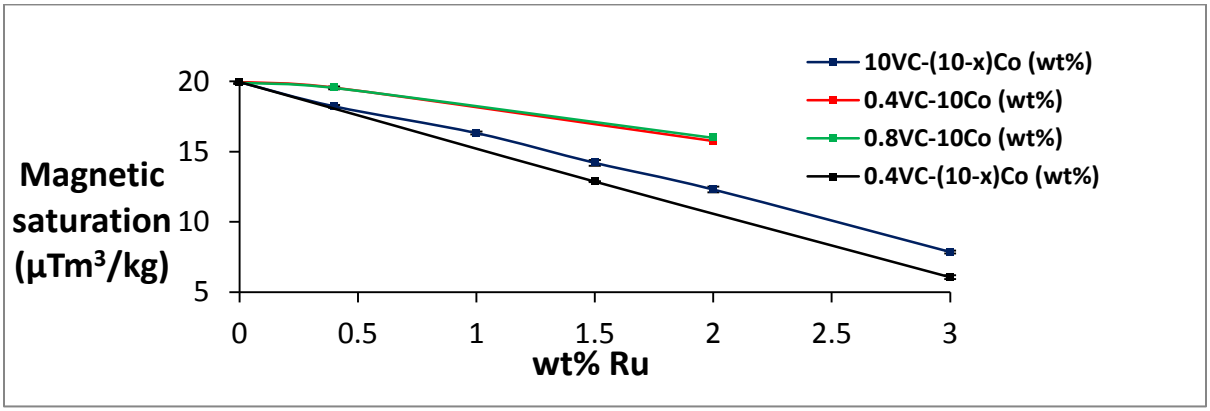

Figure 4.46. Variation of magnetic saturation with Ru content for sintered 80WC-10VC-(10-x)Co-xRu, (89.6-x)WC-0.4VC-10Co-xRu, (89.2-x)WC-0.8VC-10Co-xRu and 89.6WC-0.4VC-(10-x)Co-xRu (wt%) alloys.

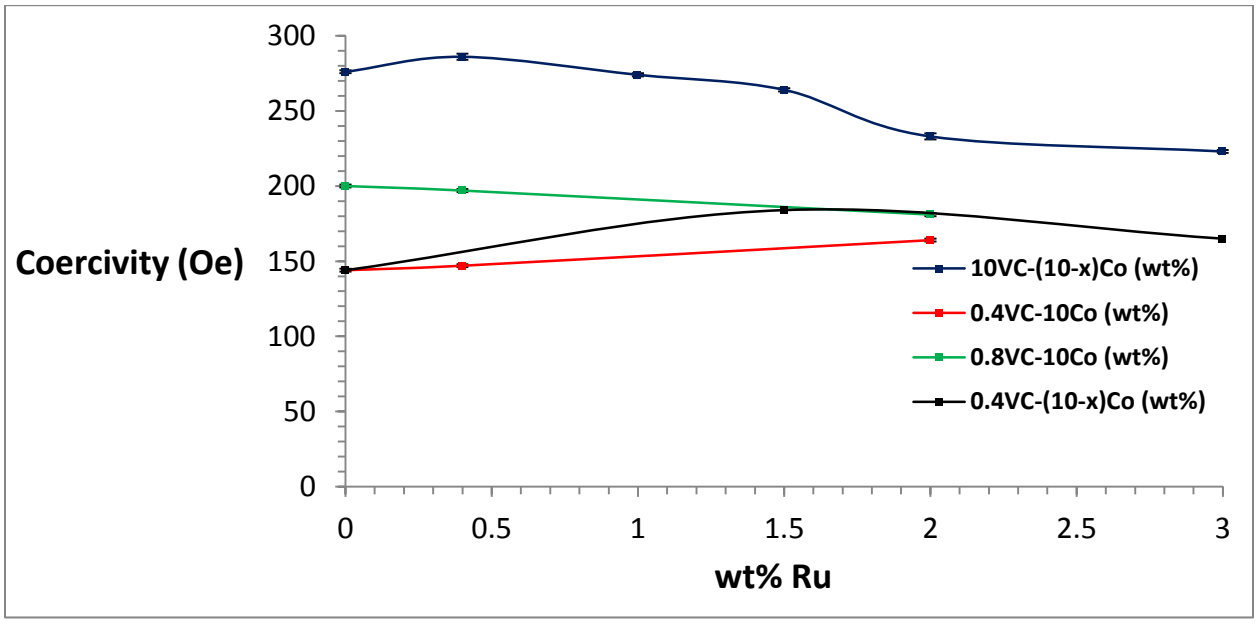

Figure 4.47. Variation of coercivity with Ru content for sintered 80WC-10VC-(10-x)Co-xRu, (89.6-x)WC-0.4VC-10Co-xRu, (89.2-x)WC-0.8VC-10Co-xRu and 89.6WC-0.4VC-(10-x)Co-xRu (wt%) alloys.

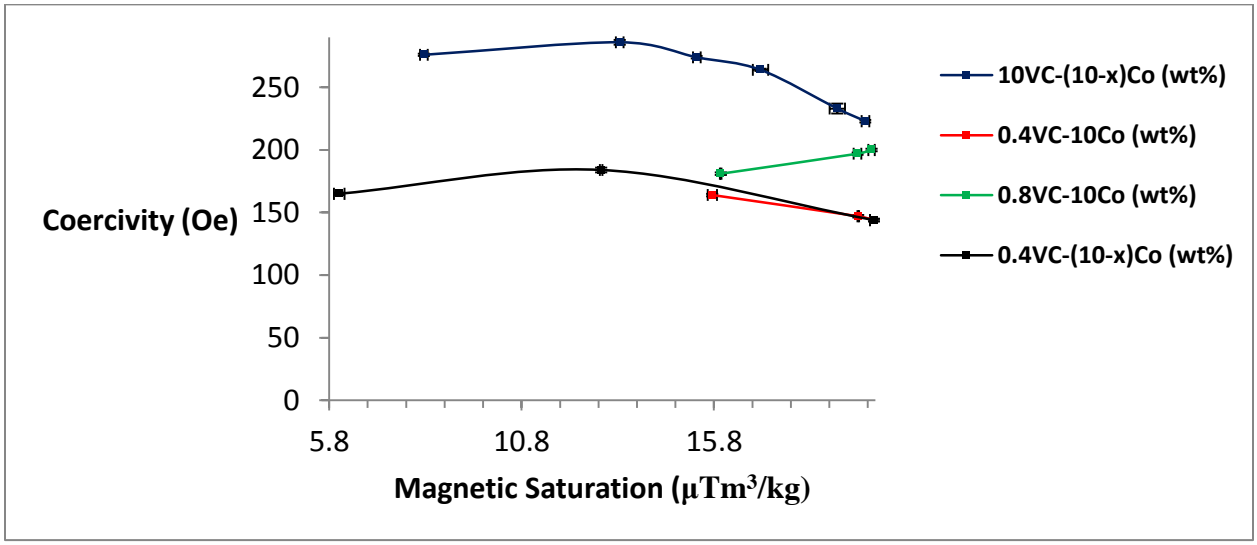

Figure 4.48. Variation of coercivity with magnetic saturation for sintered 80WC-10VC-(10-x)Co-xRu, (89.6-x)WC-0.4VC-10Co-xRu, (89.2-x)WC-0.8VC-10Co-xRu and 89.6WC-0.4VC-(10-x)Co-xRu (wt%) alloys.

4.3. Phase Identification and Microstructure Studies of Sintered Alloys

4.3.1. Qualitative Microstructural Analysis

Alloys 1 to 12 underwent SEM-EDS mapping. As an example, the EDS mapping images for the 80WC-10VC-7.0Co-3.0Ru wt% alloy are shown in Figure 4.49. The phases were matched to the areas of the microstructure as shown in Figure 4.49. To identify the phases corresponding to the elements shown in Figure 4.49, XRD analysis was done on all alloys. The light areas that were most common throughout the microstructure were deduced to be WC which constituted ~80% of the alloy composition, and also because the light areas matched the EDS maps for W (Figure 4.49f). Although it was difficult to find WC grains greater than 2 μm across, their closeness gave reliable analyses. The phase with V was deduced to be (V,W)C. It was determined that Co (Figure 4.49b) corresponded to the dark areas, and (V,W)C (Figure 4.49d) corresponded to the medium dark areas. Ruthenium (Figure 4.49e) had a similar distribution to Co (Figure 4.49b), an indication that the two metals formed a solid solution, as was expected from the Co-Ru phase diagram [1990Mas]. The EDS maps for other alloys shown in Appendix B show that the other 80WC-10VC-(10-*x*)Co-*x*Ru (wt%) alloys had the same three phases as the 80WC-10VC-7.0Co-3.0Ru wt% alloy, whereas for the (87.6-*x*)WC-10Co-0.4VC-*x*Ru, (87.2-*x*)WC-10Co-0.4VC-*x*Ru and 89.6WC-0.4VC-(10-x)Co-*x*Ru alloys, only WC and (Co) were identified. The SEM-BSE microstructures for the fourteen alloys are described in Sections 4.3.1.1 to 4.3.1.14.

4.3.1.1. 80WC-10VC-(10-x)Co-xRu (wt%) Alloys

Generally, fine WC grains of <0.3 μm were seen for the 80WC-10VC-(10-*x*)Co-*x*Ru (wt%) alloys although there were some coarser grains of ~1 μm (Figure 4.50). Areas of (V,W)C, ~1.2 μm across, were also visible throughout the microstructures (Figure 4.50). Some binder pools were also present. The EDS analyses (Tables 4.11 to 4.16) were in agreement with results from EDS mapping (Figure 4.49). The overall Co contents (Tables 4.11 to 4.16), were close to the target values (Table 3.1). The analyses of WC, (V,W)C and (Co) binder phase (Tables 4.11 to 4.16) were close to the expected stoichiometries. However, the (Co) areas were too small to analyze accurately as they were less than ~2 μm across.

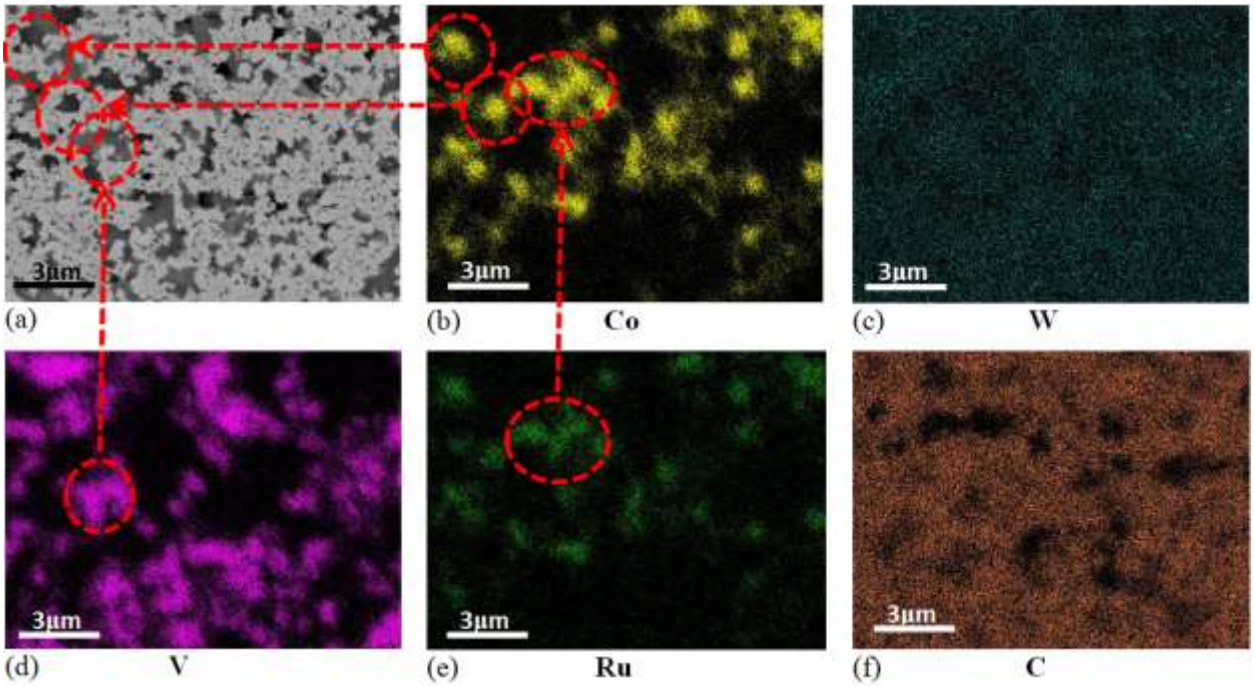

Figure 4.49. SEM-BSE EDS maps for the (a) 80WC-10VC-7.0Co-3.0Ru (wt%) alloy, showing the distribution of: b) Co, c) W, d) V, e) Ru and f) C.

Similar XRD patterns (Figure 4.51) were observed for the first six alloys, corresponding to the 80WC-10VC-(10-*x*)Co-*x*Ru series, because ruthenium was below the detection level of XRD (~4 vol.%). The phases, WC, (V,W)C and (Co) were also confirmed by XRD analysis (Figure 4.51). Mainly, the fcc Co allotrope was present in the alloys but traces of hcp Co were detected for Alloys 2 and 3. Most XRD peaks had similar intensities but there were also some slight peak shifts for WC, suggesting a solid solution.

4.3.1.2. (89.6-*x*)WC-0.4VC-10Co-*x*Ru (wt%) Alloys

A wide grain size range of ~0.1-2.5 µm was seen for the (89.6-*x*)WC-0.4VC-10Co-*x*Ru (wt%) alloys (Figure 4.52). A faceted morphology was seen for the 89.6WC-0.4VC-10Co and 89.2WC-0.4VC-10Co-0.4Ru (wt%) alloys. A more rounded WC morphology within the binder matrix, was seen for the 87.6WC-10Co-0.4VC-2.0Ru (wt%) alloy. Most grains in the 87.6WC-10Co-

0.4VC-2.0Ru (wt%) alloy were small and faceted, and the larger ones were more rounded. Therefore, the addition of Ru affected the morphology of WC grains. There were WC/WC contacts without continuous cobalt films. Generally, (Co) was well distributed between the WC grains and narrow (Co) pools were observed. Tables 4.17 to 4.19 shows the EDS analyses for the (89.6-*x*)WC-0.4VC-10Co-*x*Ru (wt%) alloys. Large errors for the dark (Co) areas were due to them being too small for accurate EDS analyses.

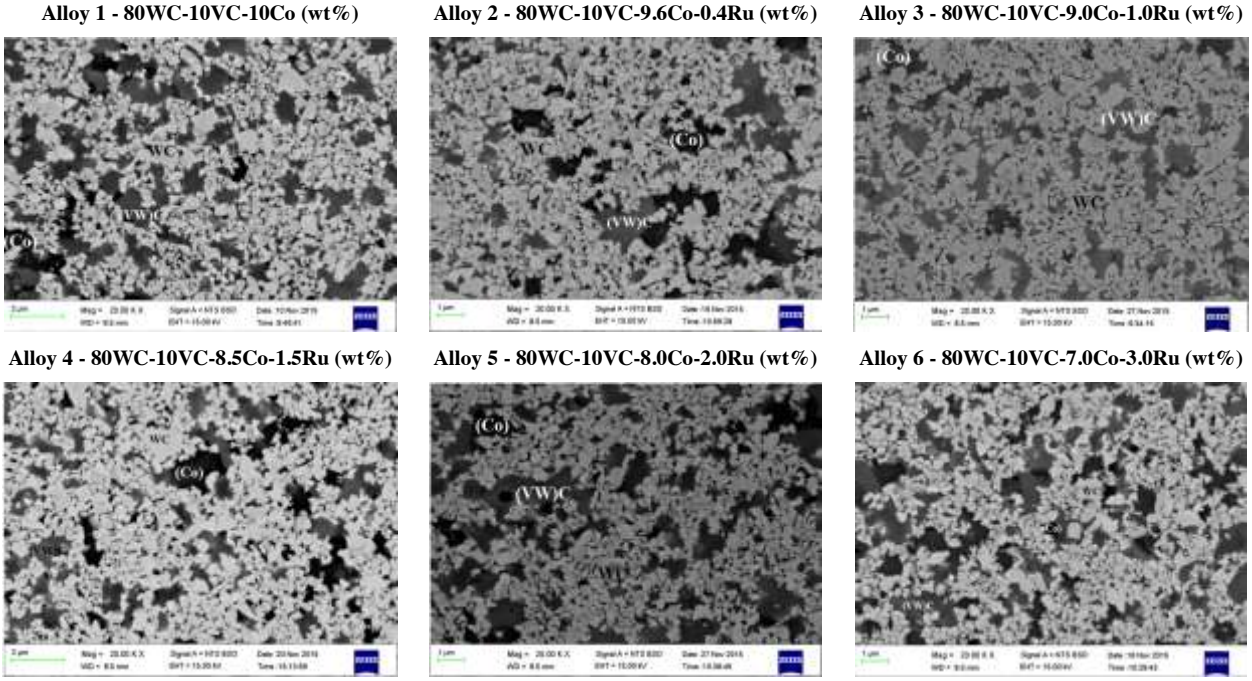

Figure 4.50. SEM-BSE images of the 80WC-10VC-(10-x)Co-xRu (wt%) alloys showing WC (light), (Co) phase (dark) and (V,W)C (medium).

The two phases, WC and (Co) were confirmed by XRD (Figure 4.53). Only the fcc Co allotrope was detected. Ruthenium and vanadium carbide could not be detected since they were below the XRD detection level of ~4 vol.%, and also because Ru formed a solid solution with Co. The peak of the fcc Co allotrope at $2\theta = 51°$ varied in intensity between the three alloys, having the most significant peak for the 87.6WC-10Co-0.4VC-2.0Ru (wt%) alloy, with the most Ru.

The narrower XRD peaks were because the analyses were done on polished alloys, unlike for Alloys 1 to 7 that were done on as-sintered alloys. However, this did not affect the analysis since peaks for the as-sintered and polished alloys matched.

4.3.1.3. (89.2-*x*)WC-0.8VC-10Co-*x*Ru (wt%) Alloys

Alloy 10 (89.2WC-10Co-0.8VC (wt%)) (Figure 4.54) had a mostly rounded WC morphology and a mixture of very fine and coarse grains. A generally fine rounded morphology of WC was observed for Alloy 11 (88.8WC-10Co-0.8VC-0.4Ru (wt%)) (Figure 4.54). A generally fine and irregular WC morphology with some very coarse grains (~2.5 μm) was observed for Alloy 12, 87.2WC-10Co-0.8VC-2.0Ru (wt%) (Figure 4.54). The alloys had many WC/WC contact regions. The largest grains might have been due to grain growth during sintering. Lines (<<1 μm) on the grains were scratches as deduced from the secondary electron images. The overall EDS analyses of the alloys are shown in Tables 4.20 to 4.22. The analyses for WC and (Co) are also shown in Tables 4.20 to 4.22. All the EDS analyses were as expected, with evidence of dissolution of W, V, C and Ru in the (Co) binder phase (Tables 4.20 to 4.22). Both WC and (Co) were deduced from XRD analyses (Figure 4.55), Co being present as the fcc allotrope. The fcc Co allotrope peak was least significant for the 89.2WC-10Co-0.8VC (wt%) alloy.

Table 4.11. EDS analyses of the WC-10VC-10.0Co (wt%) alloy.

Phase Description	Composition (wt%)					Phase
	W	V	C	Co	Ru	
Overall	73.3±0.2	8.50±0.1	8.54±0.4	9.68±0.2	-	-
Light	88.7±2.1	0.3±0.2	9.1±0.5	1.9±0.2	-	WC
Medium	57.7±1.5	31.0±2.8	10.3±0.5	1.0±0.4	-	(V,W)C
Dark	26.6±10.3	0.5±1.5	13.4±3.5	59.4±7.1	-	(Co)

Table 4.12. EDS analyses of the WC-10VC-9.6Co-0.4Ru (wt%) alloy.

Phase Description	Composition (wt%)					Phase
	W	V	C	Co	Ru	
Overall	74.1±0.8	8.57±0.01	8.14±0.7	8.81±0.2	0.41±0.2	-
Light	91.8±1.5	0.2±0.1	7.0±0.2	1.1±0.1	0.0±0.1	WC
Medium	57.8±3.5	30.9±3.0	10.2±0.9	0.8±0.3	0.3±0.3	(V,W)C
Dark	16.1±2.2	1.0±0.8	8.2±0.4	72.4±4.2	2.3±0.2	(Co)

Table 4.13. EDS analyses of the WC-10VC-9.0Co-1.0Ru (wt%) alloy.

Phase Description	Composition (wt%)					Phase
	W	V	C	Co	Ru	
Overall	73.2±0.2	8.50±0.12	8.89±0.3	8.47±0.2	0.91±0.1	-
Light	87.1±0.5	0.3±0.0	10.9±0.3	1.6±0.3	0.1±0.1	WC
Medium	56.6±2.2	30.3±1.0	11.9±0.5	0.6±0.1	0.5±0.1	(V,W)C
Dark	12.8±1.3	1.3±0.3	6.1±2.0	71.9±4.6	7.8±0.7	(Co)

Table 4.14. EDS analyses of the WC-10VC-8.5Co-1.5Ru (wt%) alloy.

Phase Description	Composition (wt%)					Phase
	W	V	C	Co	Ru	
Overall	72.8±0.1	8.47±0.09	9.57±0.3	7.79±0.1	1.40±0.2	-
Light	90.5±1.5	0.4±0.3	7.6±0.9	1.4±0.7	0.0±0.0	WC
Medium	59.1±0.2	30.2±0.5	9.4±0.4	0.7±0.1	0.6±0.2	(V,W)C
Dark	22.1±2.5	1.0±0.5	7.7±3.2	59.2±6.2	9.9±1.8	(Co)

Table 4.15. EDS analyses of the WC-10VC-8.0Co-2.0Ru (wt%) alloy.

Phase Description	Composition (wt%)					Phase
	W	V	C	Co	Ru	
Overall	73.5±0.2	8.52±0.10	8.58±0.2	7.55±0.2	1.90±0.1	-
Light	80.7±3.1	0.4±0.23	15.4±0.7	2.9±1.9	0.5±0.3	WC
Medium	54.6±0.9	25.4±0.7	16.9±2.7	0.4±0.1	0.8±0.1	(V,W)C
Dark	12.1±4.2	1.2±0.1	19.5±0.5	54.9±5.8	12.2±2.3	(Co)

Table 4.16. EDS analyses of the WC-10VC-7.0Co-3.0Ru (wt%) alloy.

Phase Description	Composition (wt%)					Phase
	W	V	C	Co	Ru	
Overall	73.8±0.4	8.42±0.15	8.27±0.4	6.68±0.1	2.87±0.1	-
Light	87.7±3.2	0.4±0.27	11.1±1.3	0.8±0.85	0.2±0.2	WC
Medium	56.3±2.1	29.2±0.2	11.9±1.3	1.2±0.2	1.3±0.2	(V,W)C
Dark	16.3±1.6	0.2±0.8	13.7±5.5	51.8±5.8	17.3±5.4	(Co)

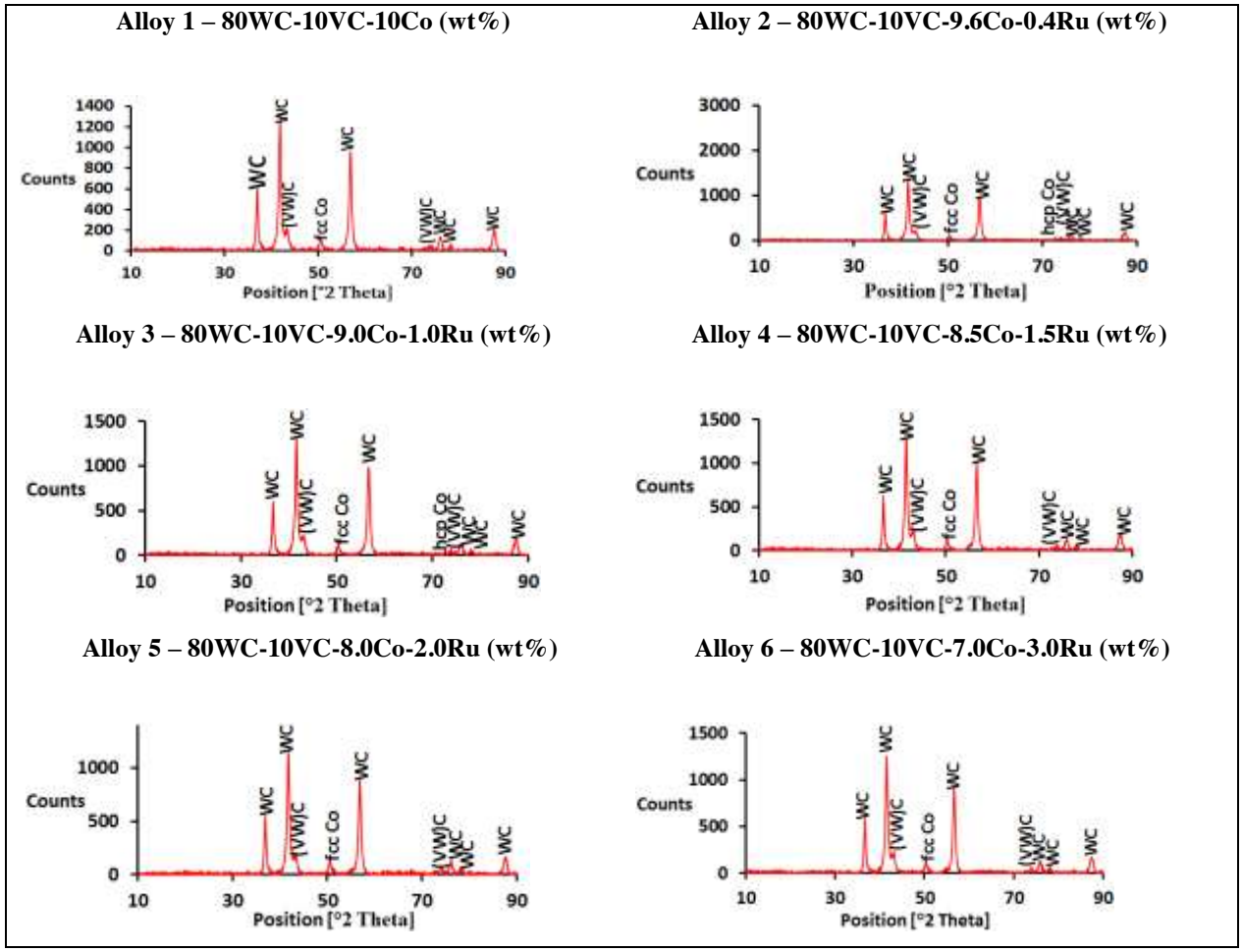

Figure 4.51. XRD patterns for the 80WC-10VC-(10-x)Co-xRu (wt%) alloys showing WC, (Co) and (V,W)C.

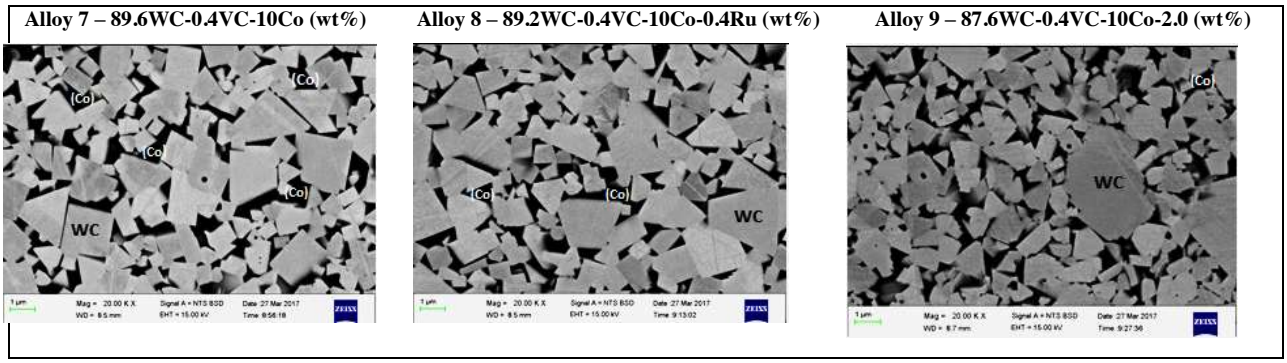

Figure 4.52. SEM-BSE images of the (89.6-x)WC-0.4VC-10Co-xRu (wt%) alloys showing WC phase (light) and (Co) phase (dark).

Table 4.17. EDS analyses of 89.6WC-10Co-0.4VC (wt%) alloy.

Phase Description	Composition (wt%)				Phase
	W	V	C	Co	
Overall	83.3±0.1	0.3±0.1	6.6±0.3	9.8±0.2	-
Light	84.6±0.3	-	14.8±0.1	0.6±0.3	WC
Dark	23.1±3.5	0.4±0.1	8.9±1.2	67.6±2.3	(Co)

Table 4.18. EDS analyses of 89.2WC-10Co-0.4VC-0.4Ru (wt%) alloy.

Phase Description	Composition (wt%)					Phase
	W	V	C	Co	Ru	
Overall	83.2±0.1	0.3±0.0	6.6±0.0	9.5±0.2	0.4±0.1	-
Light	83.5±1.6	-	16.1±1.7	0.4±0.1	-	WC
Dark	22.5±5.5	0.4±0.1	8.4±1.4	66.0±4.3	2.7±0.2	(Co)

Table 4.19. EDS analyses of 87.6WC-10Co-0.4VC-2.0Ru (wt%) alloy.

Phase Description	Composition (wt%)					Phase
	W	V	C	Co	Ru	
Overall	81.4±0.1	0.3±0.1	6.2±0.2	10.0±0.2	2.1±0.2	-
Light	86.8±0.5	-	12.8±0.4	0.4±0.1	-	WC
Dark	23.6±3.9	1.0±0.1	7.3±0.6	56.4±3.6	11.7±0.3	(Co)

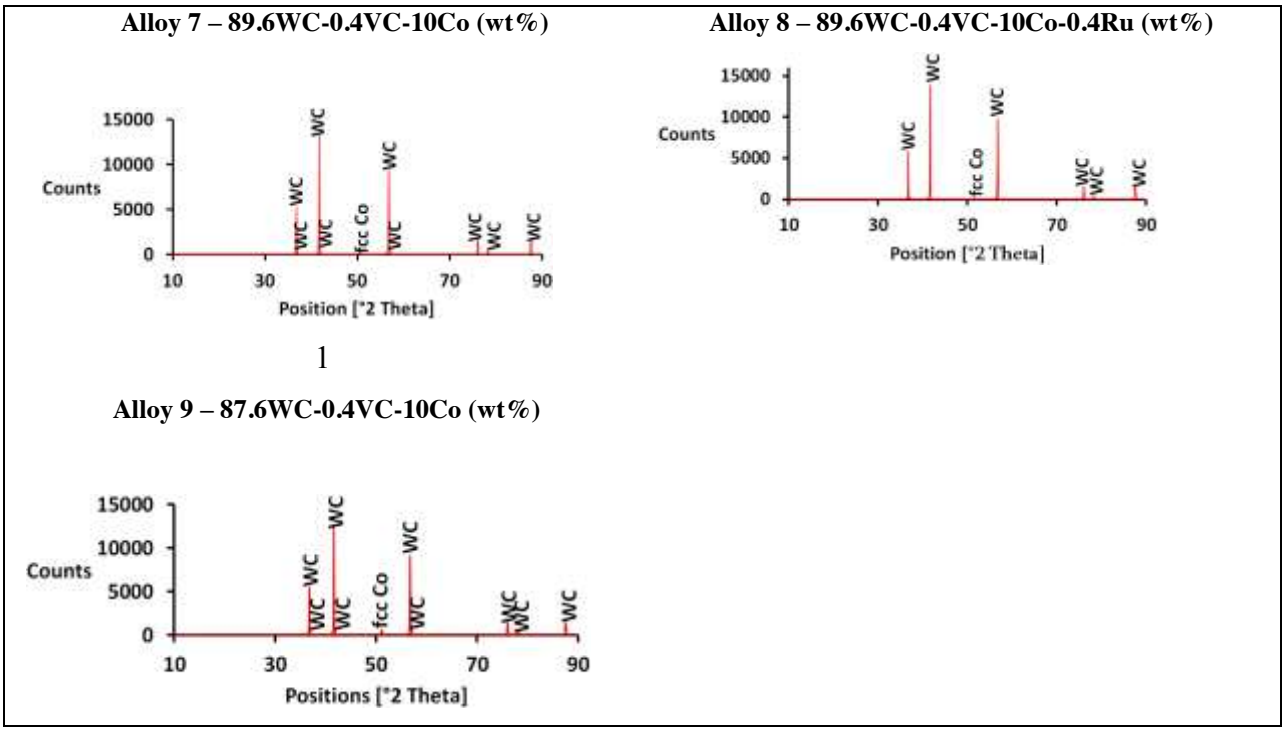

Figure 4.53. XRD patterns for the (89.6-x)WC-0.4VC-10Co-xRu (wt%) alloys showing WC and (Co).

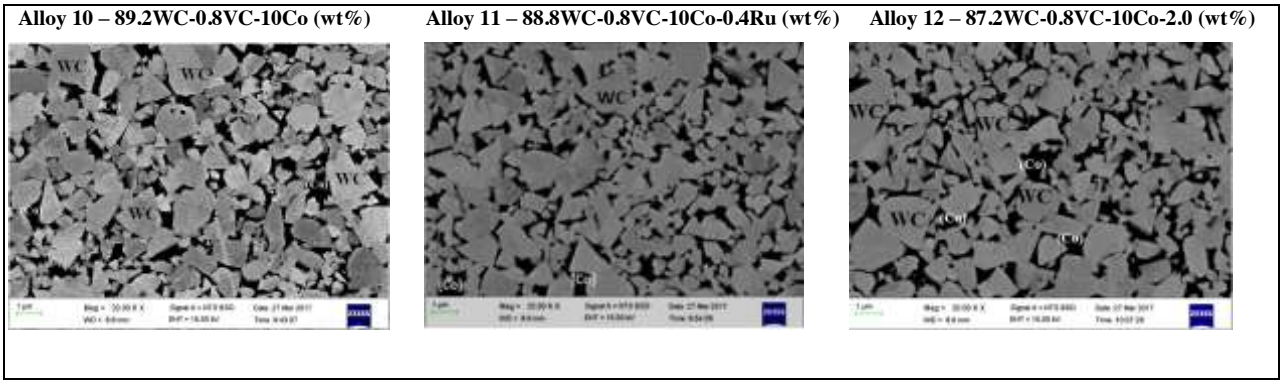

Figure 4.54. SEM-BSE images for the (89.2-x)WC-0.8VC-10Co-xRu (wt%) alloys showing WC phase (light) and (Co) phase (dark).

4.3.1.4. 89.6WC-0.4VC-(10-*x*)Co-*x*Ru (wt%) Alloys

Faceted grains were seen for all alloys in the series (Figure 4.56). A mixture of faceted and rounded grains was seen in the 89.6WC-0.4VC-8.5Co-1.5Ru (wt%) alloy (Figure 4.56). Very fine grains (~0.3 μm) were also seen in the 89.6WC-0.4VC-8.5Co-1.5Ru and 89.6WC-0.4VC-

7.0Co-3.0Ru (wt%) alloys. The 89.6WC-0.4VC-7.0Co-3.0Ru (wt%) alloy had an occasional coarse elongated morphology. Large (Co) areas between WC grains were seen. The EDS analyses for the alloys are shown in Tables 4.23 to 4.25. The EDS analyses of WC for all the alloys (Tables 4.23 to 4.25) showed no solubility of Co, Ru or V in WC. The EDS analyses for the (Co) binder phases (Tables 4.23 to 4.25) showed solubility of W, C, V and Ru. Ruthenium had the greatest solubility in the (Co) binder phase. The XRD patterns (Figure 4.57) confirmed the existence of WC and Co (fcc and hcp). The hcp Co binder phase was only seen in the XRD pattern of the 89.6WC-0.4VC-8.5Co-1.5Ru (wt%) alloy.

Table 4.20. EDS analyses of 89.2WC-10Co-0.8VC (wt%) alloy.

Phase Description	Composition (wt%)				Phase
	W	V	C	Co	
Overall	83.0±0.2	0.6±0.1	6.7±0.3	9.7±0.0	-
Light	87.8±1.6	-	11.5±1.6	0.8±0.1	WC
Dark	13.3±7.7	0.5±0.1	5.7±2.2	80.5±6.6	(Co)

Table 4.21.EDS analyses of 88.8WC-10Co-0.8VC-0.4Ru (wt%) alloy.

Phase Description	Composition (wt%)					Phase
	W	V	C	Co	Ru	
Overall	82.5±0.1	0.8±0.0	6.7±0.2	9.6±0.1	0.4±0.1	-
Light	90.2±0.7	-	8.9±0.6	0.9±0.2	-	WC
Dark	12.9±3.1	0.7±0.2	11.8±0.7	71.8±2.4	2.9±0.3	(Co)

Table 4.22.EDS analyses of 87.2WC-10Co-0.8VC-2.0Ru (wt%) alloy.

Phase Description	Composition (wt%)					Phase
	W	V	C	Co	Ru	
Overall	81.3±0.3	0.6±0.1	6.6±0.1	9.6±0.2	1.9±0.1	-
Light	82.1±1.0	-	17.0±0.1	0.9±0.1	-	WC
Dark	25.3±3.8	0.7±0.1	16.7±1.9	48.6±3.2	8.8±2.2	(Co)

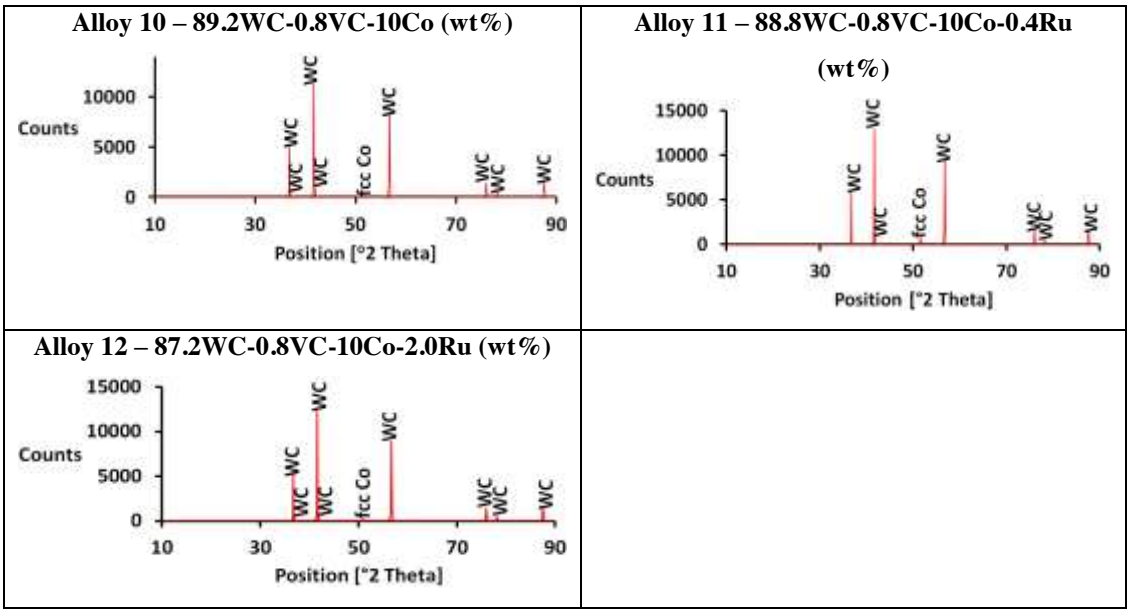

Figure 4.55. XRD patterns for the (89.2-x)WC-0.8VC-10Co-xRu (wt%) alloys showing WC and (Co).

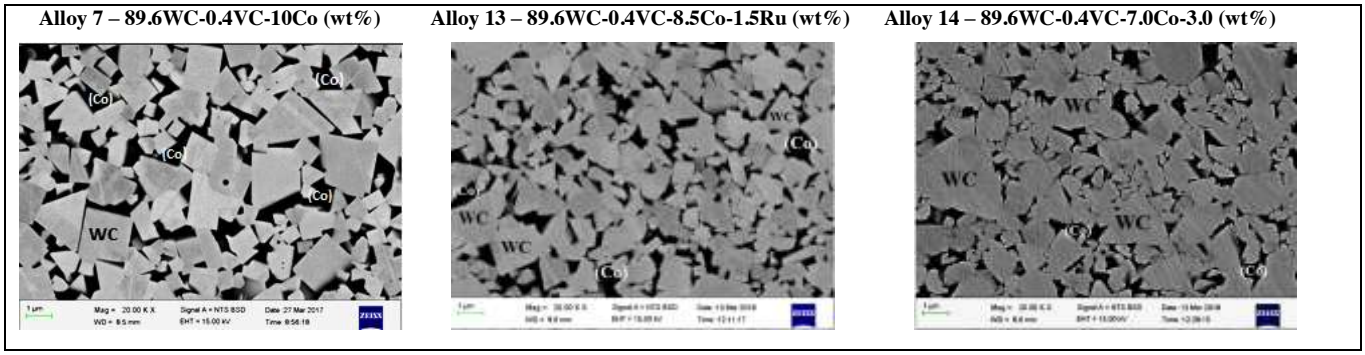

Figure 4.56. SEM-BSE images of the 89.6WC-0.4VC-(10-x)Co-xRu (wt%) alloys showing WC phase (light) and (Co) phase (dark).

Table 4.23. EDS analyses of 89.6WC-10Co-0.4VC (wt%) alloy.

Phase Description	Composition (wt%)				Phase
	W	V	C	Co	
Overall	83.3±0.1	0.3±0.1	6.6±0.3	9.8±0.2	-
Light	84.6±0.3	-	14.8±0.1	0.6±0.3	WC
Dark	23.1±3.5	0.4±0.1	8.9±1.2	67.6±2.3	(Co)

Table 4.24. EDS analyses of 89.6WC-0.4VC-8.5Co-1.5Ru (wt%) alloy.

Phase Description	Composition (wt%)					Phase
	W	V	C	Co	Ru	
Overall	82.9±0.3	0.4±0.2	6.8±0.3	8.4±0.1	1.5±0.2	-
Light	84.6±0.5	-	15.4±0.5	-	-	WC
Dark	13.8±1.6	1.1±0.1	10.9±1.9	62.8±1.9	11.4±0.5	(Co)

Table 4.25. EDS analyses of 89.6WC-0.4VC-7.0Co-3.0Ru (wt%) alloy.

Phase Description	Composition (wt%)					Phase
	W	V	C	Co	Ru	
Overall	83.8±0.1	0.3±0.0	6.1±0.2	6.7±0.1	3.1±0.1	-
Light	84.0±0.6	-	16.0±0.6	-	-	WC
Dark	14.4±2.0	1.5±0.0	10.4±0.3	48.8±1.9	24.9±0.3	(Co)

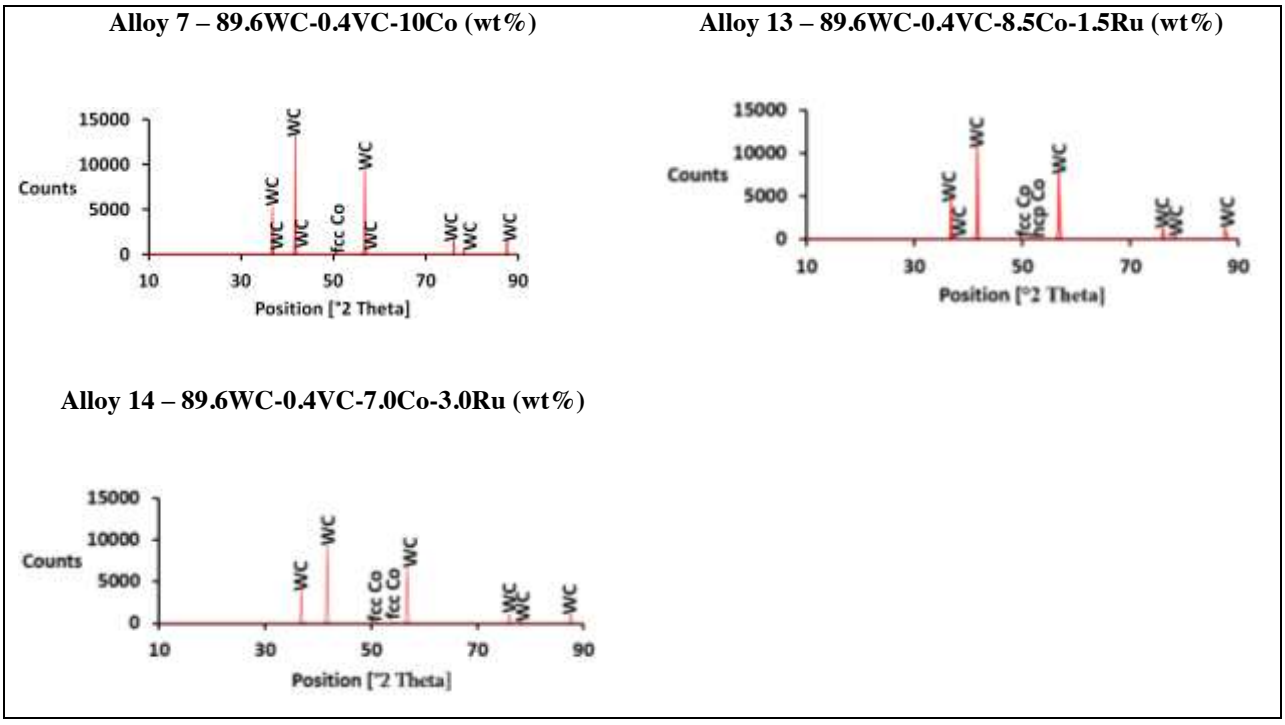

Figure 4.57. XRD patterns for the 89.6WC-0.4VC-(10-x)Co-xRu (wt%) alloys showing WC and (Co).

4.3.2. Quantitative Microstructural Analyses

4.3.2.1. Mean Grain Size Measurements from the Linear Intercept Method

Table 4.26 shows the grain sizes for all fourteen alloys. Figure 4.58 shows that there was no definite trend for the variation of grain size with Ru content in the 80WC-10VC-(10-*x*)Co-*x*Ru alloy series, especially considering that the scatter was very high. There were decreases in mean WC grain size with Ru additions for the (89.6-*x*)WC-0.4VC-10Co-*x*Ru, (89.2-*x*)WC-0.8VC-10Co-*x*Ru and 89.6WC-0.4VC-(10-*x*)Co-*x*Ru alloy series (Figure 4.58), but with a very high scatter. Although 0 and 2 wt% Ru alloys of the (89.6-*x*)WC-0.4VC-10Co-*x*Ru series had overlapping error bars their mean WC values were not the same (Figures 4.58).

The 80WC-10VC-(10-*x*)Co-*x*Ru alloys had the lowest mean WC grain sizes, followed by the (89.2-*x*)WC-0.8VC-10Co-*x*Ru alloys. There was no discernable difference between the mean WC intercept lengths for the (89.6-*x*)WC-0.4VC-10Co-*x*Ru and 89.6WC-0.4VC-(10-*x*)Co-*x*Ru alloys. The mean WC grain sizes varied inversely with VC content.

4.3.2.2. Grain Size Distribution

The graphs for the WC grain size distribution of the fourteen WC-VC-Co-Ru alloys are shown in Figures 4.59 - 4.62. For all alloys, there was no definite trend between WC grain size distribution and Ru content (Figures 4.59 – 4.62). The graph of Figure 4.59 is the most skewed left due to the presence of finer grains in the 80WC-10VC-(10-*x*)Co-*x*Ru alloys. Due to the different grain size distribution ranges between the alloy series, the corresponding graphs (Figures 4.59 – 4.62) could not have the identical scales, thus direct comparisons could not be made.

The size distribution values are summarized in Table 4.27 according to the classification proposed by Roebuck [1995Roe]. For all the 80WC-10VC-(10-*x*)Co-*x*Ru alloys, the ultra-fine class (0.1 – 0.4 μm) had highest proportion and the fine-B class was the least. No medium and coarse grains were present in the 80WC-10VC-(10-*x*)Co-*x*Ru alloy series.

Table 4.26. Relationship between Ru content and the mean grain size for 80WC-10VC-(10-x)Co-xRu, (89.6-x)WC-0.4VC-10Co-xRu, (89.2-x)WC-0.8VC-10Co-xRu and 89.6WC-0.4VC-(10-x)Co-xRu (wt%) alloys.

Series (wt%)	**Alloy Number**	**Ruthenium Content (wt%)**	**Mean WC intercept length, d_{wc} (µm)**
80WC-10VC-(10-*x*)Co-*x*Ru	1	0.0	0.25±0.14
	2	0.4	0.24±0.13
	3	1.0	0.23±0.11
	4	1.5	0.21±0.10
	5	2.0	0.23±0.11
	6	3.0	0.22±0.10
(89.6-*x*)WC-0.4VC-10Co-*x*Ru	7	0.0	0.78±0.24
	8	0.4	0.75±0.30
	9	2.0	0.60±0.25
(89.2-*x*)WC-0.8VC-10Co-*x*Ru	10	0.0	0.52±0.20
	11	0.4	0.51±0.18
	12	2.0	0.48±0.19
89.6WC-0.4VC-(10-*x*)Co-*x*Ru (*Includes Alloy 7)*	13	1.5	0.63±0.21
	14	3.0	0.59±0.18

The extra-fine size range (0.4-0.7 µm) was most common for the (89.6-*x*)WC-0.4VC-10Co-*x*Ru alloy series, whereas the ultra-fine range was the most common for the (89.2-*x*)WC-0.8VC-10Co-*x*Ru alloy series. Addition of 2 wt% Ru resulted in the absence of coarse grains (2.5-6.0µm) in the (89.6-*x*)WC-0.4VC-10Co-*x*Ru alloy series, and a decrease in medium (1.5-2.5µm) and fine-A grains (1.0-1.5µm). An increase in the ultra-fine grains (0.1-0.4µm) was also seen with addition of 2 wt% Ru for the (89.6-*x*)WC-0.4VC-10Co-*x*Ru alloy series. Nano-fine grains (<0.1µm) were present in the 80WC-10VC-(10-*x*)Co-*x*Ru and (89.2-*x*)WC-0.8VC-10Co-*x*Ru VC alloy series, and in both alloy series, no coarse grains were present. Ruthenium additions in the (89.2-*x*)WC-0.8VC-10Co-*x*Ru alloy series resulted in a general decrease in medium and fine-A grains, and an increase in the finer grain sizes. From Table 4.27 it can be established that, as

expected, Ru had less effect on grain size reduction than VC since the grain size differences were more significant across alloy series with varying VC content than within each of the alloy series with varying Ru content.

Figure 4.63 shows the closeness of the grain sizes in the 80WC-10VC-(10-*x*)Co-*x*Ru alloy series, as well as the close relationship to the cumulative distribution plots. Figure 4.63 also confirms the decrease in grain size with Ru additions up to 2 wt% for the (89.6-*x*)WC-0.4VC-10Co-*x*Ru, (89.2-*x*)WC-0.8VC-10Co-*x*Ru and the 89.6WC-0.4VC-(10-*x*)Co-*x*Ru alloy series.

Ruthenium had more effect on grain size in the (89.6-*x*)WC-0.4VC-10Co-*x*Ru and 89.6WC-0.4VC-(10-*x*)Co-*x*Ru alloys than the (89.2-*x*)WC-0.8VC-10Co-*x*Ru alloys, since the curves were more separate for the (89.6-*x*)WC-0.4VC-10Co-*x*Ru alloys. Figure 4.63 also shows that the 80WC-10VC-(10-*x*)Co-*x*Ru alloy series had the finest grain sizes, followed by the (89.2-*x*)WC-0.8VC-10Co-*x*Ru alloy series. Thus, higher VC contents gave finer grain sizes.

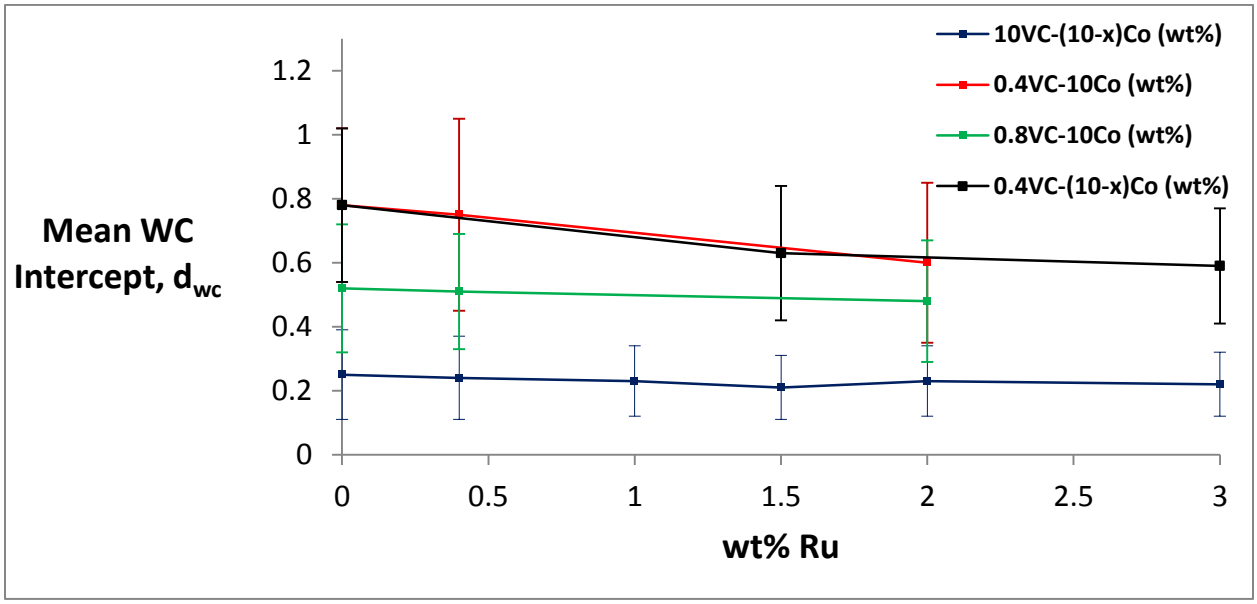

Figure 4.58. Relationship between Ru content and mean grain size for 80WC-10VC-(10-x)Co-xRu, (89.6-x)WC-0.4VC-10Co-xRu, (89.2-x)WC-0.8VC-10Co-xRu and 89.6WC-0.4VC-(10-x)Co-xRu (wt%) alloys.

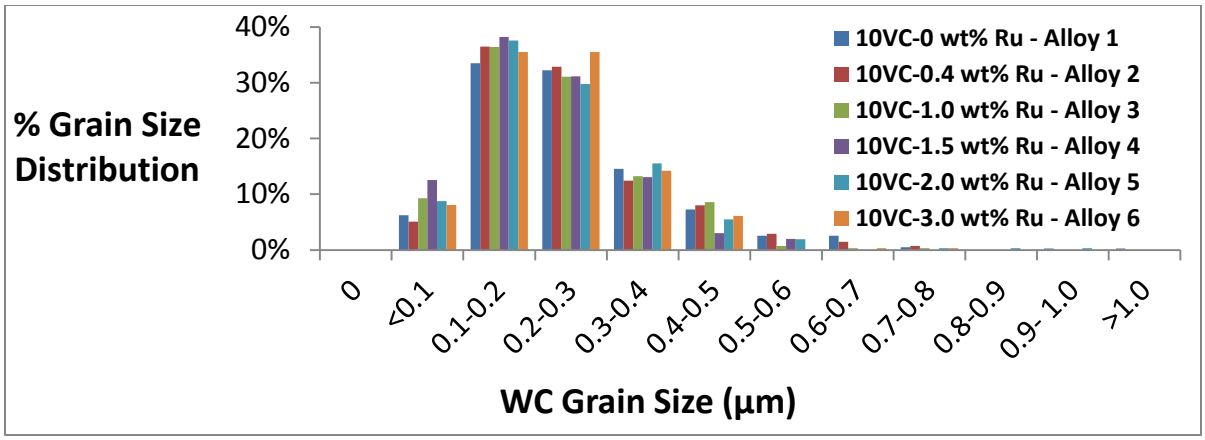

Figure 4.59. Grain size distribution for the 80WC-10VC-(10-x)Co-xRu (wt%) alloys.

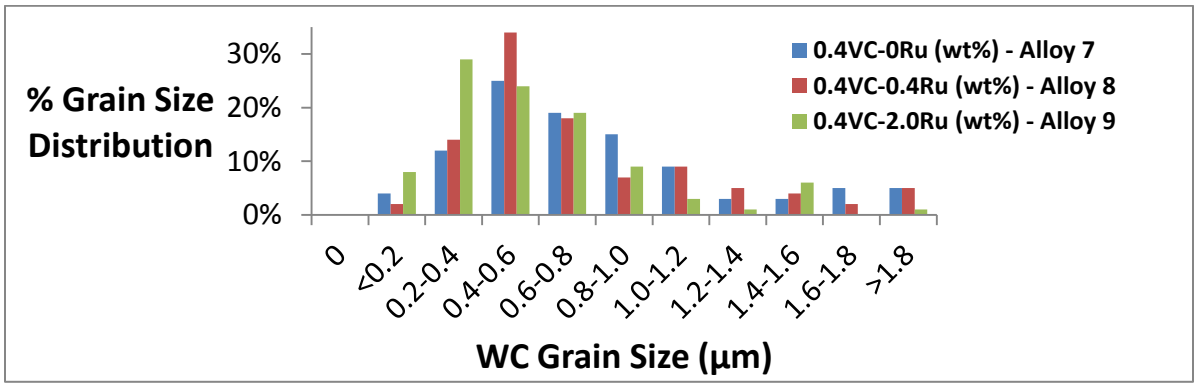

Figure 4 60. Grain size distribution for the (89.6-x)WC-0.4VC-10Co-xRu (wt%) alloys.

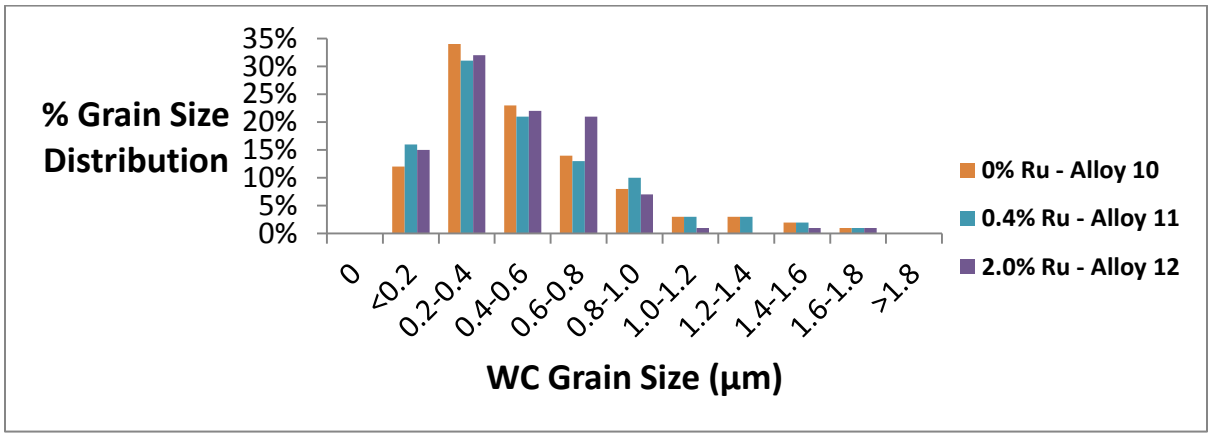

Figure 4.61. Grain size distribution for the (89.2-x)WC-0.8VC-10Co-xRu (wt%) alloys.

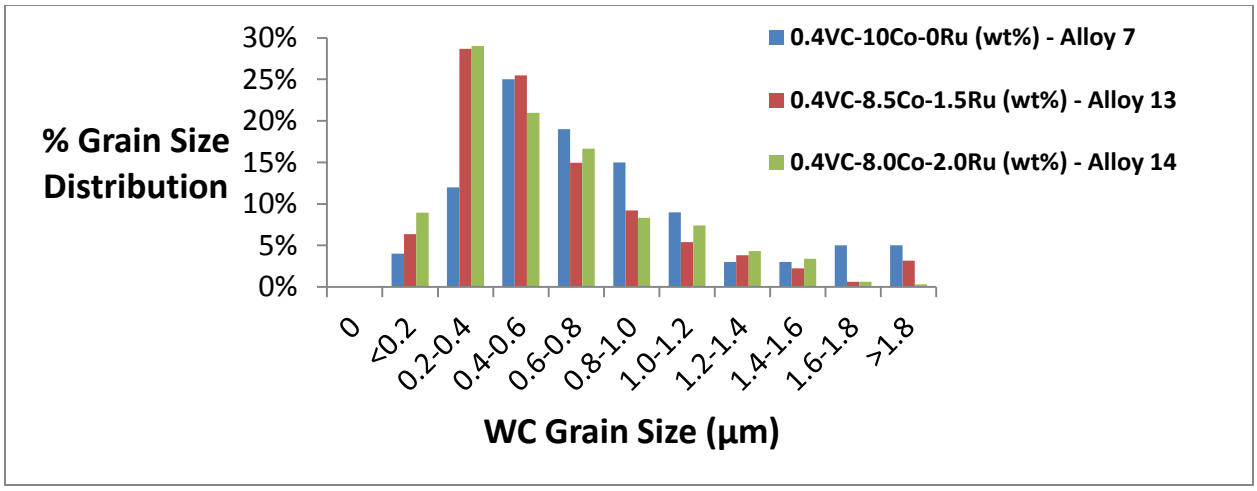

Figure 4.62. Grain size distribution for the 89.6WC-0.4VC-(10-x)Co-xRu (wt%) alloys.

4.3.2.3. Binder Mean Free Path

The values for the mean free paths for each alloy are given in Table 4.28 and plotted in Figure 4.64. For the 80WC-10VC-(10-*x*)Co-*x*Ru, (89.6-*x*)WC-0.4VC-10Co-*x*Ru and 89.6WC-0.4VC-(10-*x*)Co-*x*Ru alloys, the mean free path decreased with increased Ru additions, and there was the opposite trend for the (89.2-*x*)WC-0.8VC-10Co-*x*Ru alloy series. However, the decrease in binder mean free path for the 80WC-10VC-(10-*x*)Co-*x*Ru was very small, and probably not significant.

4.3.2.4. Contiguity

The binder volume fractions and contiguities are shown in Table 4.29. Contiguity very slightly increased with Ru content for the 80WC-10VC-(10-*x*)Co-*x*Ru and 89.6WC-0.4VC-(10-*x*)Co-*x*Ru alloys and slightly decreased for the (89.6-*x*)WC-0.4VC-10Co-*x*Ru alloys and the (89.2-*x*)WC-0.8VC-10Co-*x*Ru alloys (Figure 4.65), although these changes might not be significant. As the Ru content was increased for the 80WC-10VC-(10-*x*)Co-*x*Ru and 89.6WC-0.4VC-10(1-*x*)Co-*x*Ru alloy series, the binder volume fractions of the WC and (V,W)C increased, whereas the binder volume decreased, and this led to increased carbide contiguities (Figure 4.65).

Table 4.27. Grain size distribution for Alloys 1 to 14, using Roebuck's [1995Roe] classification.

Series	Alloy	Percentage in class						
		Coarse (2.5 - 6μm)	Medium (1.5 – 2.5μm)	Fine-B (1.0 – 1.5μm)	Fine-A (0.7 - 1μm)	Extra-fine (0.4 – 0.7μm)	Ultra-fine (0.1 – 0.4μm)	Nano-fine (<0.1μm)
80WC-10VC-(10-*x*)Co-*x*Ru	1	0	0	0.26	0.78	12.47	80.26	6.23
	2	0	0	0	0.73	12.41	81.75	5.11
	3	0	0	0	0.36	9.64	80.71	9.29
	4	0	0	0	0	5.00	82.00	13.00
	5	0	0	0	0.97	7.44	82.85	8.74
	6	0	0	0	0.32	6.45	85.16	8.07
(89.6-*x*)WC-0.4VC-10Co-*x*Ru	7	1	11	13	22	37	16	0
	8	1	10	14	15	44	16	0
	9	0	4	7	15	37	37	0
(89.2-*x*)WC-0.8VC-10Co-*x*Ru	10	0	3	6	14	31	43	3
	11	0	1	8	16	28	41	6
	12	0	1	2	16	34	44	3
89.6WC-0.4VC-(10-*x*)Co-*x*Ru	13	1	3	11	15	35	34	1
(*Includes Alloy 7*)	14	0	2	14	13	33	37	1

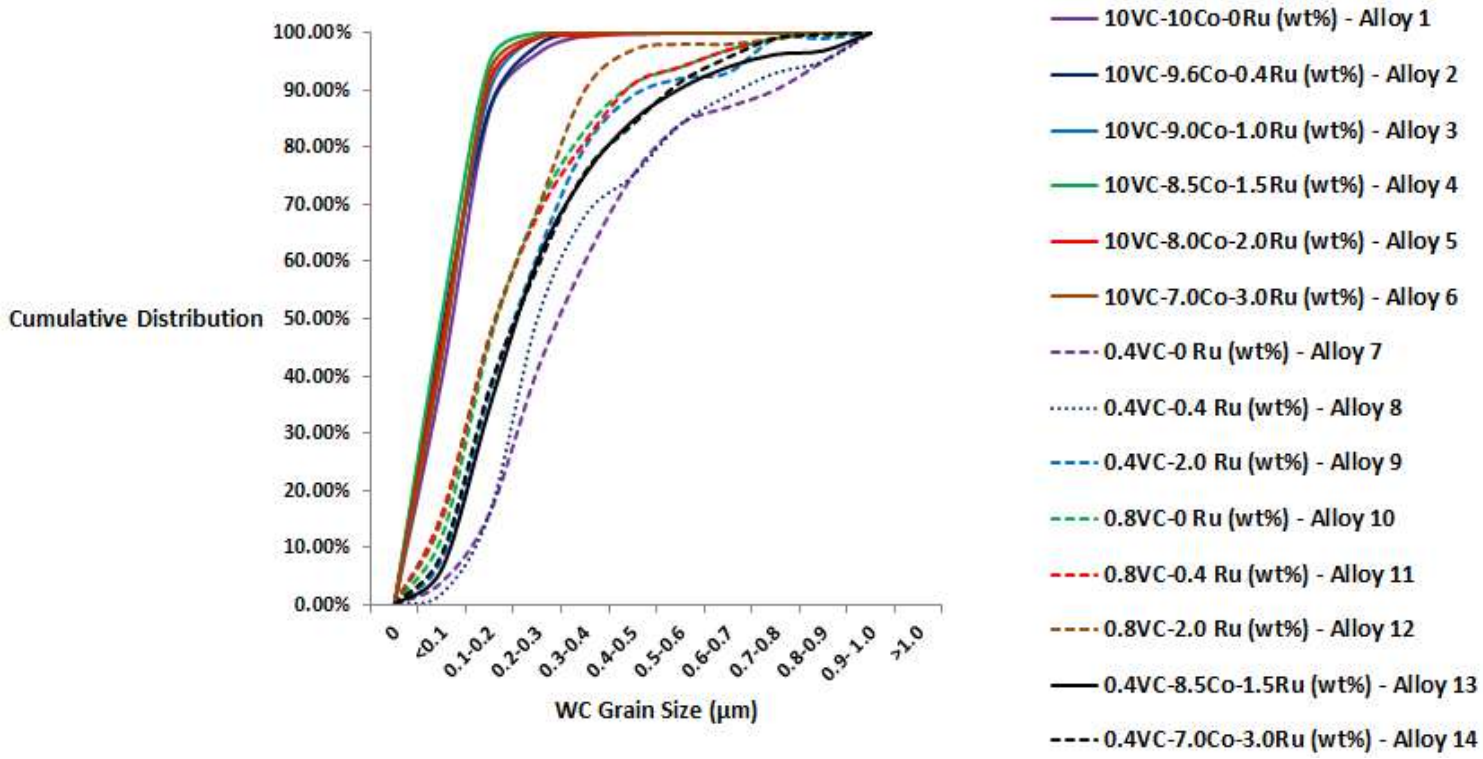

Figure 4.63. Cumulative grain size distribution for the 80WC-10VC-(10-x)Co-xRu, (89.6-x)WC-0.4VC-10Co-xRu, (89.2-x)WC-0.8VC-10Co-xRu and 89.6WC-0.4VC-(10-x)Co-xRu (wt%) alloys.

Table 4.28. Binder mean free path values for the 80WC-10VC-(10-x)Co-xRu, (89.6-x)WC-0.4VC-10Co-xRu, (89.2-x)WC-0.8VC-10Co-xRu and 89.6WC-0.4VC-(10-x)Co-xRu (wt%) alloys.

Series (wt%)	**Alloy Number**	**Ru Content (wt%)**	**Binder mean free path, λ (μm)**
80WC-10VC-(10-*x*)Co-*x*Ru	1	0.0	0.085±0.005
	2	0.4	0.081±0.007
	3	1.0	0.078±0.008
	4	1.5	0.078±0.009
	5	2.0	0.078±0.007
	6	3.0	0.074±0.005
(89.6-*x*)WC-0.4VC-10Co-*x*Ru	7	0.0	0.137±0.002
	8	0.4	0.135±0.002
	9	2.0	0.127±0.003
(89.2-*x*)WC-0.8VC-10Co-*x*Ru	10	0.0	0.119±0.003
	11	0.4	0.122±0.002
	12	2.0	0.126±0.003
89.6WC-0.4VC-(10-*x*)Co-*x*Ru (*Includes Alloy 7*)	13	1.5	0.115±0.003
	14	3.0	0.106±0.006

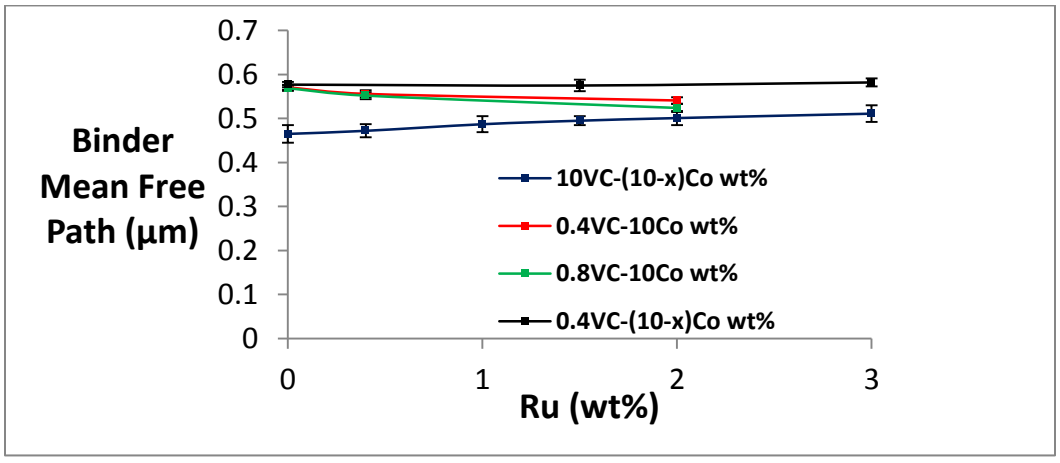

Figure 4.64. Relationship between binder mean free path and Ru content for the 80WC-10VC-(10-x)Co-xRu, (89.6-x)WC-0.4VC-10Co-xRu, (89.2-x)WC-0.8VC-10Co-xRu and 89.6WC-0.4VC-(10-x)Co-xRu (wt%) alloys.

Table 4.29. Binder volume fraction and contiguity values for the 80WC-10VC-(10-x)Co-xRu, (89.6-x)WC-0.4VC-10Co-xRu, (89.2-x)WC-0.8VC-10Co-xRu and 89.6WC-0.4VC-(10-x)Co-xRu (wt%) alloys.

Series (wt%)	**Alloy Number**	**Ru Content (wt%)**	**Binder Volume, V_β**	**Measured Contiguity**
80WC-10VC-(10-*x*)Co-*x*Ru	1	0.0	0.141	0.465±0.020
	2	0.4	0.139	0.472±0.015
	3	1.0	0.137	0.487±0.018
	4	1.5	0.135	0.495±0.010
	5	2.0	0.133	0.501±0.016
	6	3.0	0.129	0.511±0.019
(89.6-*x*)WC-0.4VC-10Co-*x*Ru	7	0.0	0.163	0.571±0.006
	8	0.4	0.167	0.556±0.008
	9	2.0	0.185	0.541±0.007
(89.2-*x*)WC-0.8VC-10Co-*x*Ru	10	0.0	0.162	0.569±0.006
	11	0.4	0.166	0.552±0.008
	12	2.0	0.184	0.524±0.009
89.6WC-0.4VC-(10-*x*)Co-*x*Ru (*Includes Alloy 7*)	13	1.5	0.157	0.575±0.013
	14	3.0	0.151	0.582±0.009

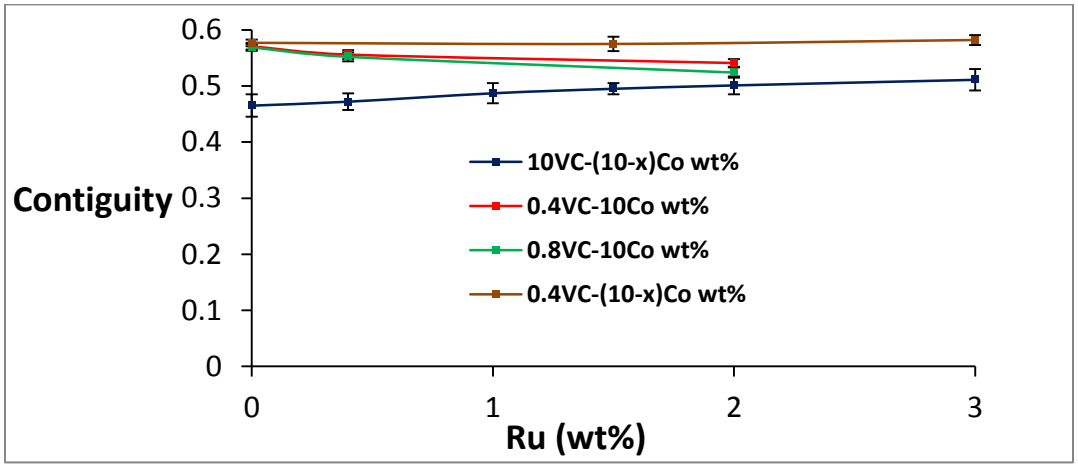

Figure 4.65. Relationship between binder mean free path and Ru content for the 80WC-10VC-(10-x)Co-xRu, (89.6-x)WC-0.4VC-10Co-xRu, (89.2-x)WC-0.8VC-10Co-xRu and 89.6WC-0.4VC-(10-x)Co-xRu (wt%) alloys.

4.4. Hardness and Fracture Toughness

4.4.1. Hardness

All Vickers hardness indentations had diagonals which differed by less than 1% as recommended by the ISO 28079:2009(E) standard [2009ISO]. Ruthenium additions increased hardnesses in all alloy series (Table 4.30 and Figure 4.66). Addition of 2 wt% Ru increased hardnesses by 8.2%, 2.9% and 2.8% for the 80WC-10VC-(10-*x*)Co-*x*Ru, 89.6-*x*)WC-10Co-0.4VC-*x*Ru and (89.2-*x*)WC-0.8VC-10Co-*x*Ru alloy series. Additions of 3 wt% Ru increased hardnesses by 11% and 12.5% for the 80WC-10VC-(10-*x*)Co-*x*Ru and 89.6WC-0.4VC-(10-*x*)Co-*x*Ru alloys. Thus, Ru additions were most effective in increasing hardness in the 89.6WC-0.4VC-(10-*x*)Co-*x*Ru alloys. Ru additions appeared to be still beneficial, even up to 3 wt %.

4.4.2. Fracture Toughness

Most hardness indentations had cracks which did not originate from the indentation apex (Figure 4.67), due to initial propagation of cracks during loading which resulted in deviations of the crack paths [1977Vis]. In accordance with the ISO 28079:2009(E) standard [2009ISO], cracks that did not coincide with the tip of the indentation diagonal, as shown in Figure 4.67, were measured from the point of emanation along the edge of the indentation.

Table 4.31 shows the ratio of crack length to half diagonal length, *l*/*a*, values for all the alloys at 5 kg, 10 kg, 20 kg, 30 kg and 50 kg loads. For the 80WC-10VC-(10-*x*)Co-*x*Ru alloy series, only indentations at 5 kg loads were within the validity range of the Palmqvist crack models ($0.25 \leq l/a \leq 1.25$) [1990Spi]. For the (89.6-*x*)WC-0.4VC-10Co-*x*Ru (wt%) alloys, the criterion for the Palmqvist crack model [1990Spi] was satisfied at 30 and 50 kg loads (Table 4.31). The (89.2-*x*)WC-0.8VC-10Co-*x*Ru (wt%) alloys satisfied the *l*/*a* criterion at 10, 20, 30 and 50 kg loads. The 89.6WC-0.4VC-(10-*x*)Co-*x*Ru (wt%) alloys satisfied the *l*/*a* criterion at 20 and 30 kg loads. A 5 kg load was thus the only suitable for the 80WC-10VC-(10-*x*)Co-*x*Ru alloy series. The loads that were used for other alloys are shown in Table 4.33.

The 80WC-10VC-(10-*x*)Co-*x*Ru alloys were used to establish the most suitable stress relief method. A comparison of total crack lengths, L, between extensively polished and heat treated samples is shown in Table 4.32 and plotted in Figure 4.68. Most of the heat treated and extensively polished samples had similar L values.

Table 4.30. Hardnesses of alloys in the 80WC-10VC-(10-x)Co-xRu, (89.6-x)WC-0.4VC-10Co-xRu, (89.2-x)WC-0.8VC-10Co-xRu and 89.6WC-0.4VC-(10-x)Co-xRu (wt%) alloys.

Series (wt%)	**Alloy**	**Ru content (wt%)**	**Hardness (GPa)**
80WC-10VC-(10-*x*)Co-*x*Ru	1	0.0	14.75±0.05
	2	0.4	14.85±0.03
	3	1.0	15.43±0.06
	4	1.5	15.50±0.04
	5	2.0	15.96±0.05
	6	3.0	16.57±0.02
(89.6-*x*)WC-0.4VC-10Co-*x*Ru	7	0.0	13.65±0.02
	8	0.4	13.88±0.03
	9	2.0	14.05±0.02
(89.2-*x*)WC-0.8VC-10Co-*x*Ru	10	0.0	14.21±0.07
	11	0.4	14.34±0.03
	12	2.0	14.61±0.02
89.6WC-0.4VC-(10-*x*)Co-*x*Ru *(Includes Alloy 7)*	13	1.5	14.87±0.08
	14	3.0	15.59±0.03

The results for the heat treated samples were more consistent than those for extensively polished samples. Overall, heat treatment was also more effective than extensive polishing, since it resulted in increased sum crack length by an average of 22%, whereas extensive polishing resulted in 13% average decrease. It was therefore concluded that although both heat treatment and extensive polishing are effective methods of removing induced stresses during grinding, heat treatment is more consistent. Thus, the reported hardness and fracture toughness results are for heat treated alloys. The results of crack resistance and Palmqvist fracture toughness for the alloys

are also shown in Table 4.33 and Figures 4.69 and 4.70. The crack resistance and Palmqvist fracture toughnesses of all samples were determined using Equations 3.18 and 3.19 [2009ISO].

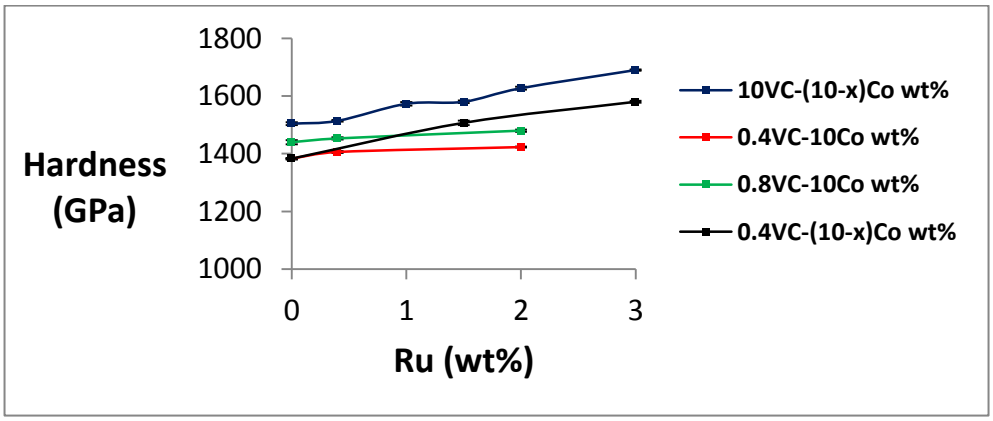

Figure 4.66. Hardnesses of alloys in the 80WC-10VC-(10-x)Co-xRu, (89.6-x)WC-0.4VC-10Co-xRu, (89.2-x)WC-0.8VC-10Co-xRu and 89.6WC-0.4VC-(10-x)Co-xRu (wt%) alloys.

As to be expected, both Palmqvist fracture toughness and crack resistance followed the same trends with respect to Ru additions. For the 80WC-10VC-(10-*x*)Co-*x*Ru alloys, Ru additions increased the crack resistance and fracture toughness up to 0.4 wt%, beyond which decreases were observed.

For the (89.6-*x*)WC-0.4VC-10Co-*x*Ru (wt%) alloys, Ru additions of 0.4 wt% also resulted in an increase in crack resistance and fracture toughness, but 2 wt% additions caused a decrease. For the (89.2-*x*)WC-0.8VC-10Co-*x*Ru (wt%) alloys, there was an increase up to 2.0 wt% Ru additions. For the 89.6WC-0.4VC-(10-*x*)Co-*x*Ru (wt%) alloys, crack resistance and fracture toughness decreased with Ru additions.

Figure 4.67. Indentation produced on 80WC-9.6Co-0.4Ru (wt%) alloy at 5 kg load with two

cracks originating from the edge (3 and 4).

Table 4.31. Ratio of crack length to half diagonal length, (l/a), at various loads for 80WC-10VC-(10-x)Co-xRu, (89.6-x)WC-0.4VC-10Co-xRu, (89.2-x)WC-0.8VC-10Co-xRu and 89.6WC-0.4VC-(10-x)Co-xRu (wt%) alloys.

Series (wt%)	**Alloy**	**Ru Content (wt%)**	**Load (kg)**				
			5	**10**	**20**	**30**	**50**
80WC-10VC-(10-*x*)Co-*x*Ru	1	0.0	0.87±0.02	1.13±0.04	1.36±0.04	1.43±0.01	-
	2	0.4	0.78±0.03	1.18±0.02	1.38±0.02	1.63±0.025	-
	3	1.0	0.93±0.03	1.18±0.03	1.43±0.03	1.79±0.09	-
	4	1.5	1.08±0.03	1.39±0.02	1.55±0.02	1.99±0.06	-
	5	2.0	1.18±0.05	1.39±0.01	1.61±0.03	2.03±0.04	-
	6	3.0	1.22±0.01	1.41±0.01	1.78±0.02	2.24±0.01	-
(89.6-*x*)WC-0.4VC-10Co-*x*Ru	7	0.0	no crack	no crack	0.20±0.02	0.28±0.04	0.66±0.02
	8	0.4	no crack	no crack	0.26±0.03	0.29±0.05	0.65±0.02
	9	2.0	no crack	0.25±0.03	0.48±0.01	0.59±0.01	0.93±0.00
(89.2-*x*)WC-0.8VC-10Co-*x*Ru	10	0.0	0.33±0.03	0.34±0.01	0.77±0.04	0.73±0.01	1.13±0.02
	11	0.4	0.11±0.01	0.42±0.02	0.65±0.02	0.79±0.02	1.12±0.03
	12	2.0	no crack	0.43±0.03	0.43±0.02	0.75±0.02	1.08±0.01
89.6WC-0.4VC-(10-*x*)Co-*x*Ru (*Includes Alloy 7*)	13	1.5	no crack	0.57±0.01	0.79±0.02	1.01±0.04	1.25±0.04
	14	3.0	0.48±0.00	0.73±0.03	1.26±0.01	1.37±0.03	-

Table 4.32. Total crack lengths (μm) for 80WC-10VC-(10-x)Co-xRu (wt%) alloys polished using two different procedures.

Alloy Number	Alloy (wt% Ru)	Extensive polishing method	Polishing + annealing
1	0.0	113±8	120±3
2	0.4	107±9	107±2
3	1.0	110±6	127±6
4	1.5	115±8	144±4
5	2.0	156±7	157±9
6	3.0	160±8	163±4

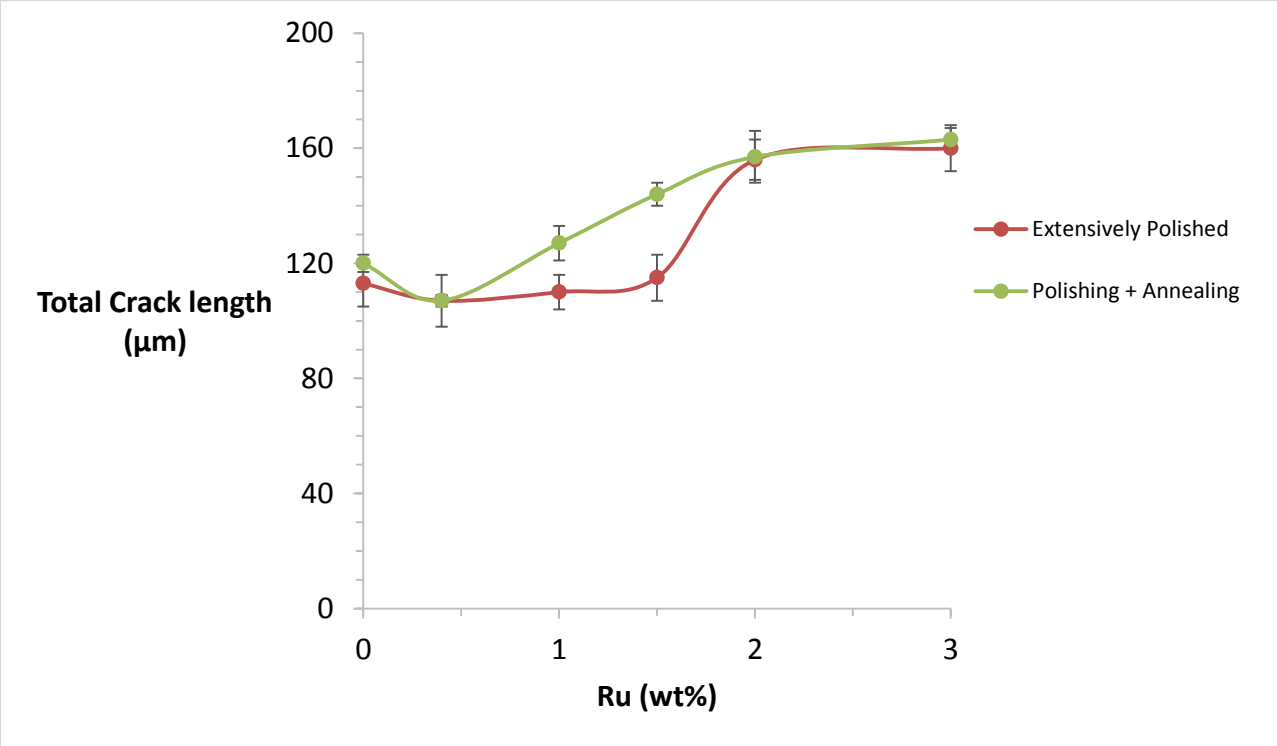

Figure 4.68. Comparison of crack lengths obtained after using different polishing procedures.

Table 4.33. Hardness results for 80WC-10VC-(10-x)Co-xRu, (89.6-x)WC-0.4VC-10Co-xRu, (89.2-x)WC-0.8VC-10Co-xRu and 89.6WC-0.4VC-(10-x)Co-xRu (wt%) alloys.

Series (wt%)	**Alloy number**	**Ru content (wt%)**	**HV load (kg)**	**Hardness, (GPa)**	**Crack resistance ($kgmm^{-1}$)**	**Palmqvist fracture toughness, W_K ($MPa.m^{-3/2}$)**
80WC-10VC-(10-*x*)Co-*x*Ru	1	0.0	5	18.47±0.08	42±1	7.71±0.02
	2	0.4	5	18.89±0.10	43±1	7.91±0.02
	3	1.0	5	19.12±0.10	40±1	7.65±0.03
	4	1.5	5	19.27±0.04	35±1	7.21±0.02
	5	2.0	5	19.52±0.05	32±1	7.03±0.02
	6	3.0	5	19.62±0.08	31±1	6.84±0.01
(89.6-*x)*WC-0.4VC-10Co-*x*Ru	7	0.0	50	12.95±0.02	146 ±4	12.09±0.02
	8	0.4	50	13.19±0.03	147±4	12.27±0.01
	9	2.0	50	14.01±0.02	107±0	10.78±0.02
(89.2-*x*)WC-0.8VC-10Co-*x*Ru	10	0.0	50	14.02±0.08	88±0	9.78±0.03
	11	0.4	50	14.07±0.06	89±3	9.82±0.02
	12	2.0	50	14.32±0.08	92±2	10.12±0.03
89.6WC-0.4VC-(10-*x*)Co-*x*Ru (*Includes Alloy 7*)	13	1.5	20	14.77±0.04	83±3	9.73±0.01
	14	3.0	10	15.43±0.05	63±1	8.66±0.01

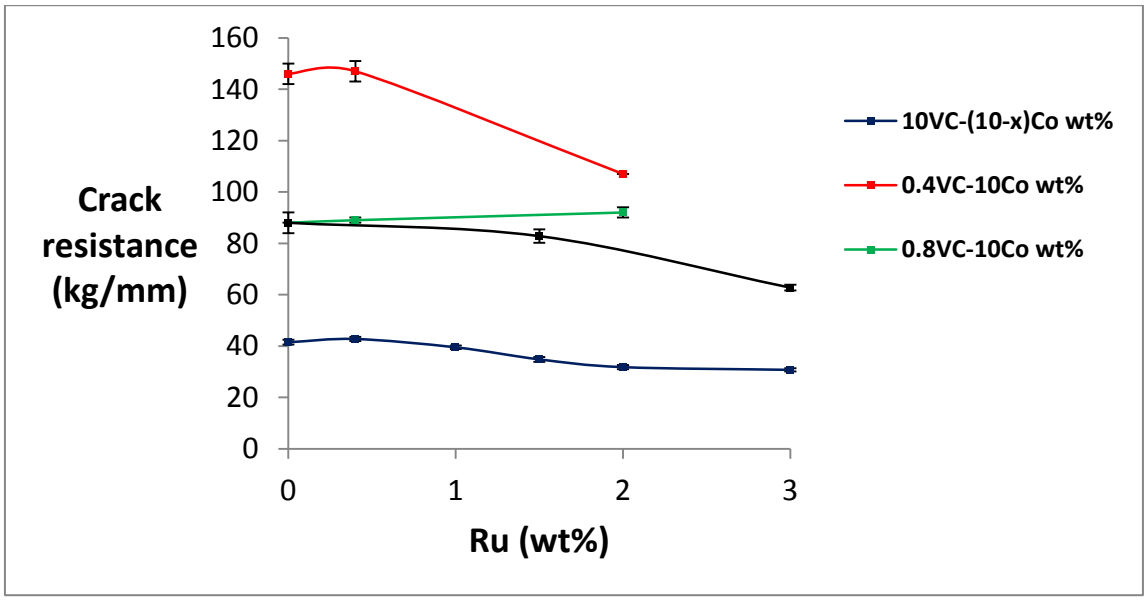

Figure 4.69. Variation of crack resistance with Ru content for 80WC-10VC-(10-x)Co-xRu, (89.6-x)WC-0.4VC-10Co-xRu, (89.2-x)WC-0.8VC-10Co-xRu and 89.6WC-0.4VC-(10-x)Co-xRu (wt%) alloys.

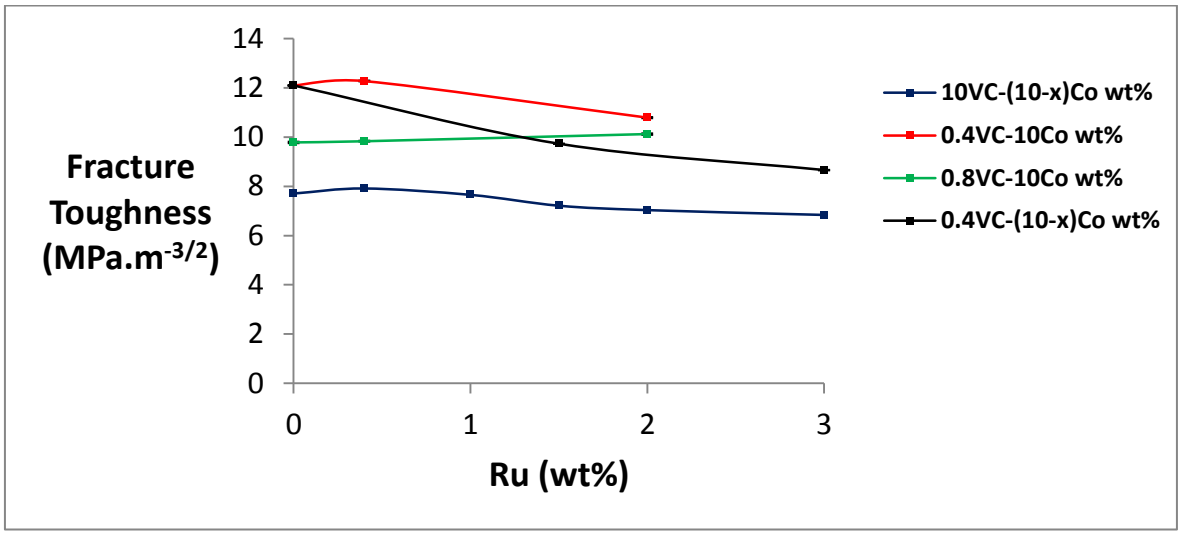

Figure 4.70. 80WC-10VC-(10-x)Co-xRu, (89.6-x)WC-0.4VC-10Co-xRu, (89.2-x)WC-0.8VC-10Co-xRu and 89.6WC-0.4VC-(10-x)Co-xRu (wt%) alloys.

4.5. Wear

4.5.1. Wear Microstructures

Generally the alloys were characterized by a mild wear mode. Carbide grain deformation was seen in the 80WC-10VC-10Co, 80WC-10VC-8.0Co-2.0Ru, 89.6WC-10Co-0.4VC and 89.6WC-0.4VC-8.5Co-1.5Ru (wt%) alloys (Figures 4.71 to 4.73). Scratching of WC grains was seen from the microstructures of 80WC-10VC-9.6Co-0.4Ru, 80WC-10VC-8.5Co-1.5Ru, 80WC-10VC-7.0Co-7.0Ru, 89.2WC-10Co-0.4VC-0.4Ru, 87.6WC-10Co-0.4VC-2.0Ru and the 89.2WC-10Co-0.8VC (wt%) alloys (Figures 4.71 and 4.72). Wavy deformations were seen for the 80WC-10VC-9.6Co-0.4Ru, 89.2WC-10Co-0.4VC-0.4Ru, 87.6WC-10Co-0.4VC-2.0Ru and 89.6WC-0.4VC-8.5Co-1.5Ru (wt%) alloys (Figures 4.71 to 4.73). Some carbide grains cracked during wear as could be seen from the microstructures of 80WC-10VC-9.0Co-1.0Ru, 87.6WC-10Co-0.4VC-2.0Ru and 89.2WC-10Co-0.8VC (wt%) alloys (Figures 4.71 and 4.72). Ploughing of WC grains was seen for the 80WC-10VC-9.0Co-1.0Ru (wt%) alloy (Figure 4.71). The 80WC-10VC-8.0Co-2.0Ru, 80WC-10VC-7.0Co-3.0Ru, 89.2WC-10Co-0.4VC-0.4Ru, 88.8WC-10Co-0.8VC-0.4Ru and 87.2WC-10Co-0.8VC-2.0Ru (wt%) alloys were characterized by fragmentation of wear debris (Figures 4.71 and 4.72). Dark tribolayers were seen in the microstructures of 80WC-10VC-9.6Co-0.4Ru, 80WC-10VC-9.0Co-1.0Ru, 87.6WC-10Co-0.4VC-2.0Ru, 88.8WC-10Co-0.8VC-0.4Ru and 87.2WC-10Co-0.8VC-2.0Ru, 89.6WC-0.4VC-7.0Co-3.0Ru and 89.6WC-0.4VC-8.5Co-1.5Ru (wt%) (Figures 4.71 to 4.73). From the analysis of the dark tribolayers (Table 4.34), it was deduced that there was removal of pin material (Si and N) during the wear process. The presence of oxygen in the EDS analysis (Table 4.34) was due to oxidation during wear.

4.5.2. Friction and Wear Rates

The variation of coefficient of friction (μ) with time for all alloys is shown in Figures 4.74 and 4.75. There was generally an abrupt increase in μ during the first few sliding oscillations (run-in stage).

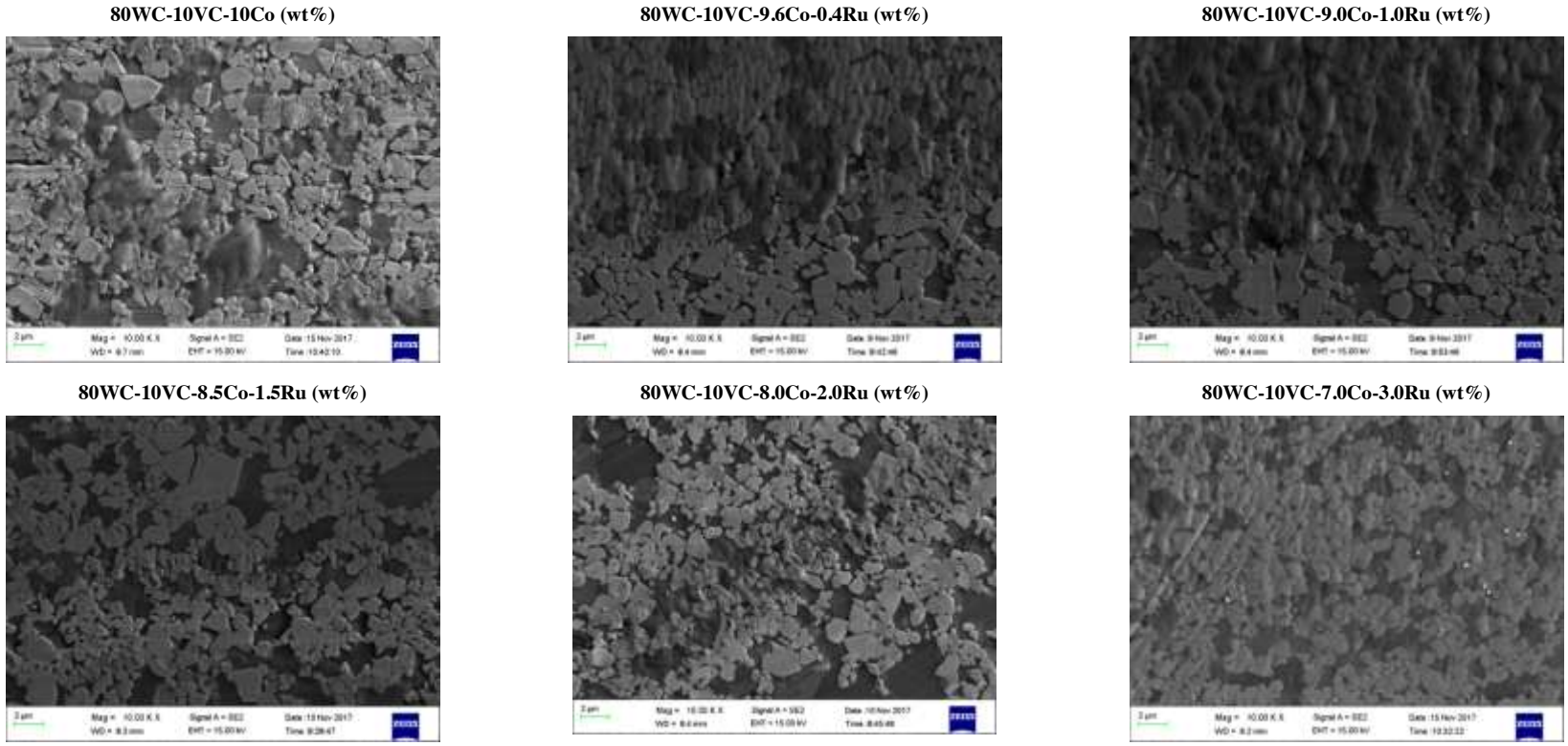

Figure 4.71. SEM-SE images showing the 80WC-10VC-(10-x)Co-xRu (wt%) alloys after sliding wear.

The increase in μ during the run-in stage was gradual for Alloys 7, 12 and 14 of the (89-*x*)WC-0.4VC-10Co-*x*Ru, (89.2-*x*)WC-0.8VC-10Co-*x*Ru and 89.6WC-0.4VC-(10-*x*)Co-*x*Ru (wt%) alloy series. After the run-in stage, there was a general drop in μ, followed by a steady state region. The average , μ, determined in the state region are shown in Table 4.35 and plotted in Figure 4.76. It can be deduced from Table 4.35 that, the alloys had generally stable μ in the steady region. Alloy 8, 89.2WC-0.4VC-10Co-0.4Ru (wt%) had the most unstable μ as deduced from the highest standard deviation (Table 4.35).

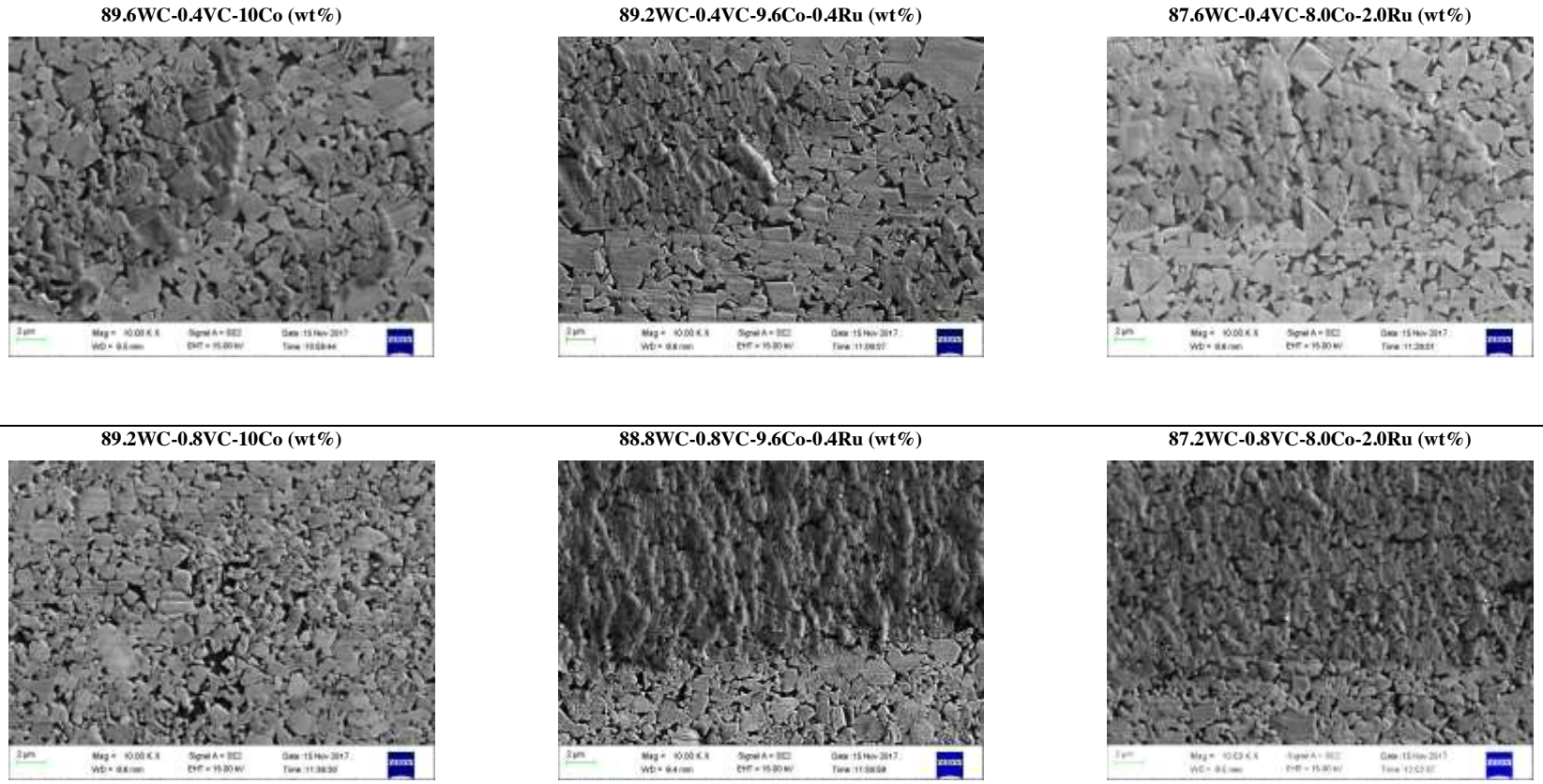

Figure 4.72. SEM-SE images showing a) (89.6-x)WC-0.4VC-10Co-xRu and, b) (89.2-x)WC-0.8VC-10Co-xRu (wt%) alloys after sliding wear.

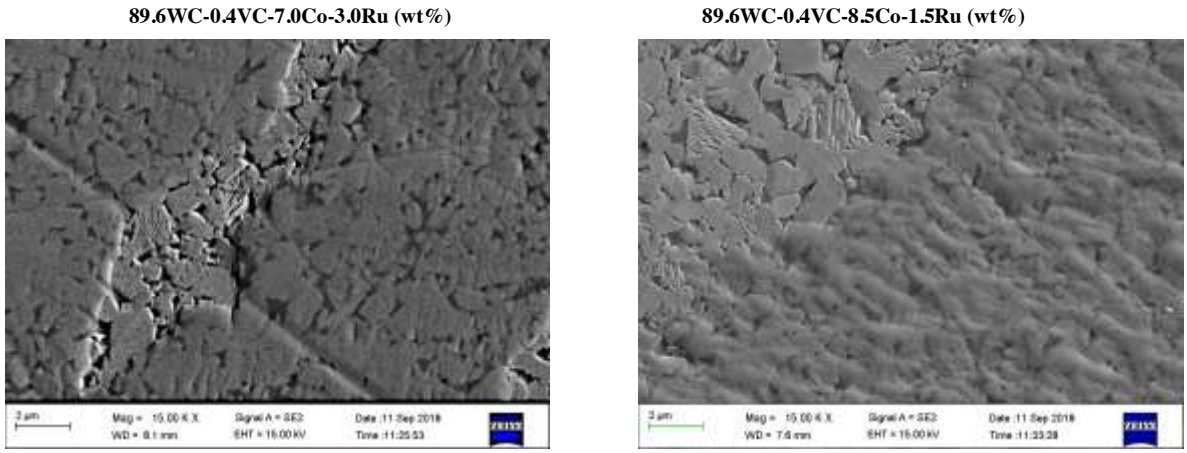

Figure 4.73. SEM-SE images showing the 89.6WC-0.4VC-(10-x)Co-xRu (wt%) alloys after sliding wear.

Table 4.34. SEM-EDS analyses of the dark tribolayers of Alloys 80WC-10VC-9.6Co-0.4Ru, 80WC-10VC-9.0Co-1.0Ru and 88.8WC-0.8VC-9.6Co-0.4Ru (wt%) alloys showing the presence of Si and N from the Si_3N_4 balls.

Alloy (wt%)	Element (wt%)						
	C	N	O	Si	V	Co	W
80WC-10VC-9.6Co-0.4Ru	5.9±0.3	0.6±0.3	16.3±2.1	0.6±0.3	8.3±1.2	6.5±1.2	61.9±0.8
80WC-10VC-9.0Co-1.0Ru	5.5±0.2	0.6±0.2	14.1±2.5	0.5±0.2	-	7.7±1.1	71.6±1.4
88.8WC-0.8VC-9.6Co-0.4Ru	5.0±0.6	0.9±0.2	16.0±3.1	1.0±0.3	5.6±1.7	7.6±0.8	63.8±1.8

The alloy wear volumes and the corresponding wear rates are also shown in Table 4.35. The alloy wear rates as a function of Ru content are plotted in Figure 4.77. There was a decrease in a wear rate with Ru additions for all alloy series. However, the values were very close in all series, and considering the errors, it can be deduced that the effect of Ru additions was not significant in most cases.

It can be deduced from Figure 4.77 that the 80WC-10VC-(10-*x*)Co-*x*Ru alloys (with the highest VC content) had the lowest wear resistance for all Ru additions. Thus, VC additions improved wear resistance among the alloys. However, VC might have had an overriding effect on Ru since

there was a more significant decrease in wear rate for the 89.6WC-0.4VC-(10-*x*)Co-*x*Ru alloys (~52%) than the 80WC-10VC-(10-*x*)Co-*x*Ru alloys (~34%) after 3 wt% Ru additions (Figure 4.77). The corresponding wear on the Si_3N_4 balls followed opposite trends in all alloy series. The significant increase in wear rate with Ru for the Si_3N_4 balls against the 80WC-10VC-(10-*x*)Co-*x*Ru alloys (Figure 4.78), confirm the opposite trend that was seen for the same alloys (Figure 4.77). The wear rates for the Si_3N_4 balls were less than for most of the corresponding alloys (Table 4.35).

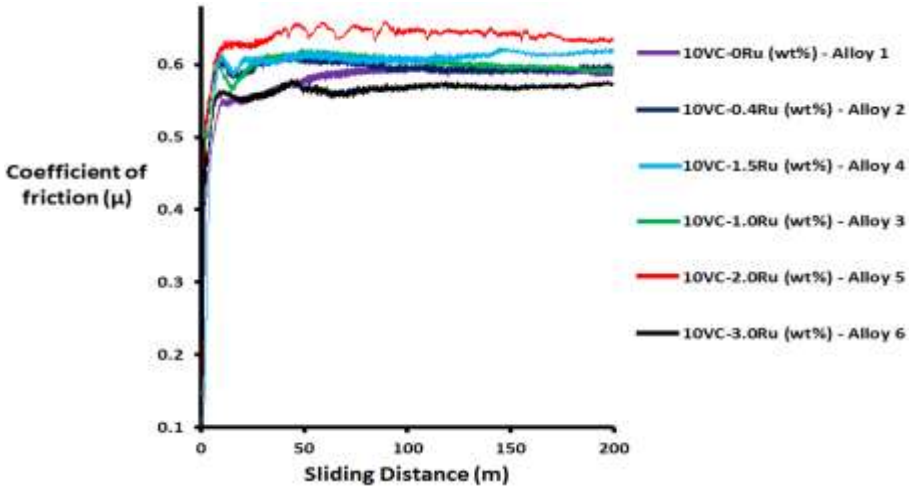

Figure 4.74. Coefficient of friction plots for the 80WC-10VC-(10-x)Co-xRu (wt%) alloys.

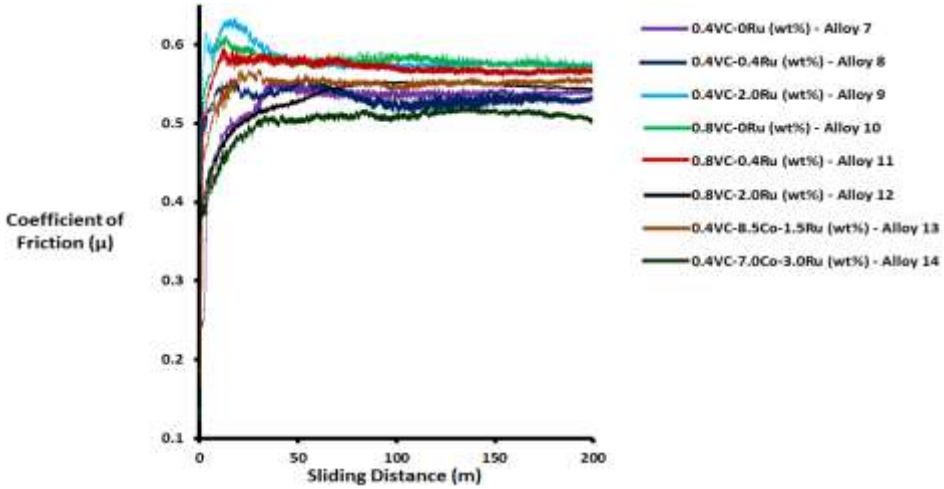

Figure 4.75. Coefficient of friction plots for the (89.6-x)WC-0.4VC-10Co-xRu, (89.2-x)WC-0.8VC-10Co-xRu and 89.6WC-0.4VC-(10-x)Co-xRu (wt%) alloys.

Table 4.35. Wear results for the 80WC-10VC-(10-x)Co-xRu, (89.6-x)WC-0.4VC-10Co-xRu, (89.2-x)WC-0.8VC-10Co-xRu and 89.6WC-0.4VC-(10-x)Co-xRu (wt%) alloys and the corresponding ball wear information.

Series (wt%)	**Alloy Number**	**Ru content (wt%)**	**Average Coefficient of Friction (μ)**	**Alloy Volume Loss ($x10^{-3}$ mm^3)**	**Alloy Wear Rate ($x10^{-6}$ mm^3/ N.m)**	**Ball Volume Loss ($x10^{-3}$ mm^3)**	**Ball Wear Rate ($x10^{-6}$ mm^3/ N.m)**
80WC-10VC-(10-*x*)Co-*x*Ru	1	0.0	0.59±0.04	10.41±1.04	5.26±0.52	0.61±0.06	3.05±0.15
	2	0.4	0.60±0.02	5.01±0.64	2.51±0.32	0.66±0.10	3.30±0.32
	3	1.0	0.61±0.02	4.04±0.44	2.02±0.22	0.66±0.08	3.32±0.20
	4	1.5	0.60±0.02	3.52±0.62	1.76±0.31	1.04±0.06	5.27±0.14
	5	2.0	0.64±0.01	1.92±0.27	0.96±0.14	1.24±0.05	6.19±0.12
	6	3.0	0.57±0.03	1.73±0.39	0.86±0.20	1.29±0.07	6.43±0.18
(89.6-*x*)WC-0.4VC-10Co-*x*Ru	7	0.0	0.54±0.05	23.27±1.58	11.64±0.79	0.43±0.07	2.16±0.17
	8	0.4	0.53±0.06	20.18±1.28	10.09±0.64	0.43±0.10	2.16±0.24
	9	2.0	0.57±0.01	18.73±1.84	9.37±0.92	0.44±0.06	2.19±0.16
(89.2-*x*)WC-0.8VC-10Co-*x*Ru	10	0.0	0.58±0.02	15.07±1.54	7.53±0.77	0.47±0.05	2.36±0.13
	11	0.4	0.57±0.03	14.25±1.05	7.13±0.53	0.51±0.08	2.57±0.19
	12	2.0	0.55±0.04	11.42±0.77	5.71±0.38	0.52±0.06	2.58±0.14
89.6WC-0.4VC-(10-*x*)Co-*x*Ru *(Includes Alloy 7)*	13	1.5	0.55±0.04	9.69±1.51	4.84±0.76	0.63±0.10	3.17±0.14
	14	3.0	0.51±0.04	3.95±0.44	1.97±0.22	0.83±0.07	4.17±0.18

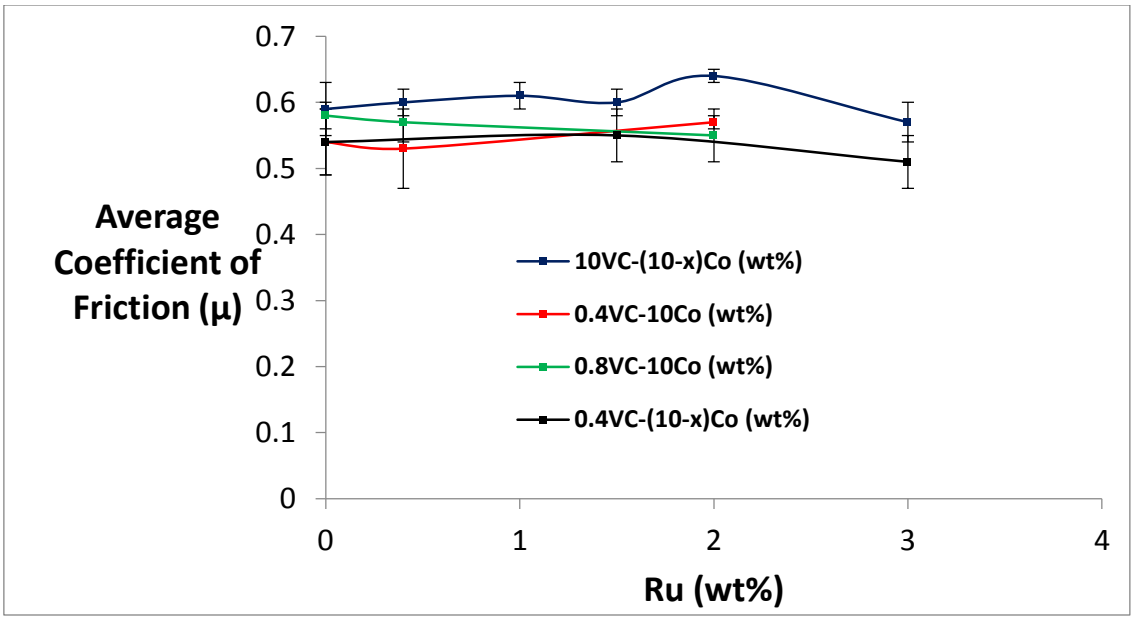

Figure 4.76. Average coefficient of friction plots for the 80WC-10VC-(10-x)Co-xRu, (89.6-x)WC-0.4VC-10Co-xRu, (89.2-x)WC-0.8VC-10Co-xRu and 89.6WC-0.4VC-(10-x)Co-xRu (wt%) alloys.

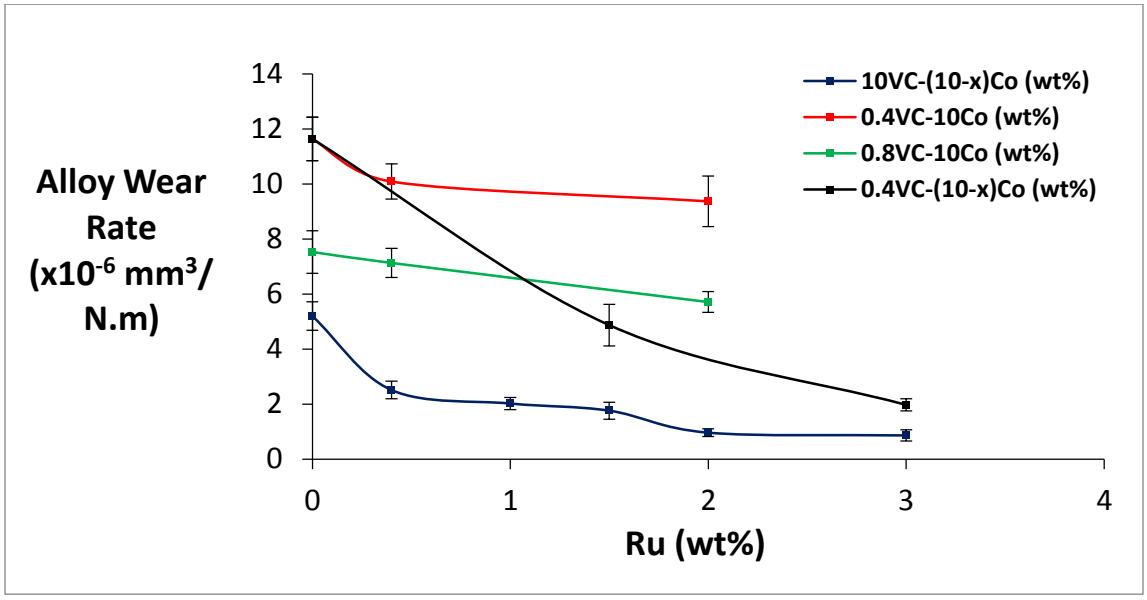

Figure 4.77. Variation of alloy wear rate with Ru content in the 80WC-10VC-(10-x)Co-xRu, (89.6-x)WC-0.4VC-10Co-xRu, (89.2-x)WC-0.8VC-10Co-xRu and 89.6WC-0.4VC-(10-x)Co-xRu (wt%) alloys.

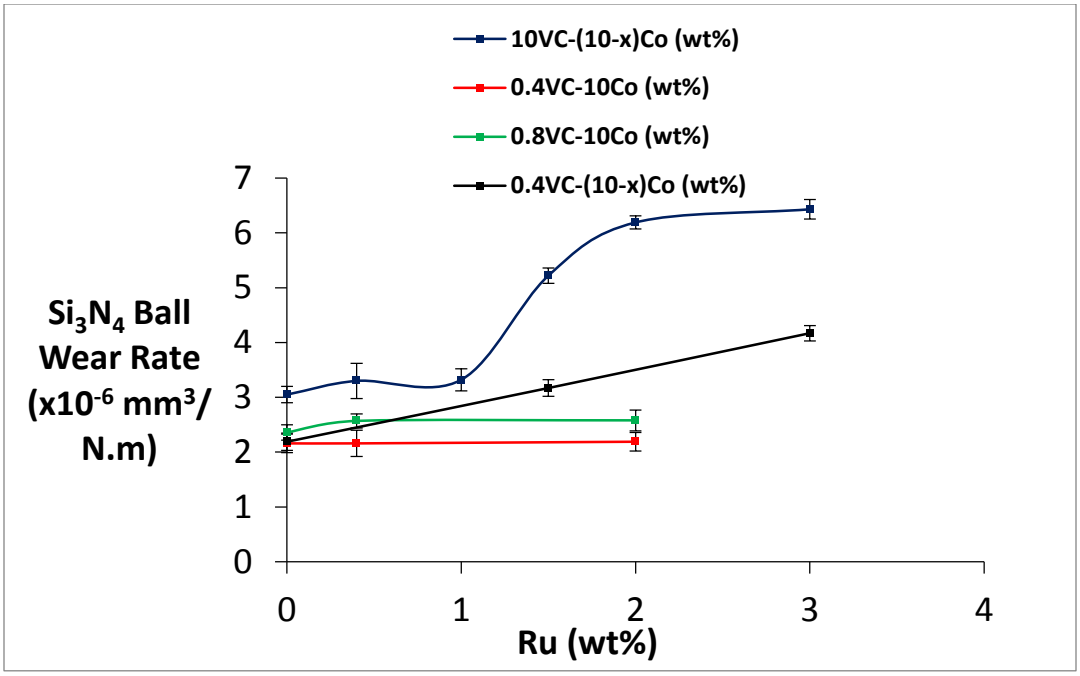

Figure 4.78. Si_3N_4 ball wear rate against the 80WC-10VC-(10-x)Co-xRu, (89.6-x)WC-0.4VC-10Co-xRu, (89.2-x)WC-0.8VC-10Co-xRu and 89.6WC-0.4VC-(10-x)Co-xRu (wt%) alloys.

4.6. Corrosion Results

4.6.1. Electrochemical Results for Corrosion in H_2SO_4

4.6.1.1. Open Circuit Potential (OCP) Measurements

The OCPs for the 80WC-10VC-(10-*x*)Co-*x*Ru, (89.6-*x*)WC-0.4VC-10Co-*x*Ru, (89.2-*x*)WC-0.8VC-10Co-*x*Ru and 89.6WC-0.4VC-(10-*x*)Co-*x*Ru (wt%) alloys are shown in Table 4.36 and Figure 4.79. Ruthenium additions resulted in more noble potentials for all the alloy series (Figures 4.79 to 4.81). Close OCP values were observed for the alloys without Ru (Alloys 1, 7 and 10), of the three alloy series (Table 4.36, Figure 4.79). The (89.6-*x*)WC-0.4VC-10Co-*x*Ru and (89.2-*x*)WC-0.8VC-10Co-*x*Ru alloy series also had close OCP values for the same Ru additions (Figure 4.79). Additions of up to 2 wt% Ru resulted in a more significant increase in OCP for the 80WC-10VC-(10-*x*)Co-*x*Ru alloys (~78%) than in (89.6-*x*)WC-0.4VC-10Co-*x*Ru and (89.2-*x*)WC-0.8VC-10Co-*x*Ru alloy series (~30%) (Table 4.36, Figure 4.79). Up to 3wt %

Ru additions resulted in a higher OCP for the 80WC-10VC-(10-*x*)Co-*x*Ru alloys than for the 89.6WC-0.4VC-(10-*x*)Co-*x*Ru. Generally, the OCP did not fluctuate significantly over the scanning period (Figures 4.80 and 4.81), and Alloys 5 and 12 had the most change in OCP of ~60 mV (Figures 4.80 and 4.81), with the OCP for Alloy 5 being relatively unstable (Figure 4.80). The corrosion currents ($E_{corr)}$, critical current densities (i_c), corrosion current densities (i_{corr}), anodic Tafel slopes (b_a) and the cathodic Tafel slope (b_c) are also given in Table 4.36.

4.6.1.2. Polarisation Behavior

The polarisation curves for the fourteen alloys (Figures 4.82 and 4.83) had the same general trend. Alloys 9, 12, 13 and 14 (with ≥1.5 wt% Ru) had unstable passive regions (Figure 4.83). All alloys e*x*hibited pseudopassivation, but at decreasing current densities with Ru additions (Figures 4.82 and 4.83). The passivity range and the critical current density also decreased with ruthenium additions. The passivation potential increased with Ru additions, except for the 3 wt% Ru alloys of the 80WC-10VC-(10-*x*)Co-*x*Ru (wt%) and 89.6WC-0.4VC-(10-*x*)Co-*x*Ru (wt%) series, that had primary passivation at significantly lower potential than the rest of the alloys. However, the primary pseudopassive range for Alloy 6 was very narrow (~125mV). There was a general increase in E_{corr} with Ru additions for all Alloy series (Table 4.36, Figure 4.84).

4.6.1.3. Corrosion Rates from Mass Loss Tests

There was a general decrease in corrosion rate with Ru additions in all alloy series (Table 4.36, Figures 4.85 and 4.86). Figure 4.86 shows the corrosion rate trends for the 80WC-10VC-(10-*x*)Co-*x*Ru (wt%) and 89.6WC-0.4VC-(10-*x*)Co-*x*Ru (wt%) alloys. For the 80WC-10VC-(10-*x*)Co-*x*Ru (wt%), (89.6-*x*)WC-0.4VC-10Co-*x*Ru (wt%) and (89.2-*x*)WC-0.8VC-10Co-*x*Ru (wt%) alloys, the 0.4 wt% Ru alloy had the highest corrosion rate (Figures 4.85 and 4.86), and these alloys that crumbled from the edges during immersion and cleaning, increasing material loss (Figure 4.87).

Table 4.36. Electrochemical parameters for the 80WC-10VC-(10-x)Co-xRu, (89.6-x)WC-0.4VC-10Co-xRu, (89.2-x)WC-0.8VC-10Co-xRu and 89.6WC-0.4VC-(10-x)Co-xRu (wt%) alloys for polarisation in 1 M H_2SO_4 (corrosion rates determined from immersion tests).

Series	**Alloy No.**	**OCP (mV)**	**E_{corr} (mV)**	**i_c ($mA.cm^{-2}$)**	**b_a (mV)**	**b_c (mV)**	**i_{corr} ($mA.cm^{-2}$)**	**Corrosion Rate ($mm.y^{-1}$)**	**Change in corrosion (%)**
80WC-10VC-(10-*x*)Co-*x*Ru	1	-324.34	-293.07	11.7	106	586	0.118	0.119±0.022	-
	2	-267.45	-266.52	9.3	109	85	0.373	0.529±0.001	345
	3	-255.46	-262.46	6.9	18	59	0.258	0.139±0.005	17
	4	-248.90	-263.42	5.6	38	50	0.046	0.062±0.001	-48
	5	-182.09	-249.49	1.4	132	31	0.008	0.007±0.000	-94
	6	-104.10	-251.59	0.1	17	1	0.001	0.004±0.000	-97
(89.6-*x*)WC-0.4VC-10Co-*x*Ru	7	-320.87	-284.90	25.2	114	132	0.096	0.094±0.008	-
	8	-268.10	-269.61	29.4	42	73	1.579	3.367±0.013	3482
	9	-223.91	-249.23	15.9	165	49	0.028	0.039±0.004	-59
(89.2-*x*)WC-0.8VC-10Co-*x*Ru	10	-322.29	-280.92	25.8	74	72	0.336	0.471±0.090	-
	11	-262.83	-263.20	28.7	32	62	0.632	1.822±0.012	287
	12	-224.10	-243.17	16.0	750	51	0.027	0.035±0.001	-93
89.6WC-0.4VC-(10-*x*)Co-*x*Ru (*Includes Alloy 7*)	13	-243.42	-248.23	16.1	108	87	0.086	0.064±0.016	-32
	14	-134.10	-126.37	0.0	8	55	0.017	0.014±0.003	-85

The crumbling was due to the weakening of the metal matrix after corrosion. Ruthenium increased corrosion resistance more for the 89.6WC-0.4VC-(10-*x*)Co-*x*Ru, 80WC-10VC-(10-*x*)Co-*x*Ru and (89.2-*x*)WC-0.8VC-10Co-*x*Ru alloys than for the (89.6-*x*)WC-0.4VC-10Co-*x*Ru alloy series (Table 4.36).

For alloys without Ru, Alloys 1, 7 and 10, there was no distinct correlation between VC content and corrosion rate (Table 4.36). However, at the same Ru additions (0.4 and 2.0 wt%), the lower VC content alloys, (89.6-*x*)WC-0.4VC-10Co-*x*Ru and (89.2-*x*)WC-0.8VC-10Co-*x*Ru had higher corrosion rates (Table 4.36). The results thus suggest that although VC on its own did not seem to have an effect on the corrosion rate, it probably promoted the effectiveness of Ru in improving corrosion resistance. Overall, 2 wt% Ru addition was the general optimum addition, as further additions did not give much improvement, especially for the 80WC-10VC-(10-*x*)Co-*x*Ru alloys (Table 4.36 and Figure 4.86).

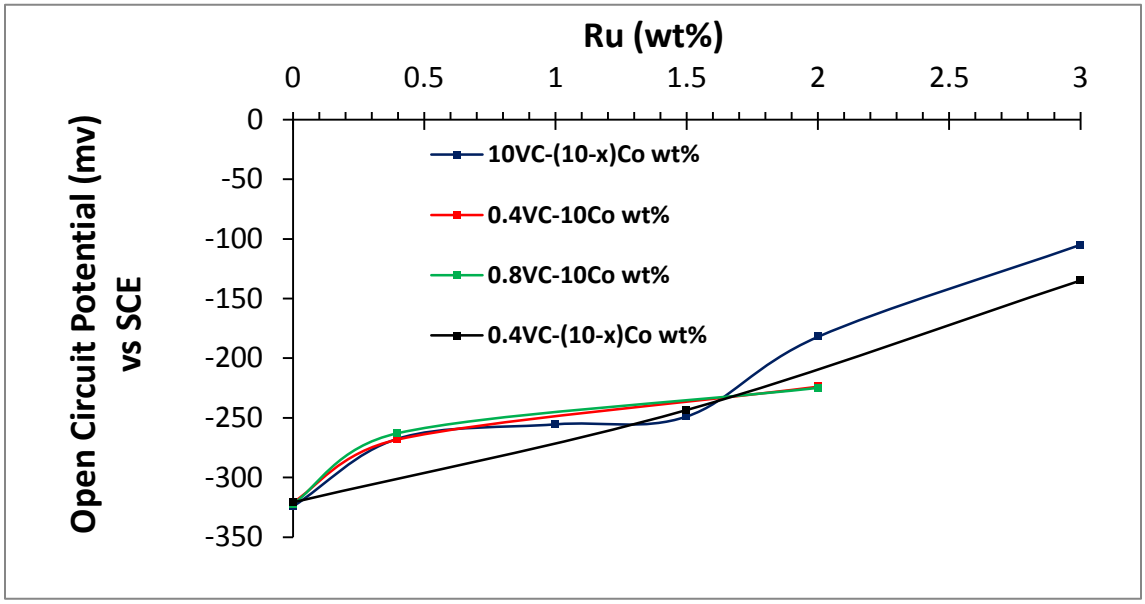

Figure 4.79. Variation of open circuit potentials with composition for 80WC-10VC-(10-x)Co-xRu, (89.6-x)WC-0.4VC-10Co-xRu, (89.2-x)WC-0.8VC-10Co-xRu and 89.6WC-0.4VC-(10-x)Co-xRu (wt%) alloys in 1 M H_2SO_4.

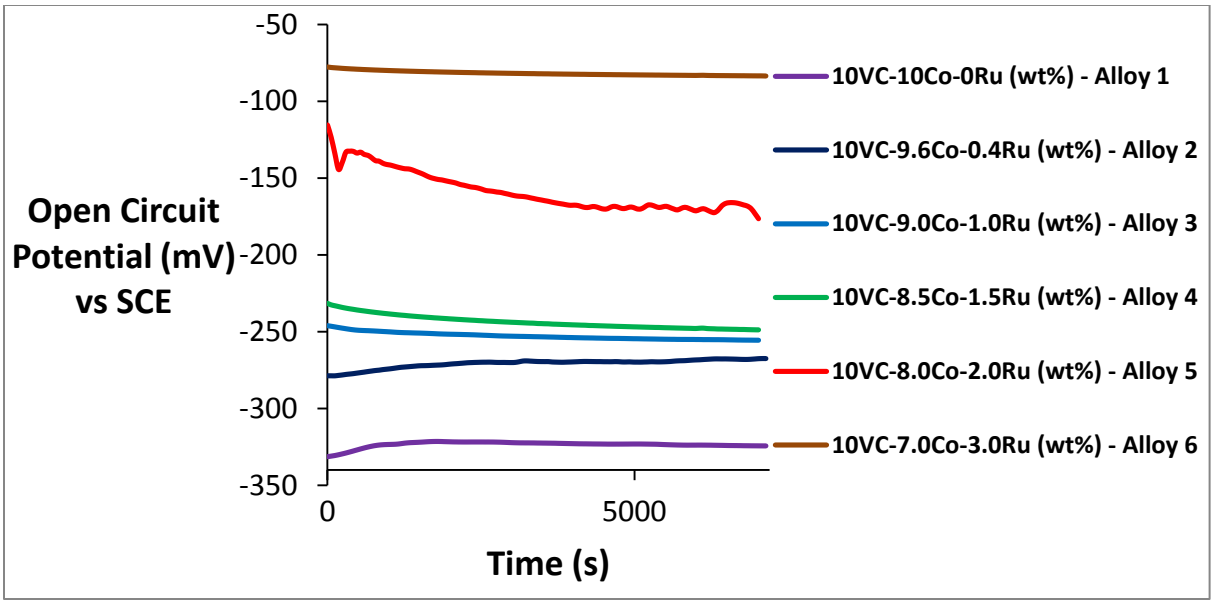

Figure 4.80. Open circuit potentials for 80WC-10VC-(10-x)Co-xRu (wt%) alloys in 1 M H_2SO_4 as a function of scanning period.

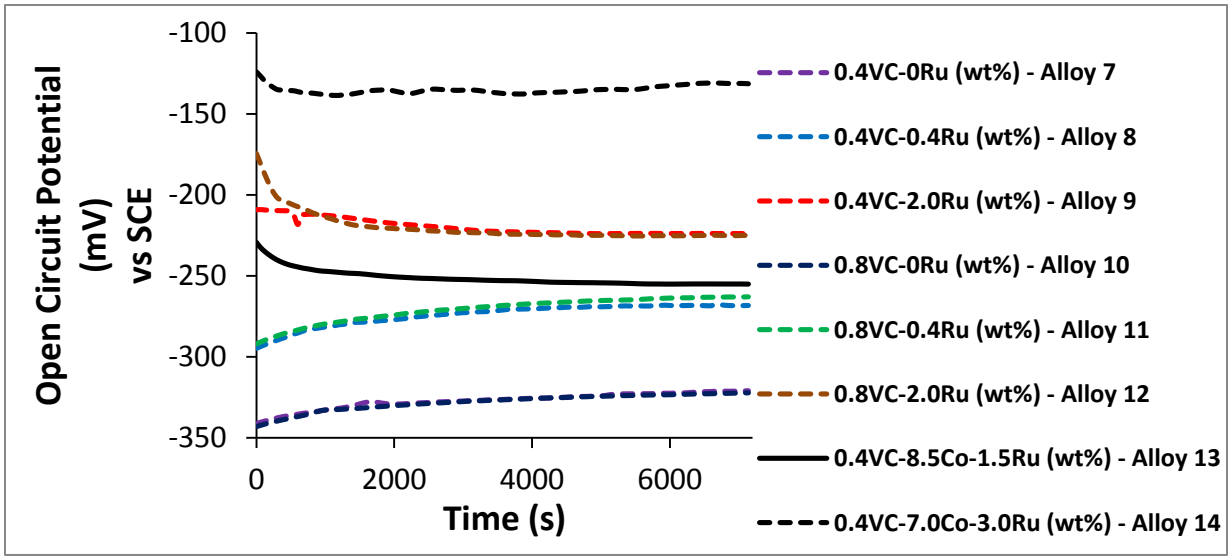

Figure 4.81. Open circuit potentials for (89.6-x)WC-0.4VC-10Co-xRu, (89.2-x)WC-0.8VC-10Co-xRu and 89.6WC-0.4VC-(10-x)Co-xRu (wt%) alloys in 1 M H_2SO_4 as a function of scanning period.

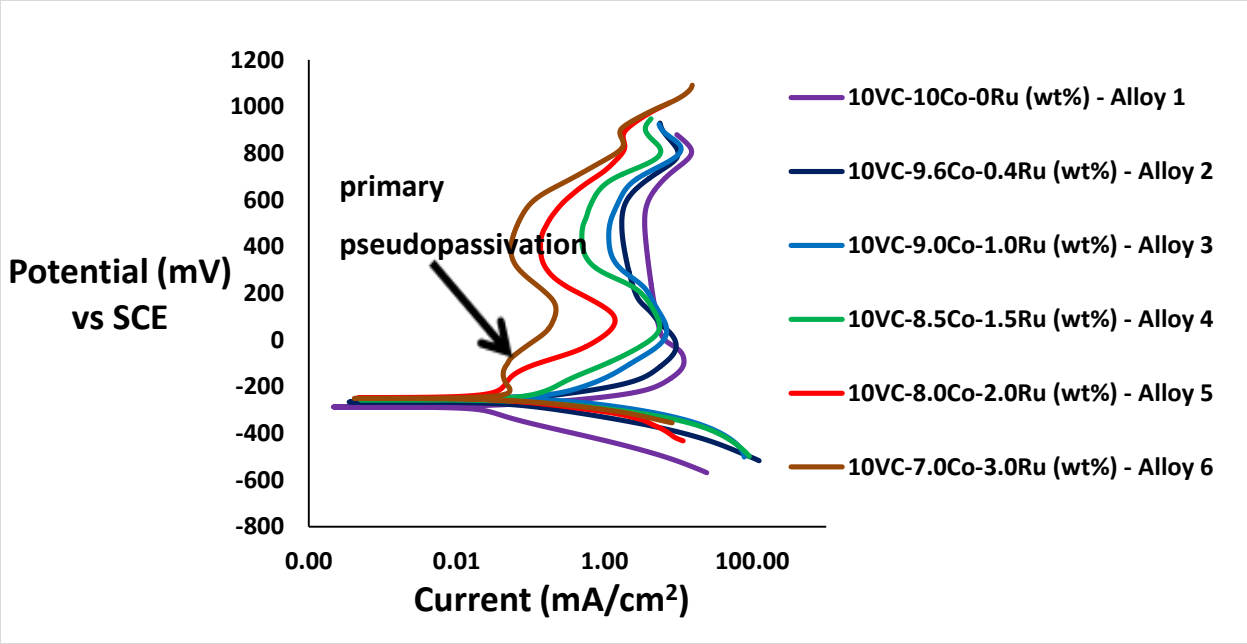

Figure 4.82. Polarisation curves for 80WC-10VC-(10-x)Co-xRu (wt%) alloys in 1 M H_2SO_4.

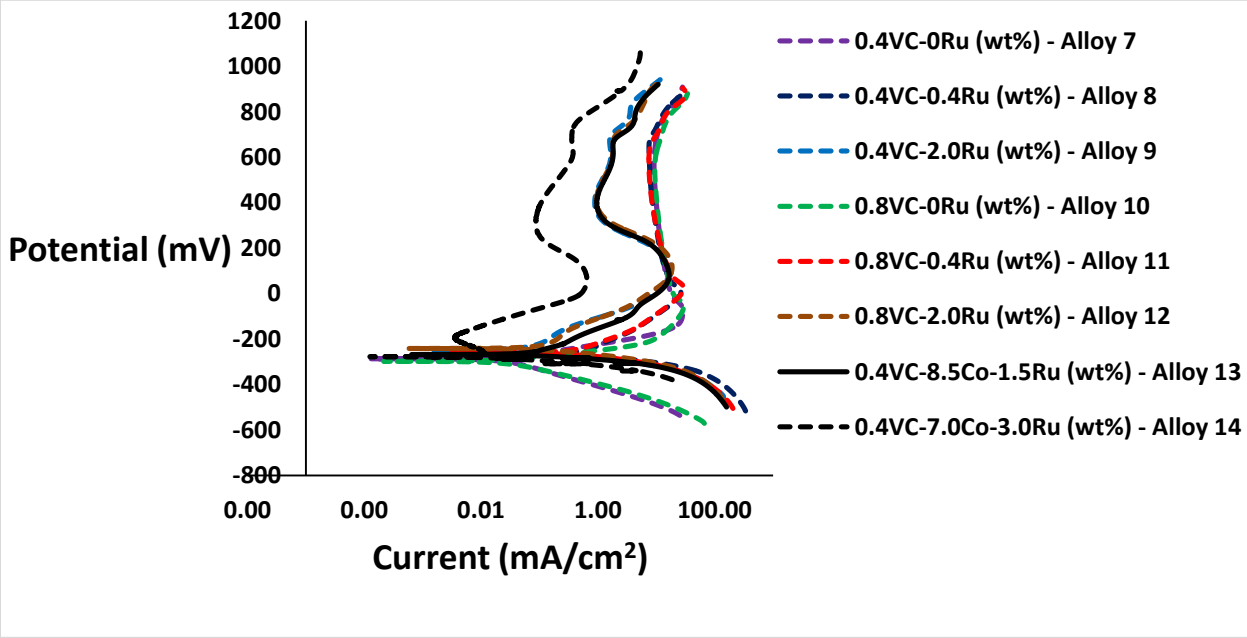

Figure 4.83. Polarisation curves for (89.6-x)WC-0.4VC-10Co-xRu, (89.2-x)WC-0.8VC-10Co-xRu and 89.6WC-0.4VC-(10-x)Co-xRu (wt%) alloys in 1 M H_2SO_4.

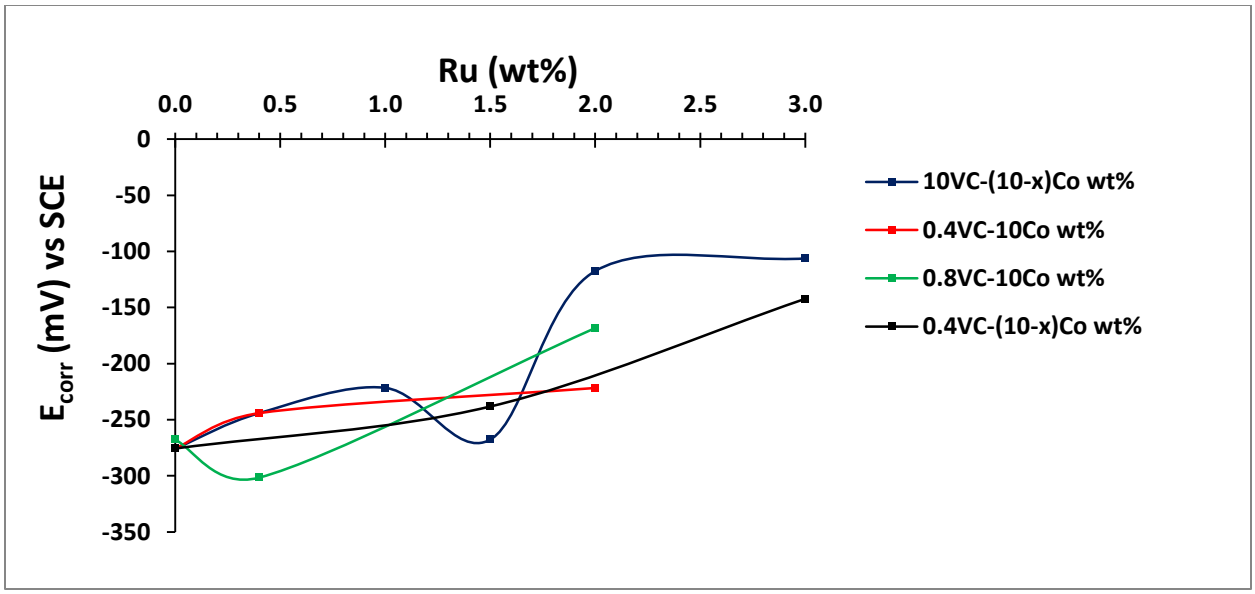

Figure 4.84. E_{corr} values for 80WC-10VC-(10-x)Co-xRu, (89.6-x)WC-0.4VC-10Co-xRu, (89.2-x)WC-0.8VC-10Co-xRu and 89.6WC-0.4VC-(10-x)Co-xRu (wt%) alloys in 1 M H_2SO_4.

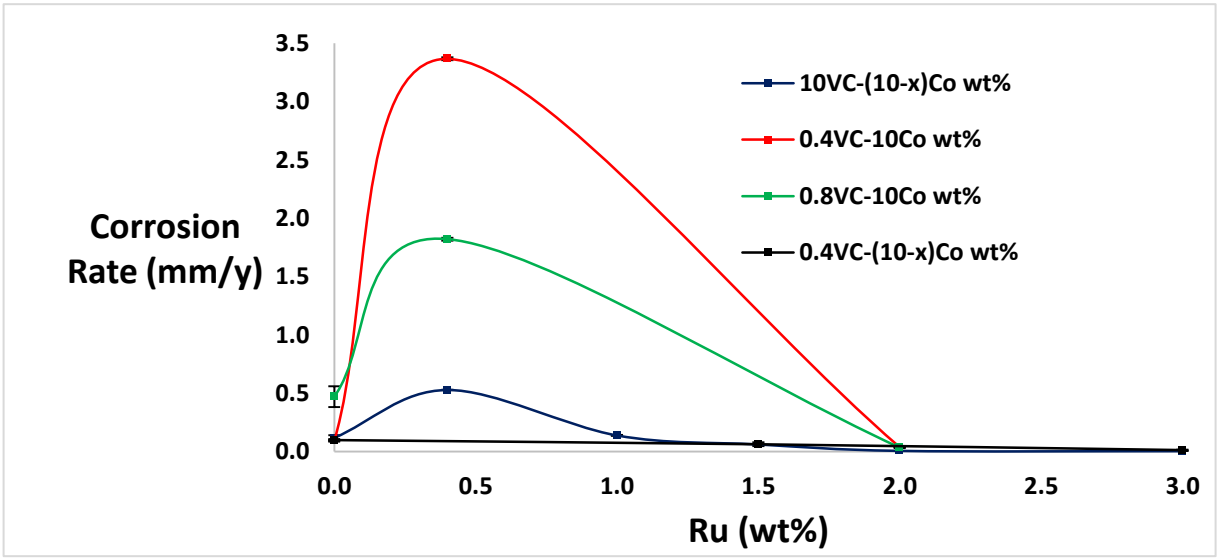

Figure 4.85. Corrosion rates for the 80WC-10VC-(10-x)Co-xRu, (89.6-x)WC-0.4VC-10Co-xRu, (89.2-x)WC-0.8VC-10Co-xRu and 89.6WC-0.4VC-(10-x)Co-xRu (wt%) alloys in 1 M H_2SO_4.

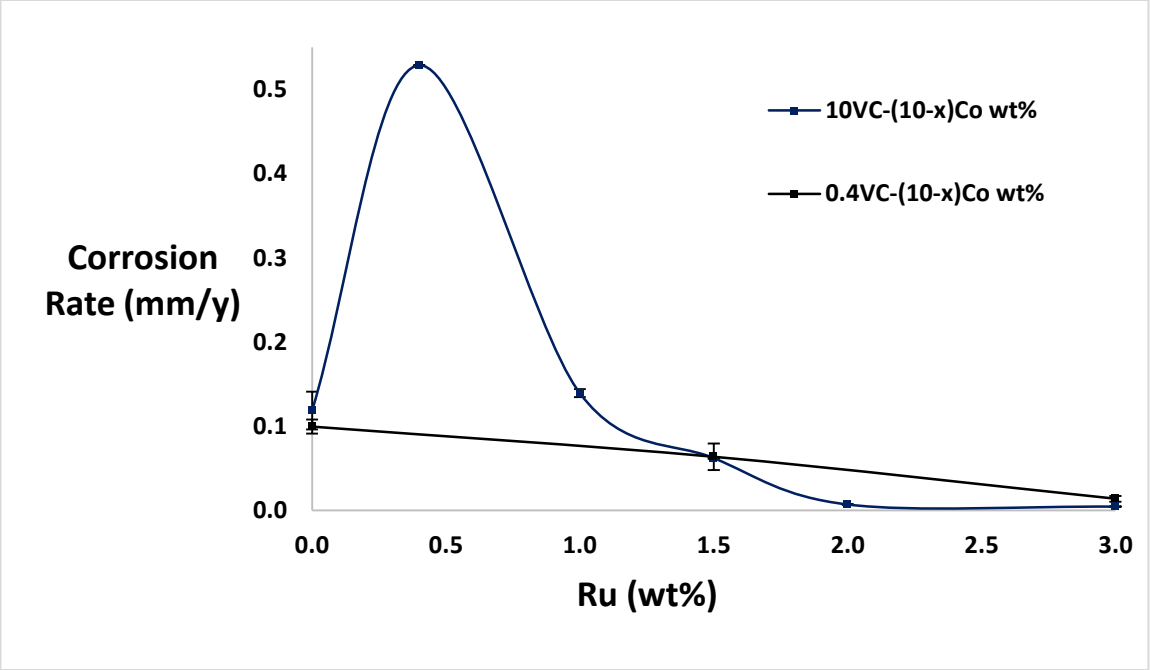

Figure 4.86. Corrosion rates for the 80WC-10VC-(10-x)Co-xRu and 89.6WC-0.4VC-(10-x)Co-xRu (wt%) alloys in 1 M H_2SO_4.

4.6.2. Surface Analysis after Corrosion in 1 M H_2SO_4

In all potentiostatic tests (Figure 4.88), there was a decrease of current with time due to the formation of passive films. By comparison with the uncorroded alloys (Section 4.3), corrosion changed the microstructure (Figures 4.89 to 4.91), with no visible WC grains. Cracks were seen in some alloys (Alloys 7, 8, 10 and 11). The microstructures in Figures 4.89 to 4.91 were due to the existence of corrosion products that were detected from XRD and Raman studies (Figures 4.92 to 4.97). Thus, corrosion films formed which covered the WC grains. Oxides of W and Co were deduced from XRD and Raman studies (Figures 4.92 to 4.97), and some very small C peaks were detected in the XRD patterns of Alloys 3 and 5 (Table 4.37 and Figure 4.92).

a)

b)

c)

Figure 4.87. Specimens after immersion tests and cleaning for the (89.6-x)WC-0.4VC-10Co-xRu (left) and 89.6WC-0.4VC-(10-x)Co-xRu (right) alloys, where x = a) 0 wt% Ru (1 and 7% weight loss), b) 0.4 wt% Ru (35 and 28% weight loss) c) 2.0 wt% Ru (0.6 and 0.5% weight.

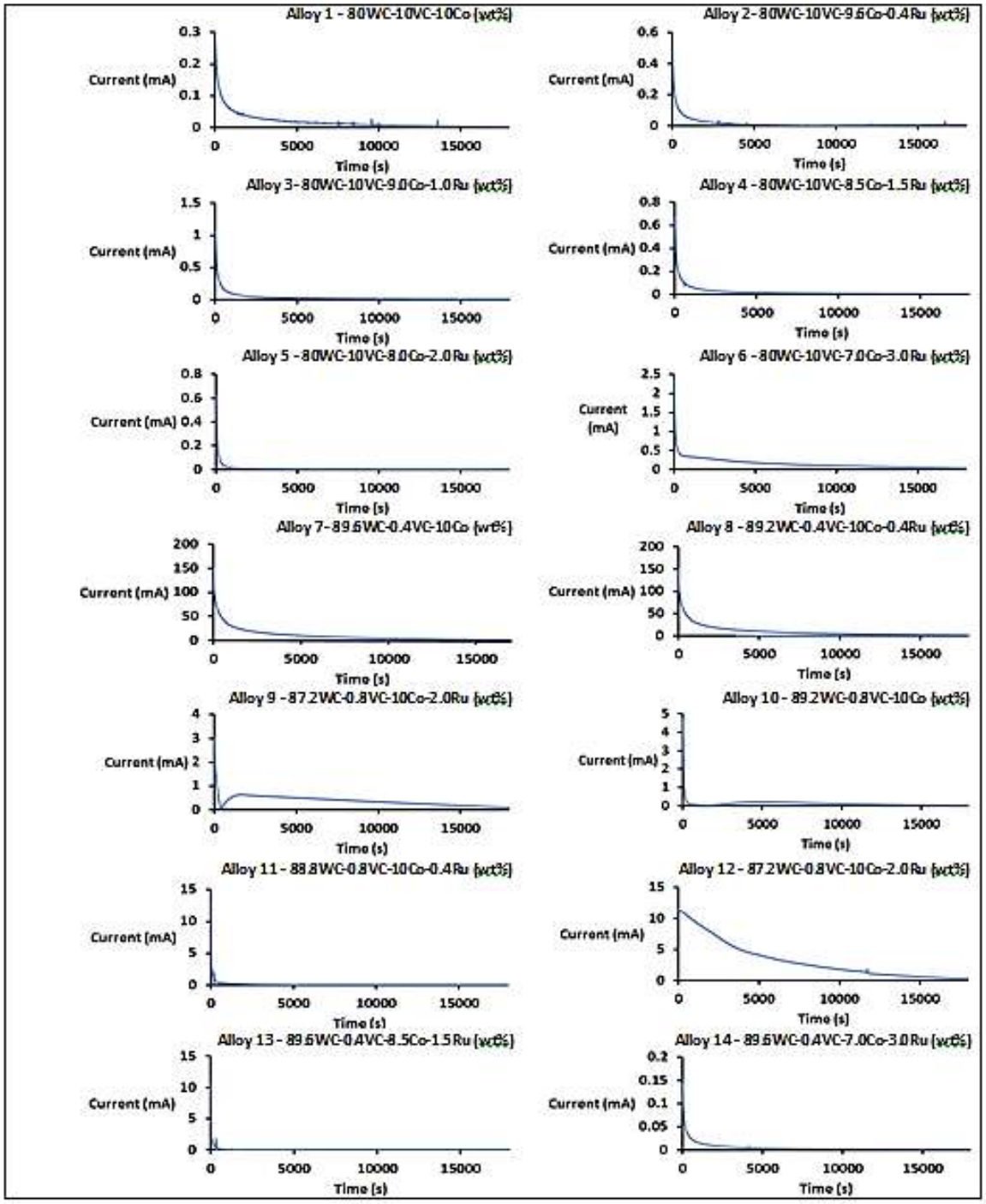

Figure 4.88. Potentiostatic measurements for 80WC-10VC-(10-x)Co-xRu, (89.6-x)WC-0.4VC-10Co-xRu, (89.2-x)WC-0.8VC-10Co-xRu and 89.6WC-0.4VC-(10-x)Co-xRu (wt%) alloys in 1 M H_2SO_4.

Alloy 1 - 80WC-10VC-10Co (wt%)

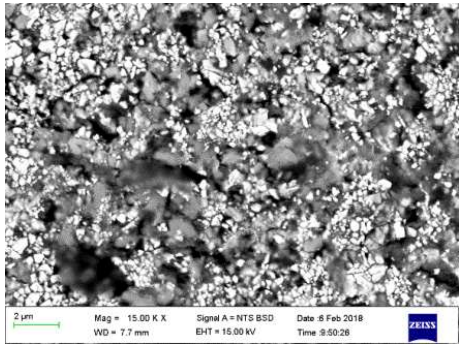

Alloy 2- 80WC-10VC-9.6Co-0.4Ru (wt%)

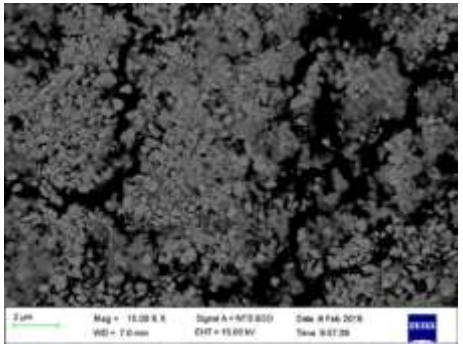

Alloy 3- 80WC-10VC-9.0Co-1.0Ru (wt%)

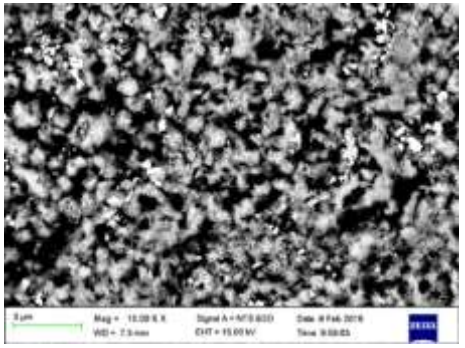

Alloy 4 - 80WC-10VC-8.5Co-1.5Ru (wt%)

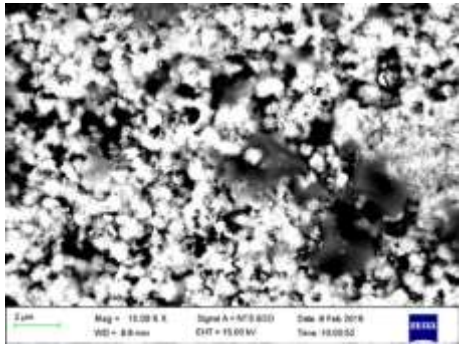

Alloy 5 - 80WC-10VC-8.0Co-2.0Ru (wt%)

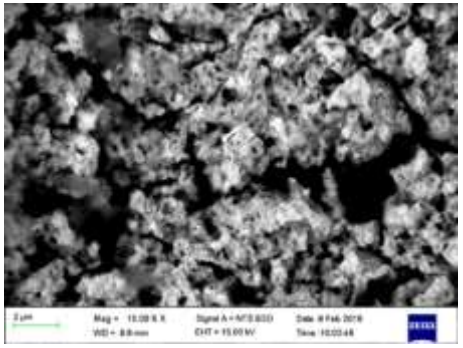

Alloy 6 - 80WC-10VC-7.0Co-3.0Ru (wt%)

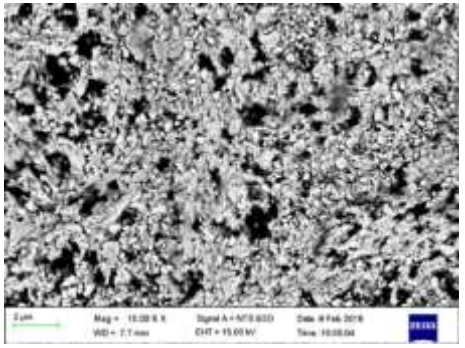

Figure 4.89. SEM-BSE images for the 80WC-10VC-(10-x)Co-xRu (wt%) alloys after exposure to 1 M H_2SO_4, showing the effects of corrosion.

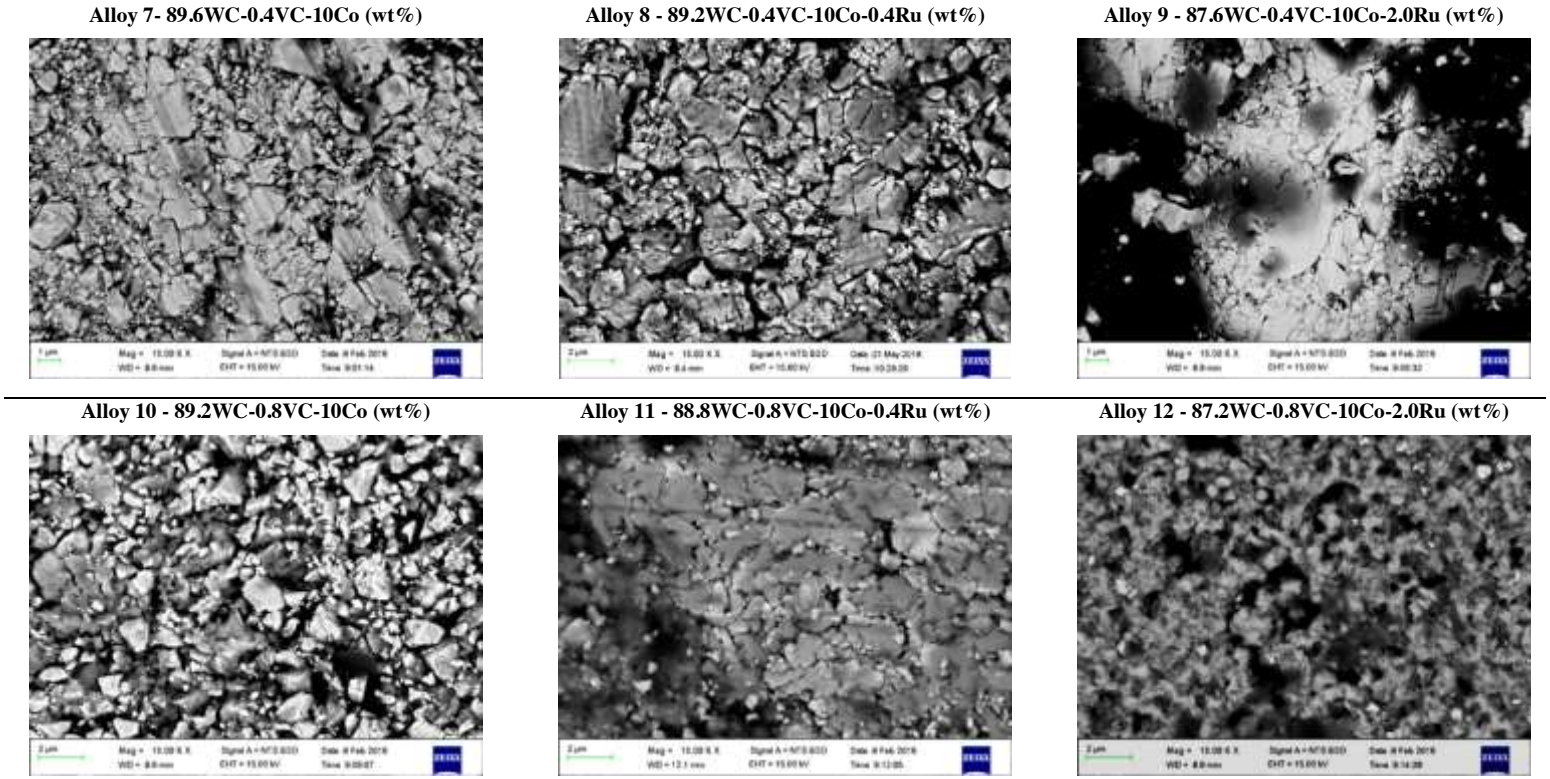

Figure 4.90. SEM-BSE images for the (89.6-x)WC-0.4VC-10Co-xRu and (89.2-x)WC-0.8VC-10Co-xRu (wt%) alloys after exposure to 1 M H_2SO_4, showing the effects of corrosion.

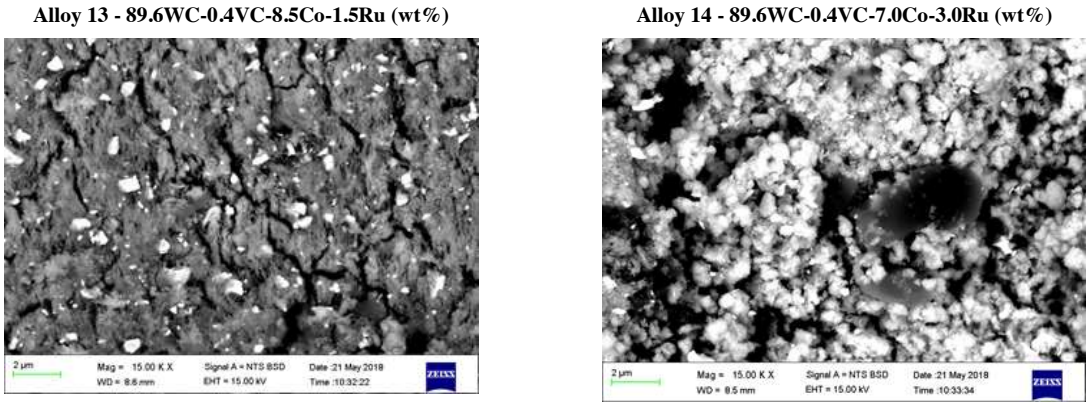

Figure 4.91. SEM-BSE images for the 89.6WC-0.4VC-(10-x)Co-xRu (wt%) alloys after exposure to 1 M H_2SO_4, showing the effects of corrosion.

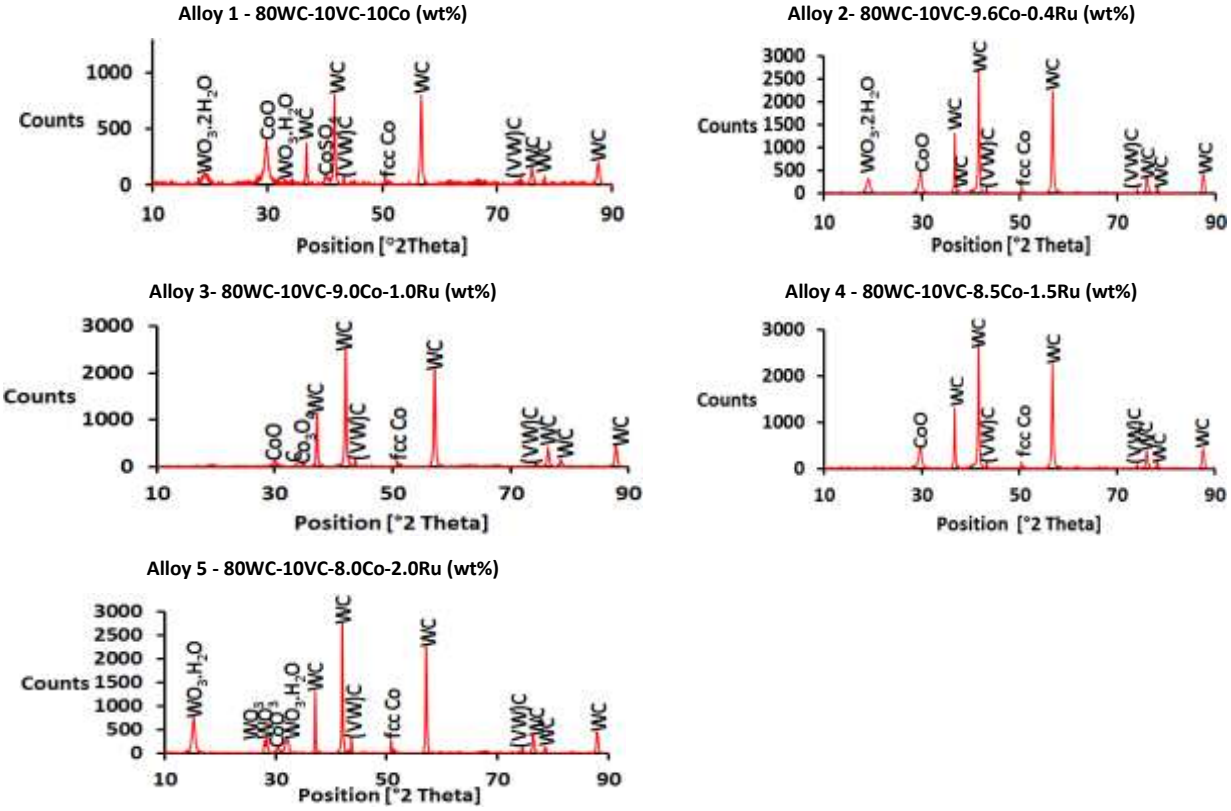

Figure 4.92. XRD patterns of the 80WC-10VC-(10-x)Co0xRu (wt%) alloys with corrosion products after exposure 1 M H_2SO_4.

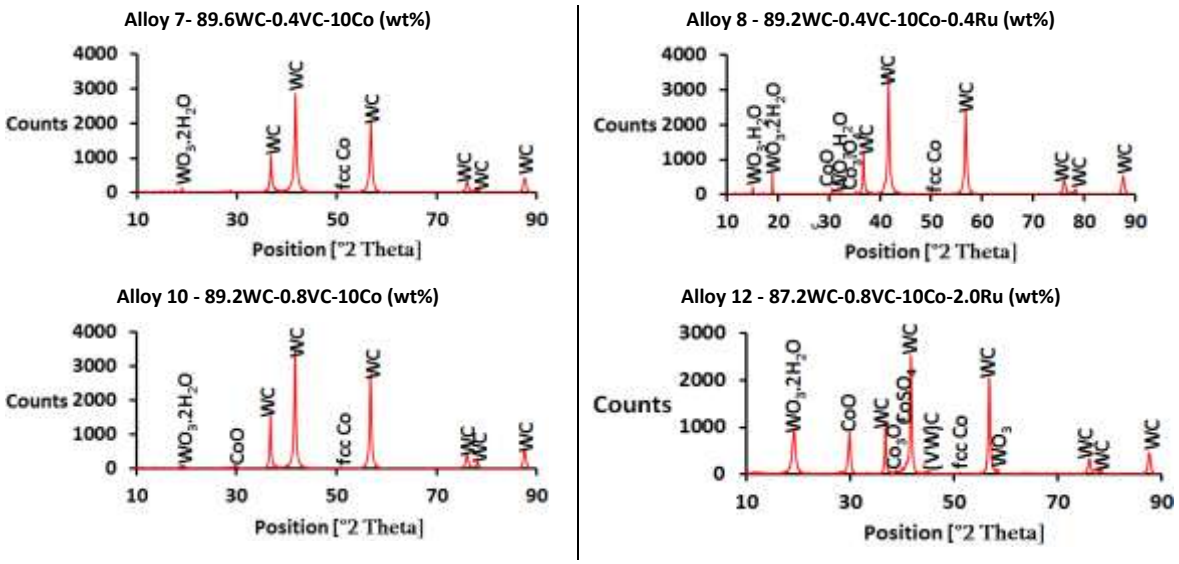

Figure 4.93. XRD patterns of alloys with corrosion products after exposure to synthetic 1 M H_2SO_4.

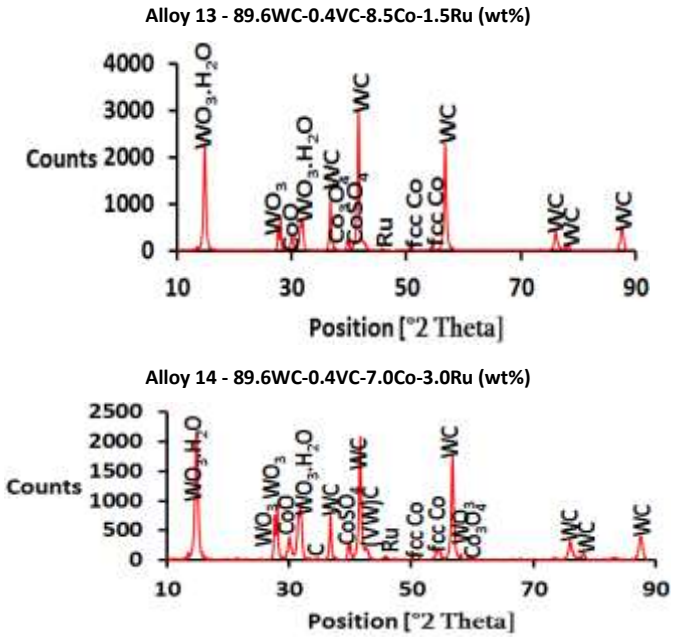

Figure 4.94. XRD patterns of alloys with corrosion products after exposure to synthetic 1 M H_2SO_4.

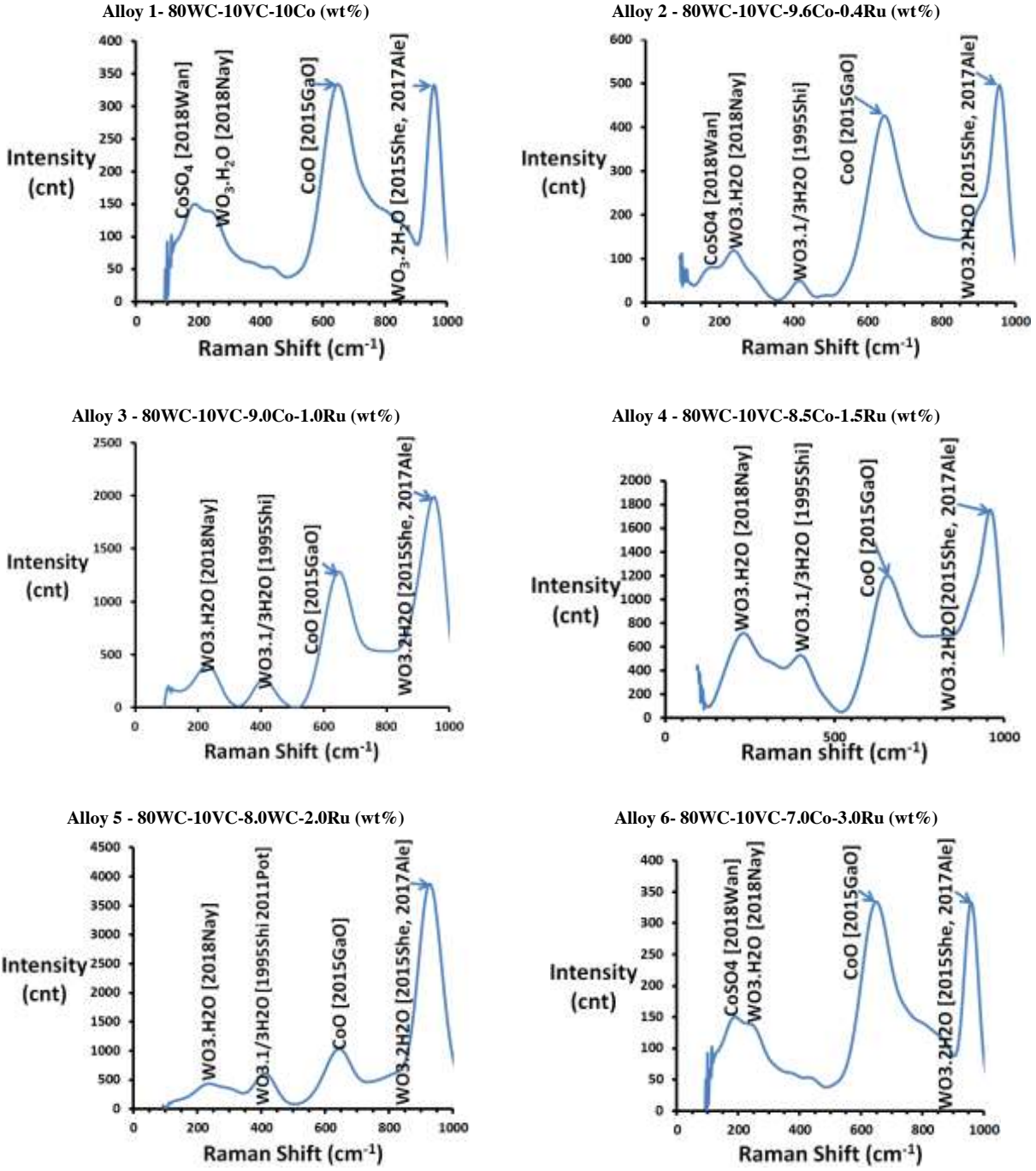

Figure 4.95. Raman peaks for the 80WC-10VC-(10-x)Co-xRu (wt%) alloys after exposure to 1 M H_2SO_4.

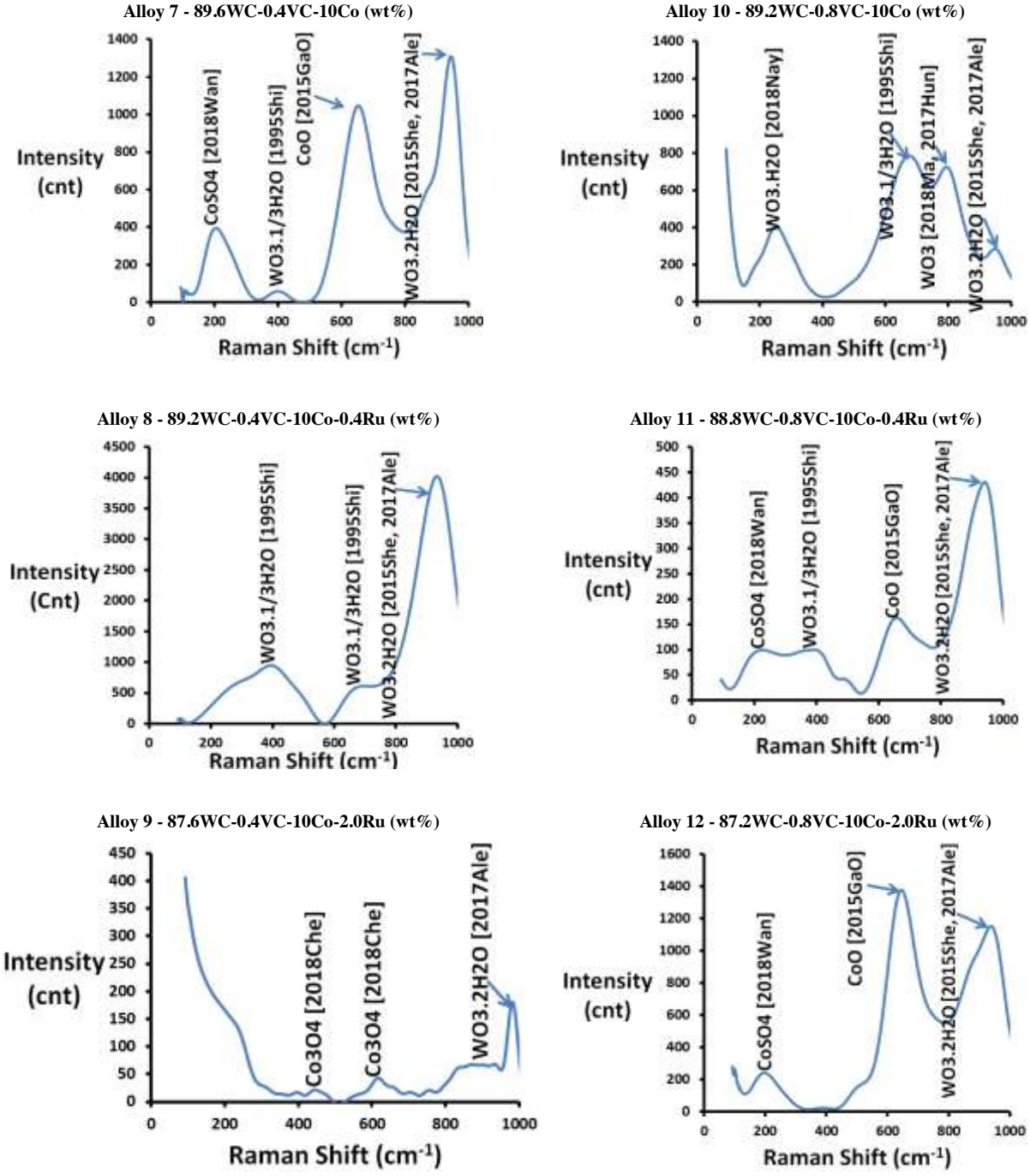

Figure 4.96. Raman peaks for the (89.6-x)WC-0.4VC-10Co-xRu and (89.2-x)WC-0.8VC-10Co-xRu (wt%) alloys after exposure to 1 M H_2SO_4.

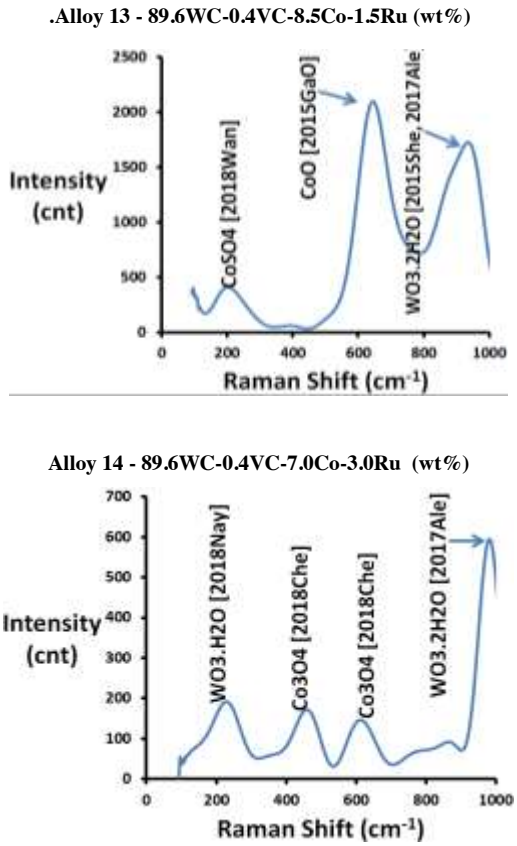

Figure 4.97. Raman peaks for the 89.6WC-0.4VC-(10-x)Co-xRu (wt%) alloys after exposure to 1 M H_2SO_4.

Table 4.37. Phases identified from Raman and XRD analyses for the 80WC-10VC-(10-x)Co-xRu, (89.6-x)WC-0.4VC-10Co-xRu, (89.2-x)WC-0.8VC-10Co-xRu and 89.6WC-0.4VC-(10-x)Co-xRu (wt%) alloys after corrosion in 1 M H_2SO_4.

Phase	**Alloys with corrosion phases identified by XRD**	**Alloys with corrosion phases identified by Raman**
$CoSO_4$	1,2,12-14	1,2,6,7,11-13
$WO_3.H_2O$	1,2,5,8,13,14	1-6,10,14
CoO	1-5,8,10,12-14	1-7,11-14
$WO_3.2H_2O$	1,2,3,6,7,10,12	1-14
$WO_3.1/3H_2O$	-	2-5,7,8,10,11
Co_3O_4	3,8,12-14	9,14
C	3, 5	-
WO_3	5	10

4.6.3. Electrochemical Results for Corrosion in NaCl

4.6.3.1. Open Circuit Potential (OCP) Measurements

The OCPs for all alloy series increased with Ru additions (Table 4.38, Figures 4.98 to 4.100). The OCPs had narrow fluctuations, within 50 mV over time, for most of the alloys. Alloys 2, 3, 4, 6, 9 and 12 had the least fluctuations (Figures 4.99 and 4.100). The OCP for Alloy 5 increased by ~70 mV in the first 1000 s before stabilising (Figure 4.99). Alloys 7, 8, 10, 11 and 14 had the most significant increases in OCP before stabilising (~50-150 mV) (Figure 4.100).

There was no definite trend in OCP, with respect to VC content, for the Alloys 1, 7 and 10, without Ru (Table 4.38). Ruthenium additions resulted in more significant increases in OCP for the 80WC-10VC-(10-*x*)Co-*x*Ru series than in the other three alloy series (Table 4.38, Figure 4.98) In the (89.6-*x*)WC-0.4VC-10Co-*x*Ru and (89.2-*x*)WC-0.8VC-10Co-*x*Ru alloy series (Figure 4.100), the alloys with most Ru (Alloys 9 and 12) had the least fluctuation in OCPs.

4.6.3.2. Polarisation Behaviour

The polarisation curves had the same general characteristics for all fourteen alloys, with narrower passive regions at higher Ru contents (Figures 4.101 and 4.102). Double passive regions were observed for alloys with higher Ru content of the 80WC-10VC-(10-*x*)Co-*x*Ru alloy series (Alloys 5 and 6) (Figure 4.101). There was mild pseudopassivation for all the alloys at decreasing current densities with Ru additions (Figures 4.101 and 4.102). For all alloys, the critical anodic current density and the pseudopassive region also decreased with increasing Ru, but the effect of Ru on the primary passive potential was not clear since it fluctuated among the alloys for increasing Ru content. The primary passive potential increased from Alloy 1 to 3, and at Alloy 6, but decreased between Alloys 3 and 5 (Figure 4.101).

Table 4.38. Electrochemical parameters for the 80WC-10VC-(10-x)Co-xRu, (89.6-x)WC-0.4VC-10Co-xRu, (89.2-x)WC-0.8VC-10Co-xRu and 89.6WC-0.4VC-(10-x)Co-xRu (wt%) alloys for polarisation in 1 M NaCl (corrosion rates determined from immersion tests).

Series	**Alloy No.**	**OCP (mV)**	**E_{corr} (mV)**	**i_c (mA.cm^{-2})**	**b_a (mV)**	**b_c (mV)**	**i_{corr} (mA.cm^{-2})**	**Corrosion Rate (x10^{-3} mm.y^{-1})**	**Change in corrosion (%)**
80WC-10VC-(10-*x*)Co-*x*Ru	1	-392.83	-374.70	22.5	89	442	0.013	2.521±0.366	-
	2	-356.77	-351.47	16.8	19	236	0.007	2.459±0.068	-2
	3	-268.97	-283.61	14.3	86	208	0.003	2.264±0.151	-10
	4	-263.67	-267.40	10.5	43	137	0.003	2.235±0.029	-11
	5	-181.15	-175.79	0.6	69	63	0.001	2.082±0.144	-17
	6	-121.06	-78.44	0.3	82	59	0.001	1.752±0.035	-31
(89.6-*x*)WC-0.4VC-10Co-*x*Ru	7	-412.39	-424.92	42.4	58	814	0.017	2.049±0.017	-
	8	-370.49	-343.86	41.9	64	737	0.012	1.713±0.013	-16
	9	-246.97	-272.76	19.0	43	95	0.002	1.586±0.004	-0.2
(89.2-*x*)WC-0.8VC-10Co-*x*Ru	10	-388.02	-304.69	60.7	71	157	0.010	2.397±0.012	-
	11	-363.76	-325.93	42.1	34	131	0.004	2.220±0.017	-7
	12	-257.90	-274.45	24.7	57	55	0.003	2.038±0.012	-15
89.6WC-0.4VC-(10-*x*)Co-*x*Ru (*Includes Alloy 7)*	13	-307.77	-289.19	18.9	34	152	0.006	1.507±0.013	-26
	14	-160.77	-138.11	0.65	97	106	0.001	1.164±0.035	-43

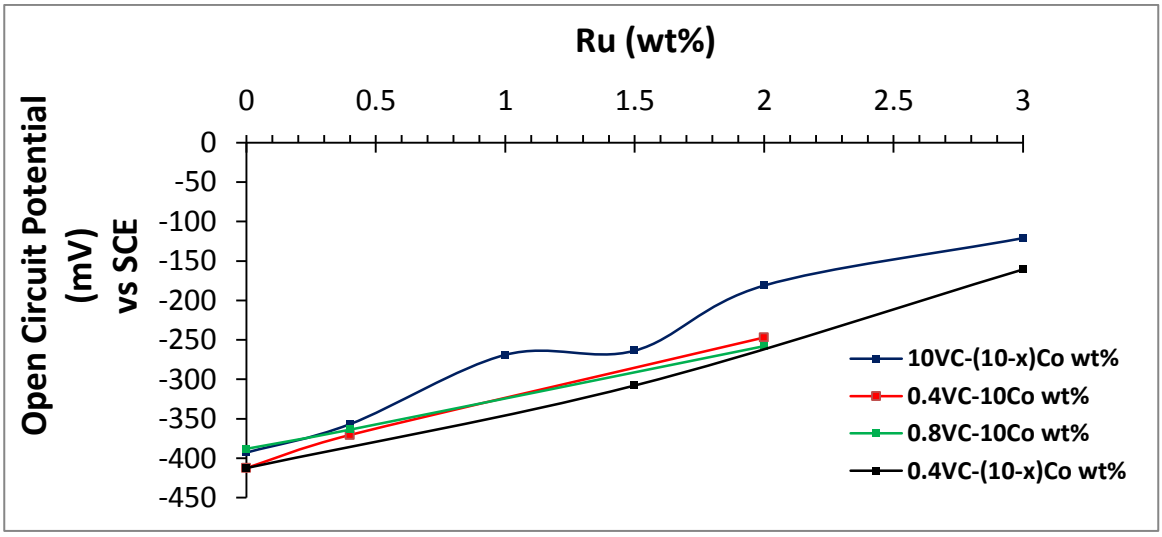

Figure 4.98. Variation of open circuit potentials with composition for 80WC-10VC-(10-x)Co-xRu, (89.6-x)WC-0.4VC-10Co-xRu, (89.2-x)WC-0.8VC-10Co-xRu and 89.6WC-0.4VC-(10-x)Co-xRu (wt%) alloys in 1 M NaCl.

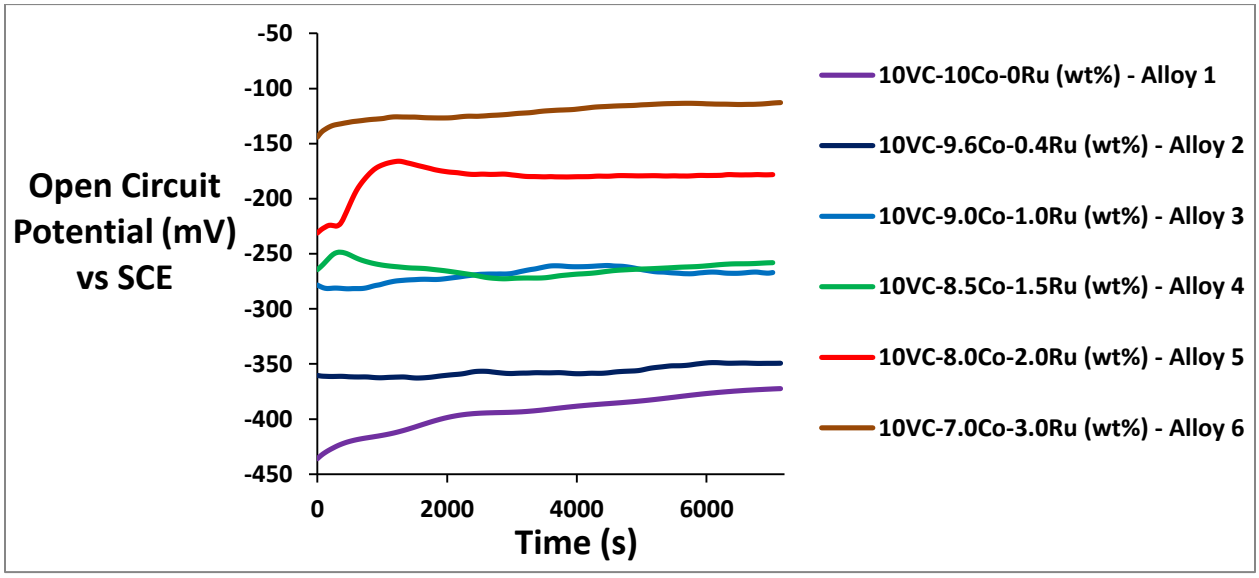

Figure 4.99. Open circuit potentials for 80WC-10VC-(10-x)Co-xRu (wt%) alloys in 1 M NaCl

The E_{corr} values generally increased with Ru additions for all alloy series (Table 4.38, Figure 4.103). Alloys 6 and 14, with the highest Ru content (3 wt%), had the highest E_{corr} values, with Alloy 6 having a higher E_{corr} than Alloy 14 (Figure 4.103). There was no correlation in E_{corr}

values between the alloy series for the same Ru contents (Figure 4.103). Thus, the effect of VC on E_{corr} was not very clear, but higher VC contents generally increased E_{corr} (Figure 4.103).

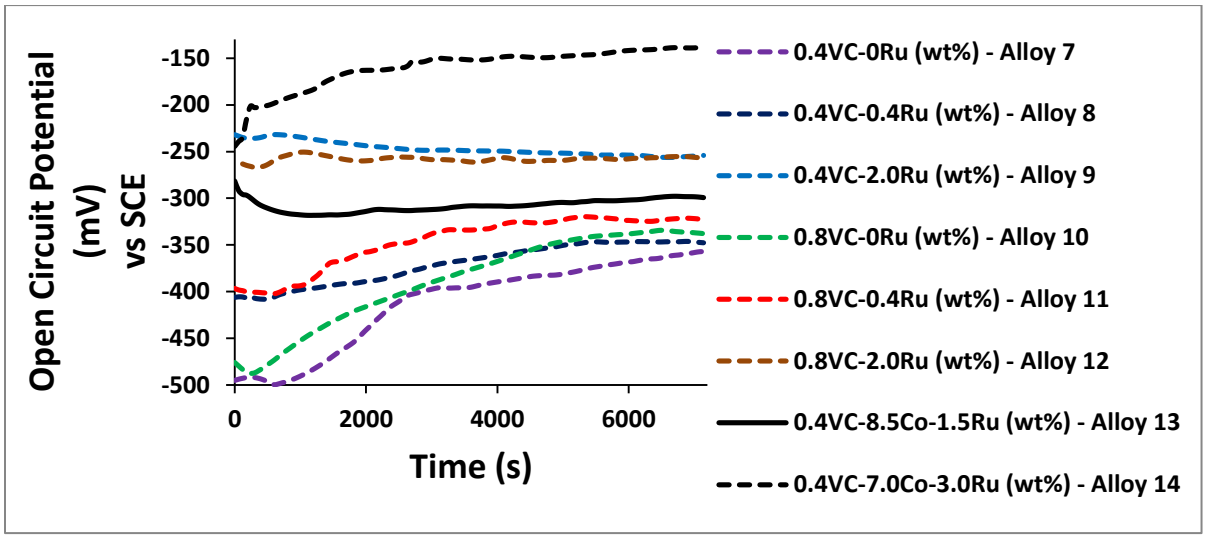

Figure 4.100. Open circuit potentials for (89.6-x)WC-0.4VC-10Co-xRu, (89.2-x)WC-0.8VC-10Co-xRu (wt%) and 89.6WC-0.4VC-(10-x)Co-xRu (wt%) alloys in 1 M NaCl.

4.6.3.3. Corrosion Rates from Mass Loss Tests

There was a decrease in corrosion rate with Ru additions in all alloy series (Table 4.38 and Figure 4.104). In NaCl, up to 3 wt% Ru additions were beneficial in improving corrosion resistance of 80WC-10VC-(10-*x*)Co-*x*Ru and 89.6WC-0.4VC-(10-*x*)Co-*x*Ru alloys (Figure 4.104). Higher VC contents were associated with higher corrosion rates (Figure 4.104).

4.6.4. Surface Analysis after Corrosion in 1 M NaCl

There was a general decrease in current with time at constant potentials for all alloys (Figure 4.105), indicating the formation of a passive film. There were some instances where current seemed to increase with time before stabilising, e.g. for Alloy 9. The increases in current might have been due to breakage of some of the surface films. However, the levelling off occurred at a very low current (~0.02 mA) suggesting more impedance due the formation of corrosion products with poor electrical conductivity. Alloys 1 to 6 still had visible WC grains after corrosion in NaCl (Figure 4.106). Porosity was most significant for Alloy 3 as deduced from the secondary SEM image (Appendix E, Figure E1). The pores appeared as dark areas in the SEM-

BSE images (Figure 4.106). No WC grains were seen for Alloys 10, 11 and 14 due to the existence of a corrosion film (Figures 4.107 and 4.108). Some NaCl particles were present that were associated with light particles seen in Alloys 5 and 11. From the EDS analysis of the light particles, Appendix E (Tables E4), the light particles were most likely WC with some NaCl and some oxide. However, the light particles were less than 2 μm across, too small to analyse accurately. Oxides of Co, W and V were deduced from XRD and Raman analyses (Figures 4.109 to 4.112). XRD analyses (Figure 4.109) showed very small C peaks after corrosion. The presence of $Na_2W_2O_7$, $Na_2W_4O_{13}$ and $Na_2O.WO_3$ showed that Na^+ ions from NaCl were involved in the formation of the corrosion films. A summary of all the phases found from XRD and Raman studies is shown in Table 4.39.

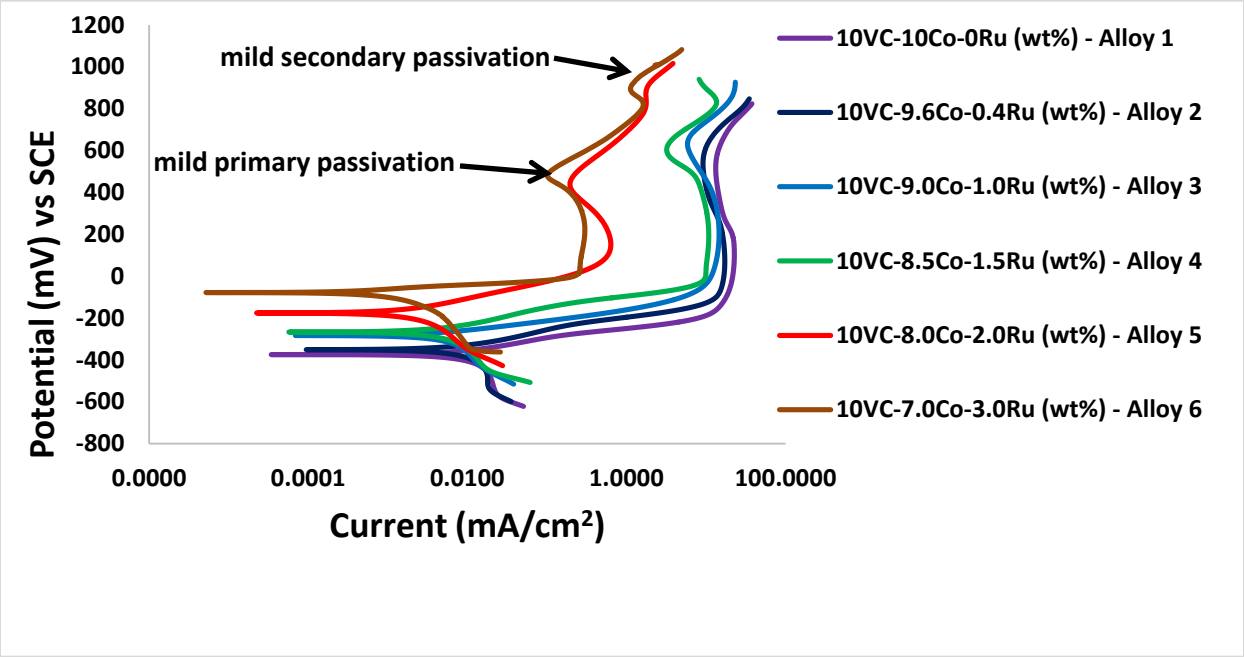

Figure 4.101. Polarisation curves for 80WC-10VC-(10-x)Co-xRu (wt%) alloys in 1 M NaCl.

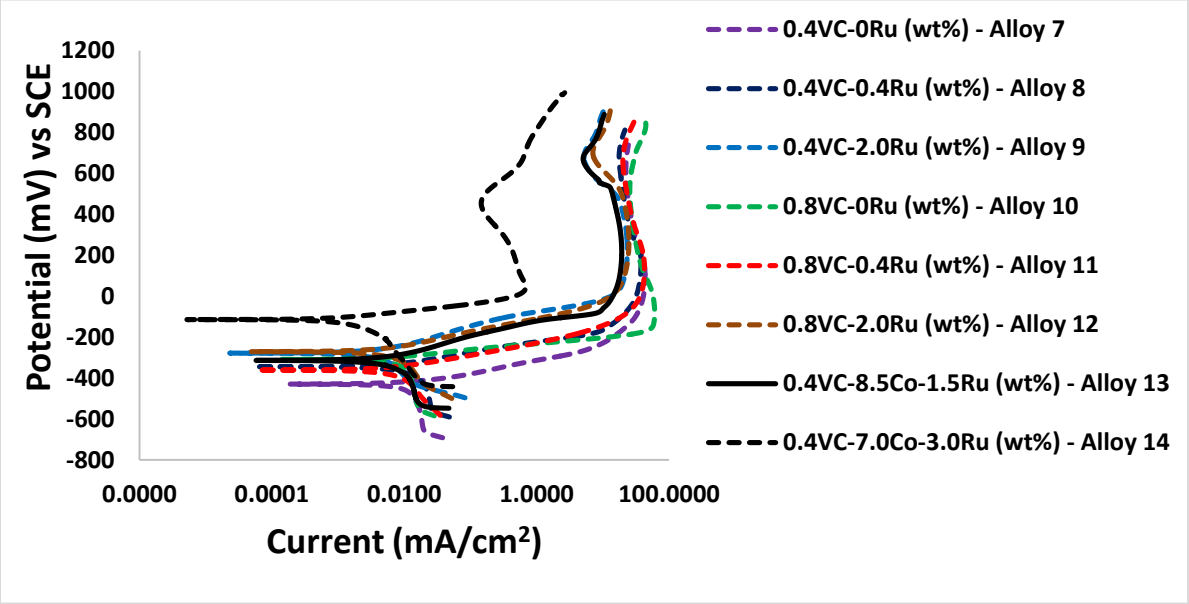

Figure 4.102. Polarisation curves for (89.6-x)WC-0.4VC-10Co-xRu, (89.2-x)WC-0.8VC-10Co-xRu 0and 89.6WC-0.4VC-(10-x)Co-xRu (wt%) alloys in 1 M NaCl.

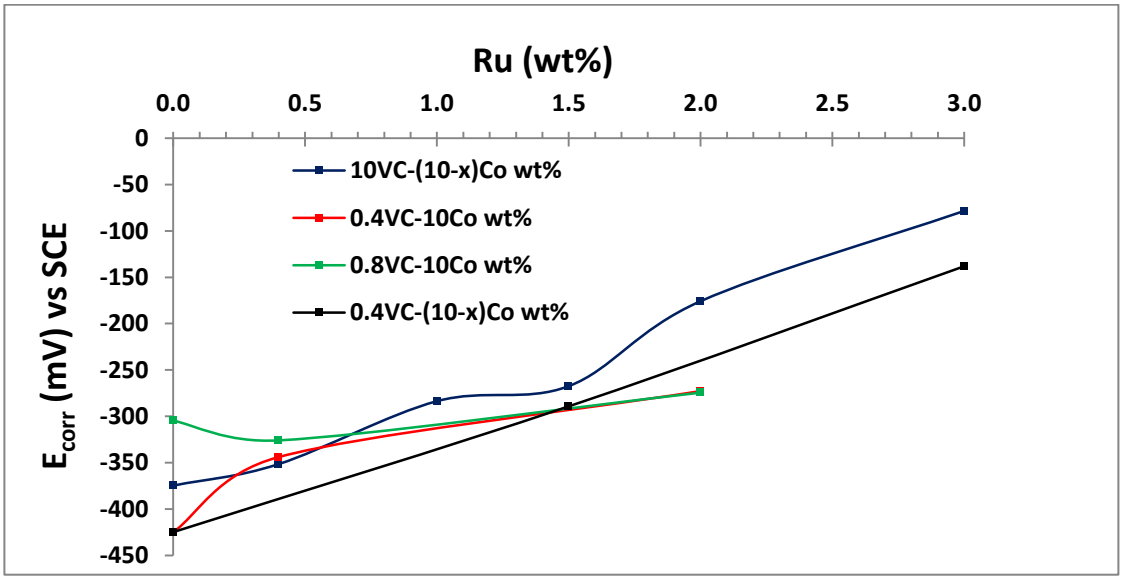

Figure 4.103. E_{corr} values for 80WC-10VC-(10-x)Co-xRu, (89.6-x)WC-0.4VC-10Co-xRu, (89.2-x)WC-0.8VC-10Co-xRu and 89.6WC-0.4VC-(10-x)Co-xRu (wt%) alloys in 1 M NaCl.

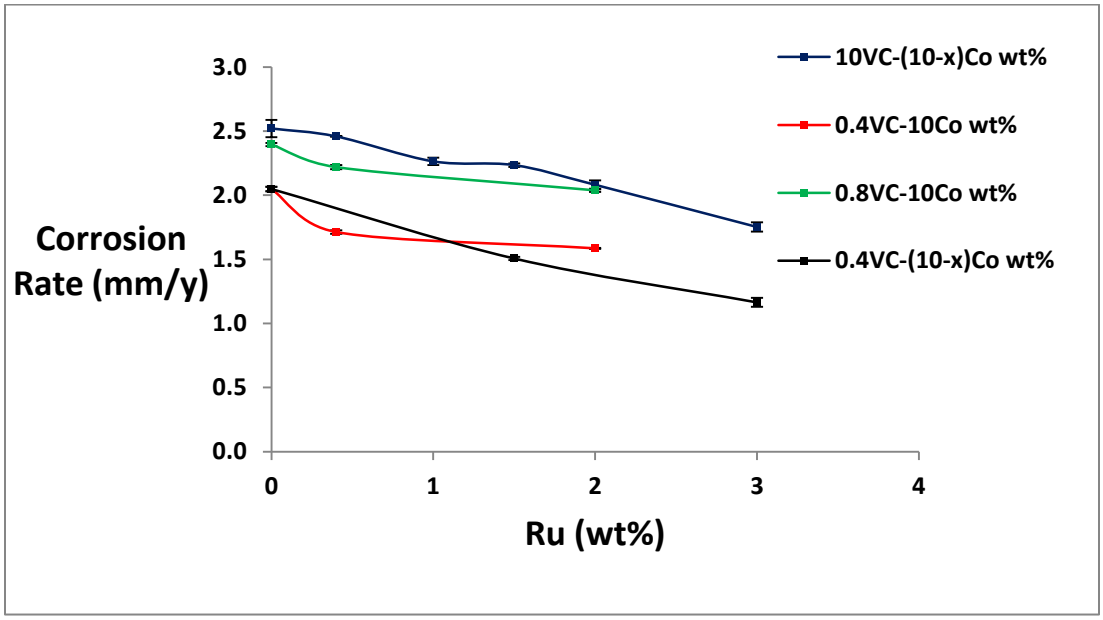

Figure 4.104. Corrosion rates for 80WC-10VC-(10-x)Co-xRu, (89.6-x)WC-0.4VC-10Co-xRu, (89.2-x)WC-0.8VC-10Co-xRu and 89.6WC-0.4VC-(10-x)Co-xRu (wt%) alloys in 1 M NaCl.

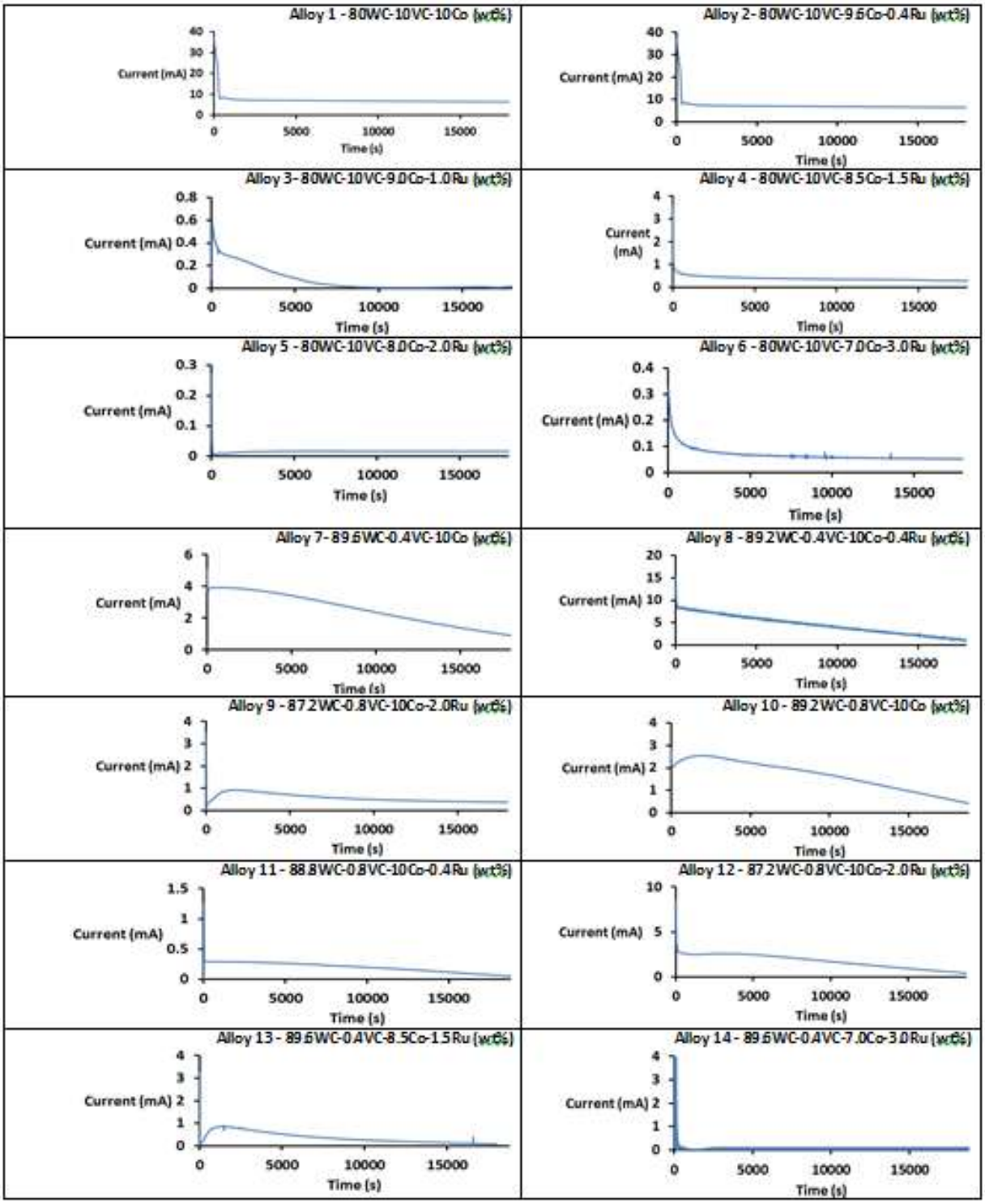

Figure 4.105. Potentiostatic measurements for 80WC-10VC-(10-x)Co-xRu, (89.6-x)WC-0.4VC-10Co-xRu, (89.2-x)WC-0.8VC-10Co-xRu and 89.6WC-0.4VC-(10-x)Co-xRu (wt%) alloys in 1 M NaCl.

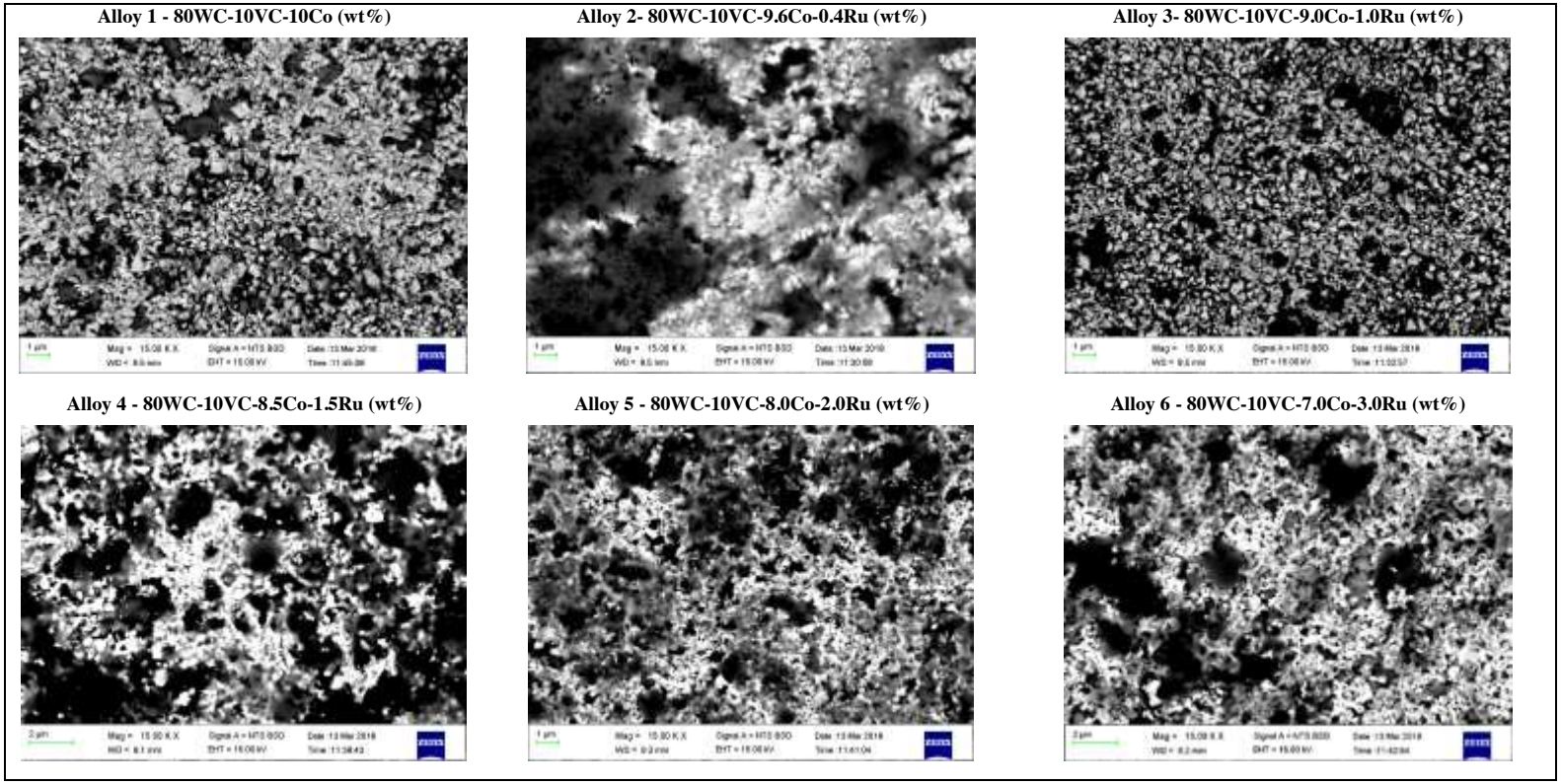

Figure 4.106. SEM-BSE images for the 80WC-10VC-(10-x)Co-xRu (wt%) alloys after exposure to 1 M NaCl, showing the effects of corrosion.

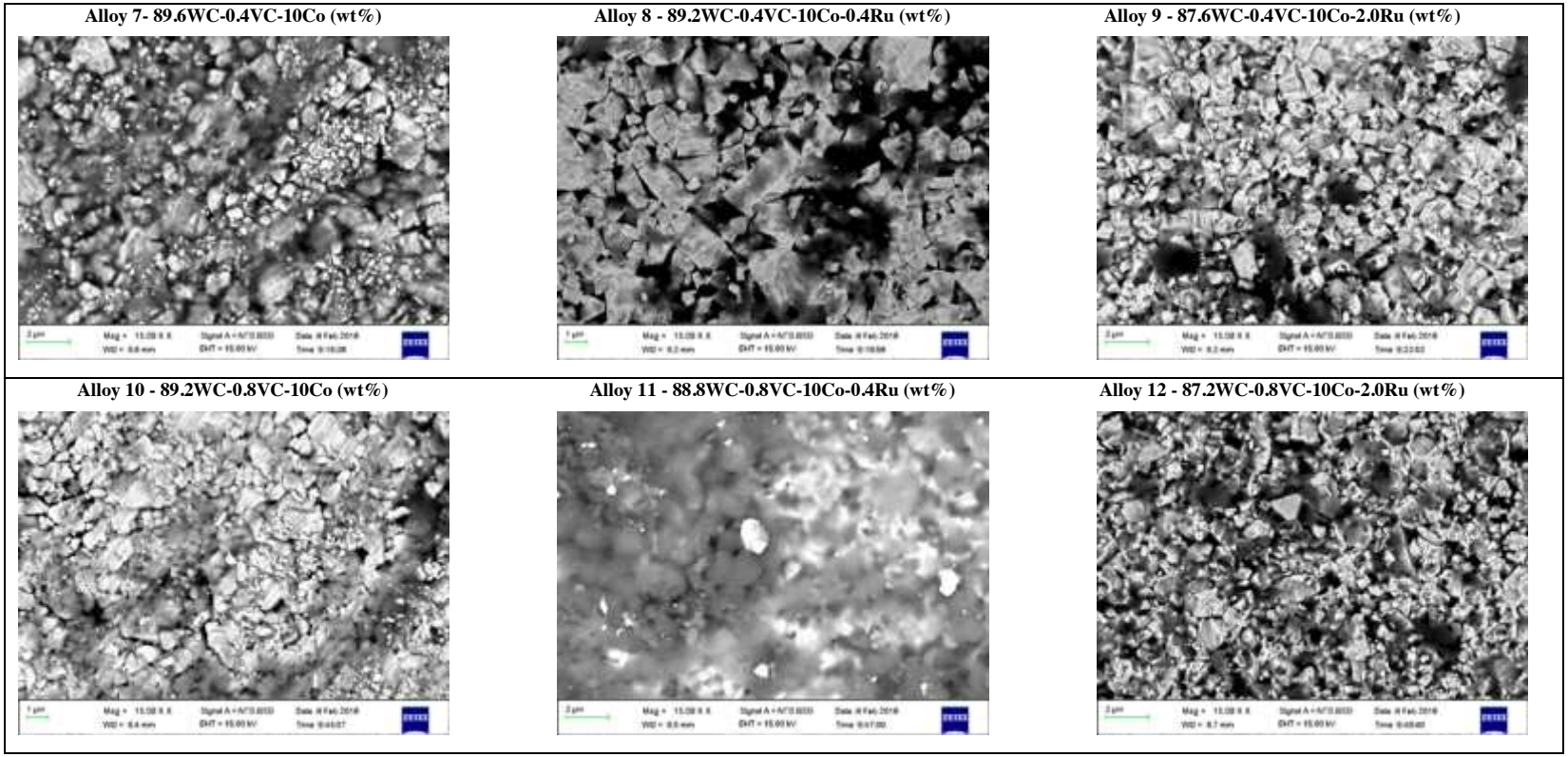

Figure 4.107. SEM-BSE images for the (89.6-x)WC-0.4VC-10Co-xRu (top) and (89.2-x)WC-0.8VC-10Co-xRu (bottom) (wt%) alloys after exposure to 1 M NaCl, showing the effects of corrosion.

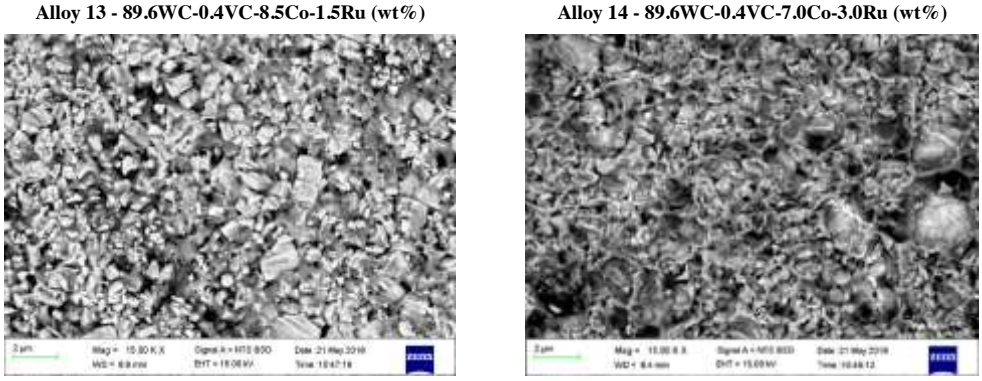

Figure 4.108. SEM-BSE images for the 89.6WC-0.4VC-(10-x)Co-xRu (wt%) alloys after exposure to 1 M NaCl, showing the effects of corrosion.

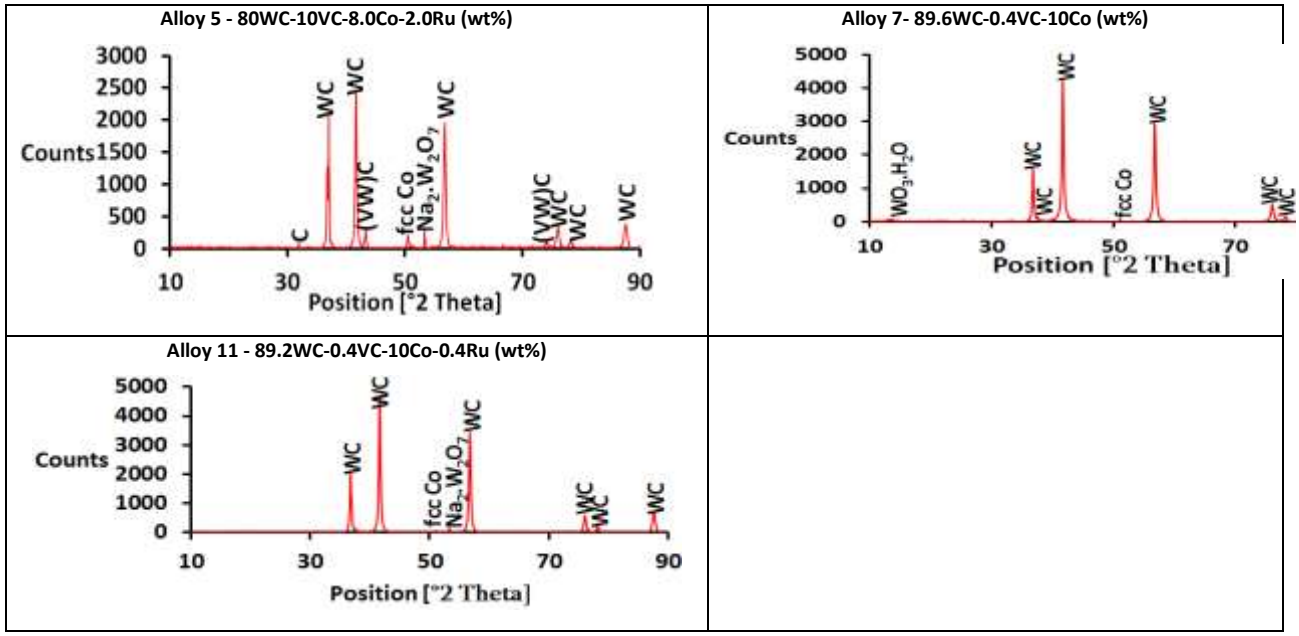

Figure 4.109. XRD patterns of alloys with corrosion products after exposure to 1 M NaCl.

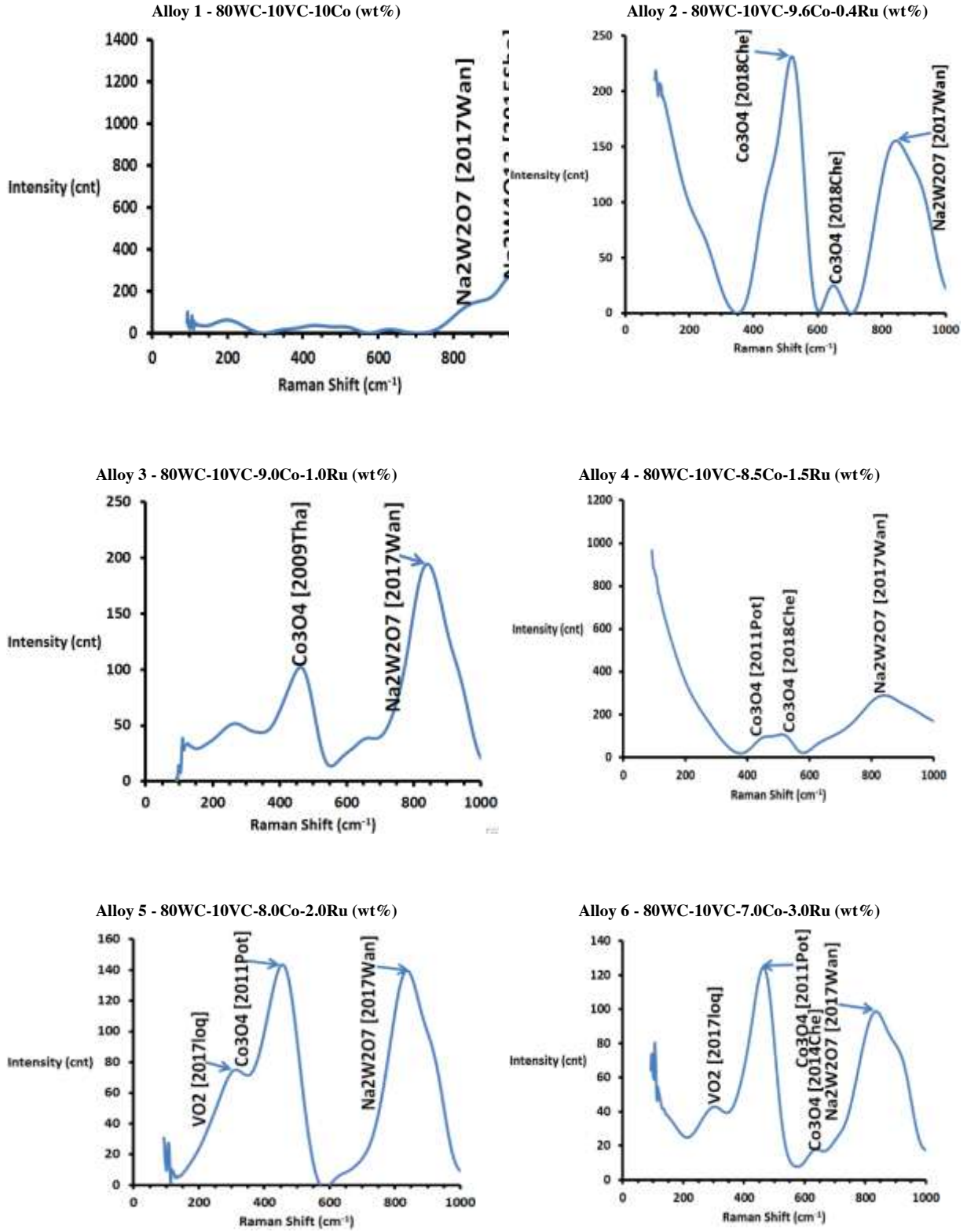

Figure 4.110. Raman peaks for the 80WC-10VC-(10-x)Co-xRu (wt%) alloys after exposure to 1 M NaCl.

Alloy 7 - 89.6WC-0.4VC-10Co (wt%) **Alloy 10 - 89.2WC-0.8VC-10Co (wt%)**

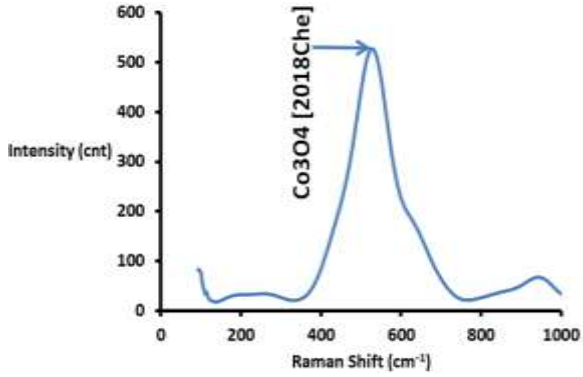

Alloy 8 - 89.2WC-0.4VC-10Co-0.4Ru (wt%)

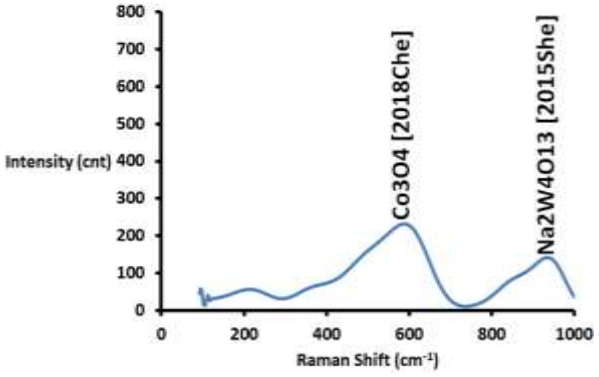

Alloy 11 - 88.8WC-0.8VC-10Co-0.4Ru (wt%)

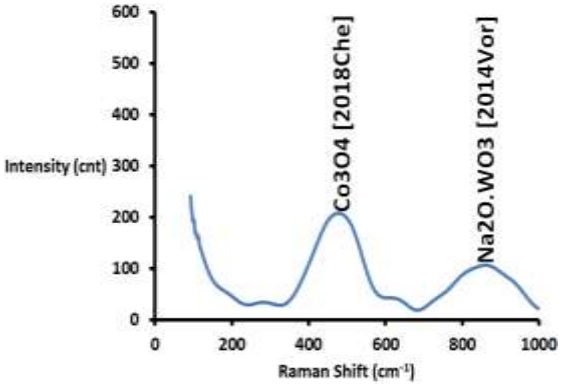

Alloy 9 - 87.6WC-0.4VC-10Co-2.0Ru (wt%)

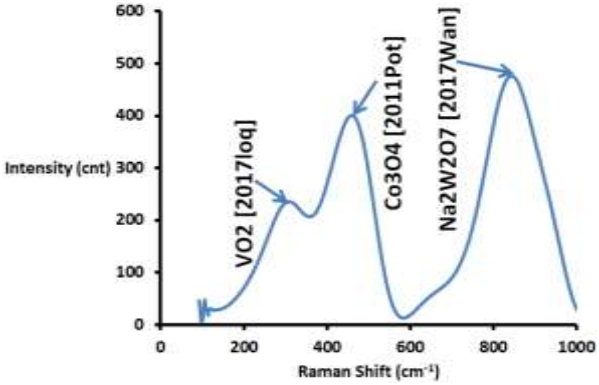

Alloy 12 - 87.2WC-0.8VC-10Co-2.0Ru (wt%)

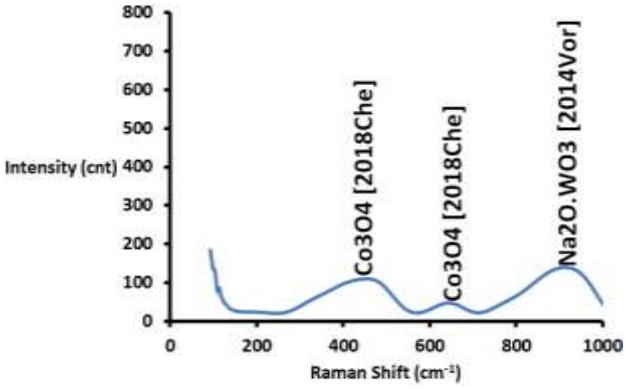

Alloy 13 - 89.6WC-0.4VC-8.5Co-1.5Ru (wt%)

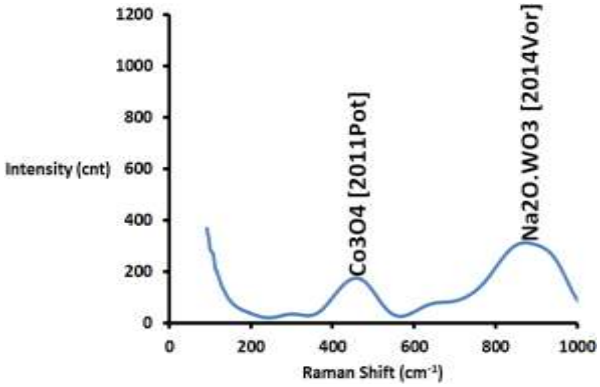

Figure 4.111. Raman peaks for the (89.6-x)WC-0.4VC-10Co-xRu, (89.2-x)WC-0.8VC-10Co-xRu and 89.6WC-0.4VC-(10-x)Co-xRu (wt%) alloys after exposure to 1 M NaCl.

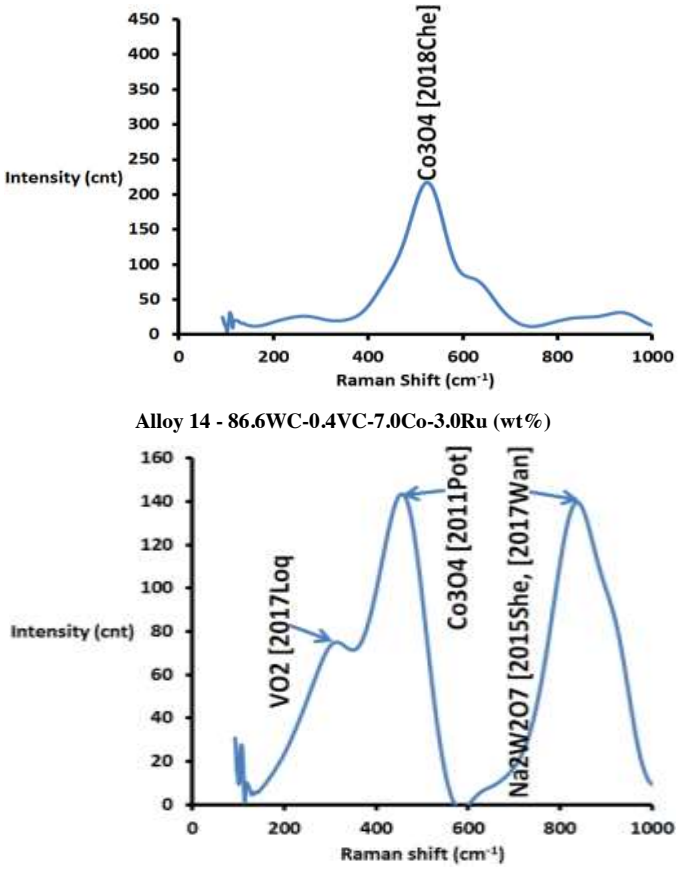

Figure 4.112. Raman peaks for the (89.6-x)WC-0.4VC-10Co-xRu, (89.2-x)WC-0.8VC-10Co-xRu and 89.6WC-0.4VC-(10-x)Co-xRu (wt%) alloys after exposure to 1 M NaCl.

Table 4.39. Phases identified from Raman and XRD analyses for the 80WC-10VC-(10-x)Co-xRu, (89.6-x)WC-0.4VC-10Co-xRu, (89.2-x)WC-0.8VC-10Co-xRu and 89.6WC-0.4VC-(10-x)Co-xRu (wt%) alloys after corrosion in 1 M NaCl.

Phase	**Alloys with corrosion phases identified by XRD**	**Alloys with corrosion phases identified by Raman**
C	1-6,8,9,12,13	-
$Na_2W_2O_7$	2,4,5	1-6,11,14
$Na_2W_4O_{13}$	-	1,10
Co_3O_4	-	2-14
VO_2	-	5,6,11,14
$Na_2O.WO_3$	-	8,9,12

4.6.5. Electrochemical Results for Corrosion in Synthetic Mine Water

4.6.5.1. Open Circuit Potential (OCP) Measurements

More noble OCPs were measured for alloys with additions of ruthenium in all alloy series (Table 4.40, Figures 4.113 to 4.115). Most alloys had slight fluctuations (<50 mV) of OCP with time (Figures 4.114 and 4.115), except for Alloys 7 and 12 which had increases of ~150mV prior to stabilising (Figure 4.115). Alloys 2, 5, 14 and 15 had slight OCP increases (~25 mV), followed by a decrease before stabilising (Figure 4.114). Alloys 1, 3, 4, 9 and 10 had general decreases in OCP before stabilising. The alloys with no ruthenium (Alloys 1, 7 and 10) had similar OCPs (Table 4.40). However, additions of up to 2 wt% Ru resulted in more significant increase in OCP for the 80WC-10VC-(10-*x*)Co-*x*Ru alloys (~78%) than in (89.6-*x*)WC-0.4VC-10Co-*x*Ru and (89.2-*x*)WC-0.8VC-10Co-*x*Ru alloy series (~30%) (Table 4.40). Additions of 3 wt% Ru resulted in ~64% increase in OCP for the 89.6WC-0.4VC-(10-*x*)Co-*x*Ru alloys (Table 4.40).

4.6.5.2. Polarisation Behaviour

Only Alloys 2, 3, 4 and 6 of the 80WC-10VC-(10-*x*)Co-*x*Ru alloys and Alloy 14 of the 89.6WC-0.4VC-(10-*x*)Co-*x*Ru alloys exhibited some mild pseudopassivation (Figures 4.116 and 4.117). The pseudopassivation range and the critical anodic current densities decreased with additions of Ru, but the primary passive potential generally increased with Ru additions. Alloys 6 and 14, with most Ru, content had the most noticeable active-passive transition. However, the pseudopassivation range for Alloy 6 was very narrow (~100 mV).

The E_{corr} generally increased with Ru additions (Table 4.40. The alloys with the highest Ru content (Alloys 6 and 14) had the highest E_{corr} values (Figure 4.118). No distinct relationship could be established between VC and E_{corr} since there were fluctuations of the relative E_{corr} values among the alloy series.

4.6.5.3. Corrosion Rates from Mass Loss Tests

There was a general decrease in corrosion rate with Ru additions in the four alloy series (Table 4.40 and Figure 4.119). For the 80WC-10VC-(10-*x*)Co-*x*Ru alloys, there was an increase in corrosion rate at 1.5 wt% Ru additions (Figure 4.119), followed by a further decrease. There was not much improvement in corrosion resistance beyond 1 wt% Ru additions to justify further Ru

additions in the 80WC-10VC-(10-*x*)Co-*x*Ru alloy series. There was also an increase of corrosion resistance with Ru content after 1.5 wt% Ru addition in the 89.6WC-0.4VC-(10-*x*)Co-*x*Ru alloy series (Figure 4.119).

Up to 2 wt% Ru additions improved corrosion resistance by ~39%, ~25% and ~30% for 80WC-10VC-(10-*x*)Co-*x*Ru, (89.6-*x*)WC-0.4VC-10Co-*x*Ru and (89.2-*x*)WC-0.8VC-10Co-*x*Ru alloy series, respectively. For the 89.6WC-0.4VC-(10-*x*)Co-*x*Ru alloys corrosion resistance improved by only ~3%.

For the alloys without Ru (Alloys 1, 7 and 10), there was no correlation between corrosion rate and VC content (Figure 4.119). The (89.2-*x*)WC-0.8VC-10Co-*x*Ru alloys had consistently higher corrosion rates than the (89.6-*x*)WC-0.4VC-10Co-*x*Ru alloys (Figure 4.119). However, the effect of VC on the corrosion rate was not conclusive since the 10 wt% VC alloys had lower corrosion rates than the 89.6WC-0.4VC-(10-*x*)Co-*x*Ru alloys (Figure 4.119). Therefore, there might be an effective limit to VC additions.

4.6.6. Surface Analysis after Corrosion in Synthetic Mine Water

The current-time at constant potential (potentiostatic) results (Figure 4.120) showed a decrease of current with time for all alloys, due to the formation of passive films. However, some alloys had relatively higher currents, indicating thinner corrosion films. The alloys with the corrosion films were studied to deduce the contents of the films (Figures 4.121 to 4.124). The WC grains from the original uncorroded alloys (Section 4.3) were still visible after corrosion of some alloys, for examples for Alloys 2 to 6 (Figure 4.121).

Table 4.40. Electrochemical parameters for the 80WC-10VC-(10-x)Co-xRu, (89.6-x)WC-0.4VC-10Co-xRu, (89.2-x)WC-0.8VC-10Co-xRu and 89.6WC-0.4VC-(10-x)Co-xRu (wt%) alloys for polarisation in synthetic mine water (corrosion rates determined from immersion tests).

Series	**Alloy No.**	**OCP (mV)**	**E_{corr} (mV)**	**i_c ($mA.cm^{-2}$)**	**b_a (mV)**	**b_c (mV)**	**i_{corr} ($mA.cm^{-2}$)**	**Corrosion Rate ($x10^{-3}$ $mm.y^{-1}$)**	**Change in corrosion (%)**
80WC-10VC-(10-*x*)Co-*x*Ru	1	-311.01	-275.72	-	0.072	0.599	0.007	2.516±0.017	-
	2	-265.86	-244.14	6.5	0.050	0.373	0.004	1.770±0.005	-29
	3	-243.62	-221.56	7.4	0.101	0.296	0.004	1.628±0.021	-35
	4	-202.31	-267.69	9.5	0.071	0.261	0.005	2.049±0.040	-19
	5	-188.68	-117.53	7.8	0.063	0.241	0.003	1.523±0.014	-39
	6	-99.22	-106.31	0.5	0.042	0.200	0.002	1.507±0.012	-40
(89.6-*x*)WC-0.4VC-10Co-*x*Ru	7	-381.40	-275.63	-	0.072	0.599	0.006	2.273±0.033	-
	8	-304.96	-244.11	-	0.101	0.309	0.005	2.068±0.053	-9
	9	-198.57	-221.70	-	0.050	0.216	0.003	1.588±0.042	-30
(89.2-*x*)WC-0.8VC-10Co-*x*Ru	10	-371.07	-267.86	-	0.087	0.284	0.012	2.691±0.012	-
	11	-333.36	-301.56	-	0.038	0.203	0.007	2.639±0.194	-2
	12	-207.65	-168.31	-	0.069	0.201	0.005	2.014±0.098	-25
89.6WC-0.4VC-(10-*x*)Co-*x*Ru (*Includes Alloy 7*)	13	-244.57	-238.22	13.2	0.055	0.252	0.012	2.670±0.034	17
	14	-136.89	-142.27	0.2	0.080	0.168	0.006	2.214±0.013	-3

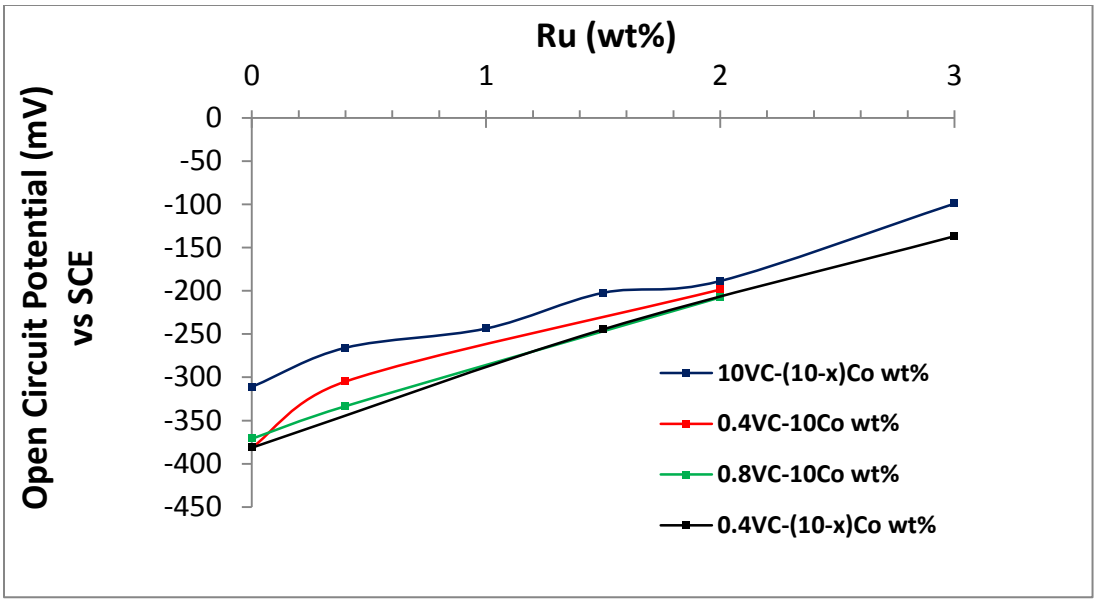

Figure 4.113. Variation of open circuit potentials with composition for 80WC-10VC-(10-x)Co-xRu, (89.6-x)WC-0.4VC-10Co-xRu, (89.2-x)WC-0.8VC-10Co-xRu and 89.6WC-0.4VC-(10-x)Co-xRu (wt%) alloys in synthetic mine water.

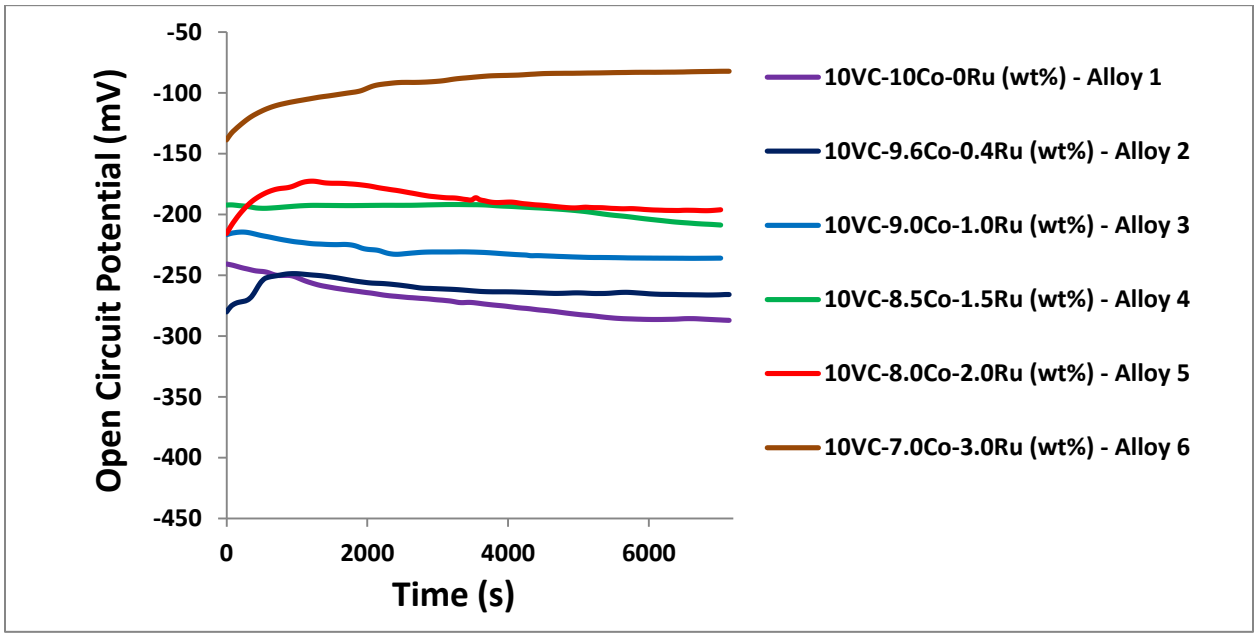

Figure 4.114. Open circuit potentials for 80WC-10VC-(10-x)Co-xRu (wt%) alloys in synthetic mine water.

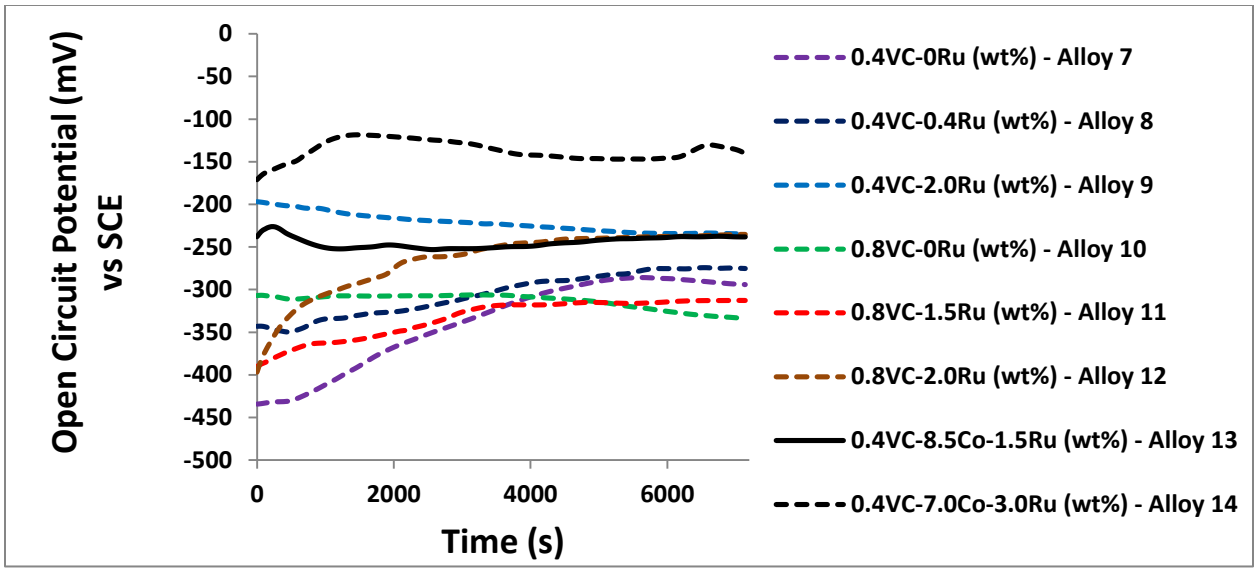

Figure 4.115. Polarisation curves for (89.6-x)WC-0.4VC-10Co-xRu, (89.2-x)WC-0.8VC-10Co-xRu and 89.6WC-0.4VC-(10-x)Co-xRu (wt%) alloys in synthetic mine water.

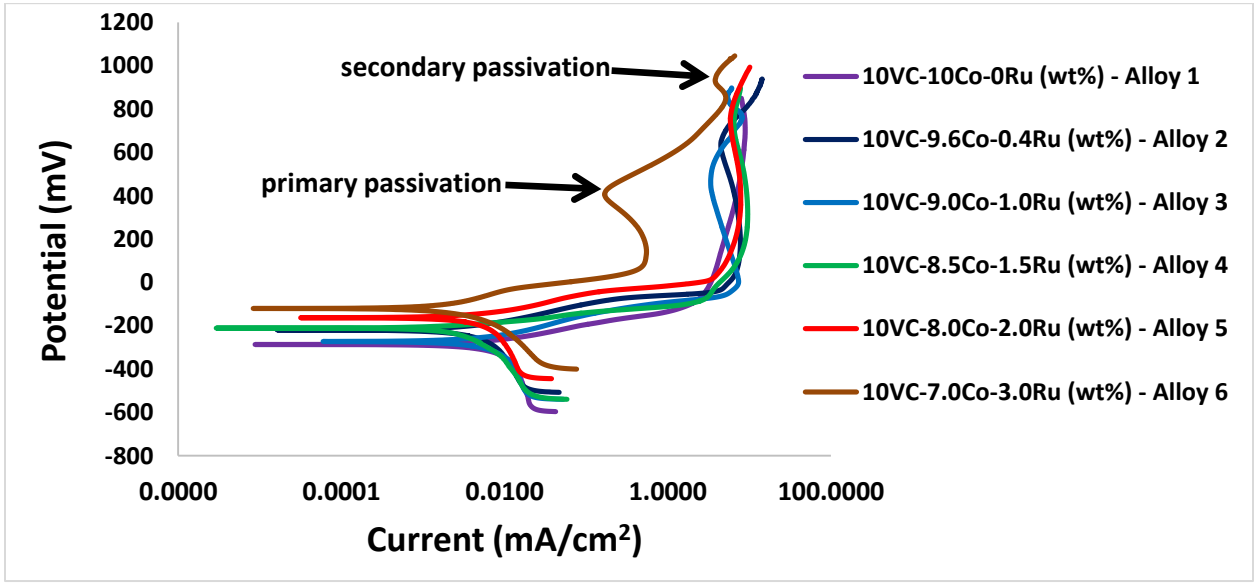

Figure 4.116. Polarisation curves for 80WC-10VC-(10-x)Co-xRu (wt%) alloys in synthetic mine water.

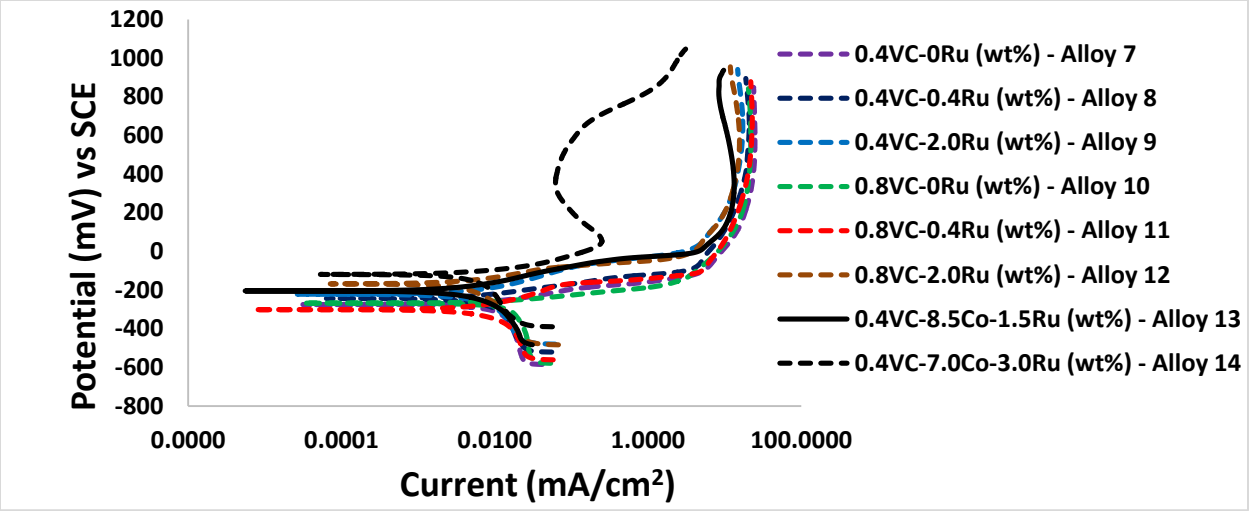

Figure 4.117. Polarisation curves for (89.6-x)WC-0.4VC-10Co-xRu, (89.2-x)WC-0.8VC-10Co-xRu and 89.6WC-0.4VC-(10-x)Co-xRu (wt%) alloys in synthetic mine water.

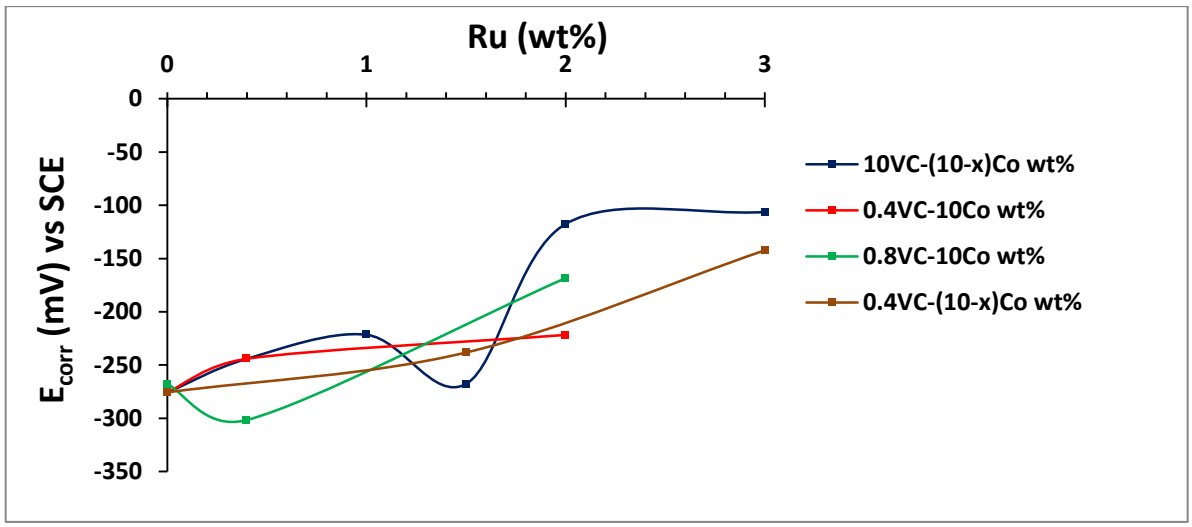

Figure 4.118. Ecorr values for 80WC-10VC-(10-x)Co-xRu, (89.6-x)WC-0.4VC-10Co-xRu, (89.2-x)WC-0.8VC-10Co-xRu and 89.6WC-0.4VC-(10-x)Co-xRu (wt%) alloys in synthetic mine water.

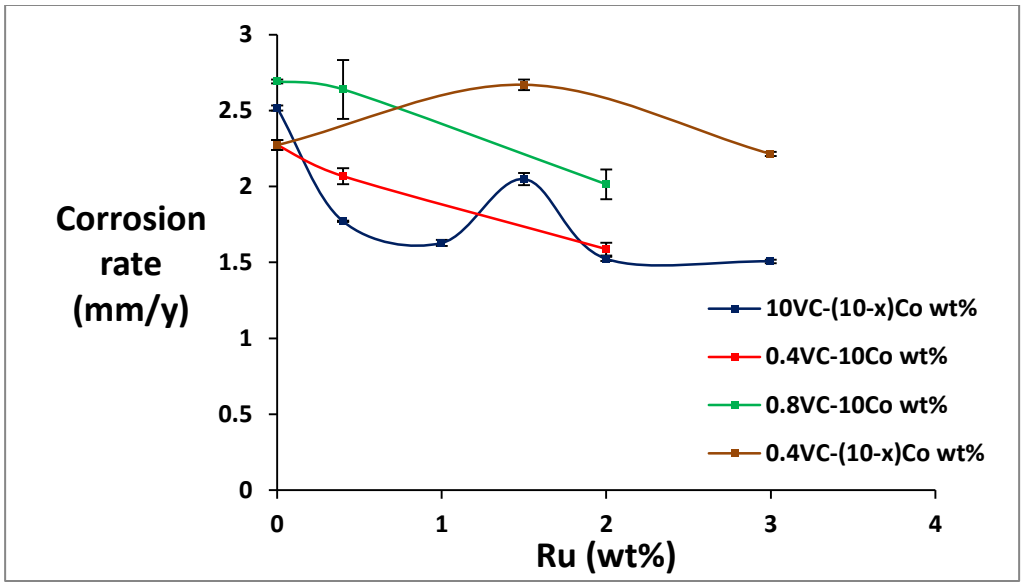

Figure 4.119. Corrosion rates for the 80WC-10VC-(10-x)Co-xRu, (89.6-x)WC-0.4VC-10Co-xRu, (89.2-x)WC-0.8VC-10Co-xRu and 89.6WC-0.4VC-(10-x)Co-xRu (wt%) alloys in synthetic mine water.

Cracking of the surfaces upon drying in air was seen in the low magnification image of 87.2WC-0.8VC-10Co-2.0Ru (wt%), Alloy 12 (Figure 4.124). Alloy 14, 89.6WC-0.4VC-7.0Co-3.0Ru (wt%), also had some dark areas within a light matrix at low magnification (Figure 4.124). The large plate-like areas in Alloy 13, 89.6WC-0.4VC-8.5Co-1.5Ru (wt%), were deduced by EDS (Appendix E, Table E6), to be from oxidation, since there was a high oxygen content of ~23 (wt%). Only Alloys 1, 80WC-10VC-10Co and 4, 80WC-10VC-8.5Co-1.5Ru (wt%) had corrosion products identified by XRD studies (Figure 4.125). However, Raman studies revealed corrosion products on all alloys (Figures 4.126 to 4.128). Table 4.41 shows all the corrosion products deduced from XRD and Raman studies.

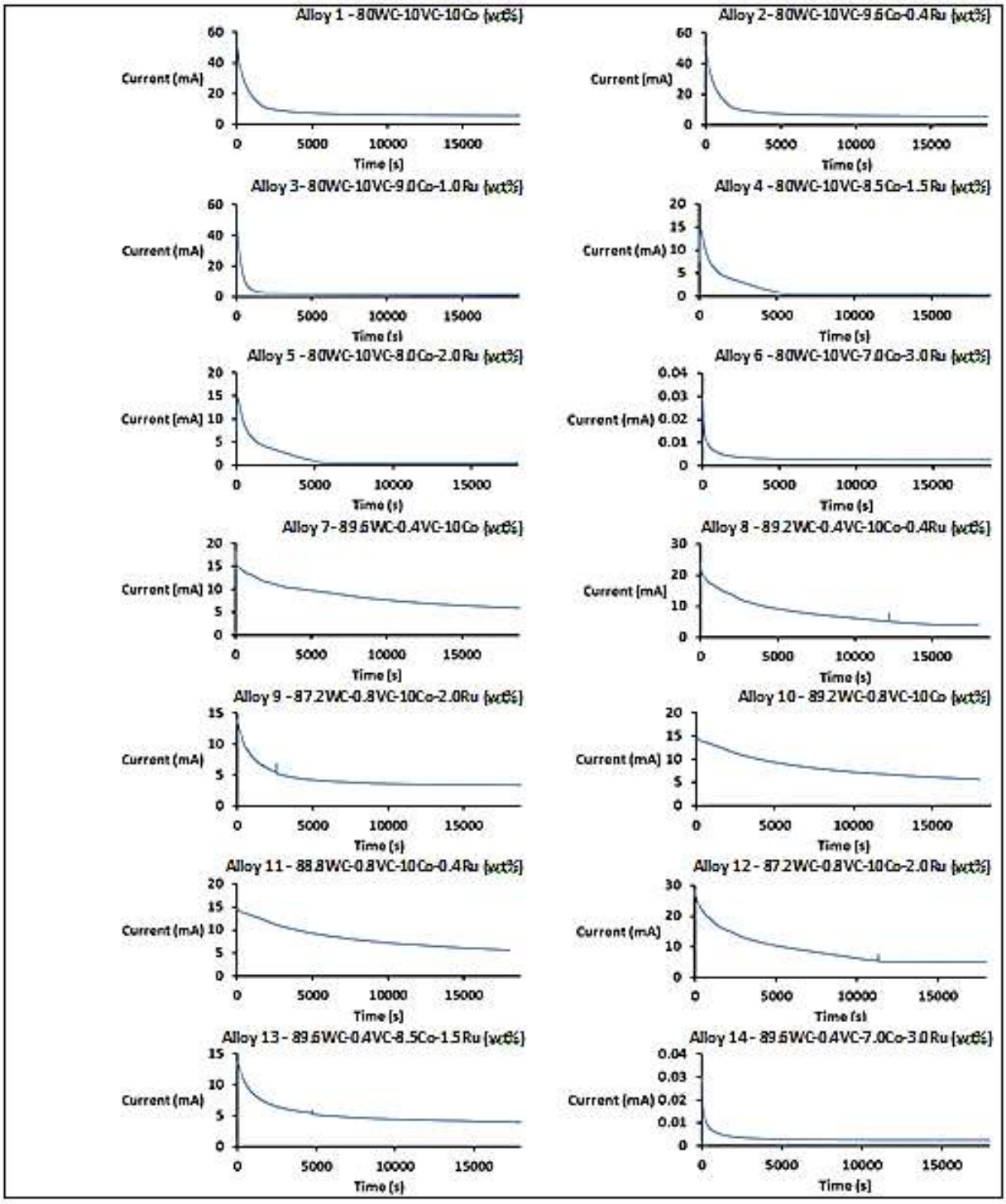

Figure 4.120. Potentiostatic measurements for 80WC-10VC-(10-x)Co-xRu, (89.6-x)WC-0.4VC-10Co-xRu, (89.2-x)WC-0.8VC-10Co-xRu and 89.6WC-0.4VC-(10-x)Co-xRu (wt%) alloys in synthetic mine water.

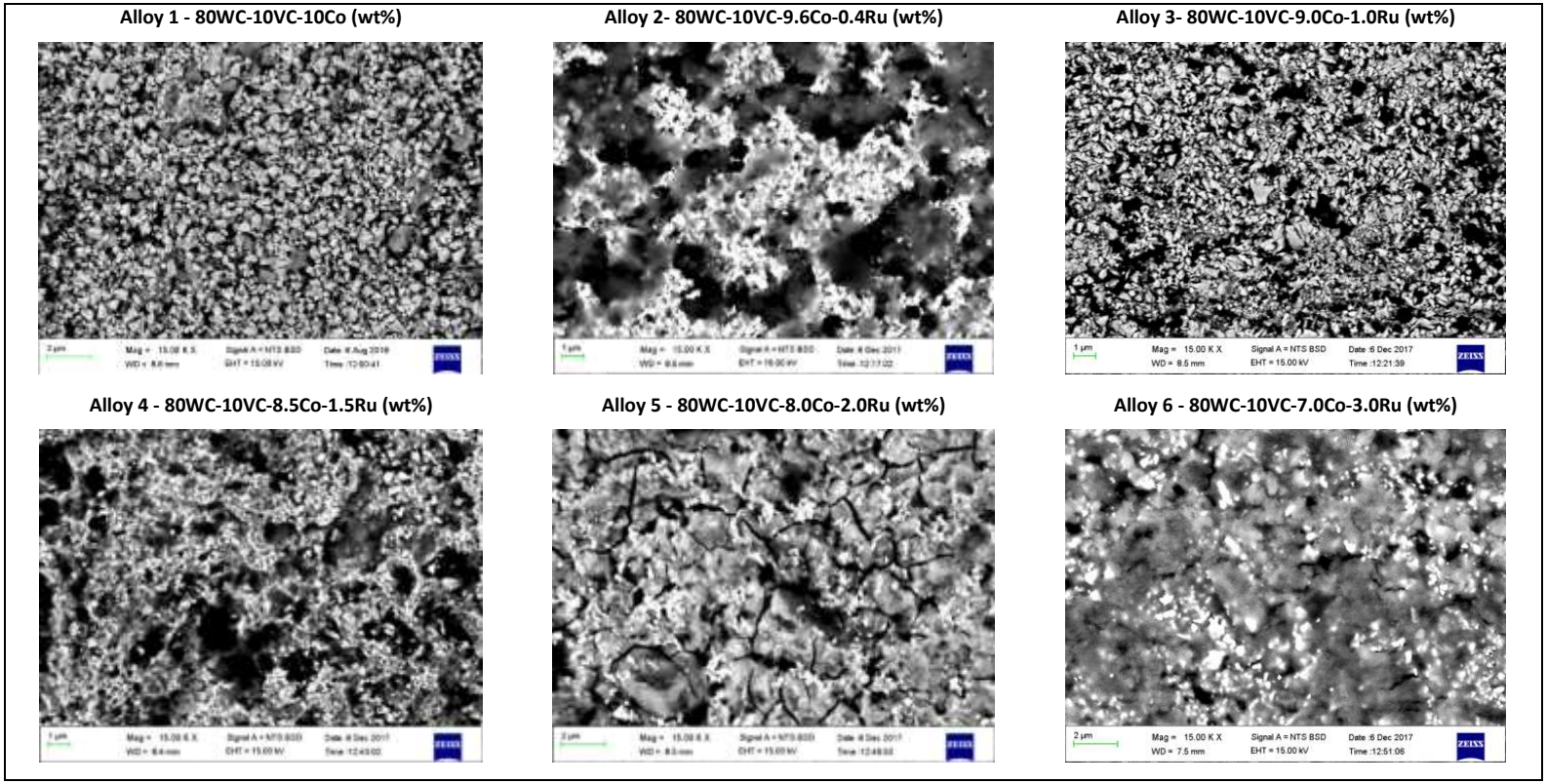

Figure 4.121. SEM-BSE images for the 80WC-10VC-(10-x)Co-xRu (wt%) alloys after exposure to synthetic mine water, showing the effects of corrosion.

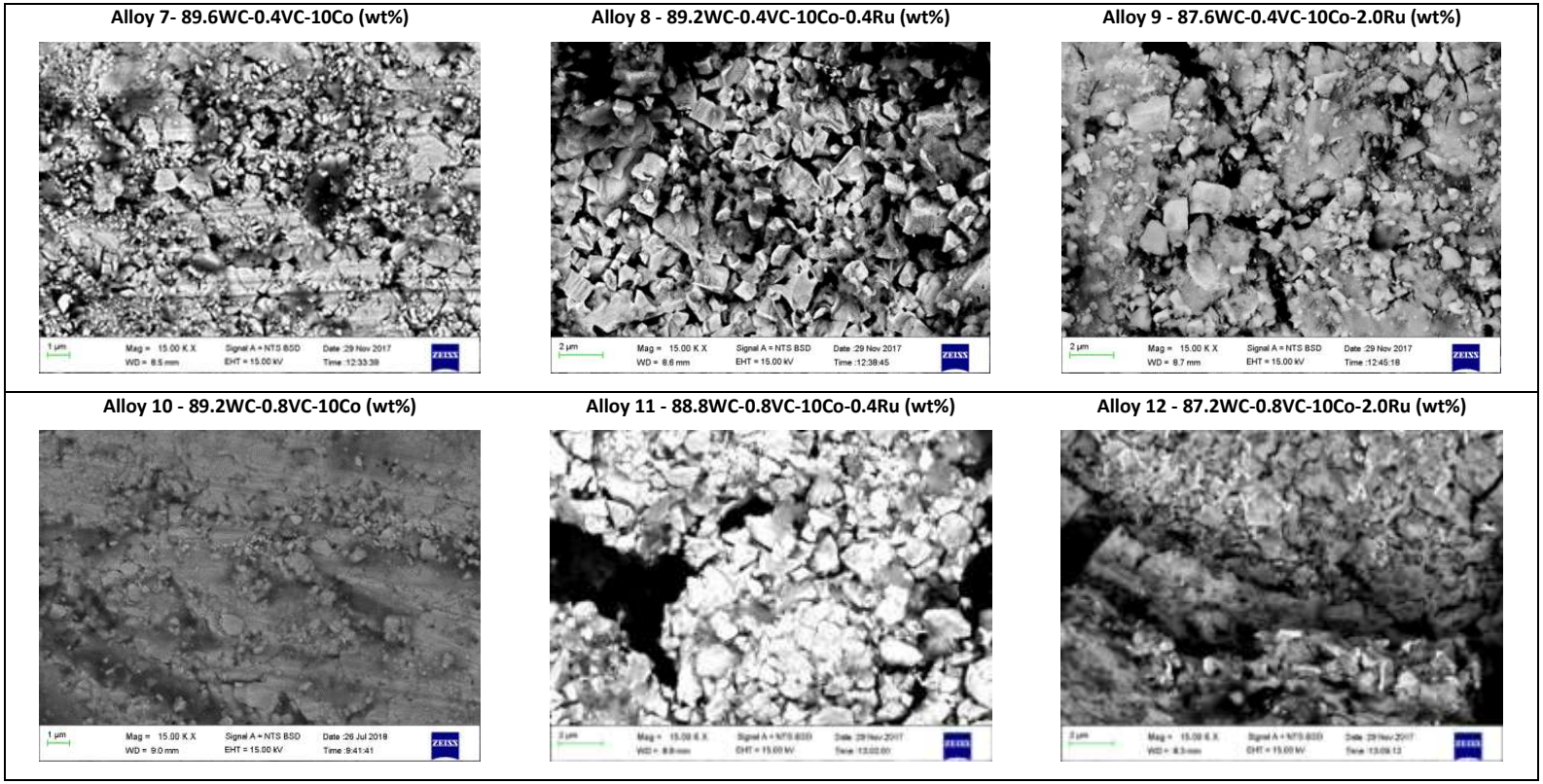

Figure 4.122. SEM-BSE images for the (89.6-x)WC-0.4VC-10Co-xRu and (89.2-x)WC-0.8VC-10Co-xRu (wt%) alloys after exposure to synthetic mine water, showing the effects of corrosion.

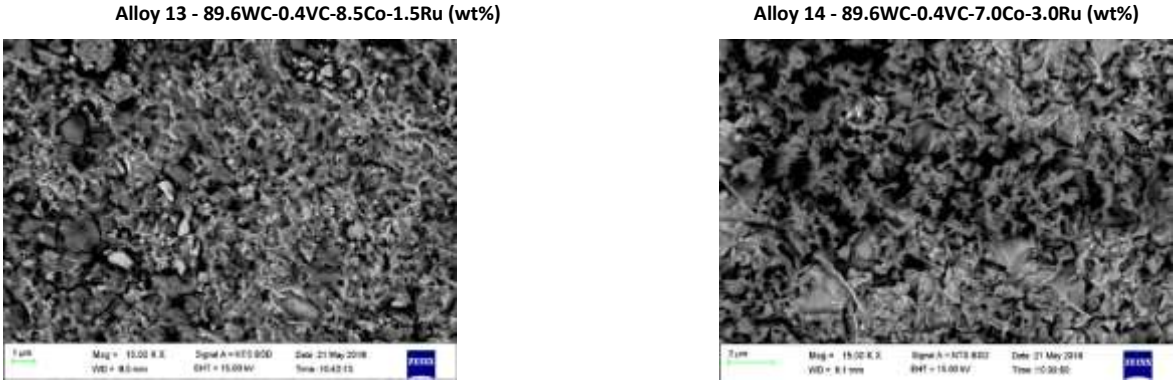

Figure 4.123. SEM-BSE images for the 89.6WC-0.4VC-(10-x)Co-xRu (wt%) alloys after exposure to synthetic mine water, showing the effects of corrosion.

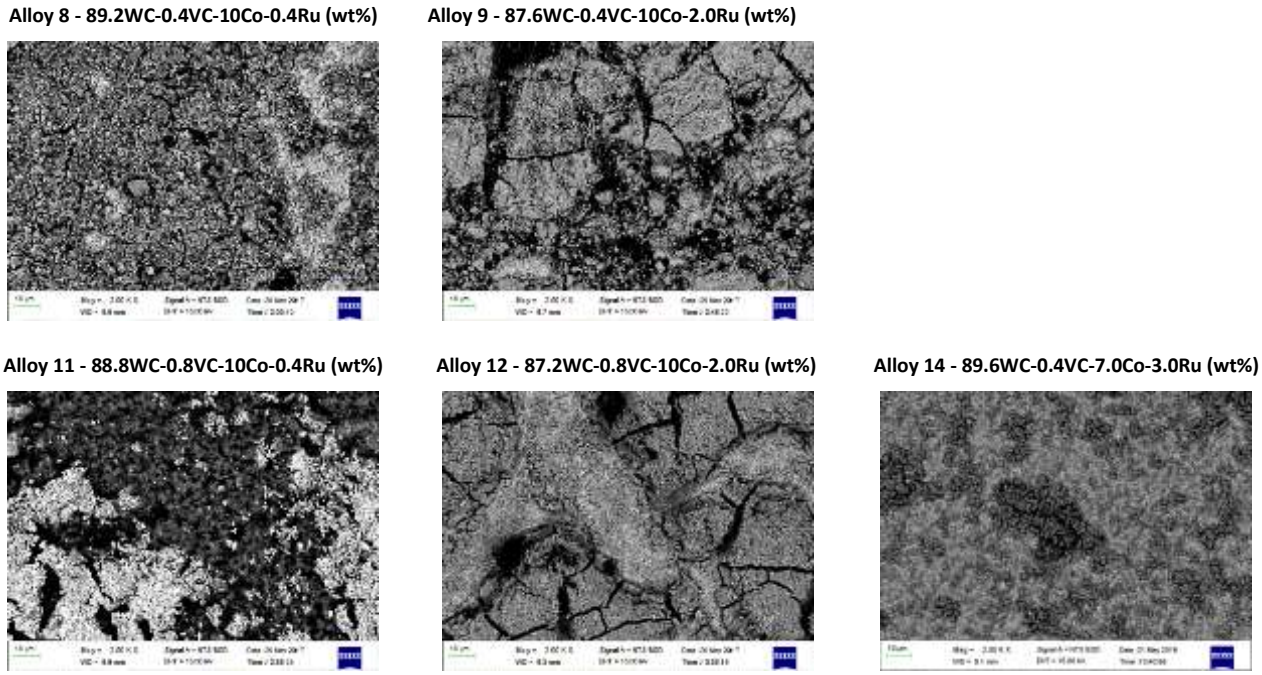

Figure 4.124. Low-magnification SEM-BSE images for the 80WC-10VC-(10-x)Co-xRu, (89.6-x)WC-0.4VC-10Co-xRu, (89.2-x)WC-0.8VC-10Co-xRu and 89.6WC-0.4VC-(10-x)Co-xRu (wt%) alloys after exposure to synthetic mine water, showing the effects of corrosion.

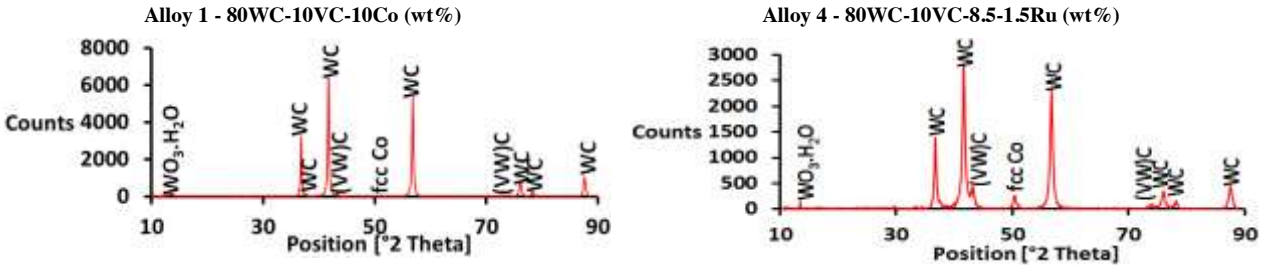

Figure 4.125. XRD patterns of alloys with corrosion products after exposure to synthetic mine water.

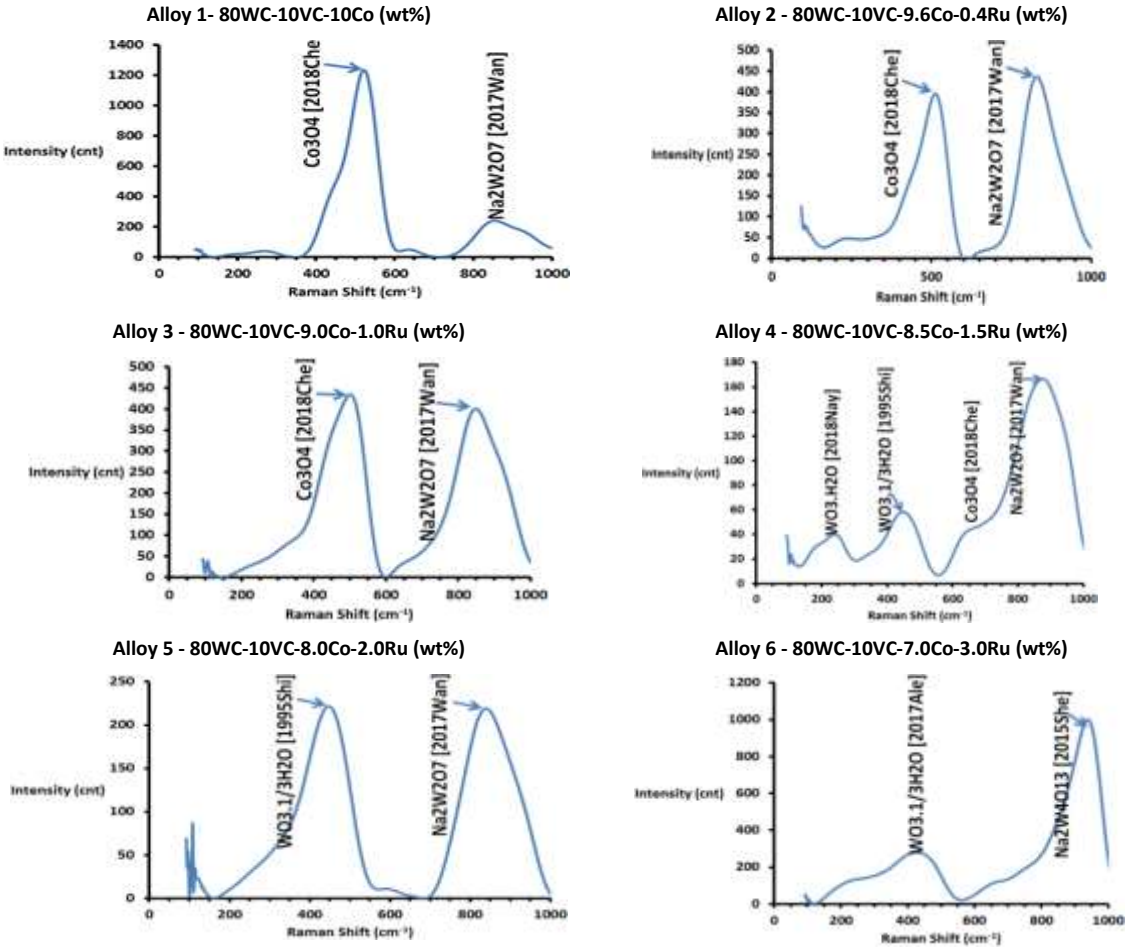

Figure 4.126. Raman peaks for the 80WC-10VC-(10-x)Co-xRu (wt%) alloys after exposure to synthetic mine water.

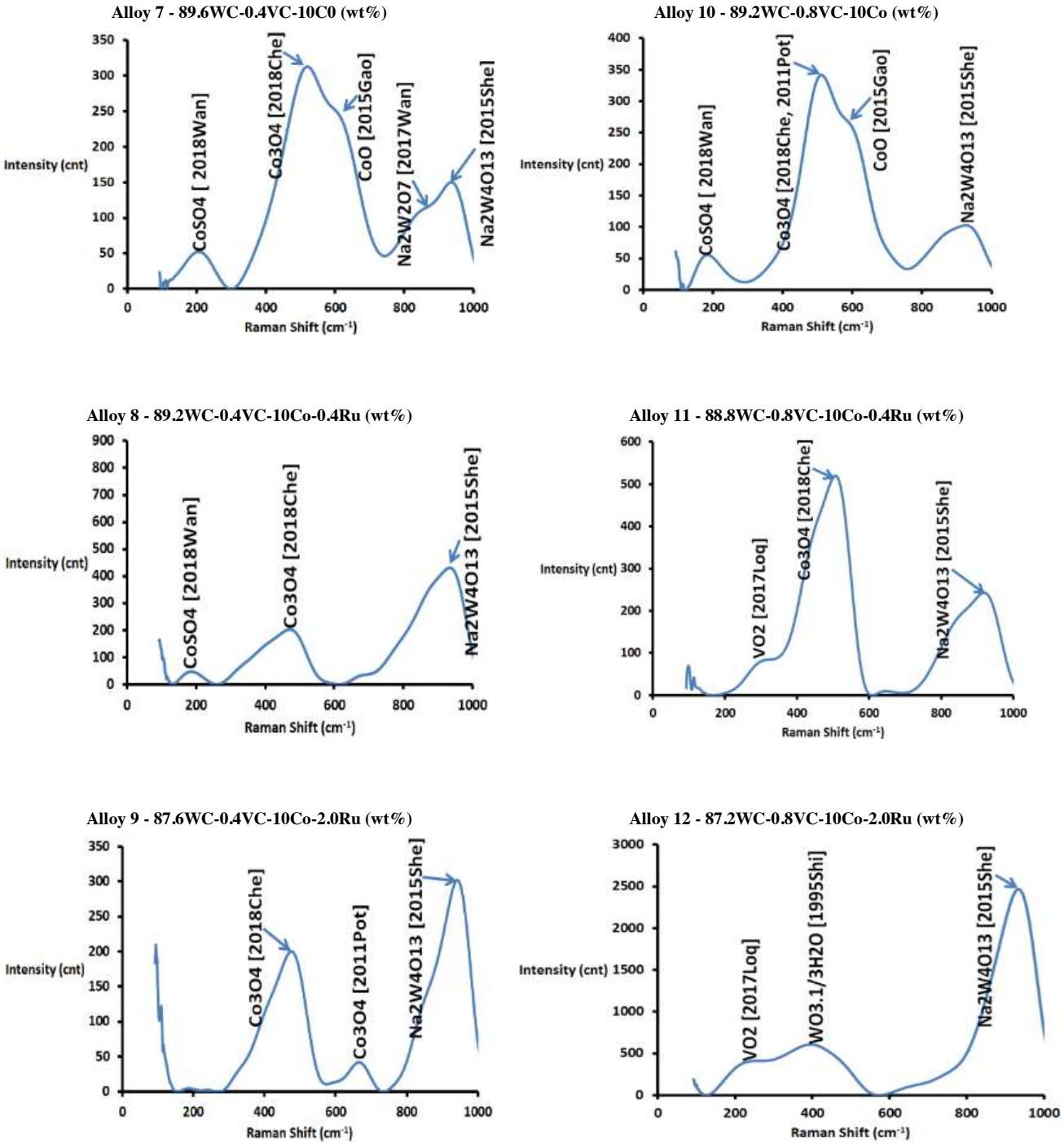

Figure 4. 127. Raman peaks for the (89.6-x)WC-0.4VC-10Co-xRu, (89.2-x)WC-0.8VC-10Co-xRu and 89.6WC-0.4VC-(10-x)Co-xRu (wt%) alloys after exposure to synthetic mine water.

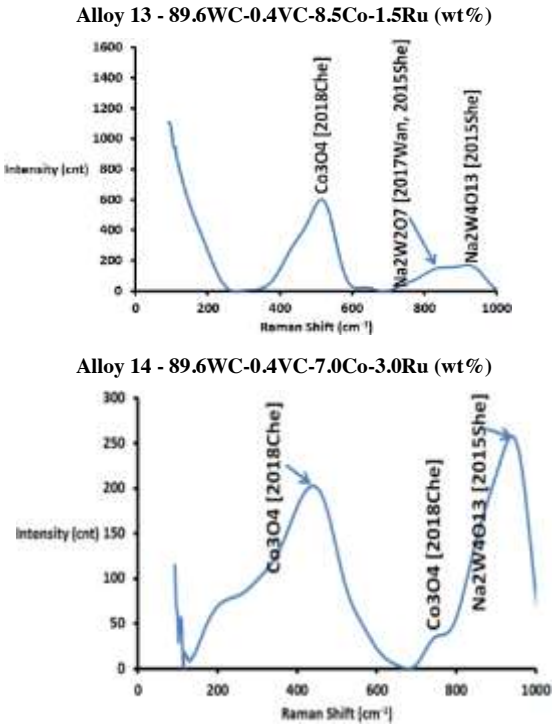

Figure 4.128. Raman peaks for the (89.6-x)WC-0.4VC-10Co-xRu, (89.2-x)WC-0.8VC-10Co-xRu and 89.6WC-0.4VC-(10-x)Co-xRu (wt%) alloys after exposure to synthetic mine water.

Table 4.41. Phases identified from Raman and XRD analyses for the 80WC-10VC-(10-x)Co-xRu, (89.6-x)WC-0.4VC-10Co-xRu, (89.2-x)WC-0.8VC-10Co-xRu and 89.6WC-0.4VC-(10-x)Co-xRu (wt%) alloys after corrosion in synthetic mine water.

Phase	**Alloys with corrosion phases identified by XRD**	**Alloys with corrosion phases identified by Raman**
$WO_3.H_2O$	1,4	4
Co_3O_4	4	1-4, 7-10, 11, 13, 14
C	1,13	-
$Na_2W_2O_7$	-	1-5, 7, 13
CoO	-	7, 10
C	4	-
VO_2	-	11-12
$CoSO_4$	-	7, 8, 10
$WO_3.1/3H_2O$	-	4-6, 12

5. DISCUSSION

5.1. Alloy Production and Quality Tests

High milling time required in the small mill could have increased the contamination, thus the decision was made to use a 1 kg mill with WC lining. Although the powders were less than optimum quantity, a high ball:powder ratio (30:1) was used to compensate for the low powder quantity. So overall, the mill had sufficient material, which stopped the falling/tumbling mechanism of the mill balls on the particles from becoming the less efficient sliding mechanism. Contamination with WC from the mill liners affects the WC proportion, but it would not be as deleterious as elements different from those in the alloys. The Microtrac S3500® operates at a higher wavelength and measurement range than the Saturn DigiSizer®, thus the differences in particle size analysis results (Table 4.1). Coercivity measurements were used to measure effectiveness of the milling process (Table 4.7) because it is expected that alloys from properly mixed powders would have similar coercivities [1998Upa]. Thus, higher errors for coercivities from powders from the 1 kg mill than those from the 100 g mill (Table 4.7) was due to lower mixing efficiencies.

All alloy densities were close to expected as shown by densification values greater than 99.0% (Table 4.8). It was not clear from Figure 4.31 whether Ru affected the densification process since the additions resulted in decreased densification for 80WC-10VC-(10-*x*)Co-*x*Ru alloys, but an opposite trend was seen for the 89.6WC-0.4VC-(10-*x*)Co-*x*Ru alloys. For the (89.6-*x*)WC-0.4VC-10Co-*x*Ru and (89.2-*x*)WC-0.8VC-10Co-*x*Ru alloys, no opposite trend was seen between densification and Ru content. The contradiction between both the densification results (Table 4.8) and the measured porosity results (Table 4.9), with the comparative porosity results for some alloys (Table 4.9) might have been due to the presence of VC. The dark spots and areas seen in all images (Figures 4.32 to 4.45) were also attributed to the presence of VC since they did not convincingly resemble any phase from the comparative charts. However, there were some images (Figures 4.32b, 4.33a, 4.33b, 4.34b, 4.35b, 4.36b and 4.37a) that had clustered spots,

which were local inhomogeneities, resembling the eta phase (Figure A4, Appendix A). But the dark eta phase only appears after etching [1998Upa], not before etching (Figures 4.33a and 4.37a). Therefore, no eta phase was present. The standard porosity chart results were created from straight WC-Co grades [1978ISO]. Thus, standard porosity charts did not seem reliable for the type of alloys used in this study. Also, since the (89.6-*x*)WC-0.4VC-10Co-*x*Ru, (89.2-*x*)WC-0.8VC-10Co-*x*Ru and 89.6WC-0.4VC-(10-*x*)Co-*x*Ru alloy series did not have any B-type porosity, the high VC content of the 80WC-10VC-(10-*x*)Co-*x*Ru (wt%) might have resulted in spots that appeared as B-type porosity at low magnifications. From SEM and XRD studies (Section 4.3), it was deduced that the (V,W)C phase was present in the 80WC-10VC-(10-*x*)Co-*x*Ru alloy series, but not in the (89.6-*x*)WC-0.4VC-10Co-*x*Ru and (89.2-*x*)WC-0.8VC-10Co-*x*Ru alloy series, and that difference might have resulted in the apparent 'B-type' porosity for the 80WC-10VC-(10-*x*)Co-*x*Ru alloy series. Alloys with 10 wt% VC content appeared to have lower densifications (Figure 4.31). The addition of VC was found to reduce the driving force for the transformation from equiaxed to faceted shapes, thus decreasing the likelihood of WC contacts [2005Fan], which in turn, resulted in lower densification. However, all fourteen alloys had greater than 98.5% densification, an indication of good sinterability. Thus, the addition of Ru to WC-VC-Co alloys did not compromise alloys' sinterability.

The decrease in magnetic saturation was due to the dissolution of Ru in (Co) (the Co solid solution), decreasing the amount of the pure Co phase, similar to W dissolving in Co [1998Upa]. The formation of the eta-phase in carbon-deficient hardmetals also leads to a decrease in the magnetic saturation [1973Til]. However, the microstructures did not exhibit any eta-phase. No free C was deduced after comparing optical micrographs with industrial porosity charts in accordance to the ISO standard for porosity/free C determination (ISO 4505) [1978ISO]. Also, no C peaks were identified from XRD. Another factor which decreases magnetic saturation is increased W in the binder solution [1973Til]. The 80WC-10VC-(10-*x*)Co-*x*Ru and 89.6WC-0.4VC-(10-*x*)Co-*x*Ru (wt%) alloys had the same W content, therefore any changes in the magnetic saturation were not due to variations in W content. The magnetic saturation values (Figure 4.46) showed that there was little solubility of W in (Co) for the alloys without Ru,

because the magnetic saturations were close to 20.2 μTm^3/kg (corresponding to 10 wt% Co [1996Roe]). Since Ru forms a solid solution with Co [1993Pre], replacing less dense Co with denser Ru could have reduced the overall binder volume fraction, and thus the total solubility of W in 80WC-10VC-(10-*x*)Co-*x*Ru and 89.6WC-0.4VC-(10-*x*)Co-*x*Ru (wt%) alloys. Furthermore, (W,V)C in 80WC-10VC-(10-*x*)Co-*x*Ru (wt%) might have precipitated from the binder phase as V exceeded its solubility limit in the binder at ~1 wt% VC [2007Has], having combined with some W, and this might have also contributed to a decreased W in the binder. Decreasing solubility of W would result in increased magnetic saturation, not the decrease observed for the 80WC-10VC-(10-*x*)Co-*x*Ru (wt%) alloys in Figure 4.46. Thus, the decrease in magnetic saturation for the 80WC-10VC-(10-*x*)Co-*x*Ru and 89.6WC-0.4VC-(10-*x*)Co-*x*Ru (wt%) alloys was due to the presence of Ru in the (Co) solid solution. However, for the (89.6-*x*)WC-0.4VC-10Co-*x*Ru and (89.2-*x*)WC-0.8VC-10Co-*x*Ru (wt%) alloys, the binder volume fraction increased with Ru additions, and the solubility of W might have increased, contributing to the decrease in magnetic saturation. The binder regions were too small (<2 μm across) for accurate SEM analyses. The larger decreases in the magnetic saturation with Ru additions for the 80WC-10VC-(10-*x*)Co-*x*Ru and 89.6WC-0.4VC-(10-*x*)Co-*x*Ru series than for the (89.6-*x*)WC-0.4VC-10Co-*x*Ru and (89.2-*x*)WC-0.8VC-10Co-*x*Ru (wt%) alloys was therefore due to Ru replacing Co instead of WC. The presence of V had no effect on the magnetic saturation [2007Sch]. From EDS analyses, most Ru was in the binder phase with very little in the (V,W)C phase, and so the Ru additions decreased magnetic saturation in all series, similar to the observations of Shing [2001Shi]. For the same Ru additions, the 89.6WC-0.4VC-(10-*x*)Co-*x*Ru alloys had lower magnetic saturations than the 80WC-10VC-(10-*x*)Co-*x*Ru alloys (Figure 4.46) due to the 89.6WC-0.4VC-(10-*x*)Co-*x*Ru alloys having more W that also dissolved in Co, decreasing the magnetic saturation [1973Til]. The same characteristic was seen for the (89.6-*x*)WC-0.4VC-10Co-*x*Ru alloys that had slightly lower magnetic saturations than the (89.2-*x*)WC-0.8VC-10Co-*x*Ru alloys (Figure 4.46.).

Tillwick and Joffe [1973Til] reported that the presence of non-magnetic precipitates in hardmetals increased the relative magnetic saturation, but decreased measured magnetic

saturation. They attributed their findings to Co precipitates contributing to the bulk magnetic saturation. Thus, the relative effect of Ru additions on the relative magnetic saturation was calculated to verify the presence of Co precipitates (Figure 5.1), and the relative magnetic saturations followed the same trend as that for the measured magnetic saturations for all alloy series (Figure 4.46). Thus, there were no Co precipitates formed in the binder solution. Cobalt would precipitate from the binder phase as Co_3W or Co_3W_3C (η phase) [1973Til], and none of these phases was identified from XRD studies (Section 4.3). Also, η was not seen in any of the alloy micrographs (Figures 4.32 to 4.45).

The general decrease in coercivity for the 80WC-10VC-(10-*x*)Co- *x*Ru and (89.2-*x*)WC-0.8VC-10Co-*x*Ru alloy series might have resulted from the decrease in the effect of the Bloch wall shift due to the (Co) solid solution with Ru [1998Upa, 1956Ker]. Bloch walls are the magnetic domain walls which are pinned by the Co/WC boundaries, so increased Co/WC boundaries would increase the magnetic pinning, increasing the coercivity [1995Roe]. Thus, the energy created by the magnetic field increased with the Co/WC boundaries. Decreases in either grain size or binder volume fraction increase the Co/WC interphase area, resulting in greater pinning of magnetic domain walls, thus increased coercivity [1995Roe]. This implies that since Ru additions resulted in decreased binder volume fraction for the 80WC-10VC-(10-*x*)Co-*x*Ru and 89.6WC-0.4VC-(10-*x*)Co-*x*Ru alloys, the coercivity was expected to increase with Ru content. The counter-intuitive decreases in coercivity with increased Ru additions were due to the corresponding increase of the Co solid solution with Ru. It seemed the Co solid solution with dissolved Ru had the same effect as Co alone: the increased solid solution proportions decreased coercivity. Since the binder volume decreased with Ru additions, but coercivity decreased, this meant that the Co solid solution with Ru had more decreased coercivity than the same volume of Co. The initial increase in coercivity up to 0.4 wt% Ru for the 80WC-10VC-(10-*x*)Co-*x*Ru and up to 1.5 wt% for the 89.6WC-0.4VC-(10-*x*)Co-*x*Ru alloys (Figure 4.47) might have been due to the combination of decreased WC grain size and binder volume reduction. The formation of the (V,W)C phase as a result of V exceeding its solubility in the binder phase for the 80WC-10VC-

(10-*x*)Co-*x*Ru alloys might have increased the pinning effect, and contributed to the relatively high values for the alloy series.

The relationship between coercivity and magnetic saturation for the 80WC-10VC-(10-*x*)Co-*x*Ru and 89.6WC-0.4VC-(10-*x*)Co-*x*Ru alloys (Figure 4.48) followed the same trend as for coercivity with Ru content (Figure 4.47). For (89.6-*x*)WC-0.4VC-10Co-*x*Ru alloys, there was a direct relationship between coercivity and magnetic saturation (Figure 4.47), whereas an inverse relationship was observed for the (89.2-*x*)WC-0.8VC-10Co-*x*Ru alloys (Figure 4.48).

Coercivity, H_c would be expected to increase with magnetic saturation according to the following relationship [1944Ker]:

$$H_c = 4 - \frac{\frac{3}{2}\lambda_s.\sigma_i + b.K}{I_S}.\frac{\delta}{S}.3\sqrt{\alpha} \qquad \text{Equation 5.1}$$

where:

λ_s = magnetostrictive saturation

σ_i = internal stress in immediate vicinity of walls

b = numerical factor, 1 (for sphere and cube)

K = crystal energy

δ = width of Bloch wall

S = distance of foreign bodies

α = volume fraction of foreign bodies

I_s = magnetic saturation.

The numerical factor, b in Equation 5.1 shows that coercivity of a material is depended on the shape. All the alloys studied in this work were cuboid and had the same dimensions for comparison. Contrary to Equation 5.1, for the 80WC-10VC-(10-*x*)Co-*x*Ru, (89.2-*x*)WC-0.8VC-10Co-*x*Ru and 89.6WC-0.4VC-(10-*x*)Co-*x*Ru alloys, the coercivity generally decreased with magnetic saturation (Figure 4.48). A similar trend was observed by Schwenke and Judy

[2007Sch] for Cr-doped alloys and was deduced to be due to Cr in the Co solid solution. However, for (89.6-*x*)WC-0.4VC-10Co-*x*Ru alloys, with the lowest VC contents, there was a direct relationship between coercivity and magnetic saturation (Figure 4.48), thus the VC content might also have affected the magnetic properties, especially coercivity. For the (89.6-*x*)WC-0.4VC-10Co-*x*Ru, (89.2-*x*)WC-0.8VC-10Co-*x*Ru and 89.6WC-0.4VC-(10-*x*)Co-*x*Ru alloys, there should have been good solubility of V in the binder, considering the VC contents that were less than 1 wt%. However, the direct relationship (for the (89.6-*x*)WC-0.4VC-10Co-*x*Ru alloys) and inverse relationship (for the (89.2-*x*)WC-0.8VC-10Co-*x*Ru and 89.6WC-0.4VC-(10-*x*)Co-*x*Ru alloys) between coercivity and magnetic saturation in Figure 4.48 cannot be attributed to the solubility of V in the binder, but to binder volume fraction and grain sizes, as explained earlier.

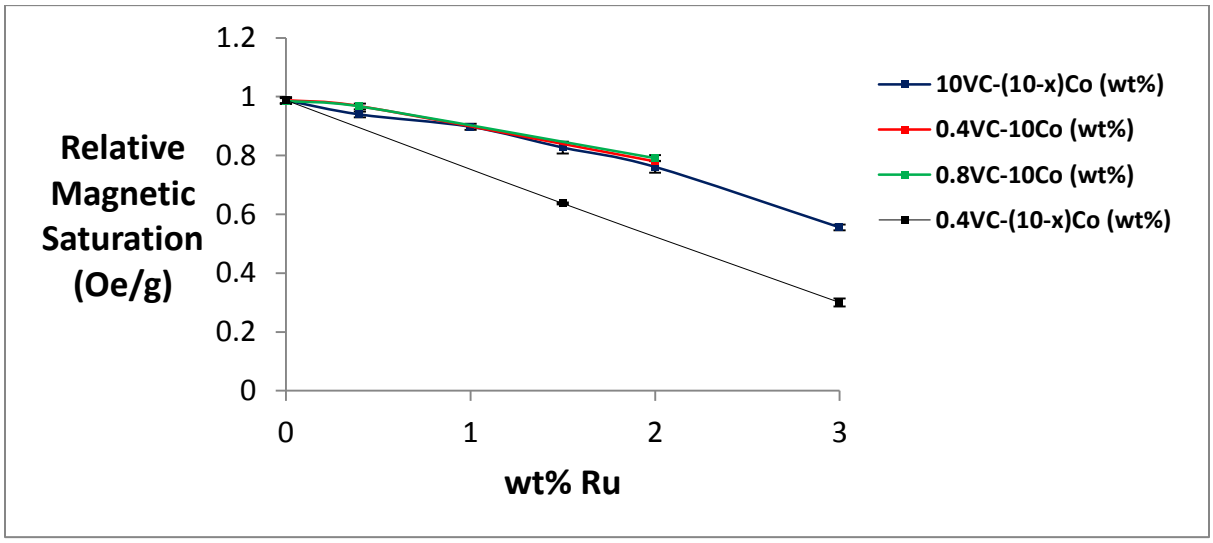

Figure 5.1. Variation of relative magnetic saturation with Ru additions for sintered 80WC-10VC-(10-x)Co-xRu, (89.6-x)WC-0.4VC-10Co-xRu, (89.2-x)WC-0.8VC-10Co-xRu and 89.6WC-0.4VC-(10-x)Co-xRu (wt%) alloys (errors too small to be seen clearly).

Roebuck [1996Roe] found that the magnetic saturation of a hardmetal with little or no dissolved W is given by Equation 5.2:

$$\text{Magnetic saturation} = 4\pi\sigma_{Co}w_f \qquad \text{Equation 5.2}$$

where σ_{Co} = magnetic saturation of pure Co (201.9 $\mu Tm^3.kg^{-1}$) and

w_f = weight fraction of Co in the hardmetal.

Using Equation 5.2, the theoretical variation of magnetic saturation with Ru content was superimposed on the experimental plots (Figure 5.2). The steeper experimental curves for the 80WC-10VC-(10-*x*)Co-*x*Ru, (89.2-*x*)WC-0.8VC-10Co-*x*Ru and (89.6-*x*)WC-0.4VC-10Co-*x*Ru alloys (Figure 5.2) confirmed that Ru additions decreased magnetic saturations.

5.2. Phase identification and Microstructural Studies

To further verify whether the target alloy qualities were achieved, the compositional analyses were evaluated by calculating the Co/Ru ratios for all alloys, and estimating the stoichiometric WC, the main component (Table 5.1). The calculated values based on EDS analyses were then compared to those expected (targeted) for the desired alloy compositions.

Table 5.1 shows that the Co:Ru ratios targeted were achieved for all the Ru-added alloys. Alloy 2 deviated from the target Co/Ru ratio by 10.5%, much more than the rest of the alloys which deviated by an average difference of ~2.1%. The deviation of Alloy 2 from the target Co/Ru ratio would not affect the trend of analyses, since it still had the highest ratio, as expected. In other words, the composition of Alloy 2 was not too far from target to affect any conclusions. The negative values are for cases where actual Co/Ru ratios were less than those targeted. The proportion of WC in the alloys was close to expected, as estimated from EDS analyses (Table 5.2). The association of Ru with Co as shown by EDS mapping (Figure 4.49e) also confirmed that it was possible to incorporate Ru into the Co binder using HIP sintering.

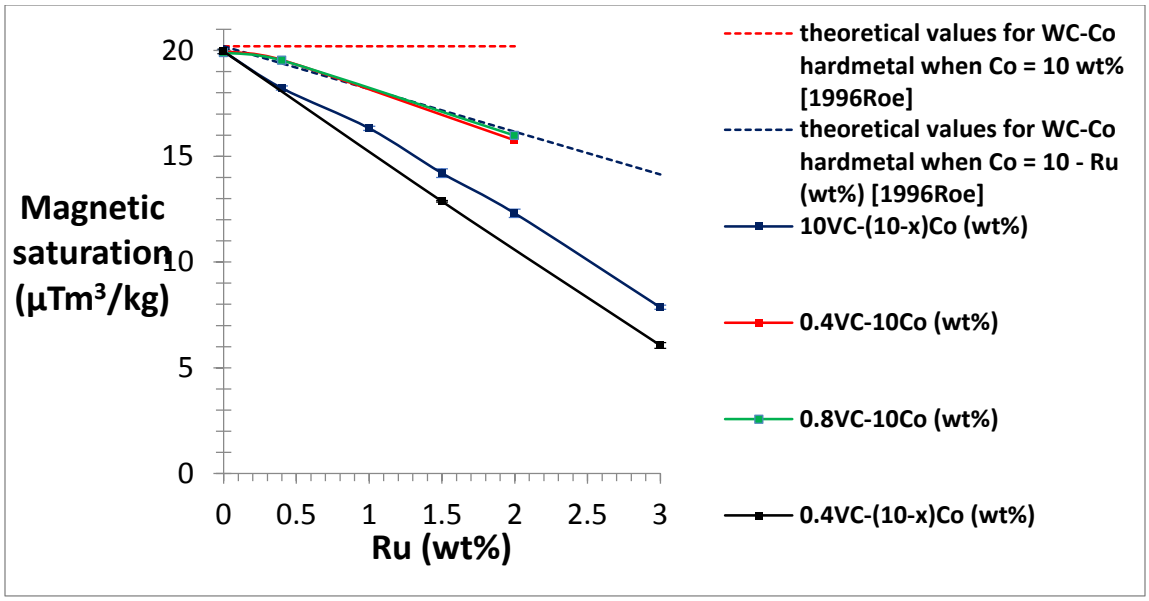

Figure 5.2. Comparison between the expected decrease of magnetic saturation in alloys without Ru and for 80WC-10VC-(10-x)Co-xRu, (89.6-x)WC-0.4VC-10Co-xRu, (89.2-x)WC-0.8VC-10Co-xRu and 89.6WC-0.4VC-(10-x)Co-xRu (wt%) alloys.

The absence of a definite relationship between d_{wc} and Ru content for 80WC-10VC-(10-*x*)Co-*x*Ru alloys (Figure 4.58) was contrary to the negative trend observed in previous work [2001Shi] on WC-Co-Ru alloys. For the (89.6-*x*)WC-0.4VC-10Co-*x*Ru and (89.2-*x*)WC-0.8VC-10Co-*x*Ru alloy series, Ru was substituting WC, and decreased WC content at constant VC contents for both series, which meant increased VC:WC ratios with Ru additions. Higher VC:WC ratios allowed greater effectiveness of VC as a WC grain growth inhibitor. Thus, the decreased grain size in the (89.6-*x*)WC-0.4VC-10Co-*x*Ru series with Ru substituting WC (Figure 4.58) could also be attributed to the increased effect of VC as a grain growth inhibitor. However, the effect of Ru on the grain size was deduced from the 89.6WC-0.4VC-(10-*x*)Co-*x*Ru alloys that had a decrease in grain size with Ru additions at constant VC:WC ratio. Smaller grain sizes for the (89.2-*x*)WC-0.8VC-10Co-*x*Ru series than the (89.6-*x*)WC-0.4VC-10Co-*x*Ru series also confirmed the decrease in WC mean intercept length at higher VC contents.

Table 5.1. Comparison between the Co:Ru ratios from EDS analyses and the targeted in 80WC-10VC-(10-x)Co-xRu, (89.6-x)WC-0.4VC-10Co-xRu, (89.2-x)WC-0.8VC-10Co-xRu and 89.6WC-0.4VC-(10-x)Co-xRu (wt%) alloys.

Series (wt%)	**Alloy Number**	**Alloy (wt% Ru)**	**Targeted Co/Ru**	**Actual Co/Ru**	**Difference (%)**
80WC-10VC-(10-*x*)Co-*x*Ru	2	0.4	24.00	21.49	10.5
	3	1.0	9.00	9.31	-1.3
	4	1.5	5.67	5.56	0.4
	5	2.0	4.00	3.97	0.1
	6	3.0	2.33	2.33	0.0
(89.6-*x*)WC-0.4VC-10Co-*x*Ru	8	0.4	25.00	23.75	-5.0
	9	2.0	5.00	4.76	-4.8
(89.2-*x*)WC-0.8VC-10Co-*x*Ru	11	0.4	25.00	24.00	-4.0
	12	2.0	5.00	5.05	1.0
89.6WC-0.4VC-(10-*x*)Co-*x*Ru	13	1.5	5.67	5.60	1.2
(*Includes Alloy 7)*	14	3.0	2.33	2.16	7.3

Table 5.2. Comparison between target and experimental WC proportions in 80WC-10VC-(10-x)Co-xRu, (89.6-x)WC-0.4VC-10Co-xRu, (89.2-x)WC-0.8VC-10Co-xRu and 89.6WC-0.4VC-(10-x)Co-xRu (wt%) alloys.

Series (wt%)	**Alloy Number**	**Ru Content (wt%)**	**Target WC (wt%)**	**Experimental WC (wt%)**	**Difference (%)**
80WC-10VC-(10-*x*)Co-*x*Ru	1	0.0	80	78.1	2.40
	2	0.4	80	78.9	1.35
	3	1.0	80	78.0	2.47
	4	1.5	80	77.5	3.09
	5	2.0	80	78.3	2.18
	6	3.0	80	78.6	1.76
(89.6-*x*)WC-0.4VC-10Co-*x*Ru	7	0.0	89.6	88.7	-1.00
	8	0.4	89.2	88.6	-0.67
	9	2.0	87.6	86.7	-1.03
(89.2-*x*)WC-0.8VC-10Co-*x*Ru	10	0.0	89.2	88.4	-0.90
	11	0.4	88.8	87.9	-1.01
	12	2.0	87.2	86.6	-0.69
89.6WC-0.4VC-(10-*x*)Co-*x*Ru	13	1.5	89.6	88.3	1.45
(*Includes Alloy 7)*	14	3.0	89.6	89.3	0.33

The absence of a significant grain size change for increased VC:WC ratios in the (89.2-*x*)WC-0.8VC-10Co-*x*Ru alloy series (Figure 4.58) suggested a limit of effectiveness for VC additions. The presence of VC resulted in the formation of (V,W)C layers surrounding WC, thus inhibiting the dissolution-reprecipitation process responsible for grain growth [2009Has].

Since the grain size did not change significantly with further additions of Ru for the 80WC-10VC-(10-*x*)-*x*Ru and 89.6WC-0.4VC-(10-*x*)-*x*Ru (wt%) alloys (Figure 4.58), the opposite effect on coercivity of the (Co) solid solution with Ru superseded that of grain size decrease at higher Ru additions, thus decreasing the overall coercivity (Figure 4.47). The decreased WC content with Ru additions in (89.2-*x*)WC-0.8VC-10Co-*x*Ru (wt%) alloys (Figure 4.58) also contributed to the decreased coercivity, as it decreased the number of WC/Co interfaces. The increased coercivity with Ru content for (89.6-*x*)WC-0.4VC-10Co-*x*Ru (wt%) alloys (Figure 4.47) was attributed to the decreased grain size (Figure 4.58).

Mean d_{wc} results (Table 4.26 and Figure 4.58) were consistent with grain size distribution results (Figures 4.79 to 4.62 and Table 4.27). For the 80WC-10VC-(10-*x*)Co-*x*Ru wt% alloys, the consistency was on the lack of correlation between Ru content and WC grain size. Also, the mean intercept lengths for all alloys were within the ultra-fine size range. For the (89.6-*x*)WC-0.4VC-10Co-*x*Ru alloy series the WC mean intercept lengths were within the modal size range of 0.4 - 0.7 μm. A lower modal size range (0.1 - 0.4 μm) was seen for the (89.2-*x*)WC-0.8VC-10Co-*x*Ru alloys, and this was to be expected because the alloys had finer WC grain sizes. In the 89.6WC-0.4VC-(10-*x*)Co-*x*Ru series, Alloys 13 and 14 had a lower modal size range (0.2 - 0.4 μm) than Alloy 13 (0.4 - 0.6 μm) (Figure 4.62) in agreement with lower mean d_{wc} results for Alloys 13 and 14, than for Alloy 7 (Table 4.26). The cumulative distribution curves (Figure 4.63) were also consistent with the mean intercept length results with respect to grain size comparison within and between the three alloy series. Figure 4.63 confirms the closeness of the grain sizes in the 80WC-10VC-(10-*x*)Co-*x*Ru alloy series, with the very close cumulative distribution plots. Figure 4.63 also confirms the decrease in grain size with Ru additions up to 2 wt% for the (89.6-*x*)WC-0.4VC-10Co-*x*Ru, (89.2-*x*)WC-0.8VC-10Co-*x*Ru and 89.6WC-0.4VC-(10-*x*)Co-*x*Ru

alloy series. Ruthenium had more effect on grain size in the (89.6-*x*)WC-0.4VC-10Co-*x*Ru alloys than the (89.2-*x*)WC-0.8VC-10Co-*x*Ru alloys, since the curves were more separate for the (89.6-*x*)WC-0.4VC-10Co-*x*Ru alloys.

Figure 4.63 also shows that the 80WC-10VC-(10-*x*)Co-*x*Ru alloy series had the finest grain sizes, followed by the (89.2-*x*)WC-0.8VC-10Co-*x*Ru alloy series. Thus, higher the VC contents gave finer grain sizes. The effect of adding up to 3 wt% Ru on the grain sizes of the 80WC-10VC-(10-*x*)Co-*x*Ru wt% alloys was masked by 10 wt% VC, since VC is a more effective grain growth inhibitor [2001Shi]. Shing *et al*. [2001Shi] reported that additions of 0.4 wt% VC to WC-Co alloys decreased the mean WC grain size by 50%, much more than the 15% decrease obtained by addition of up to 3 wt% Ru to similar alloys. Thus, the addition of 10 wt% VC might have made the effect of up to 3 wt% Ru on the WC grain size insignificant.

Any effect of adding up to 3 wt% Ru on the grain sizes of the 80WC-10VC-(10-*x*)Co-*x*Ru wt% alloys could not be noticed due to the presence of 10 wt% VC, since VC is a more effective grain growth inhibitor than Ru [2001Shi]. Shing *et al*. [2001Shi] reported that additions of just 0.4 wt% VC to WC-Co alloys decreased the mean WC grain size by 50%, much more than the decrease (15%) obtained by addition of up to 3 wt% Ru to similar alloys. Thus, the addition of 10 wt% VC might have made the effect of up to 3 wt% Ru on the WC grain size insignificant. The fineness of the grains was to be expected given the starting WC powder mean particle size (<0.8μm) and the presence of VC, a grain growth inhibitor. The effect of VC as a WC grain growth inhibitor could also be deduced from the (89.2-*x*)WC-0.8VC-10Co-*x*Ru that had a smaller grain size decrease (~8%) than the (89.6-*x*)WC-0.4VC-10Co-*x*Ru alloy series (~23%), after 2 wt% Ru additions in both cases. Furthermore, the 80WC-10VC-(10-*x*)Co-*x*Ru wt% alloy series, with most VC, had the finest grain sizes.

The presence of a main grain size class (0.1 - 0.4 μm) and the absence of medium and coarse sizes in the 80WC-10VC-(10-*x*)Co-*x*Ru alloy series, as shown in Table 4.27 also confirmed the effectiveness of VC as a grain growth inhibitor [2001Shi]. The presence of the coarse size range

only in the alloy series with the lowest VC content, i.e. the (89.6-*x*)WC-0.4VC-10Co-*x*Ru and 89.6WC-0.4VC-(10-*x*Co)-*x*Ru alloy series (Table 4.27), also confirmed the effectiveness of VC as a grain growth inhibitor. The presence of excessively large grains is detrimental to the strength of hardmetals [2000Cho].

The mean binder free path, λ and the WC mean intercept length, d_{wc} followed the same trend with respect to Ru for the 80WC-10VC-(10-*x*)Co-*x*Ru, 89.6WC-0.4VC-(10-*x*)Co-*x*Ru and (89.6-*x*)WC-0.4VC-10Co-*x*Ru alloy series (Figures 4.58 and 4.64), similar to results of Bhaumik *et al*. [1991Bha]. The general decrease of mean binder free path with Ru content for the 80WC-10VC-(10-*x*)Co-*x*Ru and 89.6WC-0.4VC-(10-*x*)Co-*x*Ru alloys was due to decreased binder phase volume fraction, since there was not significant change in grain size. For the (89.6-*x*)WC-0.4VC-10Co-*x*Ru (wt%) alloys, the decrease was due to the decreased grain size that overrode the increase binder volume fraction. The opposite trend for the (89.2-*x*)WC-0.8VC-10Co-*x*Ru alloys was due to the increase in binder volume fraction with Ru additions overriding the small decrease in WC grain size. The lack of a direct correlation between the inverse binder mean free path and coercivity for the 80WC-10VC-(10-*x*)Co-*x*Ru alloys (Figure 5.3) contradicted previous results on WC-Co alloys by Exner [1966Exn] who found a direct relationship between the inverse binder mean free path and coercivity. It seems for WC-VC-Co-Ru coercivity results can only be used as an indirect measure of mean binder free path, at low VC contents since (89.6-*x*)WC-0.4VC-10Co-*x*Ru, (89.2-*x*)WC-0.8VC-10Co-*x*Ru and 89.6WC-0.4VC-(10-*x*)Co-*x*Ru alloys demonstrated the expected relationship (Figure 5.3).

As the Ru content was increased for the 80WC-10VC-(10-*x*)Co-*x*Ru and 89.6WC-0.4VC-(10-*x*)Co-*x*Ru alloy series, the binder volume fractions of the WC and (V,W)C increased, whereas the binder volume decreased, and this led to increased carbide contiguities (Figures 4.65). The opposite trends for the (89.6-*x*)WC-0.4VC-10Co-*x*Ru alloys (Figure 4.65) and the (89.2-*x*)WC-0.8VC-10Co-*x*Ru alloys (Figure 4.65) led to increased contiguities with Ru additions. Overall, the (89.6-*x*)WC-0.4VC-10Co-*x*Ru, (89.2-*x*)WC-0.8VC-10Co-*x*Ru and 89.6WC-0.4VC-(10-*x*)Co-

*x*Ru alloys had higher contiguities than the 80WC-10VC-(10-*x*)Co-*x*Ru alloys, due to higher carbide fractions.

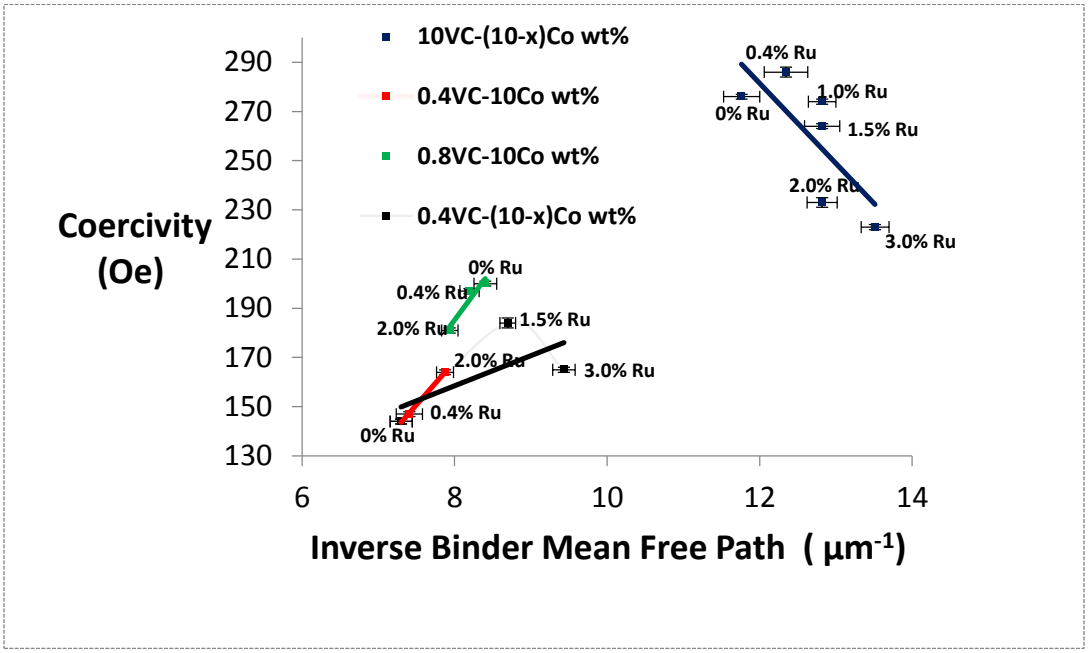

Figure 5.3. Relationship between coercivity and binder mean free path for 80WC-10VC-(10-x)Co-xRu, (89.6-x)WC-0.4VC-10Co-xRu alloys, (89.2-x)WC-0.8VC-10Co-xRu and 89.6WC-0.4VC-(10-x)Co-xRu (wt%) alloys.

The differences in the contiguity equations (Equations 3.13 to 3.15) were attributed to different alloy manufacturing conditions used for each derivation [2006Luy]. Based on mean relative errors, calculated using Equation 3.16 by Tofallis et al. [2015Tof], the 80WC-10VC-(10-*x*)Co-xRu alloys best fitted the expression $C = 1.03 \exp(-5V_\beta)$ [1966Exn], whereas the (89.6-*x*)WC-0.4VC-10Co-*x*Ru, (89.2-*x*)WC-0.8VC-10Co-*x*Ru and 80WC-10VC-(10-*x*)Co-*x*Ru alloys best fitted the expression, $C_\beta = 0.85 - 1.80V_\beta$ [1986Roe] (Table 5.3, Figures 5.5 to 5.8).

Contiguity usually depends only on the binder volume [1966Exn, 1986Roe, 2006Luy], and Equations 3.13 [1966Exn], 3.14 [1986Roe] and 3.15 [2006Luy] describe the relationship between contiguity and binder volume fraction. The variations of the measured contiguities with binder volume fractions (Table 4.29 and Figure 4.65) were consistent with other workers

[1966Exn, 1986Roe, 2006Luy]. Since the contiguities were proportional to the binder volume fractions, the results agreed with Luyckx *et al*. [2006Luy] in that contiguity is not affected by changes in grain size (Figure 5.4), as claimed by Warren and Waldron [1975War].

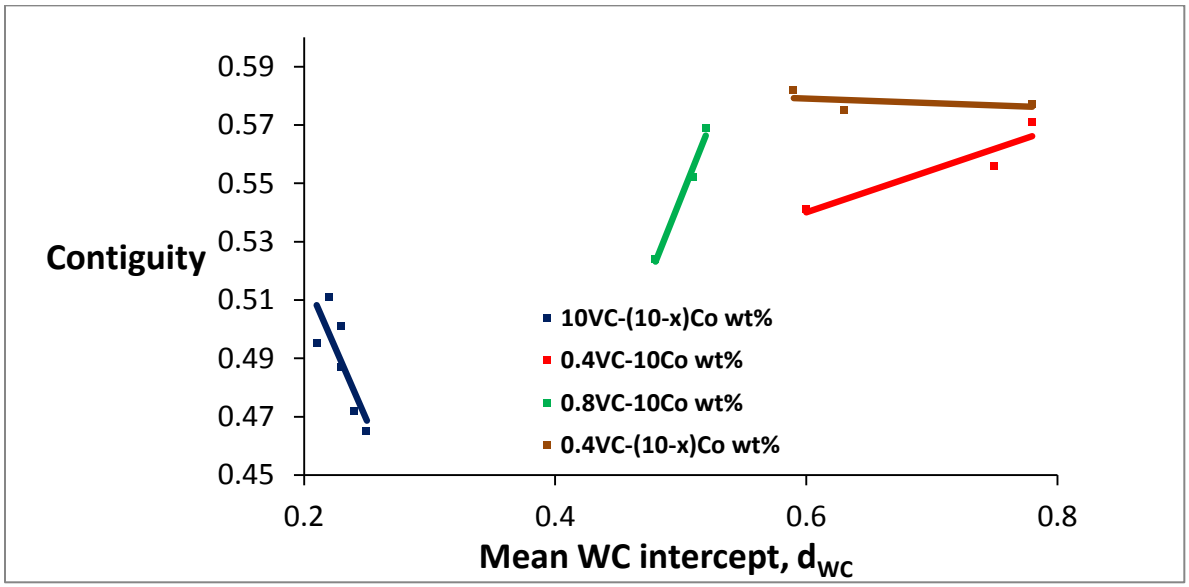

Figure 5.4. Showing no general trend between mean WC intercept length and contiguity (errors removed for clarity – shown in Figures 4.58 and 4.65).

The relationship of contiguity and the thickness of Co regions was derived using the values for λ and d_{wc}. According to Roebuck *et al*. [1986Roe], the ratio λ/d_{wc} can be compared to $f_1(V_\beta)$, $f_2(V_\beta)$, $0.1 + 0.2V_\beta$ or $V_\beta/(1-V_\beta)$, where:

$$f_1(V_\beta) = \left(\frac{V_\beta^{0.45}}{V_\beta^{0.45}-0.2}\right)\left(\frac{V_\beta}{1-V_\beta}\right) \qquad \text{Equation 5.3}$$

$$f_2(V_\beta) = \left(\frac{1}{0.15 + 1.8V_\beta}\right)\left(\frac{V_\beta}{1-V_\beta}\right) \qquad \text{Equation 5.4}$$

Roebuck *et al*. [1986Roe] stated that λ/d_{wc} would be equivalent to any of $f_1(V_\beta)$, $f_2(V_\beta)$ or $0.1 + 0.2V_\beta$ if contiguity affected the binder mean free path, otherwise $\lambda/d_{wc} = V_\beta/(1 - V_\beta)$. The experimental and calculated λ/d_{wc} values are shown in Table 5.4 and plotted in Figures 5.9 to

5.13. For the 80WC-10VC-(10-*x*)Co-*x*Ru alloys, a plot excluding $f_2(V_\beta)$ for clarity is shown in Figure 5.10. From Figure 5.10, it was deduced that λ/d_{wc} values for the 80WC-10VC-(10-*x*)Co-*x*Ru alloys were inconclusive between $f_1(V_\beta)$ and $0.1 + 0.2V_\beta$.

Table 5.3. Calculated contiguities and mean relative errors for the (80WC-10VC-(10-x)Co-xRu, (89.6-x)WC-0.4VC-10Co-xRu, (89.2-x)WC-0.8VC-10Co-xRu and 89.6WC-0.4VC-(10-x)Co-xRu (wt%) alloys.

Series (wt%)	**Alloy Number**	**Calculated Contiguity**		
		Equation 3.13 [1966Exn]	Equation 3.14 [1986Roe]	Equation 3.15 [2006Luy]
80WC-10VC-(10-x)Co-xRu	1	0.509	0.596	0.306
	2	0.514	0.600	0.311
	3	0.519	0.603	0.317
	4	0.525	0.607	0.322
	5	0.530	0.611	0.328
	6	0.540	0.618	0.338
Mean Relative Error		**0.071**	**0.303**	**0.311**
(89.6-x)WC-0.4VC-10Co-xRu	7	0.456	0.557	0.255
	8	0.446	0.549	0.245
	9	0.408	0.516	0.211
Mean Relative Error		**0.215**	**0.028**	**0.574**
(89.2-*x*)WC-0.8VC-10Co-*x*Ru	10	0.459	0.559	0.257
	11	0.449	0.551	0.247
	12	0.410	0.519	0.213
Mean Relative Error		**0.199**	**0.010**	**0.565**
89.6WC-0.4VC-(10-*x*)Co-*x*Ru (*Includes Alloy 7*)	13	0.470	0.567	0.267
	14	0.484	0.578	0.281
Mean Relative Error		**0.181**	**0.013**	**0.534**

Since both $f_1(V_\beta)$ and $0.1 + 0.2V_\beta$ only apply when contiguity affects λ, therefore, for 80WC-10VC-(10-*x*)Co-*x*Ru, the thickness of Co regions was affected by contiguity. None of the experimental values were close to $V_\beta/(1 - V_\beta)$, indicating that the binder mean free path was affected by contiguity. Figure 5.9 also shows that if contiguity had a strong effect on the binder mean free path, the experimental λ/d_{wc} values would be closer to $f_2(V_\beta)$ than to $V_\beta/(1 - V_\beta)$,

which was not the case for the 80WC-10VC-(10-*x*)Co-*x*Ru (wt%) alloys. Therefore, the effect of contiguity on binder free path of 80WC-10VC-(10-*x*)Co-*x*Ru (wt%) alloys was not very strong.

It is shown from Figures 5.11 to 5.13 that λ/d_{wc} values for the (89.6-*x*)WC-0.4VC-10Co-*x*Ru, (89.2-*x*)WC-0.8VC-10Co-*x*Ru and 89.6WC-0.4VC-(10-*x*)Co-*x*Ru alloy series best fitted the expression $V_\beta/(1 - V_\beta)$, indicating that the binder mean free path was not affected by contiguity.

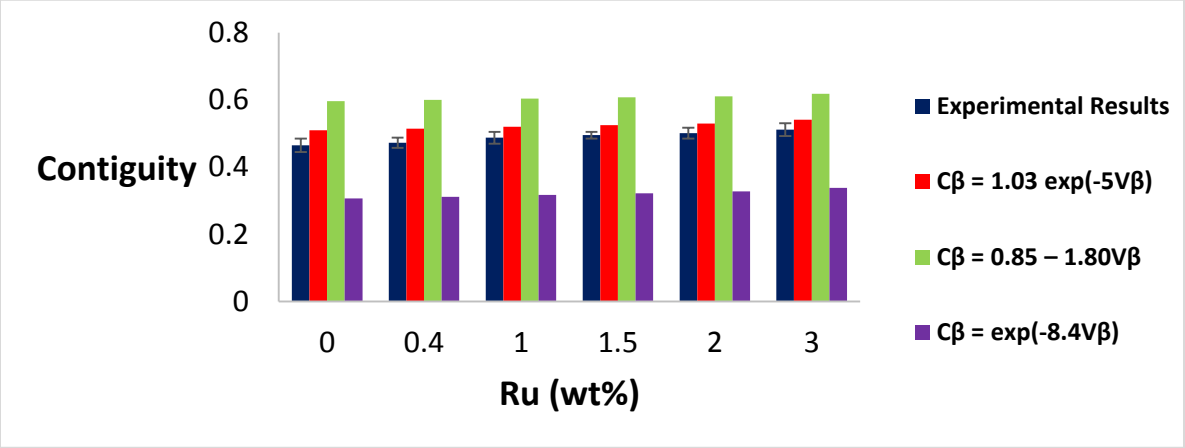

Figure 5.5. Comparison between measured and calculated contiguities for 80WC-10VC-(10-x)Co-xRu (wt%) alloys.

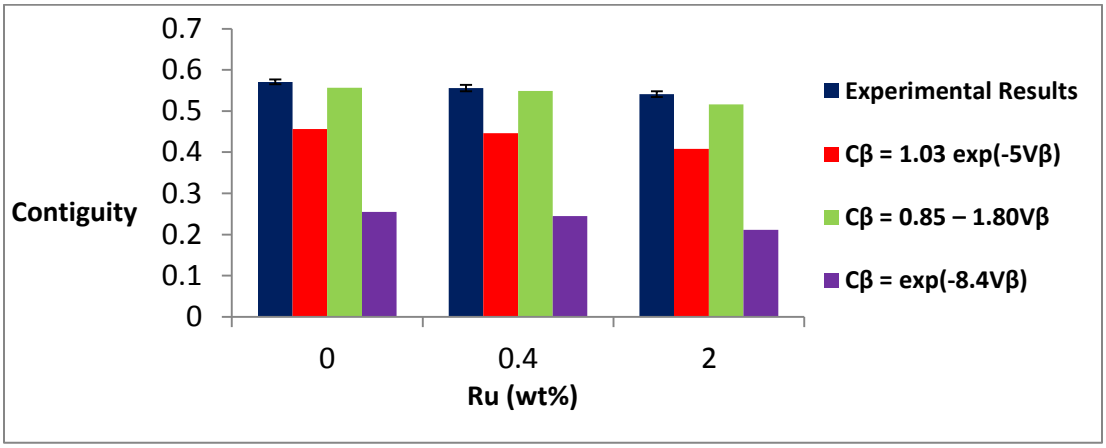

Figure 5.6. Variation of contiguity with Ru content for (89.6-x)WC-0.4VC-10Co-xRu (wt%) alloys for both measured and calculated values.

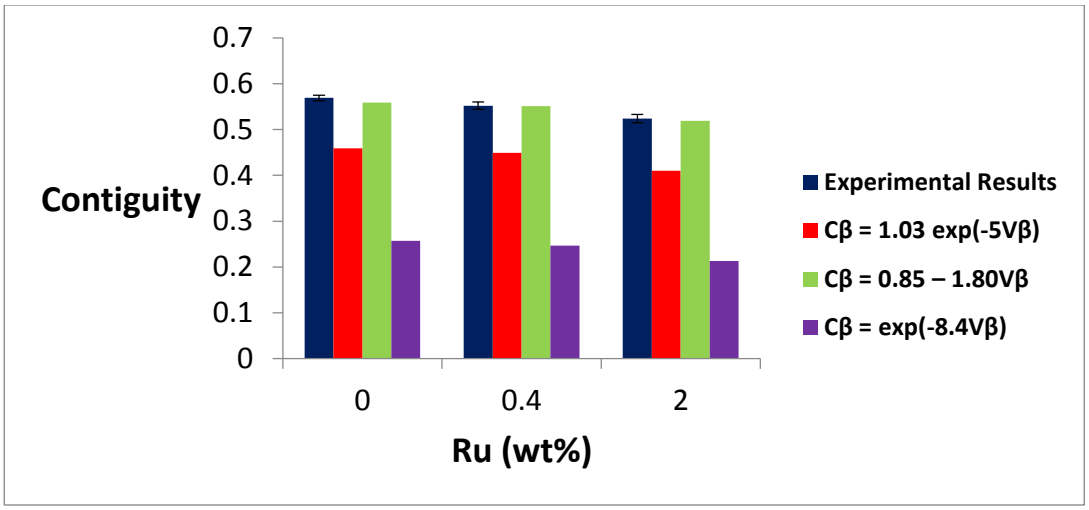

Figure 5.7. Variation of contiguity with Ru content for (89.2-x)WC-0.8VC-10Co-xRu (wt%) alloys for both measured and calculated values.

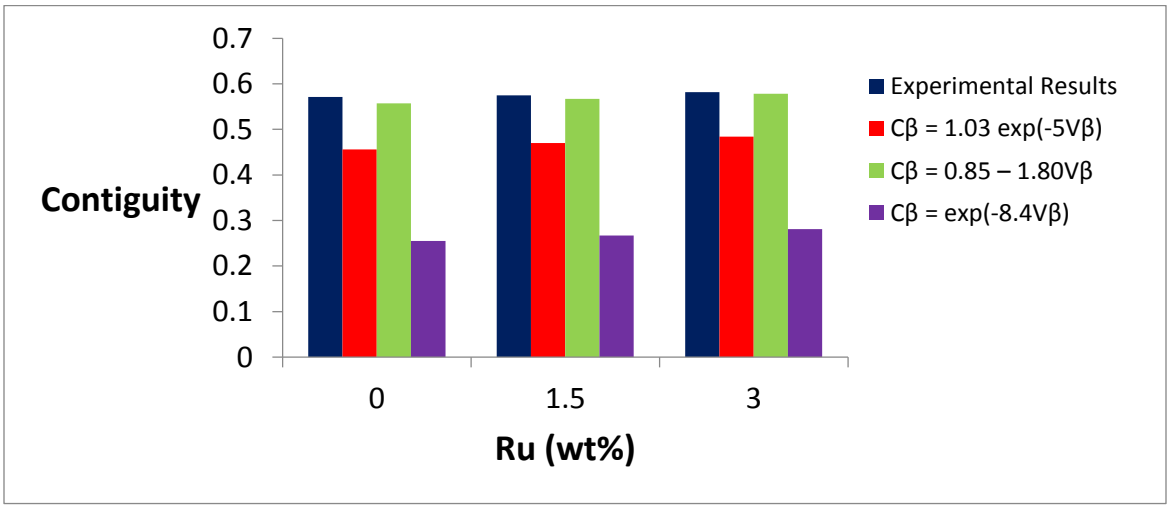

Figure 5.8. Variation of contiguity with Ru content for 89.6WC-0.4VC-10Co-xRu (wt%) alloys for both measured and calculated values.

It was also deduced that the (89.2-*x*)WC-0.8VC-10Co-*x*Ru alloys with higher VC content had boundary values close to $f_1(V_\beta)$ (Figure 5.6), where contiguity did affect the binder mean free

path. Thus, the effect of contiguity on binder mean free path increased with VC additions, so that at 10 wt% VC, contiguity affected binder mean free path (Figure 5.9).

Table 5.4. Experimental and calculated λ/dwc values for the 80WC-10VC-(10-x)Co-xRu (0 ≤ x ≤ 3), (89.6-x)WC-0.4VC-10Co-xRu (0 ≤ x ≤ 2), (89.2-x)WC-0.8VC-10Co-xRu (0 ≤ x ≤ 2) and 89.6WC-0.4VC-(10-x)Co-xRu (0 ≤ x ≤ 3) (wt%) alloys.

Series (wt%)	**Alloy Number**	**Ru Content (wt%)**	**λ/d_{wc} (Experimental)**	**λ/d_{wc} (Calculated)**			
				$f_1(V_\beta)$	$f_2(V_\beta)$	$V_\beta/(1-V_\beta)$	$0.1 + 2.0V_\beta$
80WC-10VC-(10-*x*)Co-*x*Ru	1	0.0	0.3400±0.1240	0.3173	1.3668	0.1640	0.3818
	2	0.4	0.3394±0.1214	0.3141	1.3604	0.1614	0.3780
	3	1.0	0.3391±0.1387	0.3107	1.3537	0.1587	0.3739
	4	1.5	0.3530±0.1560	0.3075	1.3473	0.1560	0.3699
	5	2.0	0.3520±0.1534	0.3042	1.3410	0.1534	0.3660
	6	3.0	0.3411±0.1482	0.2978	1.3288	0.1482	0.3581
(89.6-*x*)WC-0.4VC-10Co-*x*Ru	7	0.0	0.1857±0.1240	0.3553	0.4389	0.1945	0.4256
	8	0.4	0.1911±0.1214	0.3635	0.4454	0.2010	0.4349
	9	2.0	0.2092±0.1387	0.3970	0.4704	0.2275	0.4707
(89.2-*x*)WC-0.8VC-10Co-*x*Ru	10	0.0	0.2308±0.1560	0.3534	0.4374	0.1930	0.4235
	11	0.4	0.2392±0.1534	0.3615	0.4439	0.1994	0.4325
	12	2.0	0.2500±0.1482	0.3948	0.4688	0.2257	0.4683
80WC-10VC-(10-*x*)Co-*x*Ru (*Includes Alloy 7*)	13	1.5	0.1825±0.1205	0.3450	0.4306	0.1863	0.4141
	14	3.0	0.1797±0.1392	0.3348	0.4219	0.1781	0.4024

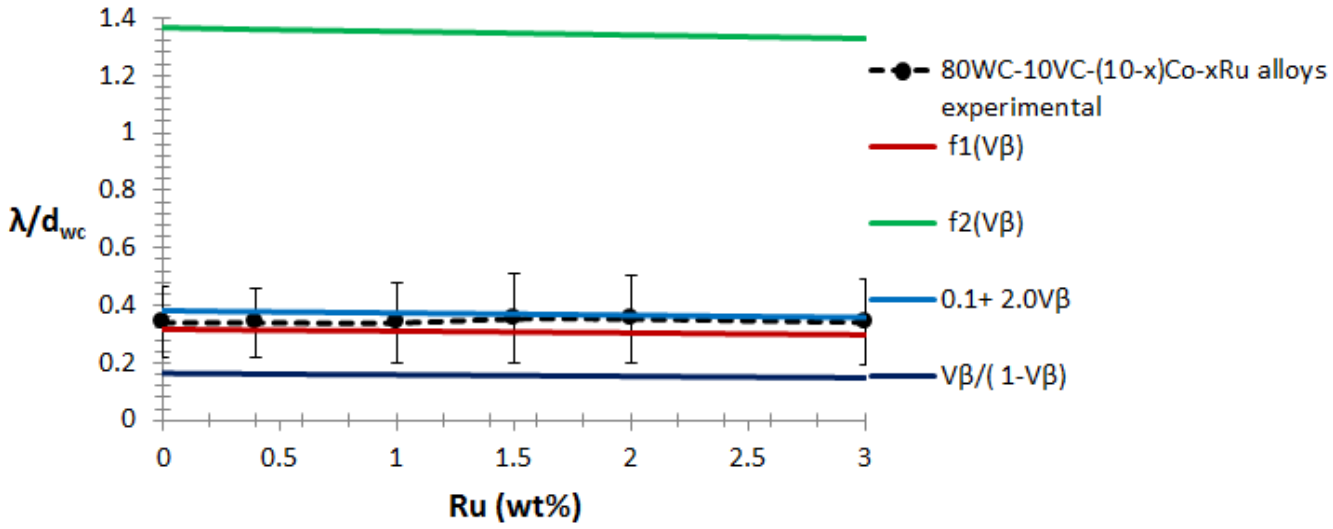

Figure 5.9. Experimental and calculated binder mean free path-mean WC intercept length ratios, λ/dwc, for 80WC-10VC-(10-x)Co-xRu (wt%) alloys.

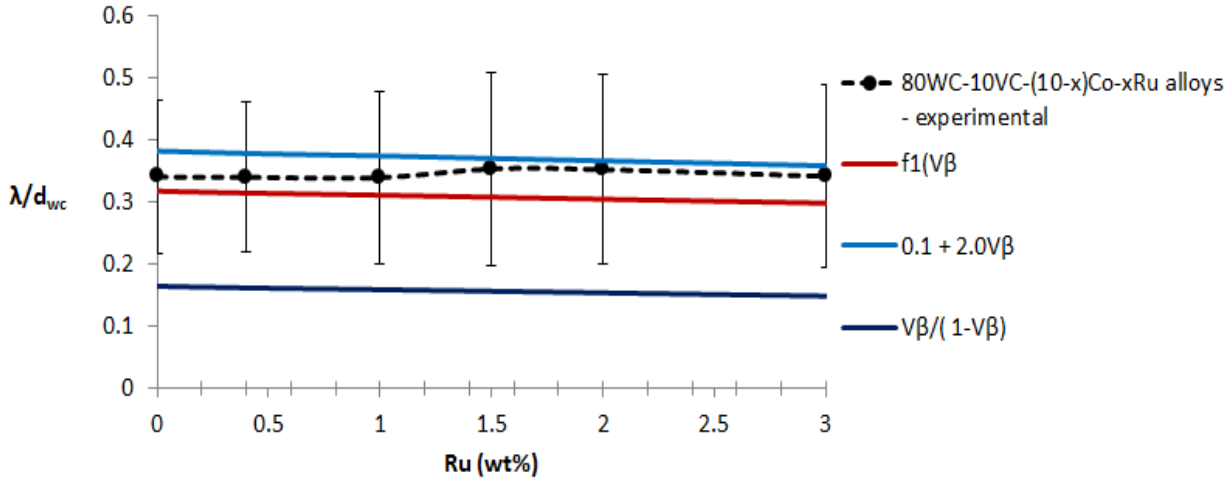

Figure 5.10. Boundary regions for 80WC-10VC-(10-x)Co-xRu) (wt%) alloys (extracted from Figure 5.3).

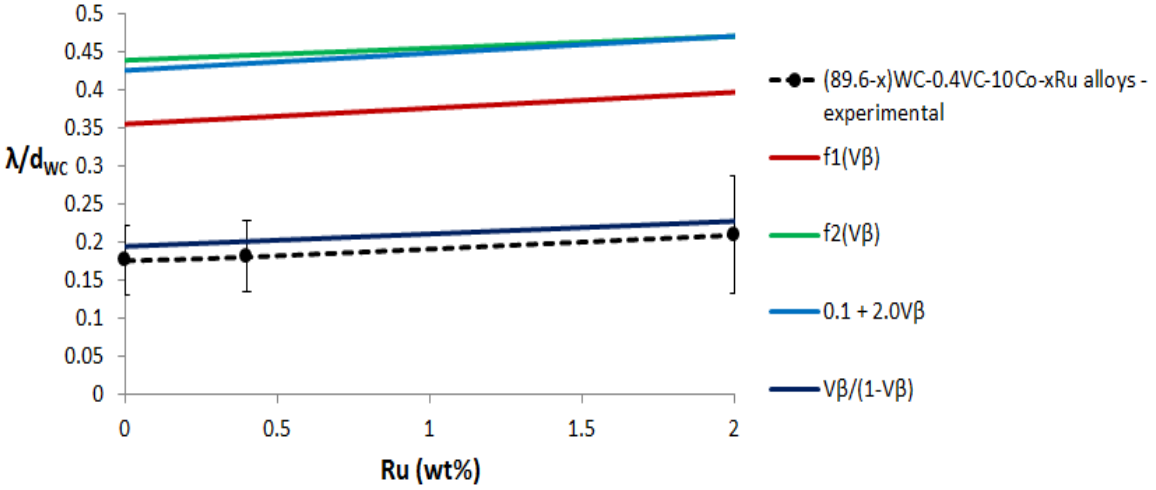

Figure 5.11. Experimental and calculated binder mean free path-mean/WC intercept length ratios, λ/dwc, for (89.6-x)WC-0.4VC-10Co-xRu (wt%) alloys.

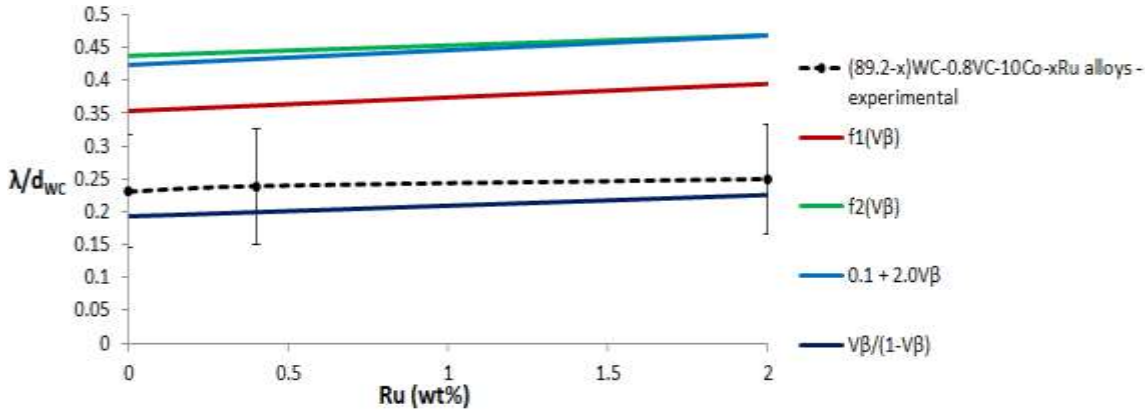

Figure 5.12. Experimental and calculated binder mean free path-mean/WC intercept length ratios, λ/dwc, for (89.2-x)WC-0.8VC-10Co-xRu (wt%) alloys.

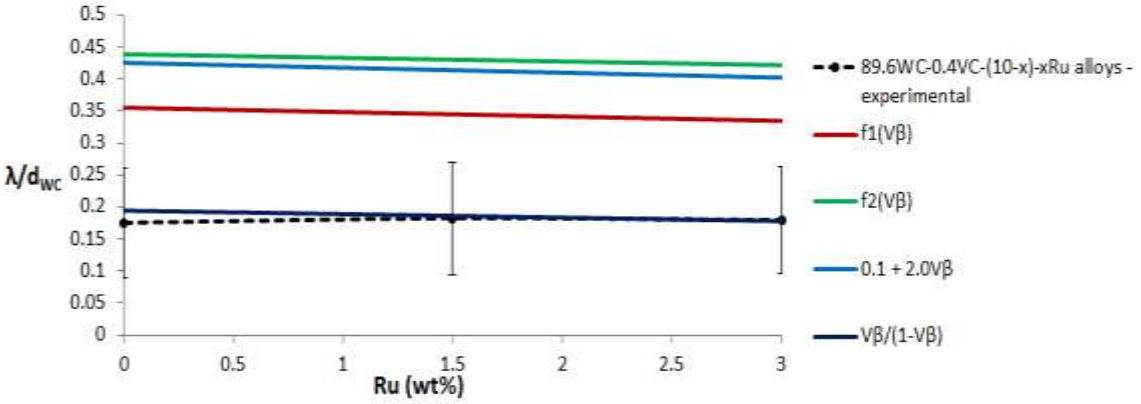

Figure 5.13. Experimental and calculated binder mean free path-mean/WC intercept length ratios, λ/dwc, for 89.6WC-0.4VC-(10-x)Co-xRu (wt%) alloys.

5.3. Hardness and Fracture Toughness

Shing *et al*. [2001Shi] attributed the increase in hardness with Ru for WC-Co-Ru alloys to the decrease in grain size. In this study, the effect of Ru additions on the grain size (mean WC intercept length) was less (Table 4.26), although there was still significant increase in hardness (Table 4.30 and Figure 4.66). The lower effect of Ru additions on the mean WC grain size was attributed to the addition of VC, since VC suppressed Ru. Increased hardness with Ru additions was therefore mainly attributed to solid solution hardening of Co with Ru, based on the Co-Ru phase diagram [1993Pre], since the Ru could completely dissolve in the Co binder. The influence of solid solution strengthening was also deduced by comparing hardnesses of the alloy series which had a grain size decrease of ~8% with 2 wt% Ru additions (Table 4.26), i.e. the 80WC-10VC-(10-*x*)Co-*x*Ru and the (89.6-*x*)WC-0.4VC-10Co-*x*Ru alloy series which had a grain size decrease of ~23%. For the same Ru additions of 2 wt%, the 80WC-10VC-(10-*x*)Co-*x*Ru had a greater increase in hardness (7.6%) than the (89.6-*x*)WC-0.4VC-10Co-*x*Ru series (2.8%). The difference in hardness increase was attributed to more solid solution strengthening in the 80WC-10VC-(10-*x*)Co-*x*Ru alloy series where Ru was replacing Co, unlike in the (89.6-*x*)WC-0.4VC-10Co-*x*Ru alloy series where the Co content was fixed, and Ru was replacing WC. The effect of solid solution strengthening was also evident from the plot of the 89.6WC-0.4VC-(10-*x*)Co-*x*Ru

alloys which went above those for the (89.6-*x*)WC-0.4VC-10Co-*x*Ru and (89.2-*x*)WC-0.8VC-10Co-*x*Ru alloys, with Ru additions (Figure 4.66).

The grain size also had an effect on hardness since there was an inverse relationship between the general grain size of the alloy series and the corresponding hardnesses (Tables 4.26 and 4.30). For the 80WC-10VC-(10-*x*)Co-*x*Ru alloys and 89.6WC-0.4VC-(10-*x*)Co-*x*Ru alloys, where Co was substituted by Ru, the 80WC-10VC-(10-*x*)Co-*x*Ru, with finer grain sizes, had higher hardnesses. For the (89.6-*x*)WC-0.4VC-10Co-*x*Ru and (89.2-*x*)WC-0.8VC-10Co-*x*Ru alloys, where WC was substituted by Ru, the (89.2-*x*)WC-0.8VC-10Co-*x*Ru alloys with finer grain sizes had higher hardnesses. Overall, the 80WC-10VC-(10-*x*)Co-*x*Ru alloys, with finest grains had the highest hardnesses.

Therefore, hardness increased by a combination of decreased grain size, and to a greater extent, by solid solution strengthening. The 80WC-10VC-(10-*x*)Co-*x*Ru and 89.6WC-0.4VC-(10-*x*)Co-*x*Ru alloys had most solid solution strengthening and thus the greatest hardness increase. The 89.6WC-0.4VC-(10-*x*)Co-*x*Ru alloys had greater increase in hardness for 3 wt% Ru additions (12.5%) than the 80WC-10VC-(10-*x*)Co-*x*Ru alloys (11.0%) (Table 4.30) due to having a combination of more significant grain size change (Table 4.26) and solid solution strengthening.

According to Engqvist *et al*. [2002Eng], the hardness is inversely related to the binder mean free path. On the other hand, the hardness of the composite, H_c, is directly related to the binder hardness, H_β according to Equation 5.5 [1978Lee]:

$$H_c = H_{wc}V_{wc}C + H_\beta(1 - V_{wc}C) \qquad \text{Equation 5.5}$$

where:
H_{wc} = *in situ* hardness of the carbide phase,
V_{wc} = volume fraction of the carbide phase, and
C = carbide contiguity.

The inverse relationship between hardness and free path can thus be deduced from Equation 5.6 [1978Lee]:

$H_\beta = 304 + 12.7\lambda^{-1/2}$ Equation 5.6

where:
H_β = binder hardness, and
$\lambda^{-1/2}$ = inverse of the root mean free path.

From Equations 5.5 and 5.6, it can be deduced that the overall hardness was directly proportional to the inverse of the root mean free path ($\lambda^{-1/2}$). Thus, trends of hardness versus root binder mean free path for all alloys were plotted as shown in Figure 5.14. As expected, a direct trend was seen between hardness and the inverse root mean free path for the 80WC-10VC-(10-*x*)Co-*x*Ru, (89.6-*x*)WC-0.4VC-10Co-*x*Ru and 89.6WC-0.4VC-(10-*x*)Co-*x*Ru alloys. However, for the (89.2-*x*)WC-0.8VC-10Co-*x*Ru alloys, there was an inverse relationship between hardness and the inverse root mean free path, due to the binder hardening effect of Ru which counteracted the effect of increased binder thickness. Conversely, this means the hardening effect of Ru in (89.2-*x*)WC-0.8VC-10Co-*x*Ru alloys was compromised by the increase in binder thickness. Therefore, the low increase in the overall hardness for the (89.2-*x*)WC-0.8VC-10Co-*x*Ru alloys can be further explained in terms of the increased binder mean free paths.

Contiguity, C_β, was considered by making the binder hardness (H_β) the subject of Equation 5.7:

$$H_\beta = \frac{H_c - H_{wc}V_{wc}C_\beta}{1 - V_{wc}C}$$ Equation 5.7

The carbide hardness, H_{wc}, was calculated according to Equation 5.8 [26]:

$$H_{wc} = 693 + \frac{2680}{\sqrt{2.1+d}}$$ Equation 5.8

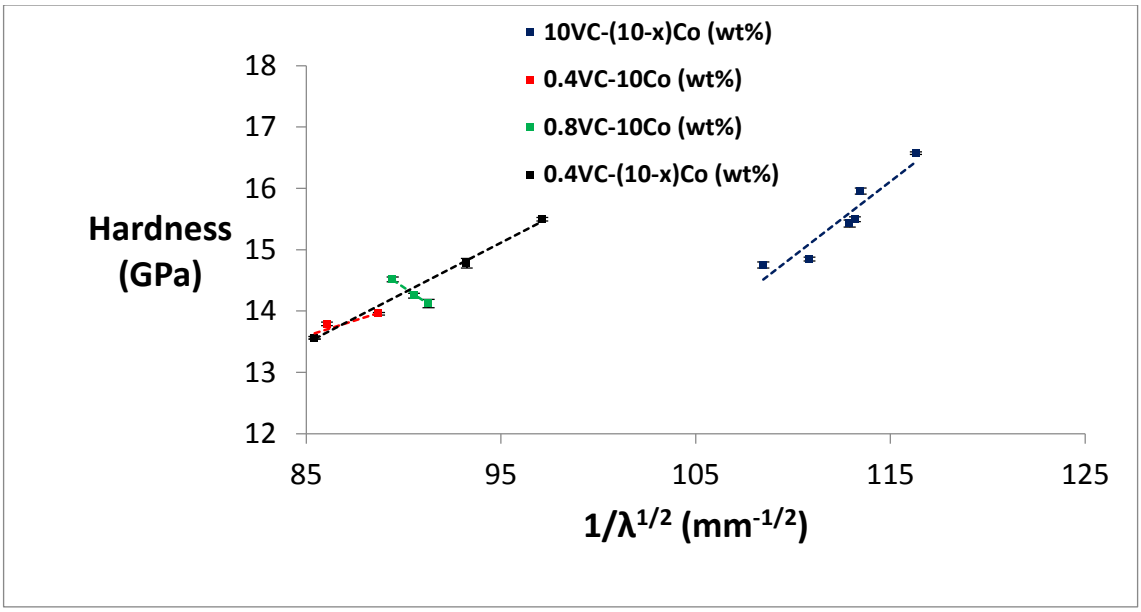

Figure 5.14. Hardness-inverse root mean free path trends for 80WC-10VC-(10-x)Co-xRu, (89.6-x)WC-0.4VC-10Co-xRu, (89.2-x)WC-0.8VC-10Co-xRu and 89.6WC-0.4VC-(10-x)Co-xRu (wt%) alloys.

The binder hardnesses for each alloy series were calculated and plotted against Ru content as shown in Figure 5.15. The plot of calculated binder hardness based on Equation 5.7 was consistent with the bulk hardness (Figure 4.66). However, since VC is not included in Equation 5.7, the binder hardnesses were not exact. Some H_β values were much higher than the hardness of Co (825HV [2002Eng]) due to the effect of solid solution strengthening on the binder hardness. Also, stresses are induced in Co due to the higher thermal coefficients for Co than WC [1952Gur, 1964Daw], resulting in hardnesses higher than for pure and unrestrained Co. It was reported that for a mixture of components, their relative moduli of elasticity affect the thermal expansions [1946Tur]. Thus, Gurland and Norton [1952Gur] concluded that the much higher modulus of elasticity for WC restrains the free expansion of Co, and this could also be the reason for the increased stresses in Co.

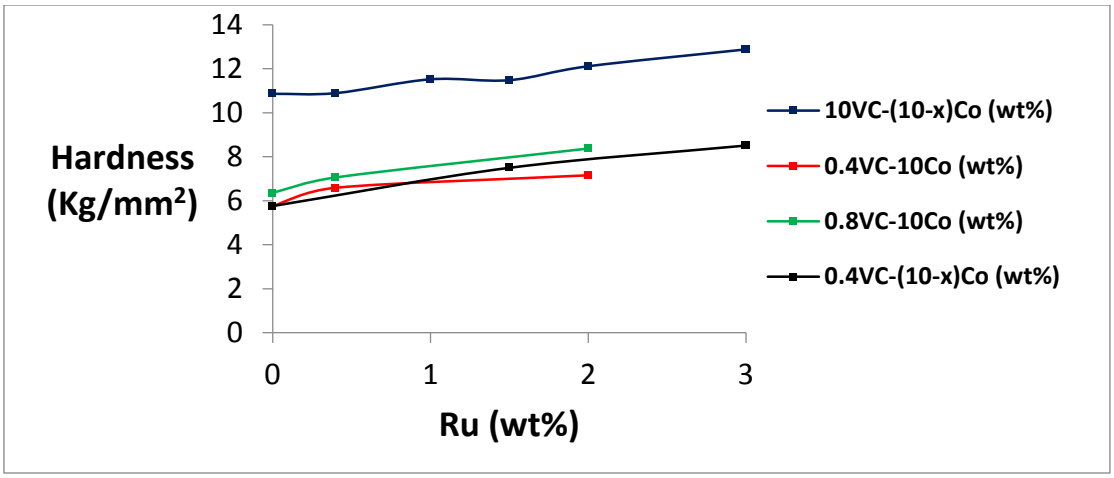

Figure 5.15. Relationship between calculated binder hardness and Ru content for 80WC-10VC-(10-x)Co-xRu, (89.6-x)WC-0.4VC-10Co-xRu, (89.2-x)WC-0.8VC-10Co-xRu and 89.6WC-0.4VC-(10-x)Co-xRu (wt%) alloys.

Since Co substitution with Ru resulted in lower binder volume fractions than when Ru replaced WC, almost all the (89.6-*x*)WC-0.4VC-10Co-*x*Ru and (89.2-*x*)WC-0.8VC-10Co-*x*Ru alloys had less than ~0.162 binder volume fraction, whereas the opposite was true for the 80WC-10VC-(10-*x*)Co-*x*Ru and 89.6WC-0.4VC-(10-*x*)Co-*x*Ru alloys. The direct relationship between hardness and binder volume fraction for the (89.6-*x*)WC-0.4VC-10Co-*x*Ru and (89.2-*x*)WC-0.8VC-10Co-*x*Ru alloys (Figure 5.16) was due to addition of Ru to Co, leading to hardening of the binder phase and increased binder volume fraction. For the 80WC-10VC-(10-*x*)Co-*x*Ru and 89.6WC-0.4VC-(10-*x*)Co-*x*Ru alloys, Ru replaced Co, decreasing the volume fraction and hardening the binder phase, thus giving an inverse relationship between hardness and binder volume fraction.

Coercivity measurements can be used to predict relative hardnesses of materials since both parameters increase as grain size decreases [1985Lau]. Therefore, a direct relationship is expected between coercivity and binder hardness, and this has been confirmed by other workers [1970Stj, 1993Zhi, 1998Upa, 2009Wei]. In this work, a positive trend between coercivity and hardness was seen for the (89.6-*x*)WC-0.4VC-10Co-*x*Ru and 89.6WC-0.4VC-(10-*x*)Co-*x*Ru alloys (Figure 5.17). However, for the 80WC-10VC-(10-*x*)Co-*x*Ru and (89.2-*x*)WC-0.8VC-

10Co-*x*Ru alloys (Figure 5.17), coercivity and hardness varied inversely, although some of the lines were drawn for a small number of data points.

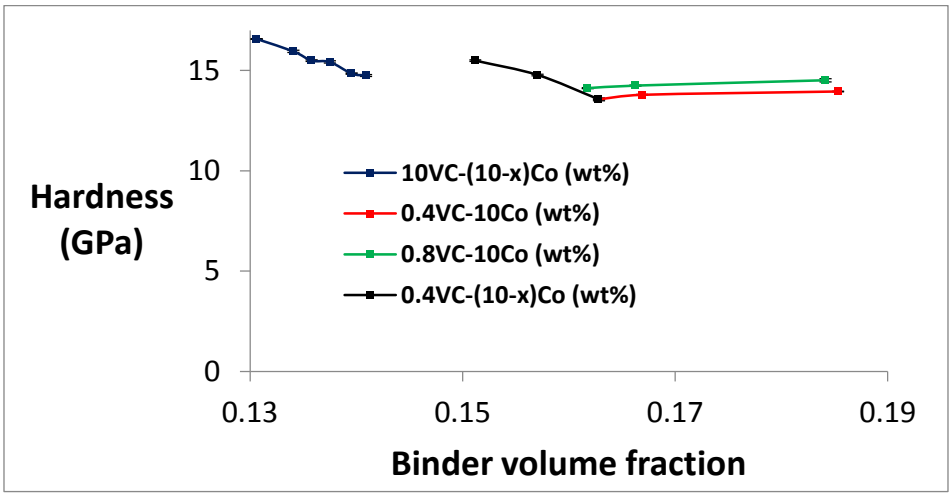

Figure 5.16. Relationship between hardness and binder volume fraction for 80WC-10VC-(10-x)Co-xRu, (89.6-x)WC-0.4VC-10Co-xRu, (89.2-x)WC-0.8VC-10Co-xRu and 89.6WC-0.4VC-(10-x)Co-xRu (wt%) alloys (errors too small to show clearly).

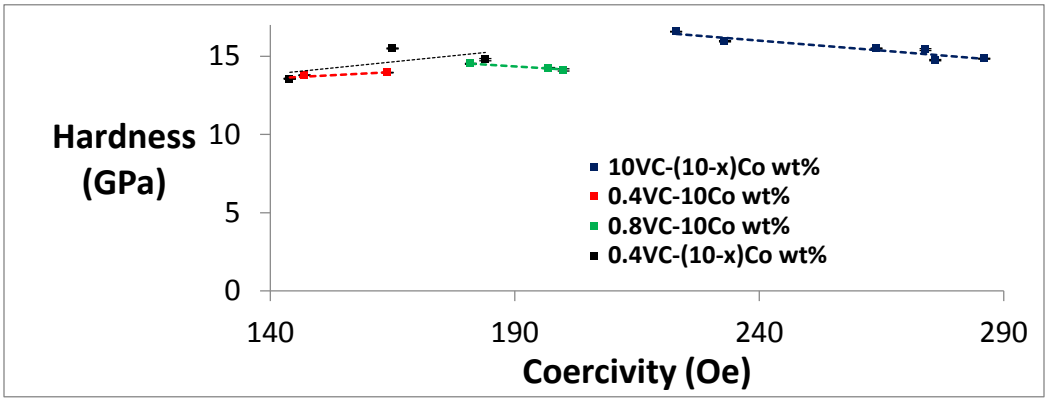

Figure 5.17. Hardness-coercivity trends for 80WC-10VC-(10-x)Co-xRu, (89.6-x)WC-0.4VC-10Co-xRu, (89.2-x)WC-0.8VC-10Co-xRu and 89.6WC-0.4VC-(10-x)Co-xRu (wt%) alloys.

The slight inverse variation of coercivity with hardness for 80WC-10VC-(10-*x*)Co-*x*Ru and (89.2-*x*)WC-0.8VC-10Co-*x*Ru alloy (Figure 5.17), suggests that either or both hardness and

coercivity were not a function of grain size. Due to the effectiveness of VC as a grain growth inhibitor [2001Are, 2015Nor, 2002Wit, 2001Shi], the 0.8 or 10 wt% VC additions resulted in so much grain growth inhibition that any addition of Ru did not affect the grain size significantly, since VC is a much more effective grain growth inhibitor than Ru [2001Shi]. Also, if Ru resulted in a significant decrease in grain size, as was observed by Shing *et al*. [2001Shi], then coercivity values would have increased in the same direction as hardness (in Figure 5.17), since coercivity increases as grain size decreases [1995Roe]. This further confirms that solid solution strengthening played a major role in increasing the hardnesses of 80WC-10VC-(10-*x*)Co-*x*Ru and (89.2-*x*)WC-0.8VC-10Co-*x*Ru alloys. The decrease in magnetic saturation shown in Figure 4.46 corresponds to increased solution hardening [2007Rah]. Thus, the magnetic saturation results also confirmed that solution hardening of the (Co) binder phase with Ru contributed to the increase in hardness.

Most hardness indentations had cracks which did not originate from the indentation apex (Figure 4.67), due to initial propagation of cracks during loading which resulted in deviations of the crack paths [1977Vis]. The use of 5, 10, 20 and 50 kg loads for fracture toughness (Table 4.31) instead of the specified 30 kg [2009ISO] could not have affected the results, since the sums of the crack lengths were ≥40 μm, as required by the same standard [2009ISO].

It is known that improving the hardness of the binder phase by modification also helps to improve fracture toughness of the overall alloy, and for a particular binder type, fracture toughness decreases with hardness [1977Vis]. Therefore, the increases of fracture toughness with Ru additions (Figure 4.70) were associated with the change from Co binder system to a Co + Ru system. Similar counter-intuitive observations were made when the Ni binder system was modified by addition of Mo [1977Vis]. The decrease in fracture toughness above 0.4 wt% Ru for the 80WC-10VC-(10-*x*)Co-*x*Ru and (89.6-*x*)WC-0.4VC-10Co-*x*Ru alloys (Figure 4.70) was attributed to increased hardening of the Co + Ru solid solution. Also, for the (89.6-*x*)WC-0.4VC-10Co-*x*Ru alloy series, there was decreased WC grain size above 0.4 wt% Ru (Table 4.26 and Figure 4.58), decreasing the fracture toughness (Figure 4.70). For the (89.2-*x*)WC-0.8VC-10Co-

*x*Ru alloy series, additions of Ru did not affect fracture toughness (Figure 4.70) due to no significant decrease in WC grain size (Table 4.26 and Figure 4.58) and little solid solution hardening, because Ru was added to Co without any Co substitution, resulting in a lower concentration of Ru in (Co) binder than for if Co was replaced. The increase in the binder volume fraction for the (89.2-*x*)WC-0.8VC-10Co-*x*Ru could have contributed to increased fracture toughness as was reported by previous workers [1978Lee]. Since hardness and toughness generally change opposite to each other, the existence of some WC-VC-Co-Ru alloys with greater hardness and toughness than alloys without Ru for the 80WC-10VC-(10-*x*)Co-*x*Ru, (89.6-*x*)WC-0.4VC-10Co-*x*Ru and (89.2-*x*)WC-0.8VC-10Co-*x*Ru (wt%) alloys (Figure 4.70), suggests that for the same hardnesses, the alloys with Ru are likely to be tougher than those without Ru.

Generally, there was an inverse hardness-fracture toughness relationship among the alloy series (Figure 5.18), as expected. The direct trend for the (89.2-*x*)WC-0.8VC-10Co-*x*Ru alloys was due binder hardening, without sufficient to lower fracture toughness, but also the values for this series were close together, so that this apparent direct relationship might not be valid, although the errors were very small, such that they are not seen beneath the symbols.

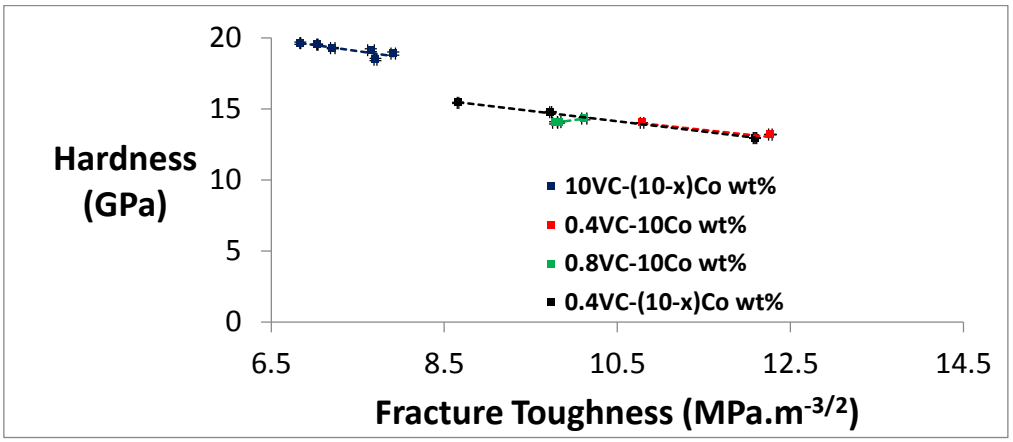

Figure 5.18. Hardness-fracture toughness trends for 80WC-10VC-(10-x)Co-xRu, (89.6-x)WC-0.4VC-10Co-xRu, (89.2-x)WC-0.8VC-10Co-xRu and 89.6WC-0.4VC-(10-x)Co-xRu

(wt%) alloys.

5.4. Wear

All alloys had WC grains less than 1 μm and such small grains were reported to be resistant to microfracture [1985Lar]. The fragmentation of WC that was seen on the 80WC-10VC-7.0Co-3.0Ru (wt%) alloy (Figure 4.71) helps to relieve the alloys from stresses [2001Eng]. The presence of cobalt also helps to resist high pressures which are encountered during sliding wear [2001Eng]. The existence of hard and binder phases under compressive and tensile stresses [1985Lar] could be the reason for the good wear resistance of cemented carbides. The addition of VC helped inhibit WC grain growth. Ruthenium modified the Co binder by forming a (Co + Ru) solid solution. Since the wear of WC-Co carbides is explained in terms of binder removal followed by fracture of intergranular boundaries and fragmentation of the carbide grains [2004Pir], the presence of VC and Ru should have disrupted the wear process.

From Figures 4.73 and 4.74, it was deduced that finer grained alloys (Figure 4.73) were associated with a more distinct 'running-in' stage than the coarser grains (Figure 4.74). The initial increase in friction coefficients (Figures 4.73 and 4.74) occurs during the formation of the contacts between the balls and samples [2010Bon]. High initial volumetric wear rates are associated with very steep 'running-in' stages [2011Bon]. Thus, the more gradual increases in the friction coefficients associated with the coarser grains (Figure 4.75) suggested that coarser grained alloys had lower initial volumetric wear rates than the finer 80WC-10VC-(10-*x*)Co-*x*Co alloys (Figure 4.74). The initial oscillations involve a lot of fragmentation and deformation [2010Bon], and these might have been stronger for the 80WC-10VC-(10-*x*)Co-*x*Co alloys. The temporary drop in the coefficient, after the running-in stage that is very prominent for the 80WC-10VC-(10-*x*)Co-*x*Ru (wt%) alloys (Figure 4.73) is a characteristic of such fine grained alloys [2011Bon]. Changes in sliding contact surface have also been reported to cause the drop in μ [2011Bon, 2011Bon1]. The state steady regions after the running-in stage (Figures 4.73 and 4.74) suggest equilibrium wear conditions [2010Bon, 2011Bon, 2011Bon1]. As the asperities were worn down during sliding, the surfaces became smoother, decreasing friction and

fluctuations, and thus a state of equilibrium [2010Bon]. Smearing of the wear balls might have contributed to ball-sample contact smoothness. The fluctuations for Alloy 5, 80WC-10VC-8.0Co-2.0Ru (wt%) (Figure 4.73) suggest that the sliding contact surface was changing throughout the sliding oscillations. Since the average μ were close among the alloy series, and considering errors and also that there were no definite trends, the different friction behaviors might not be significant.

The average μ increased with binder content [2006Pir]. Similar trends were made for the 80VC-10VC-(10-*x*)Co-*x*Ru, (89.6-*x*)WC-0.4VC-10Co-*x*Ru and 89.6VC-0.4VC-(10-*x*)Co-*x*Ru (wt%) alloys (Figure 5.19). However, an opposite trend was observed for the (89.2-*x*)WC-0.8VC-10Co-*x*Ru (wt%) alloys (Figure 5.19). It therefore appears that the direct relationship between μ and binder content might not be applicable to all cemented carbide systems.

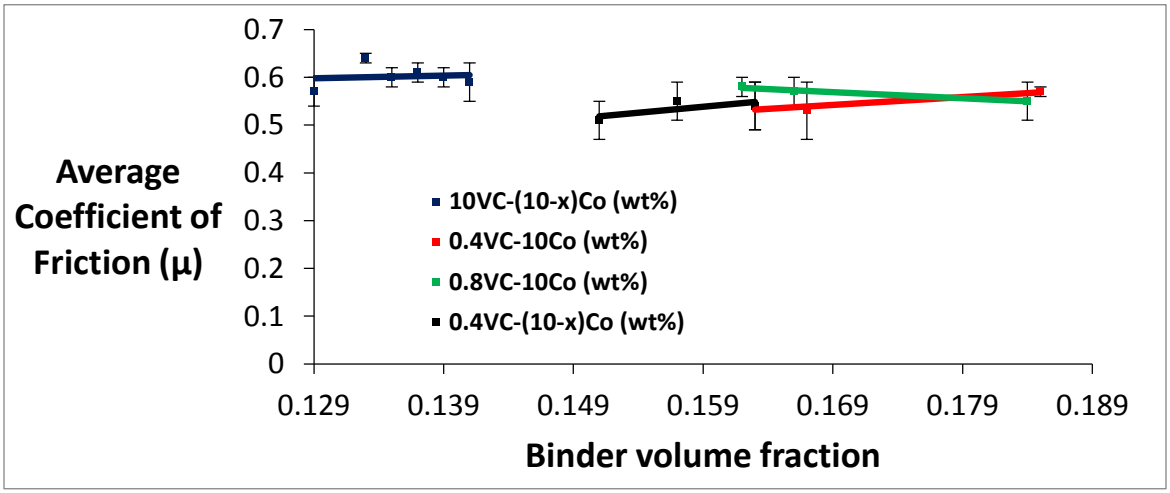

Figure 5.19. Relationship between average coefficient and binder volume fraction for the 80WC-10VC-(10-x)Co-xRu, (89.6-x)WC-0.4VC-10Co-xRu, (89.2-x)WC-0.8VC-10Co-xRu and 89.6WC-0.4VC-(10-x)Co-xRu (wt%) alloys.

For WC-Co alloys, low μ values were attributed to low WC intercept lengths [2006Sai]. In this work, no conclusive findings were made regarding the influence of WC grain size on μ (Figure

5.20). A direct relationship between μ and mean WC intercept length was seen for the (89.2-*x*)WC-0.8VC-10Co-*x*Ru and 89.6VC-0.4VC-(10-*x*)Co-*x*Ru (wt%) alloys. However, for the (89.6-*x*)WC-0.4VC-10Co-*x*Ru alloys, an inverse relationship was seen, and for the 80VC-10VC-(10-*x*)Co-*x*Ru series no definite relationship was seen. Therefore, the friction behavior was not only influenced by grain size. The high μ errors also imply the trends might not be conclusive.

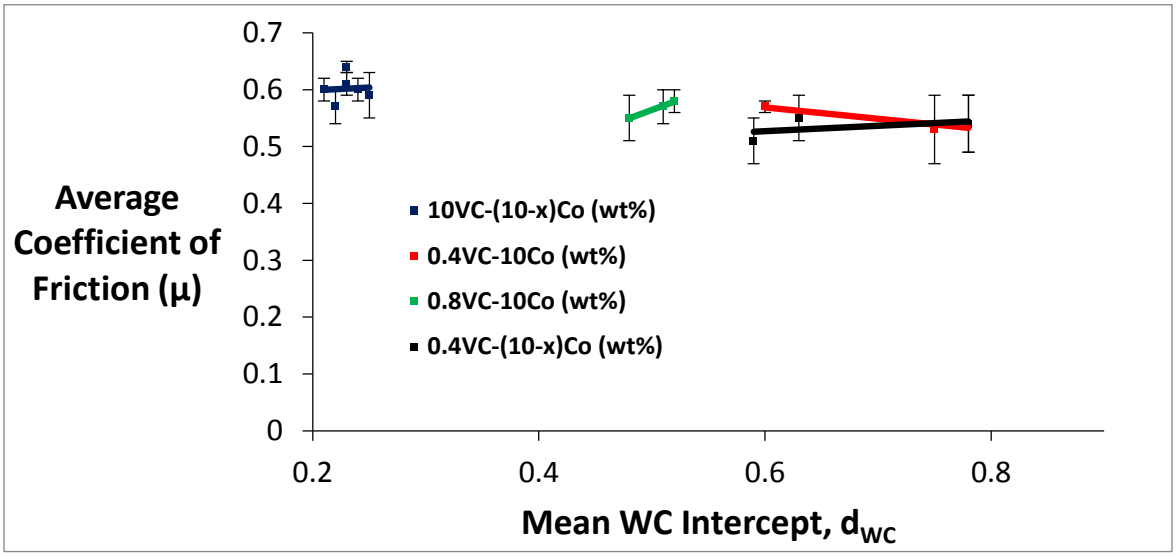

Figure 5.20. Relationship between average coefficient and the WC mean intercept length for the 80WC-10VC-(10-x)Co-xRu, (89.6-x)WC-0.4VC-10Co-xRu, (89.2-x)WC-0.8VC-10Co-xRu and 89.6WC-0.4VC-(10-x)Co-xRu (wt%) alloys.

Pirso *et al*. [2004Pir] found no definite trend between coefficient of friction and wear rate, in agreement with Figure 5.21. There was a generally an inverse relationship between the average μ and alloy wear rate for the 80VC-10VC-(10-*x*)Co-*x*Ru and (89.6-*x*)WC-0.4VC-10Co-*x*Ru (wt%) alloys. For the (89.2-*x*)WC-0.8VC-10Co-*x*Ru and 89.6VC-0.4VC-(10-*x*)Co-*x*Ru (wt%) alloys, a direct relationship was seen. Therefore, there was no clear relationship between μ and alloy wear rates. The measured μ results for the 80WC-10VC-(10-*x*)Co-*x*Ru (wt%) alloys (Table 4.35) were actually higher than those for other alloy series. Thus, the reduction of μ due to complex tribofilms associated with VC [2001Are], might have occurred

even at low VC contents (0.4 wt%).

Wear resistance of WC-Co cemented carbides was found to be influenced by binder content, binder mean free path, WC grain size and hardness [1997Jia, 2006Sai, 2004Pir, 2009Bon, 2010Bon]. However, sliding wear is a very complex phenomenon which involves aspects such as temperature, pressure, counter material, formation of surface films, phase transformations and lubrication [2001Eng]. The effects these factors have not been well investigated. Therefore, it is difficult to predict sliding wear from a single bulk property. In this study, environmental factors were the same to be able to assess the effect of the compositional differences.

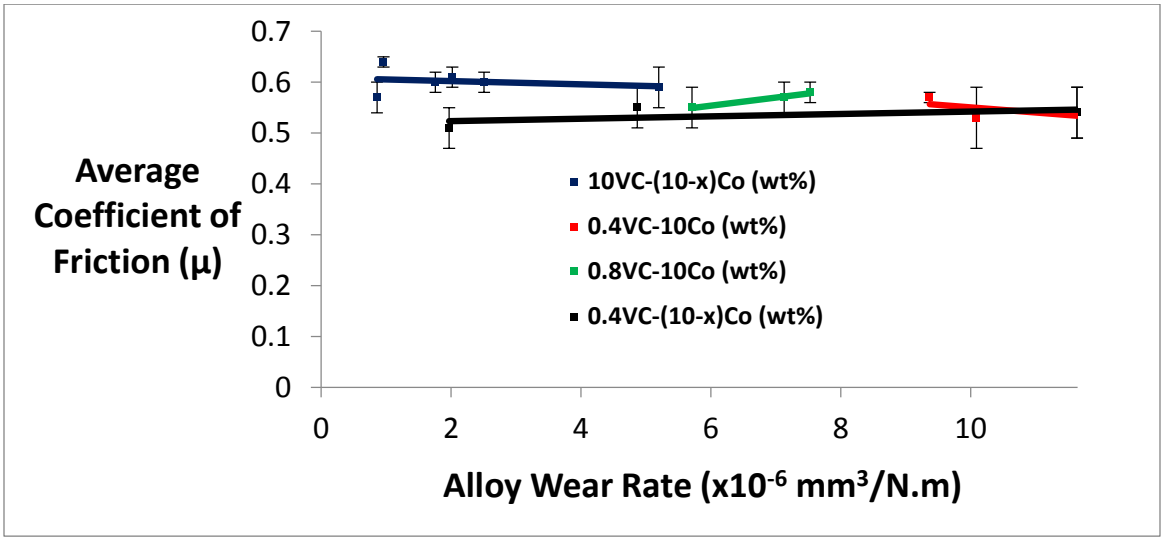

Figure 5.21. Relationship between average coefficient and the alloy wear rate for the 80WC-10VC-(10-x)Co-xRu, (89.6-x)WC-0.4VC-10Co-xRu, (89.2-x)WC-0.8VC-10Co-xRu and 89.6WC-0.4VC-(10-x)Co-xRu (wt%) alloys.

Decreasing the binder volume fraction was found to decrease the wear rate of WC-Co alloys [2004Pir, 2006Sai]. From Figure 5.22, it was deduced that increased binder volume fractions increased the wear of 80WC-10VC-(10-*x*)Co-*x*Ru and 89.6WC-0.4VC-(10-*x*)Co-*x*Ru (wt%) alloys. Therefore, decreased binder volume fractions with Ru additions contributed to the

improved wear resistance for the 80WC-10VC-(10-*x*)Co-*x*Ru and 89.6WC-0.4VC-(10-*x*)Co-*x*Ru (wt%) alloys (Figure 4.76). Opposite results were seen for the (89.6-*x*)WC-0.4VC-10Co-*x*Ru and (89.2-*x*)WC-0.8VC-10Co-*x*Ru (wt%) (Figure 5.22). Although the binder volume fraction was increasing with Ru additions for the (89.6-*x*)WC-0.4VC-10Co-*x*Ru and (89.2-*x*)WC-0.8VC-10Co-*x*Ru (wt%) alloys, the binder hardness was increasing due to solid solution strengthening. Binder hardening could thus have contributed to the decrease in wear rate seen in Figure 4.76 for the (89.6-*x*)WC-0.4VC-10Co-*x*Ru and (89.2-*x*)WC-0.8VC-10Co-*x*Ru (wt%) alloys.

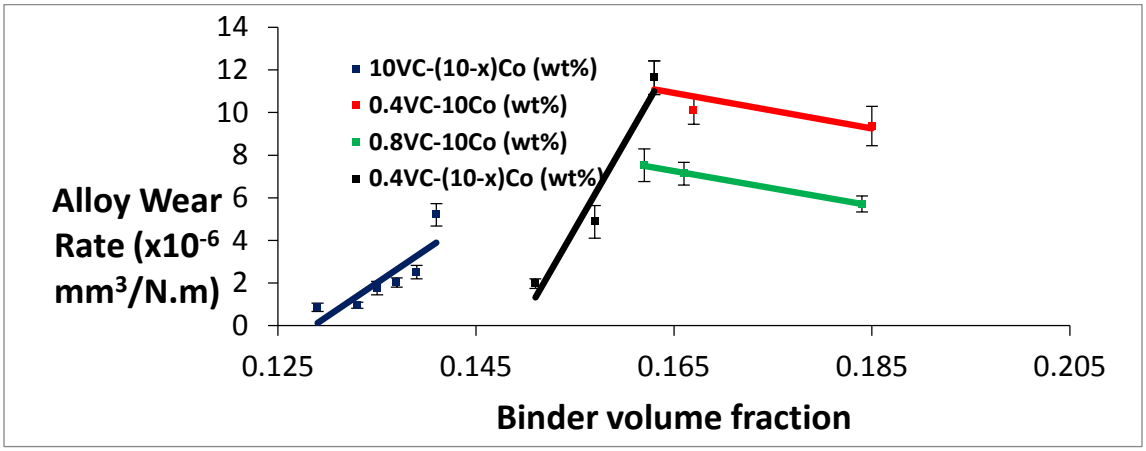

Figure 5.22. Relationship between the alloy wear rate and binder volume fraction for the 80WC-10VC-(10-x)Co-xRu, (89.6-x)WC-0.4VC-10Co-xRu, (89.2-x)WC-0.8VC-10Co-xRu and 89.6WC-0.4VC-(10-x)Co-xRu (wt%) alloys.

Reducing the binder mean free path was also found to decrease wear rate of cemented carbides [1997Jia, 2006Sai]. A direct relationship was also observed between alloy wear rate and binder mean free path for the 80WC-10VC-(10-*x*)-*x*Ru, 89.6WC-0.4VC-(10-*x*)Co-*x*Ru and (89.6-*x*)WC-0.4VC-10Co-*x*Ru (wt%) (Figure 5.23). Therefore the decreased binder mean free paths with Ru (Figure 4.64) contributed to the improved wear resistance for the 80WC-10VC-(10-*x*)-*x*Ru, 89.6WC-0.4VC-(10-*x*)Co-*x*Ru and (89.6-*x*)WC-0.4VC-10Co-*x*Ru (wt%) alloys (Figure 4.76). Decreasing the binder mean free path increases the resistance to plastic deformation of the binder phase [2004Pir]. However, for the (89.2-*x*)WC-0.8VC-10Co-*x*Ru (wt%) alloys, binder mean free path increased with Ru (Figure 4.64) but the wear rate decreased with Ru content (Figure 4.76).

This gave the inverse relationship between binder mean free path and wear rate (Figure 5.23) for the (89.2-*x*)WC-0.8VC-10Co-*x*Ru (wt%) alloys. The results suggest exceptions to the direct relationship between binder mean free path and wear rate. It was also reported by Saito *et al*. [2006Sai] that the binder mean free path alone cannot explain wear rate.

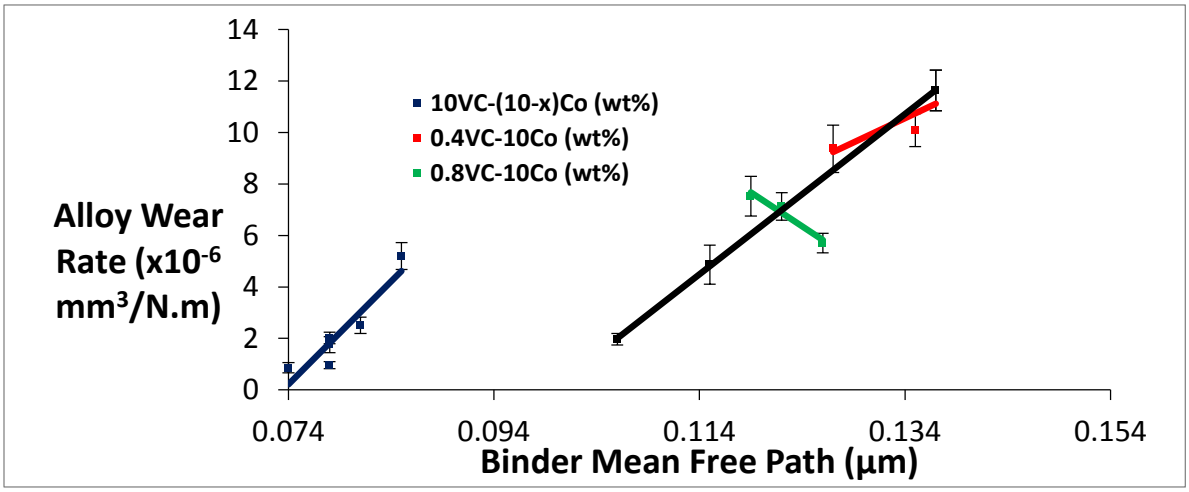

Figure 5.23. Relationship between the alloy wear rate and binder mean free path for the 80WC-10VC-(10-x)Co-xRu, (89.6-x)WC-0.4VC-10Co-xRu, (89.2-x)WC-0.8VC-10Co-xRu and 89.6WC-0.4VC-(10-x)Co-xRu (wt%) alloys.

Jia *et al*. [1997Jia] found that larger WC grains were associated with decreased wear rates. On the other hand, larger WC grains decrease hardnesses [1997Jia], which increased wear rates [1997Jia, 1997She, 2004Pir]. Jia *et al*. [1997Jia] therefore concluded that the contribution of WC grain size on the overall sliding wear rate was greater than that of hardness. In this study, the alloy wear rate increased with mean WC intercept length (Figure 5.24), in contradiction with Jia *et al*. [1997Jia]. The contradiction between results of this study and those of Jia *et al*. [1997Jia] suggests that the effect of hardness on wear resistance might have been greater than that of WC grain size. It is likely that the combination of binder hardening and WC decrease resulted in hardnesses with more effect on wear resistance than WC grain size. Jia *et al*. [1997Jia] studied WC-Co alloys, with hardnesses that increase by decreasing the WC grain size, but in this study the hardnesses were increased by a combination of decreased WC grain sizes and binder solid

solution strengthening. The decreased wear rate as hardnesses increased for all the alloy series is shown in Figure 5.25.

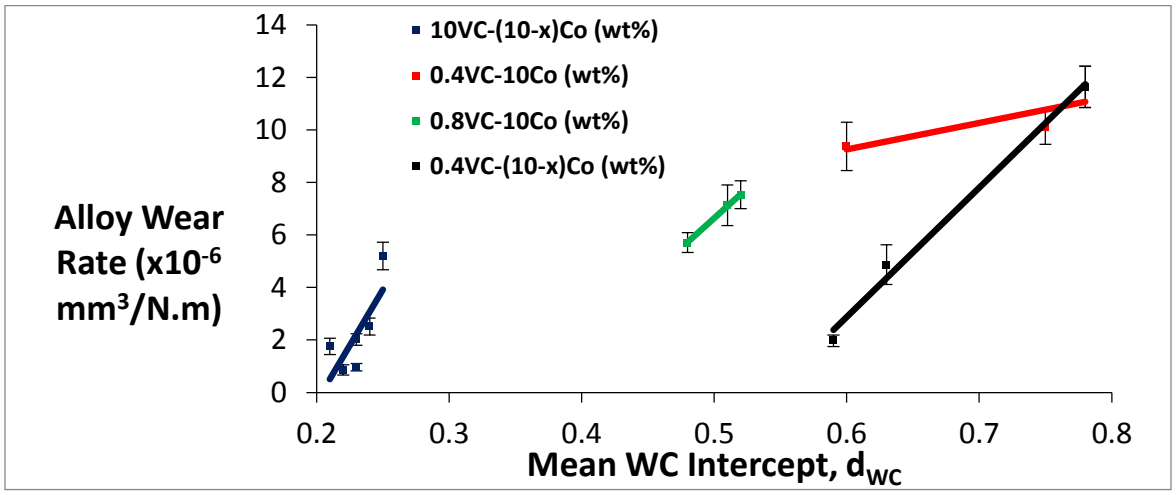

Figure 5.24. Relationship between the alloy wear rate and the WC mean intercept length for the 80WC-10VC-(10-x)Co-xRu, (89.6-x)WC-0.4VC-10Co-xRu, (89.2-x)WC-0.8VC-10Co-xRu and 89.6WC-0.4VC-(10-x)Co-xRu (wt%) alloys.

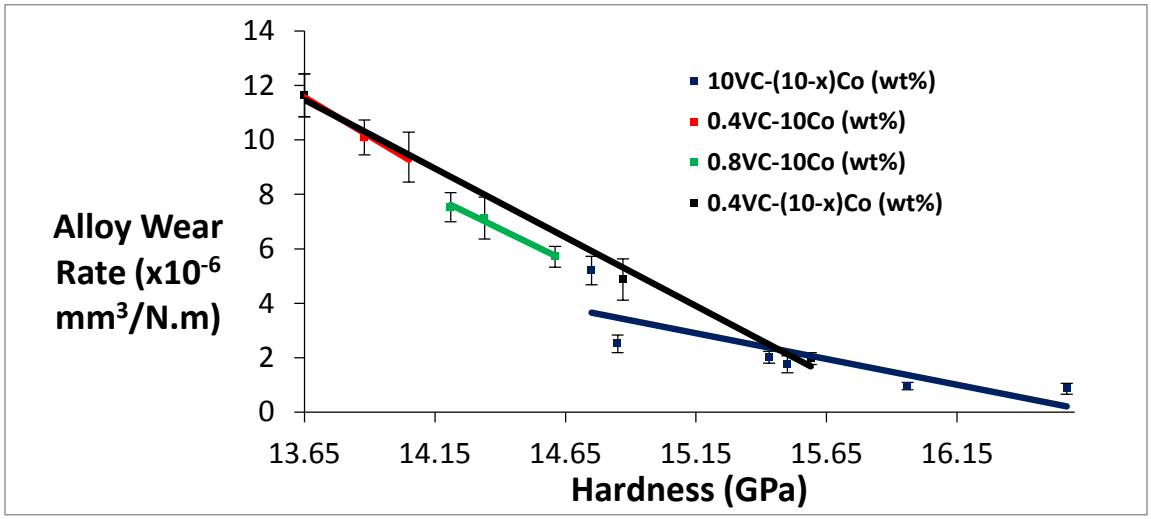

Figure 5.25. Relationship between the alloy wear rate and hardness for the 80WC-10VC-(10-x)Co-xRu, (89.6-x)WC-0.4VC-10Co-xRu, (89.2-x)WC-0.8VC-10Co-xRu and 89.6WC-0.4VC-(10-x)Co-xRu (wt%) alloys.

Increasing fracture toughness was found to decrease the wear rate of composite sialon ceramics [2003Jon]. Only the (89.2-*x*)WC-0.8VC-(10-*x*)Co-*x*Ru (wt%) alloys had decreased wear rates as fracture toughness increased (Figure 5.26.). Thus, for the (89.2-*x*)WC-0.8VC-(10-*x*)Co-*x*Ru (wt%) alloys, the increased fracture toughness with Ru content (Figure 4.70) could have contributed to the improved wear resistance (Figure 4.76). The higher the fracture toughness, the more difficult would be the crack propagation during wear. Due to the complexity of wear, fracture toughness on its own cannot be used predict wear resistance since other factors are also involved. This gave the increase in wear rate for the other three alloy series, although there was a general increase in fracture toughness.

The normalised results (Figure 5.27) show that the 80WC-10VC-(10-*x*)Co-*x*Ru (wt%) alloys had the lowest wear rates, based on the gradients (according to Equation 2.6). The 80WC-10VC-(10-*x*)Co-*x*Ru (wt%) alloys had the highest VC content, and that might have led to them having the lowest wear rates.

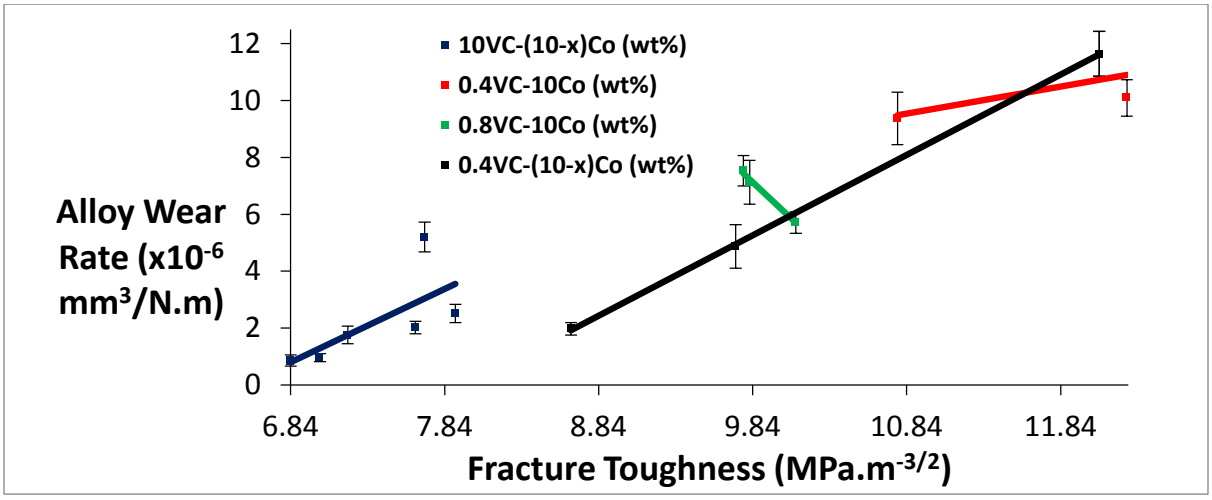

Figure 5.26. Relationship between the alloy wear rate and fracture toughness for the 80WC-10VC-(10-x)Co-xRu, (89.6-x)WC-0.4VC-10Co-xRu, (89.2-x)WC-0.8VC-10Co-xRu and 89.6WC-0.4VC-(10-x)Co-xRu (wt%) alloys.

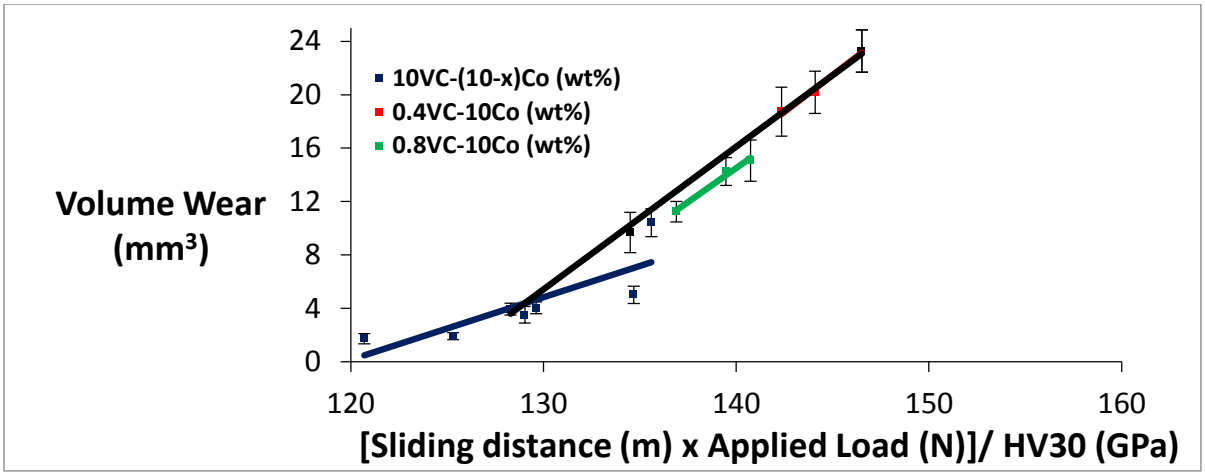

Figure 5.27. Relationship between the alloy wear rate and hardness for the 80WC-10VC-(10-x)Co-xRu, (89.6-x)WC-0.4VC-10Co-xRu, (89.2-x)WC-0.8VC-10Co-xRu and 89.6WC-0.4VC-(10-x)Co-xRu (wt%) alloys.

Since a direct relationship is expected between coercivity and hardness [1985Lau], that in turn has a direct relationship with wear resistance [1997Jia, 1997She, 2004Pir], a definite relationship between coercivity and wear resistance is therefore anticipated. The presence of two sets of trends (Figure 5.28) suggests a complex relationship between coercivity and wear resistance for WC-VC-Co-Ru alloys that are more complex than WC-Co alloys. However, as to be expected, the trends of Figure 5.28 are consistent with those from Figures 5.12 and 5.25. Thus, coercivity results can also be used to compare the wear resistance of WC-VC-Co-Ru alloys.

The wear resistance capabilities of cemented carbides are mainly exploited in cutting operations. It was therefore important to further establish the cutting potential of WC-VC-Co-Ru alloys using the method by Viswanadham *et al*. [1977Vis]. Viswanadham *et al*. [1977Vis], found a linear relationship between the inverse of crack resistance (W_G) and hardness (H) (Equation 5.9), and used this relationship to compare the cutting properties of alloy systems.

$1/W_G = AH - B$ Equation 5.9.

where A and B are constants.

Using the same approach as Viswanadham *et al*. [1977Vis], the cutting properties for the WC-VC-Co-Ru alloys were estimated from the linear plot of inverse crack resistance and hardness (Figure 5.29). Only alloys with Ru were used to estimate the cutting properties for the WC-VC-Co-Ru alloys.

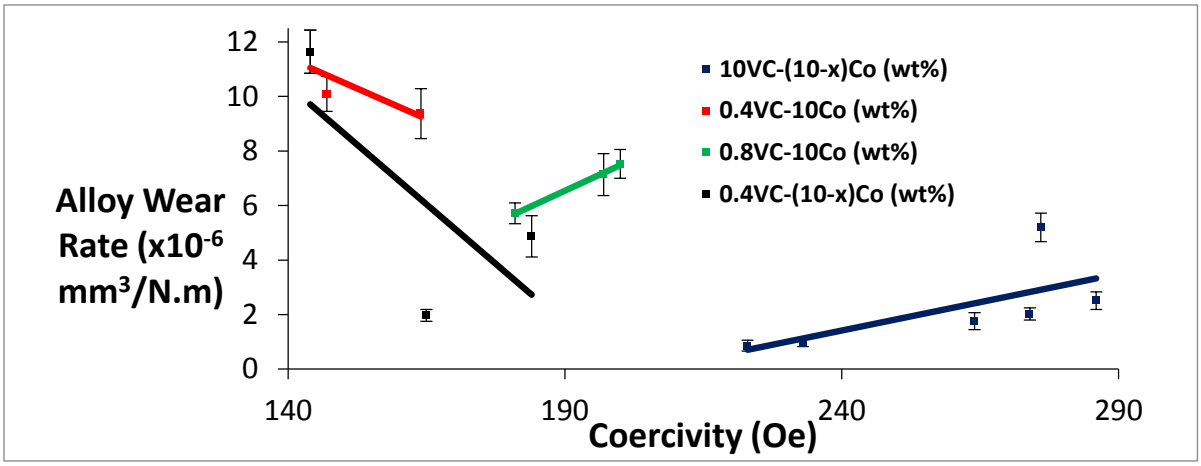

Figure 5.28. Relationship between the alloy wear rate and coercivity for the 80WC-10VC-(10-x)Co-xRu, (89.6-x)WC-0.4VC-10Co-xRu, (89.2-x)WC-0.8VC-10Co-xRu and 89.6WC-0.4VC-(10-x)Co-xRu (wt%) alloys.

From Figure 5.29, it was deduced that the overall relationship between crack resistance and hardness for WC-VC-Co-Ru alloys followed the equation:

$1/W_G = 3 \times 10^{-5}H - 0.0374$ ($10^3/W_G = 0.03H - 37.4$) Equation 5.10

For the (89.6-*x*)WC-0.4VC-10Co-*x*Ru, (89.2-*x*)WC-0.8VC-10Co-*x*Ru and 89.6WC-0.4VC-(10-*x*)Co-*x*Ru (wt%) alloys, i.e (0.4 and 0.8)VC (wt%) alloys, the equation was:

$1/W_G = 3 \times 10^{-5}H - 0.0318$ ($10^3/W_G = 0.03H - 31.8$) Equation 5.11

For the 80WC-10VC-(10-*x*)Co-*x*Ru (wt%) alloys, the following equation was obtained:

$1/W_G = 1 \times 10^{-4}H - 0.2107$ ($10^3/W_G = 0.1H - 210.7$) Equation 5.12

Using the results of Viswanadham *et al*. [1977Vis], it was deduced that alloys with greater B/A values had better crack resistance for any given hardness. For the WC-VC-Co-Ru alloys, a general B/A value of ~1247 was found using Equation 5.10. For the (0.4 and 0.8)VC and 10VC (wt%) alloys B/A, values of ~1060 and ~2107, were found. For WC-Co and (Ti,V)C-Ni alloys [1977Vis], B/A values of ~1083 and ~734, respectively, were deduced. This implies that WC-VC-Co-Ru alloys are generally expected to have better crack resistance than WC-Co and (Ti,V)C-Ni alloys for any given hardness. However, for the low VC alloys, 0.4 and 0.8 VC (wt%) alloys, the B/A value was less than that for WC-Co alloys, suggesting lower cutting potential. The higher B/A values 80WC-10VC-(10-*x*)Co-*x*Ru (wt%) alloys than the WC-Co and (Ti,V)C-Ni alloys suggests better cutting potential for the 80WC-10VC-(10-*x*)Co-*x*Ru (wt%), and is consistent with crack resistance results (Figure 4.69) and previous work [1996Luy]. From Figure 4.69, it was deduced that 80WC-10VC-(10-*x*)Co-*x*Ru alloys would have better crack resistance for any hardness than WC-VC-Co alloys, which in turn were found to have better toughness for any hardness than WC-Co alloys [1996Luy]. Luyckx *et al*. [1996Luy] also added 10 wt% VC to WC-CO alloys but without any Ru additions. It therefore appears that higher VC contents improve the cutting properties in both WC-VC-Co and WC-VC-Co-Ru alloys.

Viswanadham *et al*. [1977Vis] observed that A has a value of ~0.02 for any binder system, which was comparable to ~0.03 found in Equations 5.10 and 5.11, but very different from the value of ~210 for the 80WC-10VC-(10-*x*)Co-*x*Ru (wt%) alloys. This difference in the A (slope) value might have emanated from the load dependence of Palmqvist crack length for WC-VC-Co-Ru alloys as shown in Tables 4.31 and 4.33. The consistency in A values found by Viswanadham *et al*. [1977Vis] might have been as a result of use of using load independent alloys. Although Viswanadham *et al*. [1977Vis] found relatively close A values, they also highlighted that each carbide/binder system has its unique A and B values. It is therefore imperative to use both A and B values in cutting potential evaluation. Viswanadham *et al*. [1977Vis] also mentioned that the constants A and B, for a particular carbide/binder system are independent of factors such as grain

size, grain distribution and carbide/binder volume. In this study, there was a difference in the B/A ratios between the low and high VC alloys of the WC-VC-Co-Ru carbide/binder system, contrary to Viswanadham *et al*. [1977Vis]. This contradiction might have arisen from that at high VC content there was the formation of the (V,W)C phase that was not detected for the low VC alloys, causing differences in the apparent carbide/binder systems, and hence, the differences in the B/A values. Therefore, the assertion that a carbide/binder system has its unique A and B values [1977Vis] has exceptions.

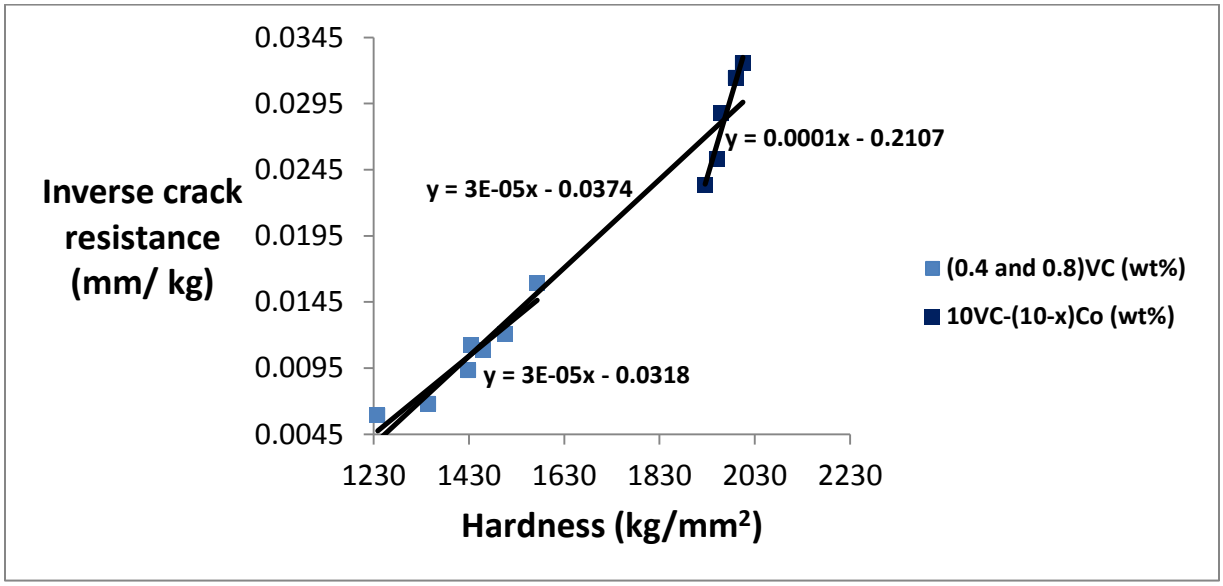

Figure 5.29. Relationship between the inverse crack resistance and hardness for the 80WC-10VC-(10-x)Co-xRu, (89.6-x)WC-0.4VC-10Co-xRu, (89.2-x)WC-0.8VC-10Co-xRu and 89.6WC-0.4VC-(10-x)Co-xRu (wt%) alloys.

5.5. Corrosion

The higher OCPs with Ru additions, in all alloy series for all corrosion environments (Figures 4.79, 4.98 and 4.113), suggest to increased spontaneity of passive film formation, making alloy dissolution more difficult [2011Pot]. It seems that VC had no effect on the formation of passive films since there was no distinct correlation between VC contents and OCPs for all three corrosion environments as plotted in Figures 4.79, 4.98 and 4.113. This deduction is consistent with Machio [2005Mac] who found VC not to be as spontaneously passivating as Ru.

The active region that was present in all polarisation curves (Figures 4.82, 4.83, 4.101, 4.102, 4.116 and 4.117) was due to oxidation of the binder [1997Hum]. This formed a thick surface deposit [1996Hum] which eventually caused the decreased current in the polarisation curves (Figures 4.82, 4.83, 4.101, 4.102, 4.116 and 4.117) creating pseudopassive regions, with higher current densities than true passivation. Human *et al*. [1998Hum] reported that the thick surface deposit is formed in layers [1998Hum]. It was also reported [1996Hum] that during pseudopassivation, the surface of the binder phase would be shielded by the WC network that would have been raised above the binder phase, since some of the binder phase would be depleted during oxidation. The presence of pores and cracks (e.g. Figure 4.124), could have created little contact between the electrolyte and the conductive metallic surface beneath the oxidation film, giving the low current densities associated with the pseudopassive regions. According to Human *et al*. [1998Hum], these pores would however be too small for ionic movements. Some of the cracks could have formed as the samples dried [2011Pot].

Human *et al*. [1997Hum] explained that the oxidation of WC caused the increased current at potentials above the pseudopassive region as potential increased (Figures 4.82, 4.83, 4.101, 4.102, 4.116 and 4.117). The polarisation curves (Figures 4.82, 4.83, 4.101, 4.102, 4.116 and 4.117) showed that, as expected, the reactions depended on the alloy compositions and the corrosion environment. The polarisation behaviour of the alloys responded to the addition of Ru and the different corrosion environments had different general polarisation characteristics. Since

Human *et al*. [1997Hum] reported that oxidation of WC occurred at potentials above the pseudopassive regions; the narrowing of the pseudopassive regions with Ru additions suggested easier WC oxidation. The formation of Co and W oxides was shown by XRD and Raman spectroscopy (Figures 4.91, 4.92, 4.103, 4.104, 4.116 and 4.117). The pseudopassive behavior exhibited during polarisation also confirmed the existence of W and Co oxides [1998Hum]. The simultaneous dissolution of W and Co was also found by Hochstrasser-Kurz *et al*. [2007Hoc]. The oxide films formed at the metal/corrosion layer interface caused the current decreases in the polarisation curves (Figures 4.82, 4.83, 4.101, 4.102, 4.116 and 4.117).

The oxidation of WC occurs according to the following equation [1985Kae]:

$$WC + 5H_2O \rightarrow WO_3 + CO_2 + 10H^+ + 10e^- \qquad \text{Equation 5.13}$$

The decrease in the passive current density with Ru (Figures 4.82, 4.83, 4.101, 4.102, 4.116 and 4.117) could also be due to the replacement with of Co atoms with Ru atoms as Co atoms dissolved by the following oxidation reaction [1986Don]:

$$Co \rightarrow Co^{2+} + 2e^- \qquad \text{Equation 5.14}$$

The dissolution reaction was confirmed by the pink colour of solutions (especially in H_2SO_4), indicating the presence of $[Co(H_2O)_6]^{2+}$ [1986Don]. However, since XRD peaks showed the presence of Co, not all Co was dissolved in the three corrosive environments, contrary to previous findings on cemented carbides [2011Pot, 2014Pot, 2013Mac]. It is not very clear why in previous work [2011Pot, 2014Pot, 2013Mac] no Co was left in the alloys after corrosion. However, they [2011Pot, 2014Pot, 2013Mac] found some Co oxides and sulphates, such as $Co_2(CO)_8$, $CoSO_4$, CoO, Co_3O_4 and Co_3S_4, similar to findings of this study.

In H_2SO_4 and NaCl, the effect of VC on the pseudopassivation range was not very clear (Figures 5.30 and 5.31). In synthetic mine water, 3 wt% Ru resulted in a wider pseudopassive region for

the 89.6WC-0.4VC-7.0Co-3.0 alloy than for 80WC-10VC-7.0Co-3.0 (wt%) (Figure 5.32). The electrochemical reactions occurred differently in the three environments. There was easier WC oxidation in synthetic mine water and NaCl than in H_2SO_4 indicated by the wider pseudopassive ranges for the alloys in H_2SO_4 (Figures 4.82, 4.83, 4.101, 4.102, 4.116 and 4.117). The existence of clear current density peaks for polarisation in H_2SO_4 (Figures 4.82 and 4.83) indicated that the binder phase was a Co solid solution (with Ru) since for pure Co, the current gradually levels off in acids [1996Hum]. Clear current density peaks were also observed for WC-Co-Ru alloys in H_2SO_4 [2011Pot], and in NaCl [2014Pot]. In synthetic mine water, no clear current density peaks were seen for the low VC content alloy series with Ru substituting WC, i.e. the (89.6-*x*)WC-0.4VC-(10-*x*)Co-*x*Ru and (89.2-*x*)WC-0.8VC-(10-*x*)Co-*x*Ru (wt%) alloys (Figure 4.117). This particular behaviour might have been caused by lower concentrations of Ru in the binder when Ru replaced WC instead of Co. At lower concentrations, Ru might have caused less pseudopassivation. The existence of clear critical current densities for the 89.6WC-0.4VC-(10-*x*)Co-*x*Ru alloys (especially Alloy 14) (Figure 4.117) showed that the critical current densities for the (89.6-*x*)WC-0.4VC-(10-*x*)Co-*x*Ru and (89.2-*x*)WC-0.8VC-(10-*x*)Co-*x*Ru alloys were affected by Ru concentration, not the low VC content.

Although the effect of varying the VC content was not as clear as that of varying Ru content, it appears that the presence of VC affected the influence of Ru on pseudopassivation (Figures 4.82, 4.83, 4.101, 4.102, 4.116 and 4.117). As mentioned earlier, the addition of Ru caused the pseudopassivation range to become narrower (Figures 4.82, 4.83, 4.101, 4.102, 4.116 and 4.117), suggesting that oxidation of WC was easier with Ru additions. For alloys without VC in H_2SO_4 [2011Pot] and NaCl [2014Pot], the addition of Ru decreased the pseudopassivation range to a significantly less extent than observed in this work. Thus, the presence of VC might have affected the binder and WC oxidation reactions by reducing the potential gap for these reactions.

The decrease in cathodic slopes with Ru additions for all alloys in all environments (Tables 4.36, 4.38, 4.40) was reported [1998Wol] to be indication of decreased hydrogen overpotential as the cathodic reaction rate increased. The values for the anodic Tafel slopes did not follow any

distinct trend, with respect to either Ru or VC (Tables 4.36, 4.38 and 4.40). Similar results were observed for WC-Co-Ru alloys [2011Pot, 2014Pot], and it was suggested that Ru specifically affected the cathodic sites resulting in improved hydrogen evolution and consequently increased corrosion kinetics.

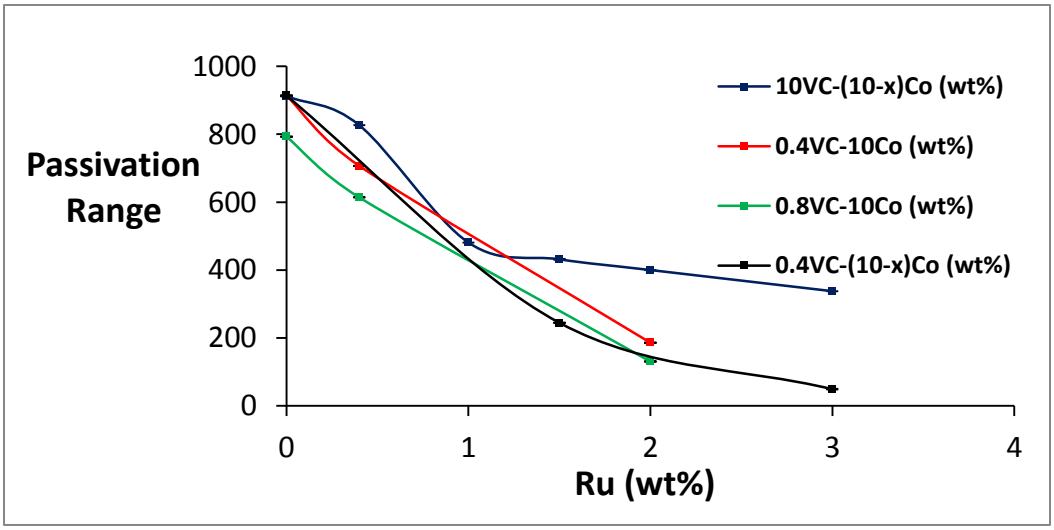

Figure 5.30. Passivation ranges for the 80WC-10VC-(10-x)Co-xRu, (89.6-x)WC-0.4VC-10Co-xRu, (89.2-x)WC-0.8VC-10Co-xRu and 89.6WC-0.4VC-(10-x)Co-xRu (wt%) alloys during polarisation in 1 M H_2SO_4.

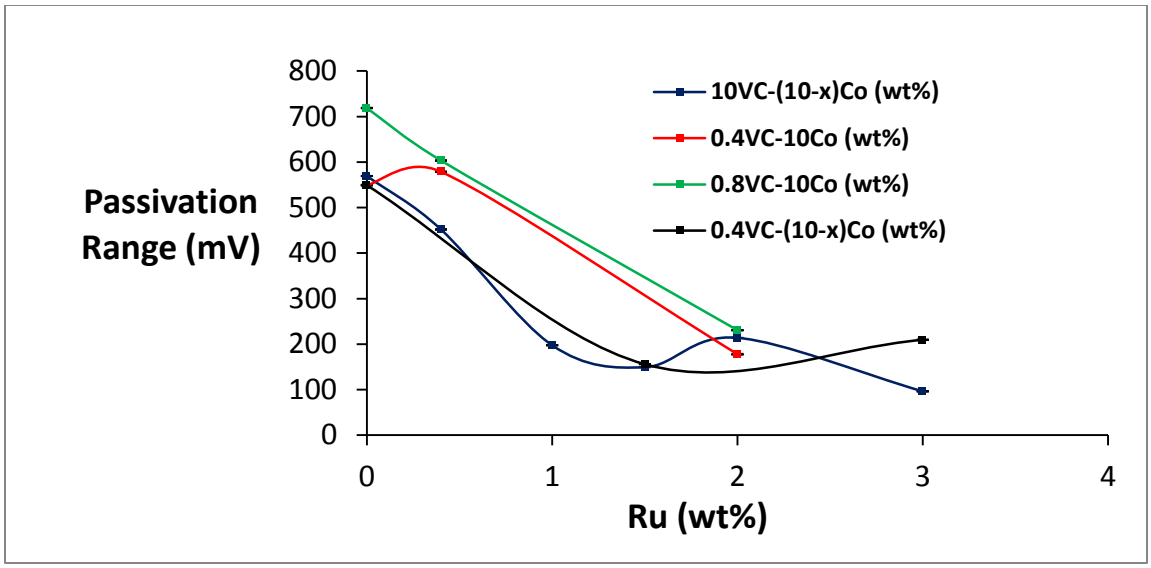

Figure 5.31. Passivation ranges for the 80WC-10VC-(10-x)Co-xRu, (89.6-x)WC-0.4VC-10Co-xRu, (89.2-x)WC-0.8VC-10Co-xRu and 89.6WC-0.4VC-(10-x)Co-xRu (wt%) alloys during polarisation in 1 M NaCl.

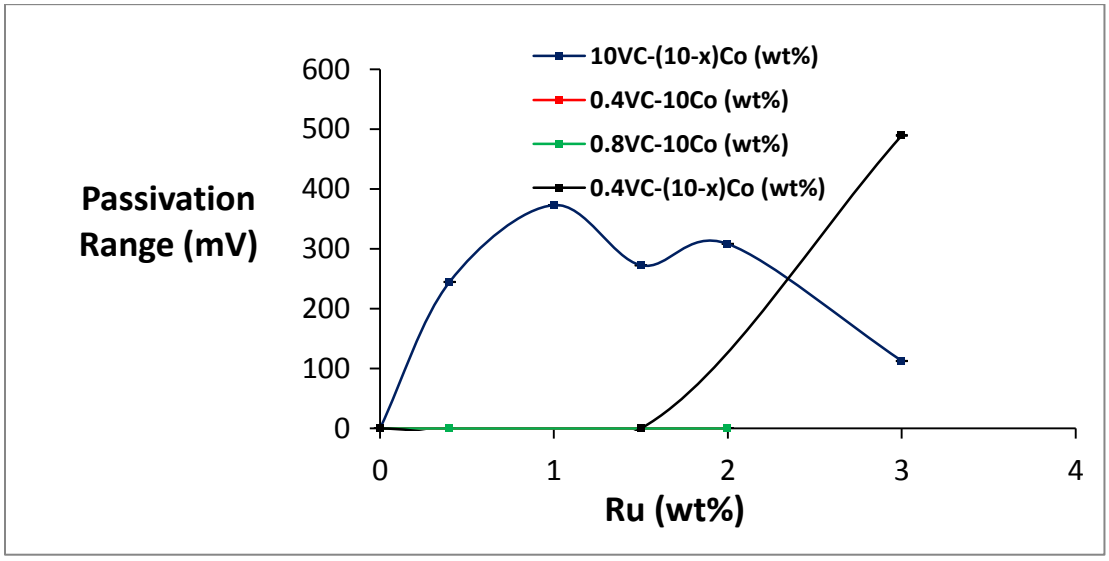

Figure 5.32. Passivation ranges for the 80WC-10VC-(10-x)Co-xRu, (89.6-x)WC-0.4VC-10Co-xRu, (89.2-x)WC-0.8VC-10Co-xRu and 89.6WC-0.4VC-(10-x)Co-xRu (wt%) alloys during polarisation in synthetic mine water (no pseudopassivation for the (89.6-x)WC-0.4VC-10Co-xRu and (89.2-x)WC-0.8VC-10Co-xRu alloys).

According to Fontana [1987Fon], all corrosion systems can be represented by the following equation:

$$\beta = \frac{\beta_a \beta_c}{2.3(\beta_a + \beta_c)} = 0.026 \text{ V} \qquad \text{Equation 5.15}$$

where:

β = Stern-Geary constant

β_a = Anodic Tafel slope

β_c = Cathodic Tafel slope.

The β values for the WC-VC-Co-Ru alloys are given in Table 5.5.

Table 5.5. β values (V) for WC-VC-Co-Ru alloys for polarisation in 1 M H_2SO_4,1 M NaCl and synthetic mine water (SMW).

Series	Alloy Number	H_2SO_4	NaCl	SMW
80WC-10VC-(10-*x*)Co-*x*Ru	1 to 6	0.014±0.007	0.018±0.009	0.021±0.007
(89.6-*x*)WC-0.4VC-10Co-*x*Ru	7 to 9	0.018±0.008	0.019±0.007	0.027±0.008
(89.2-*x*)WC-0.8VC-10Co-*x*Ru	10 to 12	0.015±0.006	0.014±0.003	0.022±0.007
89.6WC-0.4VC-(10-*x*)Co-*x*Ru	7, 13 and 14	0.018±0.008	0.020±0.007	0.024±0.005
Overall	1 to 14	0.016±0.012	0.017±0.007	0.023±0.007

Considering the errors, for the overall values (Table 5.5), some β values for the WC-VC-Co-Ru alloys were in agreement with the general value for all corrosion systems (0.026) [1986Fon]. Any variations were most likely due to absence of distinct linearity near the corrosion potential as required in the determination of β_a and β_c values [1999AST]. The absence of distinct linearity near the corrosion potential would affect corrosion rate calculations, thus, only immersion test results were used. The β value for synthetic mine water tests was closest to 0.026, and this might be due lower passivities and more linearity near E_{corr} (Figures 4.116 and 4.117). The β values for WC-VC-Co-Ru alloys were closer to 0.026 than for the WC-Co-Ru alloys for all solutions

[2011Pot, 2014Pot]. In 1 M H_2SO_4, a β value of 0.005±0.003 was deduced [2011Pot], and in 1 M NaCl and in synthetic mine water values of 0.007±0.002 and 0.005±0.004 were obtained [2014Pot]. These values were much lower than 0.026, the general value for all corrosion systems [1986Fon]. This significant difference in β values suggests different electrochemical kinetics for this study and Potgieter *et al*. [2011Pot, 2014Pot]. Potgieter *et al*. [2011Pot, 2014Pot] used de-aerated solutions but in this study, the solutions were aerated. Thus, it is not advisable to compare corrosion rates for WC-VC-Co-Ru alloys with those for WC-Co-Ru alloys [2011Pot, 2014Pot].

The calculated corrosion current densities (Tables 4.36, 4.38 and 4.40) followed the same trend as the corrosion rates (Tables 4.36, 4.38 and 4.40). Thus, there was consistency between immersion tests and accelerated corrosion results. However, the true current density values are expected to be much higher than those shown in Tables 4.36, 4.38 and 4.40, because the entire surface area was used in calculations instead of the binder surface area, since the corrosion behavior is attributed to mainly the binder phase [1997Hum]. It was deduced from both tests that there was a general decrease in corrosion rate with increased Ru additions. The decrease in corrosion rate with Ru additions was due to anodic inhibition and improved hydrogen evolution [2011Pot, 2014Pot]. This was deduced from the decrease in passive current densities with Ru additions (Figures 4.82, 4.83, 4.101, 4.102, 4.116 and 4.117) and a decrease in the β_c values (Tables 4.36, 4.38 and 4.40). The decreasing passive current densities with Ru additions are an indication that Ru helped to improve passivation [1997Tjo]. The generally increased corrosion potential with Ru (Tables 4.36, 4.38 and 4.40, Figures 4.84, 4.103 and 4.118) was reported by Tjong *et al*. [1997Tjo] to be due to increased hydrogen evolution as Ru accumulates at surface defects during the dissolution of Co into the electrolyte. The improvement in corrosion resistance with Ru additions (Tables 4.36, 4.38 and 4.40, and Figures 4.85, 4.86, 4.104 and 4.119) was also attributed to Ru being more corrosion resistant than Co, leading to decreases in critical current densities [2011Pot] as seen from Figures 4.82, 4.83, 4.101, 4.102, 4.116 and 4.117. It was also reported that Ru helps to stabilize the Co fcc structure [2011Pot] which is more corrosion resistant than the hcp structure [1998Hum, 2006Sri].

The increase in corrosion rate for Ru additions for Alloys 2, 8 and 11 in H_2SO_4 might have been due to the influence of Ru on the corrosion kinetics, suggested by the steeper active regions (Figures 4.82 and 4.83). As an example, the polarisation curves for Alloys 7 and 8 of the (89.6-*x*)WC-0.4VC-10Co-*x*Ru series are shown in Figure 5.33. The addition of Ru resulted in a steeper active region for Alloy 8, which had more Ru than Alloy 7, and this might have led to increased corrosion rates. Another reason could be that the Ru accumulation at surface defects had to reach a certain level before passivation could occur [1997Tjo]. Thus, 0.4 wt% Ru additions for Alloys 1, 7 and 10 might have been below the level for passivation, increasing the corrosion rate since the cathodic reaction increased with Ru additions (Table 4.36). Figure 5.34 shows an SEM-BSE image and the EDS analysis of the outer (severe corrosion) and inner (mild corrosion) regions for Alloy 8, the optical images of which are shown in Figure 4.87(b). The EDS analyses revealed a concentration gradient, particularly with respect to Ru, between the outer and inner regions. The outer regions had significantly more Ru than the inner region. Therefore, there could have been some galvanic corrosion, leading to more severe corrosion around the edges as shown in Figure 4.87b. Since addition of Ru beyond 0.4 wt% did not cause severe corrosion, Ru additions are supposed to exceed a certain level, where passivation could occur, to be beneficial in improving corrosion properties by passivation. The mechanism by which the low Ru contents reduced the corrosion of WC-Co-VC-Ru alloys in sulphuric acid was not clear. Higher magnification images (Figure 5.35) revealed the existence of a corrosion film on the inner region of Alloy 8 (Figure 5.35a) and exposed WC grains for the outer regions (Figure 5.35b) due to the removal of the (Co + Ru) binder. The presence of different surfaces in contact might have caused a galvanic effect which increased the corrosion rate at the outer regions. The removal of material at the edges was more significant for the 89.2WC-0.4VC-10Co-0.4Ru and 88.8WC-0.8VC-10Co-0.4Ru (wt%) alloys (with lower Ru concentrations) than the 80WC-10VC-9.6Co-0.4Ru (wt%) alloys. Thus, Ru had to be above a certain level for complete surface passivation to occur, although it was not clear why films formed only on the inner regions of the alloys.

In synthetic mine water, Ru additions increased corrosion rate for Alloys 4 and 13. A common feature in the polarisation curves for Alloys 4 and 13 was the wide transition region between active and passive regions. The polarisation curves for Alloys 3 and 4 of the 80WC-10VC-(10-*x*)Co-*x*Ru (wt%) series are shown in Figure 5.36. Alloy 4 had a higher critical current density and a more positive primary passive potential, which might have prevented pseudopassivation according to Fontana [1986Fon]. For passivation to occur, the nose of the anodic polarisation curve must be cleared by the cathodic process [1986Fon]. The wide anodic polarisation noses for Alloys 4 and 13 might therefore have affected passivation, unlike for Alloy 3 (Figure 5.36) which had a narrow anodic polarisation nose, thus having better passivation.

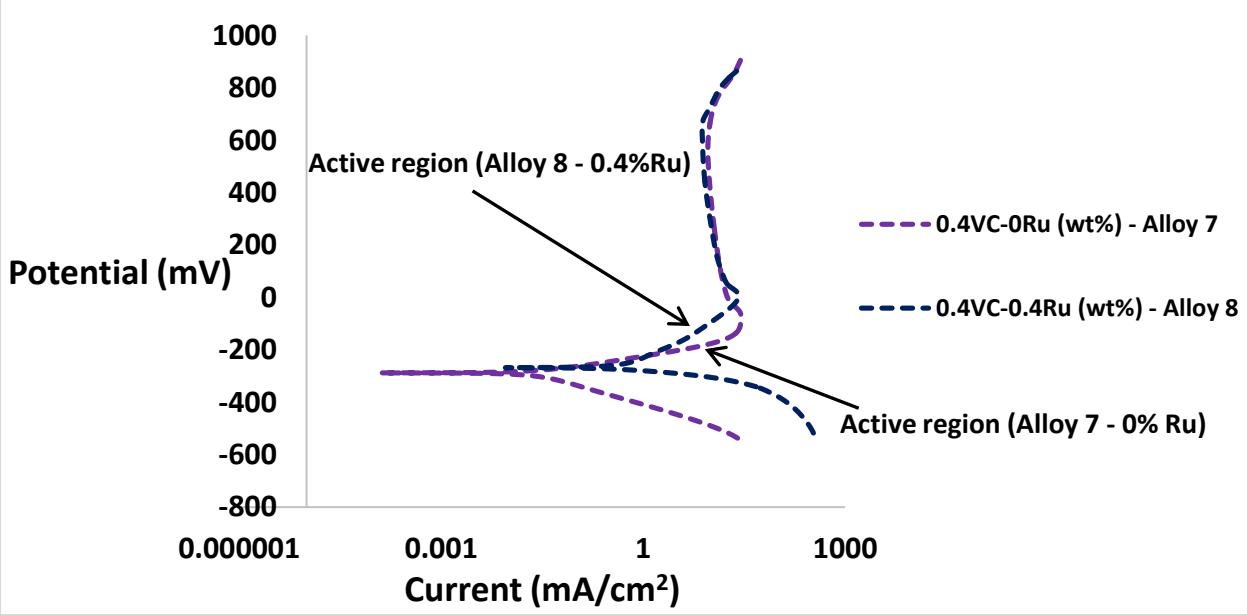

Figure 5.33. Polarisation curves for Alloys 7 and 8, showing a steeper active region for Alloy 8.

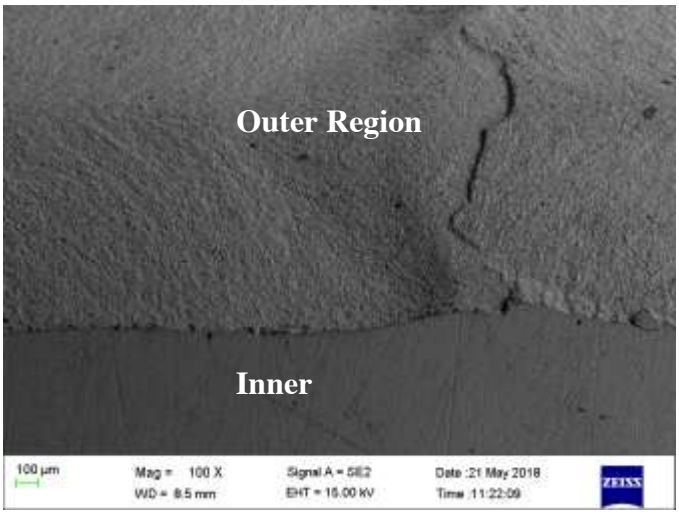

Element	Outer Amount (wt%)	Inner Amount (wt%)
C	9.7±1.4	10.3±1.2
O	5.9±0.4	5.9±0.4
S	0.4±0.1	0.2±0.1
V	0.2±0.0	0.6±0.1
Co	1.3±0.1	1.1±0.3
Ru	0.3±0.0	1.9±0.1
W	82.2±1.7	80.0±1.9

Figure 5.34. SEM-BSE image and EDS analyses of Alloy 8 (89.2WC-0.4VC-10Co-0.4Ru (wt%)) showing the outer and inner regions and of the corroded alloy after immersion test in 1 M H_2SO_4.

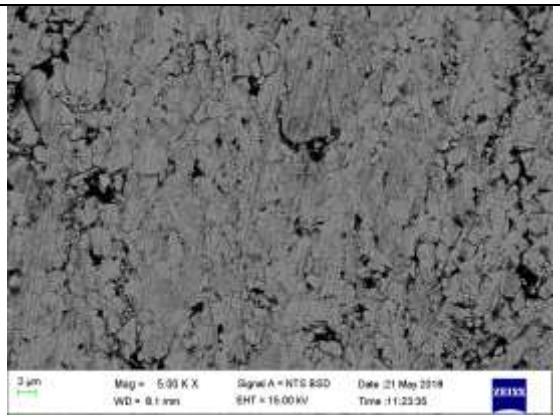

(a)

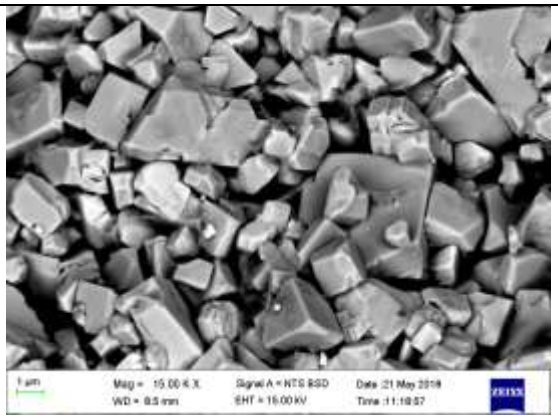

(b)

Figure 5.35. High magnification SEM-BSE images of: a) inner and b) outer regions shown in Figure 5.34.

The effect of VC on corrosion properties was deduced by comparing polarisation behaviour and corrosion rates for Alloys 1, 7 and 10 which had no Ru (Figures 4.82, 4.83, 4.101, 4.102, 4.116

and 4.117). In H_2SO_4 and NaCl, higher critical and passive current densities were associated with Alloys 7 and 10 of the (89.6-*x*)WC-0.4VC-Co-*x*Ru and (89.2-*x*)WC-0.8VC-Co-*x*Ru series (Figures 4.83, 4.102 and 4.117, and Tables 4.36, 4.38 and 4.40). It therefore appears that VC helped to reduce both the critical and current densities, making it easier for the alloys to passivate. However, the low passive and critical current densities for Alloys 13 and 14 (Tables 4.36, 4.38 and 4.40), both of which had low VC content, made the effect of VC content not very clear. Also, previous studies on the addition of VC to WC-Co alloys showed no definite trends of critical and passive current densities for corrosion in H_2SO_4 [2010Kon] and NaCl [2013Mac]. Alloys with Ru had higher critical and passive current densities for the (89.6-*x*)WC-0.4VC-Co-*x*Ru and (89.2-*x*)WC-0.8VC-Co-*x*Ru alloys, which had low VC contents (Figures 4.83, 4.102 and 4.117, and Tables 4.36, 4.38 and 4.40). However, this trend was not conclusive, since the 89.6WC-0.4VC-(10-*x*)Co-*x*Ru alloys, also with low VC, had much lower critical and passive current densities. In synthetic mine water (Figures 4.116 and 4.117) there was no pseudopassivation for alloys 1, 7 and 10 which did not have Ru, and the same results were seen in previous work [2013Mac]. The effect of VC, if any, on the polarisation behaviour is therefore not clear.

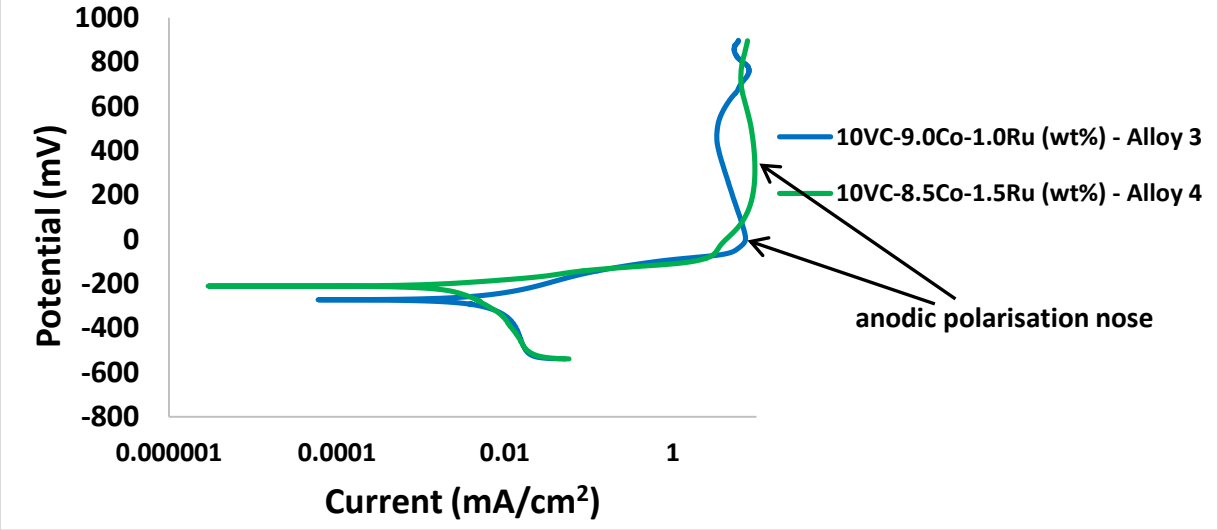

Figure 5.36. Polarisation curves for Alloys 3 and 4 showing a wider anodic polarisation curve for Alloy 4 (80WC-10VC-8.5Co-1.5Ru than for Alloy 3 (80WC-10VC-9.0Co-1.0Ru (wt%)).

The VC content had no effect on the corrosion rate for all environments (Figures 4.85, 4.86 4.104 and 4.119). Machio *et al*. [2013Mac] made a similar claim with respect to VC additions to WC-Co alloys corroding in NaCl environments. However in synthetic mine water, VC additions were beneficial in improving corrosion resistance [2013Mac]. In H_2SO_4, VC additions to WC-Co alloys were beneficial [2010Kon, 2011Pot]. The increase in corrosion resistance due to VC additions was attributed to the resulting decrease in binder volume fractions [2010Kon]. In this work, corrosion resistance generally improved with a decrease in binder volume fractions for the 80WC-10VC-(10-*x*)Co-*x*Ru and the 89.6WC-0.4VC-(10-*x*)Co-*x*Ru alloys, in all environments. However, the effect of binder volume was not clear, since there was a corresponding increase in Ru content. Also, for the (89.6-*x*)WC-0.4VC-10Co-*x*Ru and (89.2-*x*)WC-0.8VC-10Co-*x*Ru alloys, there was still improved corrosion resistance, yet the binder volume increased. Human *et al*. [1996Hum] found binder composition, not binder fraction, affected critical current densities. Changes in binder volume fractions are usually accompanied by changes in binder composition [1971Rud]. So the changes in corrosion resistance that were found by Konadu *et al*. [2010Kon] might have been due to changes in binder composition, not binder volume fraction.

Overall, Ru additions generally improved corrosion resistance for all alloy series, in all three corrosion environments. The highest corrosion rates were in H_2SO_4. The 80WC-10VC-(10-*x*)Co-*x*Ru alloys had slightly higher corrosion rates in NaCl than in synthetic mine water, and the opposite was observed for the (89.6-*x*)WC-0.4VC-10Co-*x*Ru, (89.2-*x*)WC-0.8VC-10Co-*x*Ru and 89.6WC-0.4VC-(10-*x*)Co-xRu alloys. The optimum Ru content was 2 wt% for H_2SO_4 and NaCl, but in synthetic mine water, 1 wt% was the optimum. Although there was a general decrease in corrosion, there were exceptions at 0.4 wt% (in H_2SO_4) and 1.5 wt% (in synthetic mine water), where the corrosion rate increased. All alloys (except in H_2SO_4 for Alloys 6 and 14, with 3 wt% Ru) were expected to have remained in the active state during immersion tests in all three environments, since the critical current densities were most likely to be higher than would be expected in an immersion test cell. For instance, the maximum current density in an aerated solution of pH around 7 was found to be ~100 μA [1985Kae], much less than the critical current

densities obtained in this study for all corrosion environments. The corrosion products detected from XRD and Raman spectroscopy summarized in Tables 4.37, 4.39 and 4.41, were consistent with the components of the alloys and solutions. The (Co) binder, WC, H_2O and O_2 were the source of the elements that resulted in the formation for the formation of Co oxides, W oxides and W hydroxides (Tables 4.37, 4.39 and 4.41). The sulphate ions from H_2SO_4 and $CaSO_4$ (from the synthetic mine water) reacted with Co, resulting in $CoSO_4$ (Tables 4.37 and 4.41). Sodium from NaCl reacted with W from the alloys forming sodium tungsten oxides e.g. $Na_2W_2O_7$ (Tables 4.39 and 4.41). Vanadium also oxidized in some alloys, resulting in the formation of VO_2 (Tables 4.39 and 4.41). The oxides and hydroxides of W and C, as well as $CoSO_4$, were also found for WC-Co-Ru and WC-VC-Co alloys in H_2SO_4 [2011Pot, 2010Kon], synthetic mine water [2013Mac] and in NaCl [2013Mac]. Sodium tungsten oxides were also found for the corrosion of WC-VC-Co alloys in NaCl [2013Mac]. Instead of $CaSO_4$ found in this study, $CaWO_4$ was identified by Machio *et al*. [2013Mac] after the corrosion of WC-VC-Co alloys in synthetic mine water. In H_2SO_4, $VOSO_4.H_2O$ was also found after the corrosion of WC-VC-Co alloys by Konadu *et al*. [2010Kon], but not in this work.

The alloys in this investigation were more complex than most of the alloys in literature, thus some relationships observed for WC-Co alloys were not always observed. Alloy 6, 80WC-10VC-7.0Co-3.0Ru (wt%) was the most wear resistant and the most corrosion resistant in H_2SO_4 and in synthetic mine water. However, the 80WC-10VC-8.0Co-2.0Ru (wt%) alloy (Alloy 5) would be the optimum alloy since it had almost the same wear resistance and corrosion resistance as Alloy 6, but having less Ru and so would be cheaper. Although Alloy 14, 89.6WC-0.4VC-7.0Co-3.0Co (wt%), had the best corrosion resistance in NaCl, Alloy 5 still had comparable corrosion resistance.

6. CONCLUSIONS AND RECOMENDATIONS

The properties of the WC-VC-Co-Ru alloys studied were affected by both VC and Ru contents. The properties depended on whether binder modification with Ru involved Co replacement or WC replacement. At 0.8 wt% VC, the WC mean intercept length decreased significantly, so additions up to 10 wt% VC might not be necessary. Overall, the property interrelationships for WC-VC-Co-Ru alloys were more complicated than the conventional hardmetals, because of the effects of both VC and Ru.

At low VC contents, the WC-VC-Co-Ru alloys had the same magnetic response as conventional WC-Co alloys, since there was a direct relationship between coercivity and magnetic saturation for only the (89.6-*x*)WC-10Co-0.4VC-*x*Ru alloy series. At ≥0.8 wt% VC, an inverse relationship was observed between magnetic saturation and coercivity. Thus, the use of magnetic properties, especially coercivity, to predict microstructural characteristics was not as straight-forward for WC-VC-Co-Ru alloys as for WC-Co alloys. The WC mean grain size decreased with Ru additions for the (89.2-*x*)WC-10Co-0.8VC-*x*Ru and 89.6-*x*)WC-10Co-0.4VC-*x*Ru alloy series. The effect of Ru additions on the microstructure became insignificant as VC content was increased. The 80WC-10VC-(10-*x*)Co-*x*Ru alloys fitted best the expression $C=1.03\ \exp.(-5V\beta)$ [1966Exn], whereas the (89.6-*x*)WC-10Co-0.4VC-*x*Ru alloys and (89.2-*x*)WC-10Co-0.8VC-*x*Ru alloys fitted best with the expression, $C\beta=0.85–1.80V\beta$ [1986Roe]. The effect of contiguity on the binder mean free path appeared to increase with VC.

Ruthenium additions improved hardnesses of all the WC-VC-Co-Ru alloys at both high (10 wt%) and low (0.4 and 0.8 wt%) VC contents. Hardness increased by a combination of grain size decrease, and to a greater extent, solid solution strengthening. Ruthenium additions were more effective in improving hardness when substituting Co than when replacing WC. There was a general decrease in fracture toughness of WC-VC-Co- Ru alloys with Ru additions. However, Ru additions improved fracture toughness of WC-VC-Co-Ru alloys up to 0.4 wt% Ru for the

80WC-10VC-(10-*x*)Co-*x*Ru and (89.6-*x*)WC-10Co-0.4VC-*x*Ru alloys, and up 2 wt% Ru for the (89.2-*x*)WC-10Co-0.8VC-*x*Ru alloys. The amount of Ru which can be added to improve fracture toughness depended on the grain size change which occurred, and whether Ru was substituting Co or replacing WC. The 80WC-10VC-(10-*x*)Co-*x*Ru (wt%) alloy series with the highest VC content had the hardest alloys, but the alloys had the least fracture toughnesses.

There was a general improvement in corrosion resistance with Ru additions in all three corrosion environments. However, 0.4 wt% Ru additions significantly decreased corrosion resistance in 1 M H_2SO_4 for the 80WC-10VC-(10-*x*)Co-*x*Ru, (89.6-*x*)WC-10Co-0.4VC-*x*Ru and (89.2-*x*)WC-10Co-0.8VC-*x*Ru (wt%) alloys. The decrease in corrosion resistance with 0.4 wt% Ru additions was attributed to the negative influence on the corrosion kinetics by Ru and/or Ru being below the concentration to cause passivation. A galvanic reaction could also have been responsible for the high corrosion rate that occurred at the edges of the sample with 0.4 wt% Ru as was deduced from EDS analyses which gave different Ru amounts for the surface edges and the inner regions. In synthetic mine water, 1.5 wt% Ru additions also decreased corrosion resistance. The additions of 1.5 wt% Ru resulted in higher critical current densities and more positive primary passive potentials, and this might have prevented pseudopassivation. The VC content did not seem to have any effect on corrosion resistance in any of the three environments studied. The highest corrosion rates were seen in 1 M H_2SO_4 and there was not much difference between the corrosion rates in 1 M NaCl and in synthetic mine water. The 80WC-10VC-7.0Co-3.0Ru (wt%) alloy was the most corrosion resistant in H_2SO_4 and in synthetic mine water. In 1 M NaCl, the 89.6WC-0.4VC-7.0Co-3.0Ru (wt%) alloy had most corrosion resistance.

All alloy series were characterised by a mild wear mode after sliding wear. There was an increase in wear resistance for all alloy series with Ru additions. The 80WC-10VC-(10-*x*)Co-*x*Ru (wt%) alloy series with the highest VC content had the lowest wear rates. However, VC might have had an overriding effect on Ru since there was a more significant decrease in wear rate for the 89.6WC-0.4VC-(10-*x*)Co-*x*Ru alloys (~52%) than the 80WC-10VC-(10-*x*)Co-*x*Ru alloys (~34%) after 3 wt% Ru additions. Ruthenium and VC additions affected on the

microstructural and mechanical properties of WC-VC-Co-Ru alloys, which in turn contributed to increased wear resistance.

The alloys in this study were more complex than those found in literature, and this resulted in some different relationships. The 80WC-10VC-8.0Co-2.0Ru (wt%) alloy was the optimum for the properties investigated.

For future work, it would be worthwhile investigating the addition of 0.4 wt% Ru to 89.6WC-0.4VC-(10-*x*)Co-*x*Ru (wt%) alloys, to establish whether there would be the same increase in corrosion rate as observed after the addition of 0.4 wt% Ru in the 80WC-10VC-(10-*x*)Co-*x*Ru, (89.6-*x*)WC-0.4VC-10Co-*x*Ru and (89.2-*x*)WC-0.8VC-10Co-*x*Ru (wt%) alloys. Also, the (89.6-*x*)WC-0.4VC-10Co-*x*Ru, (89.2-*x*)WC-0.8VC-10Co-*x*Ru alloys might have to be investigated at higher Ru contents, for example up to 3 wt%. This might help ascertain some relationships, for example the magnetic saturation-coercivity trend. It would also be worthwhile investigating the alloys for other wear types, such as abrasion. Investigations using another manufacturing technique, such as SPS, are also recommended. It might also be beneficial to make cutting tools based on the compositions of this study to further validate the findings.

REFERENCES

[1933Ade] V. Adelsköld, A. Sundelin and A. Westgren, Carbide in KohlenstoffhaltigenLegierungen von Wolfram und Molybdän mit Chrom, Mangan, Eisen, Kobalt und Nickel, *Zeitschrift für Anorganische und Allgemeine Chemie*, 212(4) (1933) 401-409.

[1943Kis] E.N. Kislyakova, Determination of the Crystal Structure and Composition of the Double Carbides W-Co-C System by Investigation of Relative Potency of the Debay Lines, *Zhur Fiz. Khimii* ,17 (1943) 108-114.

[1944Ker] M. Kersten, Grundlagen einer neuen Theorie der ferromagnetischen Hysterese und der Koerzitivkraft, Leipzig (1944), *Zeitschrift für Angewandte Physik*, 8 (1956) 496.

[1946Tur] P.S. Turner, Thermal Expansion Stresses in Reinforced Plastics, *Journal of Research of the National Bureau of Standards*, 37 (1946) 241.

[1947Met] A.G. Metcalfe, Hard Tools Limited, Sandford and Trent, 38 (1947) 84 (unpublished reports).

[1951Hal] E.O. Hall, The Deformation and Ageing of Mild Steel, *Proceedings of the Physical Society B*, 64(9) (1951) 747-753.

[1952Kie] R. Kiessling, Proceedings of the International Symposium on the Reactivity of Solids, Gothenburg, Sweden, (1952) 1065-1068.

[1952Gur] J. Gurland and J.T. Norton, Role of the Binder Phase in Cemented Tungsten Carbide-Cobalt Alloys, *Journal of Metals*, (1952) 1051-1056.

[1952Rau] P.D.Rautala and J.T. Norton, Tungsten-Cobalt-Carbon System, *Proceedings of the first Plansee Seminar*, *Reutte Planseewerke*, (1952) 303.

[1952Rau1] P.D.Rautala and J.T. Norton, Tungsten-Cobalt-Carbon System, *Transactions of the Metallurgical Society of AIME*, 194(4) (1952) 1045-1050.

[1953Arc] J.F. Archard, Contact and Rubbing of Flat Surfaces, *Journal of Applied Physics*, 24(8) (1953) 981-988.

[1953Pet] N.J. Petch, The Cleavage Strength of Polycrystals, *Journal of the Iron and Steel Institute*, 174 (1953) 25-28.

[1954Gur] J. Gurland, Study of the Effect of C on the Structure and Grain Size of Sintered WC-Co Alloys, *Transactions of the American Institute of Mining and Metallurgical Engineers*, 2 (1954) 255-290.

[1955AST] ASTM 373-88, Standard Test Method For Water Absorption Bulk Density Apparent Porosity and Apparent Specific Gravity of Fired Whiteware Product, (1955).

[1955Gur] J. Gurland and P. Bardzil, Relation of Strength, Composition, and Grain Size of Sintered WC-Co alloys, *Transactions of the American Institute of Mining and Metallurgical Engineers*, 203(2) (1955) 311-315.

[1956Gre] G.W. Greenwood, The Growth of Dispersed Precipitates in Solutions, *Acta Metallurgica*, 4 (1956) 243-248.

[1957Pal] S. Palmqvist, A Method to Determine the Toughness of Brittle Materials, Especially Hard Materials, *Sartryck ur Jernkontorets Annale*., 141 (1957) 303-307.

[1958Gur] J. Gurland, The Measurement of Grain Contiguity in Two-phase Alloys, *Transactions of the Metallurgical Society of AIME*, 212 (1958) 452-455.

[1958Han] M. Hansen, Constitution of Binary Phase Diagrams, *McGraw Hill*, (1958) 83.

[1959Gur] J. Gurland, Observations on the Structure and Sintering Mechanism of Cemented Carbides, *Transactions of the American Institute of Mining and Metallurgical Engineers*, 215(4) (1959) 601-608.

[1959Gru] M. Gruter, Undersuchwgen in den systemen Co-C, Co-WC, Thesis, Universitat Munster, German, 1959.

[1963Gur] J. Gurland, Fracture Strength of Sintered Tungsten Carbide-Cobalt Alloys in Relation to Composition and Particle Spacing, *Transactions of the Metallurgical Society of AIME*, 227(5) (1963) 1146.

[1963Tre] E.M. Trent, Cutting Steel and Iron with Cemented Carbide Tools, Part I. An Analysis of Tool Wear, *Journal of the Iron and Steel Institute*, 201 (1963) 847-855.

[1964Daw] W. Dawihl and B. Frisch, The Mechanical Characteristics of the Cobalt Phase in Tungsten Carbide-Cobalt Hard Metals, *Cobalt*, 22 (1964) 22-30.

[1965Fis] H.F. Fischmeister and H.E. Exner, Beobachtungen über den Mahlvorgang bei Hartmetallpulvern, *Planseeber Pulvermet*, 13 (1965) 178-198.

[1965Kie] R. Kieffer and F. Benesovsky, Hartmetalle, *Springer-Verlag*, 5(A-1010) 1965 541 (In German).

[1966Exn] H.E. Exner and H.F. Fischmeister, Structure of Sintered Tungsten Carbide-Cobalt Alloys, *Arch Eisenhuttenw*, 37(5) (1966) 417-426.

[1966Fis] H. Fischmeister and H.E. Exner, The Mechanical Properties of Cemented Tungsten Carbide-Cobalt Alloys in Relation to the Structure, *Archiv für das Eisenhüttenwesen*, 37 (1966) 499-510.

[1966Gur] J. Gurland, The measurement of grain contiguity in two-phase alloys, *Transactions of the Metallurgical Society of AIME*, 212 (1966) 452-455.

[1967Lan] J.K. Lancaster, The Influence of Substrate Hardness on the Formation and Endurance of Molybdenum Disulphide Films, *Wear*, 10(2) (1967) 103-117.

[1968Sch] F. Schuckher, Grain Size, Quantitative Microscopy, McGraw-Hill, New York, (1968) 201-265.

[1968War] R. Warren, The Interaction between Liquid Platinum and some Transitiom Metal Carbides, *Journal of Nuclear Materials*, 25 (1968) 117-119.

[1969Exn] H.E. Exner, The Influence of Sample Preparation on Palmqvists Method for Toughness Testing of Cemented Carbides, *Transactions of the Metallurgical Society of AIME*, 245(4) (1969) 677-683.

[1969Gur] J. Gurland, Microstructural Aspects of the Strength and Hardness of Cemented Tungsten Carbide, Division of Engineering, Brown University, 1969.

[1970Ett] P. Ettymayer and R. Suchentrunk, About Thermal Stability of Eta Carbides, *Monatshefte fiir Chemie*, 101 (1970) 1098-1103 (In German).

[1970Exn] H.E. Exner and J. Gurland, A Review of Parameters Influencing Some Mechanical Properties of Tungsten Carbide-Cobalt Alloys, *Powder Metallurgy*, 13(25) (1970) 13-31.

[1970Pol] C.B. Pollock and H.H. Stadelmaier, The Eta Carbides in the Fe-W-C and Co-W-C Systems, *Metallurgical Transactions*, 1 (1970) 767-770.

[1970Stj] K.G. Stjernberg, Some Relations Between the Structure and Mechanical Properties of WC-TiC-Co Alloys, *Powder Metallurgy*, 13(25) (1970) 1-12.

[1971Rud] O. Rüdiger, D. Hirschfeld, A. Hoffmann, J. Kolaska, G. Ostermann and J. Willbrand, Composition and Properties of the Binder Metal in Cobalt Bonded Tungsten Carbide, *International Journal of Powder Metallurgy*, 7 (1971) 29.

[1972Hay] K. Hayashi, Y. Fuke and H. Suzuki, Effects of Additions of Carbides on the Grain size of WC-Co Alloy, *Journal of the Japan Society of Powder and Powder Metallurgy*, 19 (1972) 67-71.

[1972Und] E. Underwood, The Mathematical Foundations of Quantitative Stereology, *Stereology and Quantitative Metallography, ASTM International* (1972).

[1973Gre] H. Grewe, H. E. Exner and P. Walter, Behinderung des Kornwachstums in Hartmetall-Legierungen vom ISO-K10-Typ durch Zusatzkarbide, *Zeitschrift für Metallkunde*, 64(2) (1973) 85.

[1973Til] D.L. Tillwick and I. Joffe, Magnetic Properties of Co-W Alloys in Relation to Sintered WC-Co compacts, *Scripta Metallurgica*, 7 (1973) 479-484.

[1974Ben] J. S. Benjamin and T. E. Volin, The Mechanism of Mechanical Alloying, *Metallurgical Transactions*, 5 (1974) 1929-1934.

[1974Blo] R.I. Blombery, C.M. Perrot and P.M. Robinson, Abrasive Wear of Tungsten Carbide-Cobalt Composites. I. Wear Mechanisms, *Materials Science and Engineering*, 13 (1974) 93-100.

[1974Gra] G. Grathwohl and R. Warren, The Effect of Cobalt Content on the Microstructure of Liquid-Phase Sintered TaC-Co Alloys, *Materials Science and Engineering*, 14 (1974) 55-65.

[1974Lar] J. Larsen-Basse, C.M. Perrott and P.M. Robinson, Abrasive Wear of Tungsten Carbide-Cobalt Composites. I. Rotary Drilling Tests, *Materials Science and Engineering*, 13 (1974) 83-91.

[1975War] R. Warren and M.B. Waldron, The Microstructure and Properties of Sintered TiC-Ruthenium Alloys, *Powder Metallurgy International*, 7 (1975) 18-21.

[1976Nar] N. Narutaki and Y. Yarmane, Wear Mechanisms of Carbide Tools Based on the Reaction between Tool and Work Material, Part II, Cutting and the Consideration of Tool Wear Mechanism, *Bulletin of the Japanese Society of Precision Engineering*, 10 (1976) 133-138.

[1976Uhr] B. Uhrenius, B. Carlsson and T. Franzen, Study of the Co-W-C System at Liquidus Temperatures, *Scandinavian Journal of Metallurgy*, 5 (2) (1976) 49-56.

[1977Amb] S. Amberg and H. Doxner, Porosity in Cemented Carbide, *Powder Metallurgy*, 1 (1977) 1-10.

[1977Bri] British Standards Institution, Methods of Test for Plane Strain Fracture Toughness (Kic) of Metallic Materials, BS 5447 (1977).

[1977Che] J.L. Chermant, A. Deschanvres and F. Osterstock, Factors Influencing the Rupture Stress of Hardmetals, *Powder Metallurgy*, 2 (1977) 63-69.

[1977Fre] J. Freytag and H.E. Exner, Influence of Tungsten and Carbon Additions on the Sintering and the Magnetic Properties of WC-12Co Cemented Carbide, *Modern Developments in Powder Metallurgy*, 10 (1977) 511-523.

[1977Mad] W. Mader, R. Kieffer, H. Nowotny and P. Ettmayer, Pseudoquaternary System WC-TaC-TiC-VC and VC Containing Cemented Carbides, *International Journal of Powder Metallurgy and Powder Technology*, 13(1) (1977) 41-49.

[1977Nae] Y. Nacrheim and E.M. Trent, Diffusion Wear of Cemented Carbide Tools When Cutting Steel at High Speeds, *Metal Technology*, 4 (1977) 548.

[1977Per] C.M. Perrot, Elastic-Plastic Indentation: Hardness and Fracture, *Wear*, 45 (1977) 293-309.

[1977Vis] R.K. Viswanadham and J.D. Venables, A Simple Method for Evaluating Cemented Carbides, *Metallurgical Transactions A,* 8A (1977) 187-191.

[1978ISO] ISO Standard, Standard IS0-4505, (1978) 1-6.

[1978Joh] T. Johansson and B. Uhrenius, Phase Equilibria, Isothermal Reactions, and a Thermodynamic Study in the Co-W-C System at 1150°C, *Metal Science*, 12 (1978) 83-94.

[1978Lee] H.C. Lee and J. Gurland, Hardness and Deformation of Cemented Tungsten Carbide, *Materials Science and Engineering*, 33 (1978) 125-133.

[1978War] R. Warren, Measurement of the Fracture Properties of Brittle Solids by Hertzian Indentation, *Acta Metallurgica*, 26 (1978) 1759-1769.

[1978Exn] H.E. Exner, J.R. Pickens and J. Gurland, *Metallurgical Transactions A,* 9A (1978) 736.

[1979Exn] H.E. Exner, Physical and Chemical Nature of Cemented Carbides, *International Metals Reviews - The Metals Society and the American Society for Metals*, 4 (1979) 149-73.

[1979Pet] C.T. Peters, The Relationship between Palmqvist Indentation Toughness and Bulk Fracture Toughness for Some WC-Co Cemented Carbides, *Journal of Materials Science*, 14 (1979) 1619-1623.

[1980Aka] T. Akawawa, Y. Hashiguti and K. Suzuki, Crater Wear Mechanism of WC-Co Tools at High Cutting Speeds, *Wear*, 65 (2) (1980) 141-150.

[1980Bon] C. Bonjour, Nouveaux Développements dans les outils de coupe en Cárbure Fritte *Wear*, 62 (1980) 83-112.

[1980Kim] D.Y. Kim and A. Accary, Mechanisms of Grain Growth Inhibition During Sintering of WC-Co Based Hard Metals, *Sintering Processes, Materials Science Research*, 13 (1980) 235-244.

[1980Hag] S. Hagege, G. Nouet and P. Delavignette, Grain Boundary Analysis in TEM. IV. Coincidence and the Associated Defect Structure in Tungsten Carbide, *Physica Status Solidi (a),* 62 (1980) 97-107.

[1980Gha] M.H. Ghandehari, Anodic Behavior of Cemented WC-6% Co Alloy in Phosphoric Acid Solutions, *Journal of the Electrochemical Society*, 127(10) (1980) 2144-2147.

[1981Kod] M. Kodama, M. Nakano, M. Miyake and A. Hara, *Proceedings of the 10th Plansee Seminar*, 3 (1981) 97-112.

[1982AST] ASTM E-399-78:1982, Annual Book of ASTM Standards, Philadelphia, 10 (1982).

[1982Bet] W. Betteridge, Cobalt and its Alloys, John Wiley and Sons, New York, 1982.

[1983Bol] J.D. Bolton and R.J. Keely, Fracture Toughness (K_{ic}) of Cemented Carbides, *Fibre Science and Technology*, 19 (1983) 37-58.

[1983Bro] K.J.A. Brooks, Cemented Carbides for Engineers and Tool Users, International Carbide Data, East Barnet, U.K. (1983).

[1983ISO] International Standard ISO3878:1983, Hardmetals - Vickers Hardness Test, 2nd Edition, (1983)1-2.

[1983Sch] T. Schmitt, M Schreiner, P Ettmayer, E Lassner and B Lux, On Solution-Reprecipitation Processes During Liquid Phase Sintering of WC/Co, *International Journal of Refractory Metals and Hard Materials*, 2 (1983) 78-83 (In German).

[1984Des] V.M. Desai, C.M. Rao, T.H. Kosel and N.F. Fiore, Effect of Carbide Size on the Abrasion of Cobalt-Base Powder Metallurgy Alloys, *Wear*, 94 (1984) 89-101.

[1984Ega] T. Egami and Y. Waseda, Atomic Size Effect on the Formability of Metallic Glasses, *Journal of Non-Crystalline Solids*, 64 (1984) 113-134.

[1985Goo] R. Goodson, F. Larson and L. Sheehan, Energy Input Monitoring During Attritor Milling, *International Journal of Refractory Metals and Hard Materials*, 4(2) (1985) 70-76.

[1985Gur] J. Gurland, Application of Quantitative Microscopy to Cemented Carbides, In: J.L. McCall, J.H. Steele Jr., Editors, Practical Application of Quantitave Metallography. STP 839, Philadelphia, PA, USA, ASTM (1985) 65.

[1985Kae] H. Kaesche, Metallic Corrosion, NACE, Houston, 1985.

[1985Lar] J. Larsen-Basse, Binder Extrusion in Sliding Wear of WC-Co Alloys, *Wear*, 105 (3) (1985) 247-256.

[1985Lau] M.T. Laugier, Coercivity, Hardness and Microstructure in WC-Co Composites, *Journal of Materials Science Letters*, 4 (1985) 211-216.

[1985She] D.K. Shetty, L.G. Wright, P.N. Mincer and A.H. Clauer, Indentation Fracture of WC-Co Cermets, *Journal of Materials Science*, 20 (1985) 1873-1882.

[1985Van] G.F. Vander Voort, H.M. James, Metallography and Microstructures, *ASM Metals Handbook*, ASM Metals Park, OH, USA, 9 (9) (1985) 282.

[1986Don] J.D. Donaldson, in W. Gerhartz (ed.), Ullmann's Encyclopedia of Industrial Chemistry, Weinheim VCH, (5) 1986 281-312.

[1986Fon] M.G. Fontana, Corrosion Engineering, 3rd Edition., McGraw-Hill Book Company, New York, USA, (1986).

[1986Roe] B. Roebuck and E.G. Bennett, Phase Size Distribution in WC/Co Hardmetal, *Metallography*, 19 (1986) 27-47.

[1987Aro] B. Aaronsson, Influence of Processing on Properties of Cemented Carbide, *Powder Metallurgy*, 30(3) (1987) 175-181.

[1987Lim] S.C. Lim, M.F. Ashby and J.H. Brunton, Wear-Rate Transitions and Their Relationship to Wear Mechanisms, *Acta Metallurgica*, 35(6) (1987) 1343-1348.

[1988Alm] E.A. Almond and B. Roebuck, Identification of Optimum Binder Phase Compositions for Improved WC Hard Metals, *Materials Science and Engineering*, A105/106 (1988) 237-248.

[1988Gur] J. Gurland, New Scientific Approaches to Development of Tool Materials, *International Metal Reviews*, 33(3) (1988) 151-166.

[1988Ols] M. Olsson, B. Stridh, S. Söderberg and U. Jansson, Sliding Wear of Hard Materials - The Importance of a Fresh Counter-material Surface, *Wear*, 124(2) (1988) 195-216.

[1988Par] J.K. Park, K.Y. Eun and D.N. Yoon, Anomalous Growth of the Complex Carbide Phase in Carbon-deficient WC-Co Hard Metal during the Infiltration of Eutectic Liquid, *Materials Science and Engineering*, A105/106 (1988) 233-236.

[1988Por] R. Porat and J. Malek, Binder Mean-free-path Determination in Cemented Carbide by Coercive Force and Material Composition, *Materials Science and Engineering*, A105/106 (1988) 289-292.

[1988Roe] B. Roebuck and E.A. Almond, Deformation and Fracture Processes and the Physical Metallurgy of WC-Co Hardmetals, *International Materials Reviews*, 3(2) (1988) 90-112.

[1988Tom] W.J. Tomlinson and C.R. Linzell, Anodic Polarization and Corrosion of Cemented Carbides with Cobalt and Nickel Binders, *Journal of Materials Science, and Engineering*, 23 (1988) 914-918.

[1988Van] F.R. Vandeput and N. Mastrantonis, A Comparison of the Strength of WC-Co Measured by Ring and Transverse Rupture Strength Specimens, *Materials Science and Engineering*, A105/106 (1988) 423-428.

[1989Ett] P. Ettmayer, Hardmetals and Cermets, *Annual Review of Materials Science*, 19 (1989) 145-164.

[1990Mas] T.B. Massalski, H. Okamoto, P.R. Subramanian and L. Kacprzak, Binary Alloy Phase Diagrams, Ohio, USA, ASM International, 3 (1990) 1485.

[1990Mas1] T.B. Massalski, Ni-Ru (Nickel-Ruthenium), Binary Alloy Phase Diagrams, 2nd Edition. Ohio, USA, ASM International, (1990) 2850-2851.

[1990Spi] R. Spiegler, S. Schmadder and L.S. Sigl, Fracture Toughness Evaluation of WC-Co Alloys by Indentation Testing, *Journal of Hard Materials*, 1(3) (1990) 147-158.

[1991Bha] S.K. Bhaumik, G.S. Upadhyaya and M.L. Vaidya, Advances in Powder Metallurgy, Metal Powder Industries Federation, Princeton, 6 (1991) 439.

[1991Hed] P. Hedenqvist and M. Olsson, Sliding Wear Testing of Coated Cutting Tool Materials, *Tribology International*, 24(3) (1991) 143-150.

[1991Lis] A.F. Lisovsky, N.Y. Tkachenko and V. Kebko, Structure of a Binding Phase in Re-alloyed WC-Co Cemented Carbides, *International Journal of Refractory Metals and Hard Materials*, 10 (1991) 33-36.

[1991McC] L.E. McCandlish, B.H. Kear and B.K. Kim, Chemical Processing of Nanophase WC-Co Composite Powders, *Journal of Material Science and Technology*, 6 (1991) 953-956.

[1991Pot] J.H. Potgieter, Alloys Cathodically Modified with Noble Metals, *Journal of Applied Electrochemistry*, 21(6) (1991) 471-482.

[1992Bha] S.K. Bhaumik, J.B. Zu, I.M. Hutchings, G.T. Burstingumik, G.S. Upadhyaya and M.L. Vaidya, Microstructure and Mechanical Properties of WC-TiN-10Co and WC-TiN-Mo_2C-Co(Ni) Cemented Carbides, *Ceramics International*, 18 (1992) 327-336.

[1992Bro] K.J.A. Brookes, Hardmetals and Other Hard Materials, International Carbide Data, East Barnet (United Kingdom) 1992.

[1992Che] L. Chenguang, Composition, Morphology and Distribution of RE Element Containing Phases in Cemented Carbide, *International Journal of Refractory Metals and Hard Materials*, 11 (1992) 295-302.

[1993Fan] F. Zhigang and J.W. Eason, Nondestructive Evaluation of WC-Co Composites Using Magnetic Properties, *International Journal of Powder Metallurgy*, 29(3) (1993) 259-265.

[1993Mas] M. Masuda, Y. Kuroshima and Y. Chujo, Failure of Tungsten Carbide-Cobalt Alloy Tools in Machining of Carbon Materials, *Wear*, 169(2) (1995) 135-140.

[1993Pot] J.H. Potgieter, Effect of Minor Ruthenium Additions on the Corrosion Behavior of Duplex Stainless-Steels in Sulfuric Acid, *South African Journal of Chemistry-Suid-Afrikaanse Tydskrif Vir Chemie*, 46(3-4) (1993) 58-64.

[1993Pre] B. Predel, Co-Ru (Cobalt-Ruthenium). In: Madelung O. (eds) Ca-Cd – Co-Zr. Landolt-Börnstein - Group IV Physical Chemistry (Numerical Data and Functional Relationships in Science and Technology), Springer, Berlin, Heidelberg, 5c (1993).

[1993Zhi] F. Zhigang and J.W. Eason, Nondestructive Evaluation of WC-Co Composites Using Magnetic Properties, *International Journal of Powder Metallurgy*, 29 (3) (1993) 259-265.

[1995Gui] A.F. Guillermet, V. Ozoliņš, G. Grimvall and M. Körling, Phase Stabilities in the Pt-W System: Thermodynamic and Electronic-structure Calculations, *Physical Review B,* 51(16) (1995) 10364.

[1995Sch] W.D. Schubert, A. Bock and B. Lux, General Aspects and Limits of Conventional Ultrafine WC Powder Manufacture and Hard Metal Production, *International Journal of Refractory Metals and Hard Materials*, 13 (1995) 281-296.

[1995Spr] G.E. Spriggs, A History of Fine Grained Hardmetal, *International Journal of Refractory Metals and Hard Materials*, 13 (1995) 241-255.

[1995Pra] L.J. Prakash, Application of Fine Grained Tungsten Carbide Based Cemented Carbides, *International Journal of Refractory Metals and Hard Materials*, 13 (1995) 257-264.

[1995Roe] B. Roebuck, Terminology, Testing, Properties, Imaging and Models for Fine Grained Hardmetals, *International Journal of Refractory Metals and Hard Materials*, 13 (1995) 265-269.

[1995Wen] E.J. Wentzel and C. Allen, Erosion-Corrosion Resistance of Tungsten Carbide Hardmetals with Different Binder Compositions, *Wear*, 181-83 (1995) 63-69.

[1996Ger] R.M. German, Sintering Theory and Practice, New York, USA, Wiley and Sons, (1996) 108.

[1996Hum] A.M. Human and H.E. Exner, Electrochemical Behaviour of Tungsten-Carbide Hardmetals. *Materials Science and Engineering*, A209 (1996) 180–91.

[1996Luy] S. Luyckx, C. Osborne, L.A. Cornish and D. Whitefield, Fine Grained WC-VC-Co Hardmetal, *Powder Metallurgy*, 13(39) (1996) 210-212.

[1996Roe] B. Roebuck, Magnetic Moment (Saturation) Measurements on Hardmetals, *International Journal of Refractory Metals and Hard Materials*, 14 (1996) 419-424.

[1996Wan] Y. Wang and S.M. Hsu, Wear and Wear Transition Mechanisms of Ceramics, *Wear*, 195 (1-2) (1996) 112–122.

[1997AST] ASTM Standards E112–96: Standard Test Method for Determining Average Grain Size, (1997) 227-249.

[1997Cho] S. Cho, A. Hernandez, J. Ochoa and J. Lira-Olivares, Phase Relations, Microstructure and Mechanical Properties of VC Substituted WC-10Co Cemented Carbide Alloys, *International Journal of Refractory Metals and Hard Materials*, 15 (1997) 205-214.

[1997Hum] A.M. Human and H.E. Exner, The Relationship Between Electrochemical Behaviour and In-service Corrosion of WC Based Cemented Carbides, *International Journal of Refractory Metals and Hard Materials*, 15 (1997) 65-71.

[1997Jia] K. Jia and T.E. Fischer, Sliding Wear of Conventional and Nanostructured Cemented Carbides, *Wear*, 203-204 (1997) 310-318.

[1997Osb] C. Osborne, L.A. Cornish and S. Luyckx, On the Preparation of Fine V_8C_7-WC and V_4C_3-WC Powders, *International Journal of Refractory Metals and Hard Materials*, 15 (1997) 163-168.

[1997She] D. Sherman, Fracture Toughness Evaluation of Small Thin Ceramic Specimens, *Journal of the American Ceramic Society*, 80(7) (1997) 1904-1906.

[1997Tjo] S.C. Tjong, J.S. Ku and N.J. Ho, Laser Surface Alloying of Ferritic Fe-40Cr Alloy with Ruthenium, Surface and Coatings Technology, 90(3) (1997) 203-209.

[1997Wan] G.M. Wang, S.J. Campbell, A. Calka and W.A. Kaczmarek, Synthesis and Structural Evolution of Tungsten Carbide Prepared by Ball Milling, *Journal of Materials Science*, 32(6) (1997) 1461-1468.

[1997Whi] D.J. Whitefield, S. Luyckx, M.J. Witcomb and L.A. Cornish, Microstructure and Properties of Fine Grained WC-VC-Co Hardmetal with Cobalt Content Ranging from 10 to 15 wt %, *Proceedings of the 14th International Plansee Seminar*, 2 (1997) 477-484.

[1998Are] F. Arenas, I.B. de Arenas, J. Ochoa and S.A. Cho, Influence of VC on the Microstructure and Mechanical Properties of WC-Co Sintered Cemented Carbides, *International Journal of Refractory Metals and Hard Materials*, 17 (1999) 91-97.

[1998Hum] A.M. Human, B. Roebuck and H.E. Exner, Electrochemical Polarisation and Corrosion Behaviour of Cobalt and (Co, W) Alloys in 1N Sulphuric Acid, *Material Science and Engineering*, A241 (1998) 202-210.

[1998Jar] A. Jaroenworaluck, T. Yamamoto, Y. Ikuhara and T. Sakuma, Segregration of Vanadium at the WC/Co Interface in VC Doped WC-Co, *Journal of Materials Research*, 13 (1998) 2450-2452.

[1998Lov] H.L. de Villiers Lovelock, Powder/Processing/Structure Relationships in WC-Co Thermal Spray Coatings: A Review of the Published Literature, *Journal of Thermal Spray Powders*, 7(3) 1998 357-373.

[1998Lov1] H.L. de Villiers Lovelock, P.W. Richter, J.M. Benson, and P.M. Young, Parameter Study of HP/HVOF Deposited WC-Co Coatings, *Journal of Thermal Spray Powders*, 7(1) 1998 97-107.

[1998Lov2] H.L. de Villiers Lovelock, J. Kinds, and P.M. Young, Characterisation of WC-12Co Thermal Spray Powders and HPHVOF Wear Resistant Coatings, *Powder Metallurgy*, 41(4) (1998) 292-299.

[1998Luy] S. Luyckx, D. Whitefield, M. Witcomb and L.A. Cornish, The Development of WC-VC-Co Hardmetal: A Review of Past Work and New Results, 1998 International Conference on Powder Metallurgy and Particulate Materials, Las Vegas, Nevada, USA, Volume 1, 31st May-4th June 1998.

[1998Myb] G. Myburg, K. Varga, W.O. Barnard, P. Baradlai, L. Tomcs´anyi, J.H. Potgieter, C.W. Louw and M.J. van Staden, Surface Composition of Ru Containing Duplex Stainless Steel after Passivation in Non-oxidizing Media, *Applied Surface Science*,136 (1998) 29-35.

[1998Sch] W.D. Schubert, H. Neumeister, G. Kinger and B. Lux, Hardness to Toughness Relationship of Fine-grained Hardmetals, *International Journal of Refractory Metals and Hard Materials*, 16 (1998) 133-142.

[1998Upa] G.S. Upadhyaya, Cemented Tungsten Carbides: Production, Properties and Testing, New Jersey, USA, Noyes Publications, 1998.

[1998Wol] I.M. Wolff, L.E. Iorio, T. Rumpf, P.V.T. Scheers and J.H. Potgieter, Oxidation and Corrosion Behaviour of Fe-Cr and Fe-Cr-Al Alloys with Minor Alloying Additions, *Materials Science and Engineering A*, 241 (1-2) 1998 264-276.

[1999Lav] O. Lavergne and C.H. Allibert, Dissolution Mechanisms of WC in Co-based Liquids, *Journal of High Temperature High Presssures*, 31 (1999) 347-355.

[1999Mil] Yu.V. Milman, S. Luyckx and I.T. Northrop, Influence of Temperature, Grain Size and Cobalt Content on the Hardness of WC-Co Alloys, *International Journal of Refractory Metals and Hard Materials*, 17 (1999) 39-44.

[1999She] J.Y. Sheikh-Ahmad and J.A. Bailey, The Wear Characteristics of Some Cemented Tungsten Carbides in Machining Particleboard, *Wear*, 225-229 (1999) 256-266.

[1999Tru] A.R. Trueman, D.P. Schweinsberg and G.A. Hope, A Study of the Effect of Cobalt Additions on the Corrosion of Tungsten Carbide/Carbon Steel Metal Matrix Composites, *Corrosion Science*, 41 (1999) 1377-1389.

[2000AST] ASTM G5-95a:2000, Standard Testing Method for Wear Testing with a Pin-on-Disk, (2000) 1-6.

[2000Cho] K. Choi, N.M. Hwang and D.Y. Kim, Effect of VC on Microstructural Evolution of WC-Co alloy: Mechanism of Grain Growth Inhibition, *Powder Metallurgy*, 43(2) (2000) 168-172.

[2000Eng] H. Engqvist, H. Högberg, G.A. Botton, N. Axén, S. Ederyd and S. Hogmark, Tribofilm Formation on Cemented Carbides in Dry Sliding Conformal Contact, *Wear*, 239 (2) (2000) 219-228.

[2000Lov] H.L.L. De Villiers Lovelock, The Effect of Vanadium Carbide Additions on the Microstructure and Wear Resistance of WC-Co HP/HVOF Thermal Spray Coatings, MSc. Dissertation, University of the Witwatersrand, Johannesburg, 2000.

[2000Ran] D. du Randt, S. Luyckx, D. Marcoulides, I.T. Northrop and D.J. Whitefield, A Comparison Between Ultrafine WC-Co and fine WC-VC-Co alloys, *International Journal of Materials and Product Technology*, 15 (2000) 270-274.

[2000Shi] T.L. Shing, An Investigation on the Effect of Ruthenium Additions on Properties of WC-Co, MSc. Dissertation, University of the Witwatersrand, Johannesburg, 2000.

[2001All] C.H. Allibert, Sintering Features of Cemented Carbides WC-Co Processed from Fine Powders, *International Journal of Refractory Metals and Hard Materials*, 19 (2001) 53-61.

[2001Are] F.J. Arenas, A. Matos, M. Cabezas, C. Di Rauso and C. Gridorescu, Densification, Mechanical Properties and Wear Behaviour of WC-VC-Co-Al Hardmetals, *International Journal of Refractory Metals and Hard Materials*, 19 (2001) 381-387.

[2001Kis] J. Kishino, H. Nomura, S.G. Shin, H. Matsubara and T. Tanase, Computational Study on Grain Growth in Cemented Carbides, *Proceedings of the 15th International Plansee Seminar*, 2 (2001) 50-64.

[2001Luy] S. Luyckx and M.Z. Alli, Comparison between V_8C_7 and Cr_3C_2 as grain refiners for WC-Co, *Materials and Design*, 22 (2001) 507-510.

[2001Obb] E.G. Obbard, S. Luyckx, S. Hamar-Thibault and C.H. Allibert, Determination of the Composition Range Suitable to the Formation of WC-(V,W)C*x*-Co Materials, *International Journal of Refractory Metals and Hard Materials*, 19 (2001) 349-357.

[2001Shi] T.L. Shing, S. Luyckx, I.T. Northrop and I. Wolff, The Effect of Ruthenium Additions on the Hardness, Toughness and Grain Size of WC-Co, *International Journal of Refractory Metals and Hard Materials*, 19 (2001) 41-44.

[2001Sur] C. Suryanarayana, Mechanical Alloying and Milling, *Progress in Materials Science*, 46 (2001) 1-184.

[2001Tan] M. Tanaka, G. Girard, R. Davis, A. Peuto and N. Bignell, Recommended Table for the Density of Water Between 0°C and 40°C Based on Recent Experimental Reports, *Metrologia*, 38 (2001) 301-309.

[2001Upa] G.S. Upadhyaya, D. Sarathy and G. Wagner, Advances in Sintering of Hardmetals, *Materials and Design*, 22 (2001) 499-506.

[2001Upa1] G.S. Upadhyaya, Materials Science of Cemented Carbides - An Overview, *Materials and Design*, 22 (2001) 483-489.

[2001Zin] J. Zinyana, S. Broccardo, S. Hamar-Thibault, L.A. Cornish, M.J. Witcomb, C.H. Allibert and S. Luyckx, Effect of Composition on the (V,W)C Constitution in V-W-C-Co Alloys, *15th International Plansee Seminar*, 4 (2001) 291-296.

[2002Bhu] B. Bhushan, Introduction to Tribology, John Wiley and Sons Inc., New York, USA, 2002.

[2001Eng] H. Engqvist, S. Ederyd, B. Uhrenius and S. Hogmark, Sliding Wear of Cemented Carbides, *15th International Plansee Seminar*, 2 (2001) 267-278.

[2002Eng] H. Engqvist, S. Jacobson and N. Axén, A Model for the Hardness of Cemented Carbides, *Wear*, 252 (2002) 384-393.

[2002Gil] G. Gille, B. Szesny, K. Dreyer, H. van den Berg, J. Schmidt, T. Gestrich and G. Leitner, Submicron and Ultrafine Grained Hardmetals for Microdrills and Metal Cutting Inserts, *International Journal of Refractory Metals and Hard Materials*, 20 (2002) 3-22.

[2002Wan] Y. Wang, M. Heusch, S. Lay and C.H. Allibert, Microstructure Evolution in the Cemented Carbides WC-Co, I. Effect of the C/W Ratio on the Morphology and Defects of the WC Grains, *Physica Status Solidi (a),* 193(2) (2002) 271-283.

[2002Wit] B. Wittmann, W.D. Schubert and B. Lux, WC Grain Growth and Grain Growth Inhibition in Nickel and Iron Binder Hardmetals, *International Journal of Refractory Metals and Hard Materials*, 20 (2002) 51-60.

[2003Bro] S.P. Broccardo, An Investigation into the Corrosion Resistance of WC-VC-Co Alloys, M.Sc Dissertation, University of the Witwatersrand, Johannesburg, 2003.

[2003Cha] V. Chabretou, C.H. Allibert and J.M. Missiaen, Quantitative Analysis of the Effect of the Binder Phase Composition on Grain Growth in WC-Co Sintered Materials, *Journal of Materials Science*, 38 (2003) 258-2590.

[2003Jon] M.I. Jonesa, K. Hiraoa, H. Hyugab, Y. Yamauchia and S. Kanzakia, Wear Properties of Y-α/β Composite Sialon Ceramics, *Journal of the European Ceramic Society*, 23 (2003) 1743-1750.

[2003Sut] S. Sutthiruangwong and G. Mori, Corrosion Properties of Co-based Cemented Carbides in Acidic Solutions, *International Journal of Refractory Metals and Hard Materials*, 21 (2003) 135-145.

[2004Pir] J. Pirso, S. Letunovitš and M. Viljus, Friction and Wear Behaviour of Cemented Carbides, *Wear*, 257 (2004) 257-265.

[2004Roe] B. Roebuck and P. Brewin, Toughness testing of hardmetals, *Powder Metallurgy*, 47(21) (2004) 15-16.

[2004Sch] B. Schnyder, C. Stössel-Sittig, R. Kötz, S. Hochstrasser-Kurz, S.Virtanen, C. Jaeggi, N. Eichenberger and H. Siegenthaler, Investigation of the Electrochemical Behaviour of WC–Co Hardmetal with Electrochemical and Surface Analytical Methods, *Surface Science*, 566-568 (2004) 1240-1245

[2004Shi] X. Shi, G. Shao, X. Duan, G. Zhang and W. Zhang, Influence of VC, Cr_3C_2 on Sintering Properties of Nanocrystalline WC-Co Composite Powders, *Journal of University of Science and Techonology Beijing*, 26(6) (2004) 612-615.

[2005Fan] Z. Fang, P. Maheshwari, X. Wang, H.Y. Sohn, A. Griffo, R. Riley, An Experimental Study of The Sintering of Nanocrystalline WC–Co Powders, *International Journal of Refractory Metals and Hard Materials*, 23 (4-6) (2005) 249-257.

[2005Mac] C.N. Machio, G. Akdogan, M.J. Witcomb and S. Luyckx, Performance of WC-VC-Co Thermal Spray Coatings in Abrasion and Slurry Erosion Tests, *Wear*, 258 (2005) 434-442.

[2005Mar] A. Markström, K. Frisk and B. Sundman, A Revised Thermodynamic Description of the Co-W-C System, *Journal of Phase Equilibria and Diffusion*, 26(2) (2005) 152-160.

[2005Mor] C.W. Morton, D.J. Wills and K. Stjernberg, The Temperature Ranges for Maximum Effectiveness of Grain Growth Inhibitors in WC–Co Alloys, *International Journal of Refractory Metals and Hard Materials*, 23 (2005) 287-293.

[2005Sut] S. Sutthiruangwong, G. Mori and G. Kosters, Passivity and Pseudopassivity of Cemented Carbides, *International Journal of Refractory Metals and Hard Materials*, 23 (2005) 129-136.

[2005Upa] A. Upadhyaya and D. Sarathy, Advances in Alloy Design of Hardmetals, *Transactions of the Indian Ceramic Society*, 64(4) (2005) 197-202.

[2006Cho] J.E. Choa, S.Y. Hwang and K.Y. Kima, Corrosion Behavior of Thermal Sprayed WC Cermet Coatings Having Various Metallic Binders in Strong Acidic Environment, *Surface and Coatings Technology*, 200 (2006) 2653-2662.

[2006Luy] S. Luyckx and A. Love, The Dependence of the Contiguity of WC on Co Content and its Independence from WC Grain Size in WC–Co Alloys, *International Journal of Refractory Metals and Hard Materials*, 24 (2006) 75-79.

[2006Pir] J. Pirso, M. Viljus and S. Letunovitš, Friction and Dry Sliding Wear Behaviour of Cermets, *Wear*, 260(7-8) (2006) 815-824.

[2006Sai] H. Saito, A. Iwabuchi and T. Shimizu, Effects of Co Content and WC Grain Size on Wear of WC Cemented Carbide, *Wear*, 261(2) (2006) 126-132.

[2006Sri] M. Srivastava, V.E. Selvi, V.K.W. Grips and K.S. Rajam, Corrosion Resistance and Microstructure of Electrodeposited Nickel-Cobalt Alloy Coatings, *Surface Coatings Technology*, 201 (2006) 3051-3060.

[2007Has] N.G. Has, J.H. Neethling, P.R. Berndt, H-O. Andrén and S. Norgren, A Comparison of the Microstructures of WC–VC–Tic–Co and WC–VC–Co Cemented Carbides, *International Journal of Refractory Metals and Hard Materials*, 25(3) (2007) 207-213.

[2007Hoc] S. Hochstrasser-Kurz, Y. Mueller, C. Latkoczy, S. Virtanen and P. Schmutz, Analytical Characterization of the Corrosion Mechanisms of WC-Co by Electrochemical Methods and Inductively Coupled Plasma Mass Spectroscopy, *Corrosion Science*, 49 (2007) 2002-2020.

[2007Hua] S.G. Huang, L. Li, K. Vanmeensel, O. Van der Biest and J. Vleugels, VC, Cr_3C_2 and NbC Doped WC–Co Cemented Carbides Prepared by Pulsed Electric Current Sintering, *International Journal of Refractory Metals and Hard Materials*, 25 (2007) 417-422.

[2007Luy] S. Luyckx and C.N. Machio, Characterization of WC–VC–Co Thermal Spray Powders and Coatings, *International Journal of Refractory Metals and Hard Materials*, 25 (2007) 11-15.

[2007Rah] V. Rahimi Dizaji, M. Rahmani, M. Faghihi Sani, Z. Nemati and J. Akbari, Microstructure and Cutting Performance Investigation of Ti(C,N)-based Cermets Containing Various Types of Secondary Carbides, *International Journal of Machine Tools and Manufacture*, 47 (2007) 768-772.

[2007Sch] G. Schwenke and V.S. Judy, Magnetic Saturation and Coercivity Measurements on Chromium-doped Cemented Carbides, *International Journal of Powder Metallurgy*, 43(2) (2007) 21-31.

[2007Siv] D. Sivaprahasam, S.B. Chandrasekar and R. Sundaresan, Microstructure and Mechanical Properties of Nanocrystalline WC–12Co Consolidated by Spark Plasma Sintering, *International Journal of Refractory Metals and Hard Materials*, 25 (2007) 144-152.

[2008Aw] P.K. Aw, A.L.K. Tan, T.P. Tan and J. Qiu, Corrosion Resistance of Tungsten Carbide Based Cermet Coatings Deposited by High Velocity Oxy-Fuel Spray Process, *Thin Solid Films*, 516 (2008) 5710-5715.

[2008Hoc] S. Hochstrasser-Kurz, D. Reiss, T. Suter, C. Latkoczy, D. Günther, S. Virtanen, P.J. Uggowitzer and P. Schmutz, ICP-MS, SKPFM, XPS, and Microcapillary Investigation of the Local Corrosion Mechanisms of WC–Co Hardmetal, *Journal of The Electrochemical Society*, 155(8) (2008) 415-426.

[2008Hua] S.G. Huang, R.L. Liu, L. Li, O. Van der Biest and J. Vleugels, NbC as Grain Growth Inhibitor and Carbide in WC–Co Hardmetals, *International Journal of Refractory Metals and Hard Materials*, 26 (2008) 389-395.

[2008Lay] S. Lay, C.H. Allibert, M. Christensen and G. Wahnstrom, Morphology of WC Grains in WC–Co Alloys, *Materials Science and Engineering*, A 486 (2008) 253-261.

[2008Wan] X. Wang, Z.Z. Fang and H.Y. Sohn, Grain Growth During the Early Stage of Sintering of Nanosized WC-Co Powder, *International Journal of Refractory Metals and Hard Materials*, 26 (2008) 232-241.

[2008Zha] L. Zhang, Y. Wang, X. Yu, S. Chen and X. Xiong, Crack Propagation Characteristic and Toughness of Functionally Graded WC-Co Cemented Carbide, *International Journal of Refractory Metals and Hard Materials*, 26 (2008) 295-300.

[2009Bon] K. Bonny, P. De Baets, J. Vleugels, S. Huang, O. Van der Biest and B. Lauwers, Impact of Cr_3C_2/VC addition on the Dry Sliding Friction and Wear Response of WC-Co Cemented Carbides, *Wear*, 267(9-10) (2009) 1642-1652.

[2009Has] N.G. Hashe, S. Norgren, H.-O. Andrén, J.H. Neethling and P.R. Berndt, Reduction of Carbide Grain Growth in WC-VC-Co by Sintering in a Nitrogen Atmosphere, *International Journal of Refractory Metals and Hard Materials*, 27 (2009) 20-25.

[2009Hew] S.A. Hewitt and K.A. Kibble, Effects of Ball Milling Time on the Synthesis and Consolidation of Nanostructured WC–Co composites, *International Journal of Refractory Metals and Hard Materials*, 27 (2009) 937-948.

[2009ISO] International Standard ISO28079, Hardmetals – Palmqvist Toughness, International Standard Organisation, 1st Edition (2009) 1-10.

[2009Kon] I. Konyashin, S. Hlawatschek, B. Ries, F. Lachmann, F. Dorn, A. Sologubenko and T. Weirich, On the Mechanism of WC Coarsening in WC–Co Hardmetals with Various Carbon Contents, *International Journal of Refractory Metals and Hard Materials*, 27 (2009) 234-243.

[2009Wei] J. Weidow, S. Norgren and A. Hans-Olof, Effect of V, Cr and Mn Additions on the Microstructure of WC-Co, *International Journal of Refractory Metals and Hard Materials*, 27 (2009) 817-822.

[2009Mah] M. Mahmoodan, H. Aliakbarzadeh and R. Gholamipour, Microstructural and Mechanical Characterisation of High Energy Ball Milled and Sintered WC-10wt%Co-*x*TaC Nano-powders, *International Journal of Refractory Metals and Hard Materials*, 27 (2009) 801-805.

[2009Yan] D.Y. Yang and S.L. Kang, Suppression of Abnormal Grain Growth in WC–Co via Pre-sintering Treatment, *International Journal of Refractory Metals and Hard Materials*, 27 (2009) 90-94.

[2010AST1] ASTM G5-94:2010, Annual Book of ASTM Standards, Philadelphia, 45-55 (2010).

[2010AST2] ASTM G102-89:2010, Annual Book of ASTM Standards, Philadelphia, 422-427 (2010).

[2010Bon] K. Bonny, P. De Baets, Y. Perez, J. Vleugels and B. Lauwers, Friction and Wear Characteristics of WC-Co Cemented Carbides in Dry Reciprocating Sliding Contact, *Wear*, 268 (2010) 1504-1517.

[2010BS] BS EN ISO 3369; 2010.

[2010Kon] D.S. Konadu, J. van der Merwe, J.H. Potgieter, S. Potgieter-Vermaak and C.N. Machio, The Corrosion Behaviour of WC-VC-Co Hardmetals in Acidic Media, *Corrosion Science*, 52 (2010) 3118-3125.

[2011Bol] A.S. Bolokang, M.J. Phasha, C. Oliphant and D. Motaung, XRD Analysis and Microstructure of Milled and Sintered V, W, C, and Co powders, *International Journal of Refractory Metals and Hard Materials*, 29 (2011) 108-111.

[2011Bon] K. Bonny, P. De Baets, J. Vleugels, A. Salehi, O. Van der Biest, B. Lauwers and W. Liu, Sliding Wear of Electrically Conductive ZrO_2-WC Composites against WC-Co Cemented Carbide, *Tribology Letters*, 30(3) (2008) 191-198.

[2011Bon1] K. Bonny, Y.P. Delgado, P. De Baets, J. Sukumaran, J. Vleugels, O. Malek and B. Lauwers, Impact of Wire-EDM on Tribological Characteristics of ZrO_2-based Composites in Dry Sliding Contact with WC–Co-Cemented Carbide, *Tribology Letters*, 43 (1) (2011) 1-15.

[2011Mah] M. Mahmoodan, H. Aliakbarzadeh and R. Gholamipour, Sintering of WC-10%Co Nano Powders Containing TaC and VC Grain Growth Inhibitors, *Transactions of Nonferrous Metals Society of China*, 21 (2011) 1080-1084.

[2011Pot] J.H. Potgieter, N. Thanjekwayo, P. Olubambi, N. Maledi and S.S. Potgieter-Vermaak, Influence of Ru Additions on the Corrosion Behaviour of WC–Co Cemented Carbide Alloys in Sulphuric Acid, *International Journal of Refractory Metals and Hard Materials*, 29(4) (2011) 478-487.

[2011Whi] D.J. Whitefield, The Optimisation and Evaluation of VC-WC-Co Alloys, PhD Thesis, University of the Witwatersrand, Johannesburg, 2011.

[2012AST] ASTM G31-12a:2012, Standard Guide for Laboratory Immersion Corrosion Testing of Metals, NACE International/ ASTM International, 2012.

[2012Lin] N. Lin, C.H. Wu, Y.H. He and D.F. Zhang, Effect of Mo and Co Additions on the Microstructure and Properties of WC-TiC-Ni Cemented Carbides, *International Journal of Refractory Metals and Hard Materials*, 30 (2012) 107-113.

[2013Ben] B. Herd, J.C. Goritzka and H. Over, Room Temperature Oxidation of Ruthenium, *The Journal of Physical Chemistry*, 117 (2013) 15148−15154.

[2013ISO] International Standard ISO3326:2013, Hardmetals - Determination of (the Magnetization) Coercivity, 2 (2013).

[2013Mac] C.N. Machio, D.S. Konadu, J.H. Potgieter, S. Potgieter-Vermaak and J. Van der Merwe, Corrosion of WC-VC-Co Hardmetal in Neutral Chloride Containing Media, *Hindawi Publishing Corporation*, (2013) 1-10.

[2013Ogu] E.N. Ogunmuyiwa, Processing, Characterization and Tribological Assessment of Novel WC-VC-Co Coatings and Alloys, PhD Thesis, University of the Witwatersrand, Johannesburg, 2013.

[2013Seb] T. Sebeya, An Investigation into the Causes of the Difference in the Corrosion Behaviour of WC-Co and WC-VC-Co Hardmetals, M.Sc Dissertation, University of the Witwatersrand, Johannesburg, 2013.

[2014Bor] I. Borgh, P. Hedström, A. Borgenstam, J. Ågren and J. Odqvist, Effect of Carbon Activity and Powder Particle Size on WC Grain Coarsening During Sintering of Cemented Carbides, *International Journal of Refractory Metals and Hard Materials*, 42 (2014) 30-35.

[2015Nor] S. Norgren, J. García, A. Blomqvist and L. Yinc, Trends in the P/M hard metal industry, *International Journal of Refractory Metals and Hard Materials*, 48 (2015) 31-45.

[2015Tof] C. Tofallis, A Better Measure of Relative Prediction Accuracy for Model Selection and Model Estimation, *Journal of the Operational Research Society*, 66 (2015) 1352-1362.

[2017Bro] K.J.A. Brookes, Hardmetal Processing, *Metal Powder Report*, 72(3) (2017) 151-167.

[2017Kon] I. Konyashin, A.A. Zaitsev, D. Sidorenko, E.A. Levashov, S.N. Konischev, M. Sorokin, S. Hlawatschek, B. Ries, A.A. Mazilkin, S. Lauterbach and H.J. Kleebe, On the Mechanism of Obtaining Functionally Graded Hardmetals, *Materials Letters*, 186 (2017) 142-145.

[2017Kon1] I. Konyashin, A.A. Zaitsev, D. Sidorenko, E.A. Levashov, B. Ries, S.N. Konischev, M. Sorokin, A.A. Mazilkin, M. Herrmann and A. Kaiser, Wettability of Tungsten Carbide by Liquid Binders in WC–Co Cemented Carbides: Is it Complete for all Carbon Contents?, *International Journal of Refractory Metals and Hard Materials*, 62 (2017) 134-148.

[2018Kon] I. Konyashin, A. Sologubenko, T.B. Weirich and B. Ries, Complexion at WC-Co Grain Boundaries of Cemented Carbides, *Materials Letters*, 76 (2018) 7-10.

[2018Liu] X. Liu, X. Song, H. Wang, X. Liu, F. Tang and H. Lu, Complexions in WC-Co Cemented Carbides, *Acta Materialia*, 149 (2018) 164-178.

[2018Pot] J. Potschke, T. Gestrich and V. Richter, Grain Growth Inhibition of Hardmetals During Initial Heat-up, *International Journal of Refractory Metals and Hard Materials*, 72 (2018) 117-125.

APPENDICES

Appendix A – Standard Charts for Porosity Determination (IS0 4505/ ASTM B276-91 (2000)).

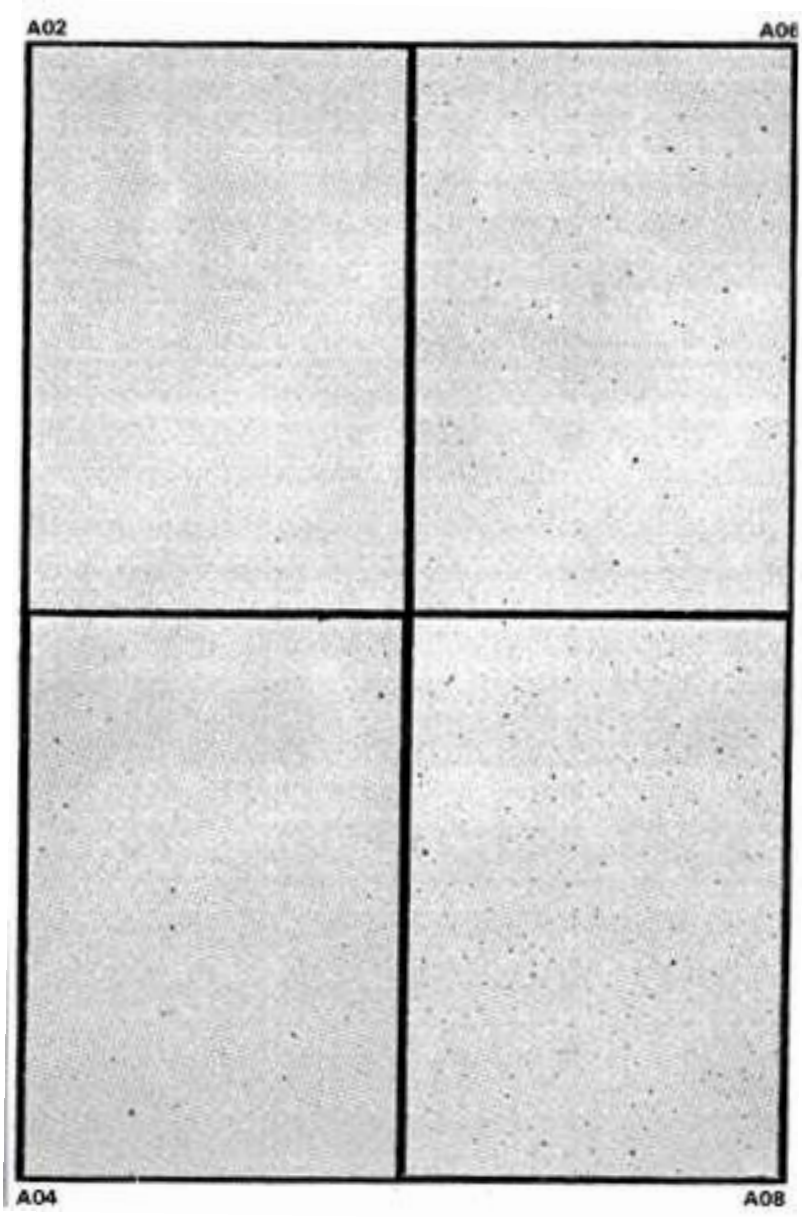

Figure A1. Type A apparent porosity: A02 = 0.02 vol.%, A04 = 0.06 vol.%, A06 = 0.2 vol.% and A08 = 0.4 vol.%.

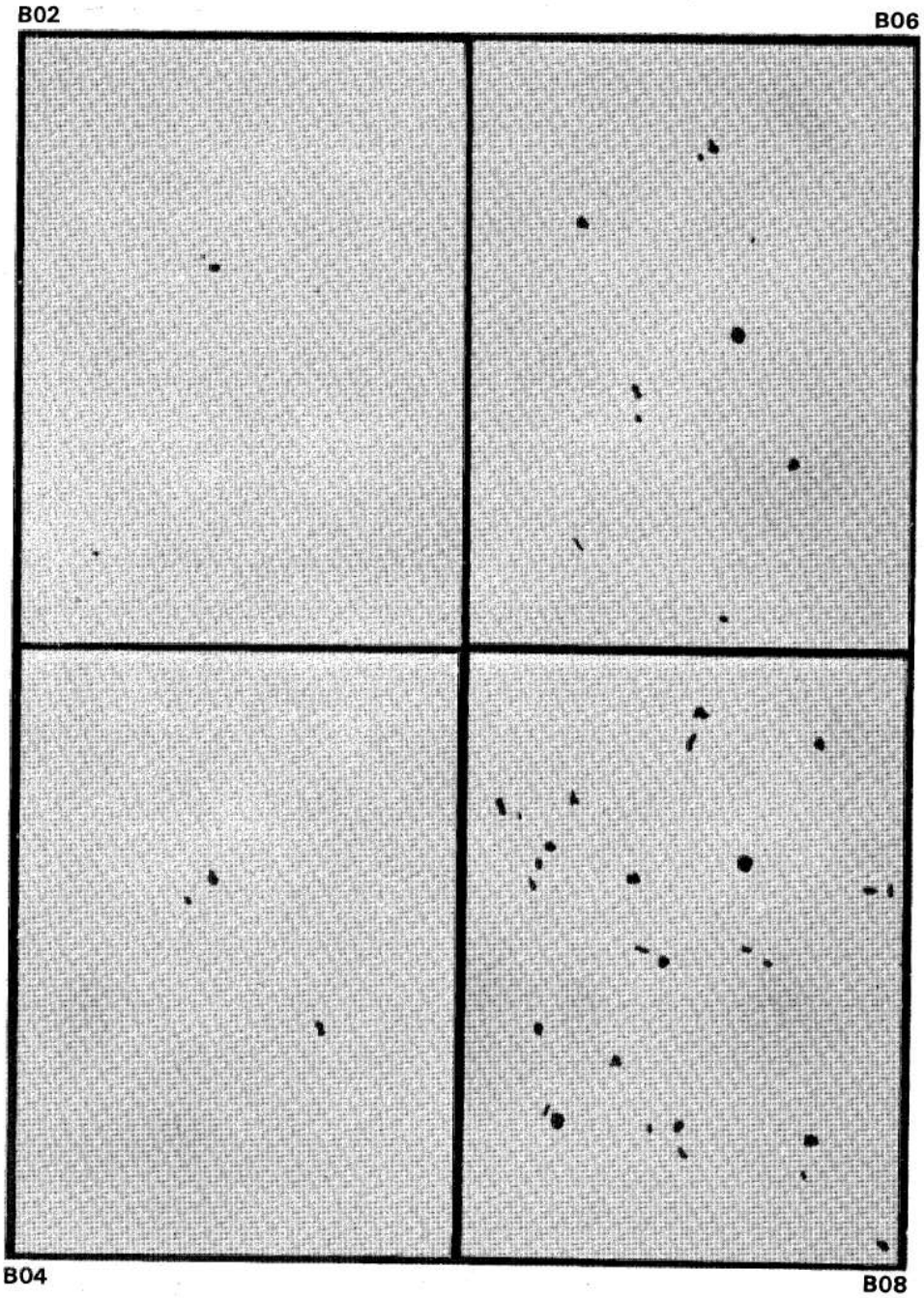

Figure A2. Type B apparent porosity: B02 = 0.02 vol.%, B04 = 0.06 vol.%, B06 = 0.2 vol.% and B08 = 0.4 vol.%.

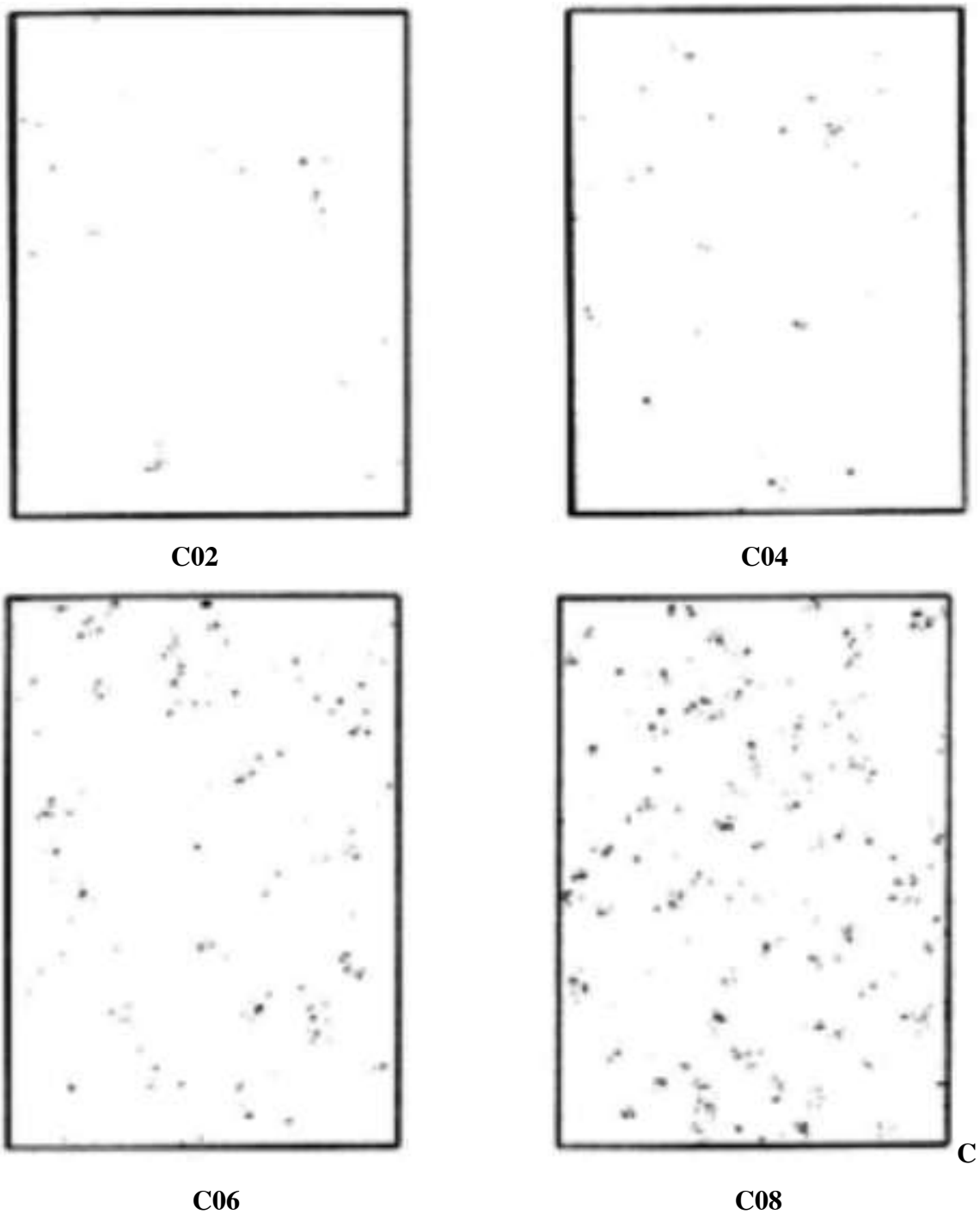

Figure A3. Type C apparent porosity (ratings do not correspond to total pore volume as in A and B type porosities.

Figure A4. Eta phase in a WC-10Co (wt%) alloy – etched for 15s (courtesy of Pilot Tools (Pty) Ltd).

Appendix B – SEM-EDS Maps for 80WC-10VC-(10-*x*)Co-*x*Ru, (89.6-*x*)WC-0.4VC-10Co-*x*Ru and (89.2-*x*)WC-0.8VC-10Co-*x*Ru (wt%) alloys.

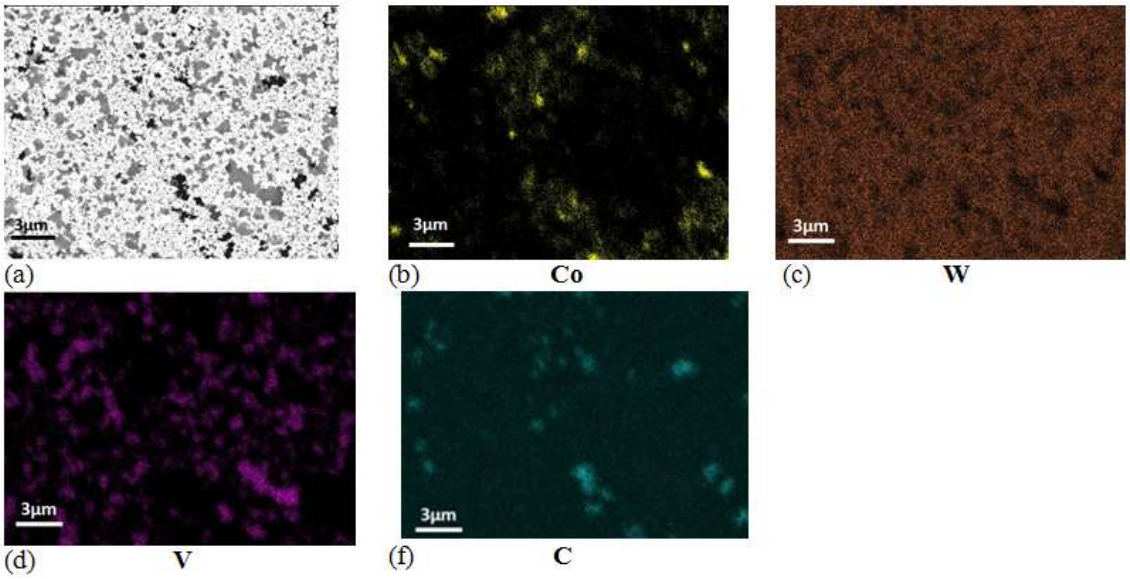

Figure B1. SEM-BSE EDS maps for the (a) 80WC-10VC-10Co (wt%) alloy, showing the distribution of: b) Co, c) W, d) V, and e) C.

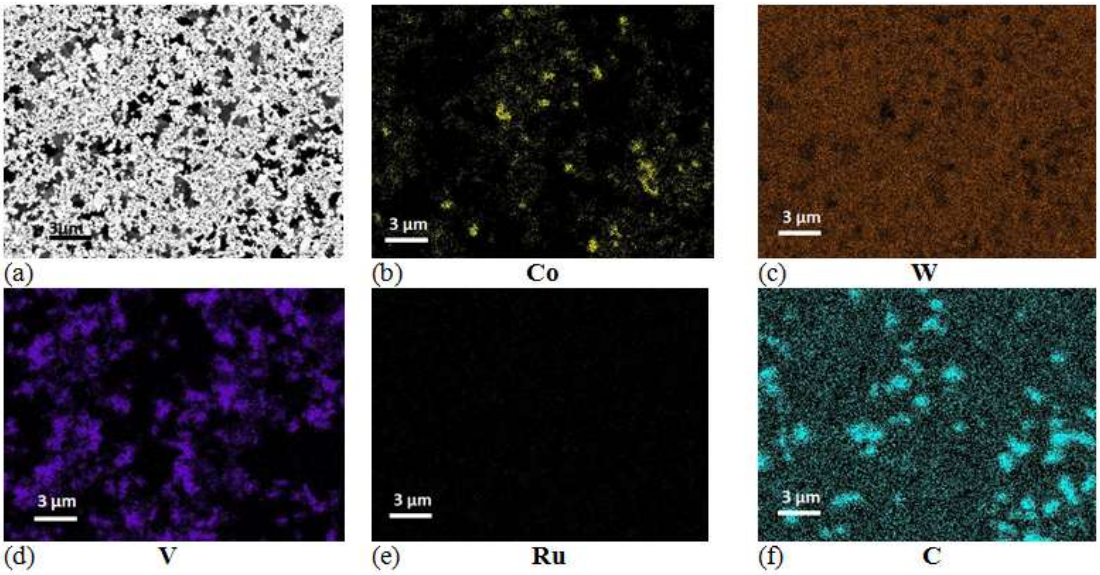

Figure B2. SEM-BSE EDS maps for the (a) 80WC-10VC-9.6Co-0.4Ru (wt%) alloy, showing the distribution of: b) Co, c) W, d) V, e) Ru and f) C.

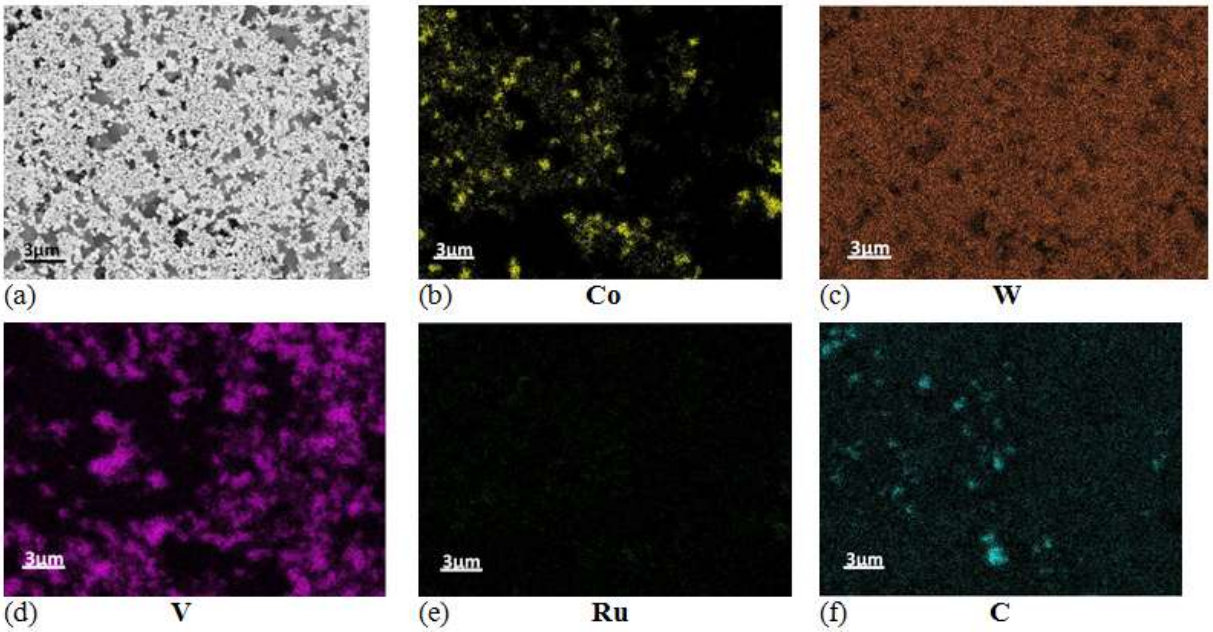

Figure B3. SEM-BSE EDS maps for the (a) 80WC-10VC-9.0Co-1.0Ru (wt%) alloy, showing the distribution of: b) Co, c) W, d) V, e) Ru and f) C.

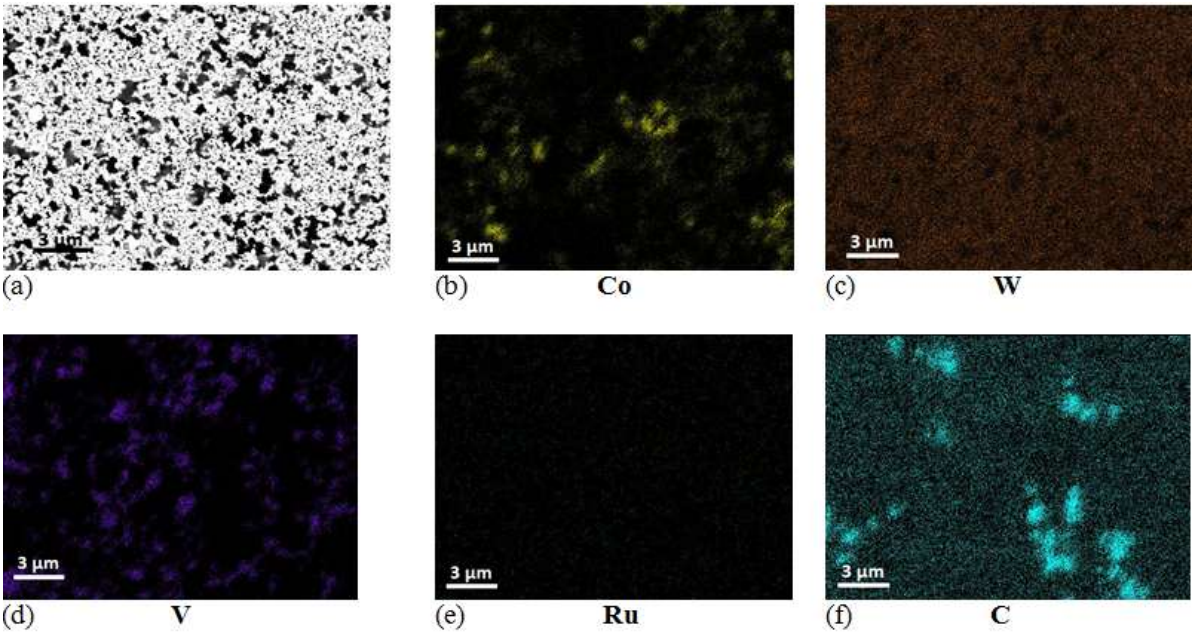

Figure B4. SEM-BSE EDS maps for the (a) 80WC-10VC-8.5Co-1.5Ru (wt%) alloy, showing the distribution of: b) Co, c) W, d) V, e) Ru and f) C.

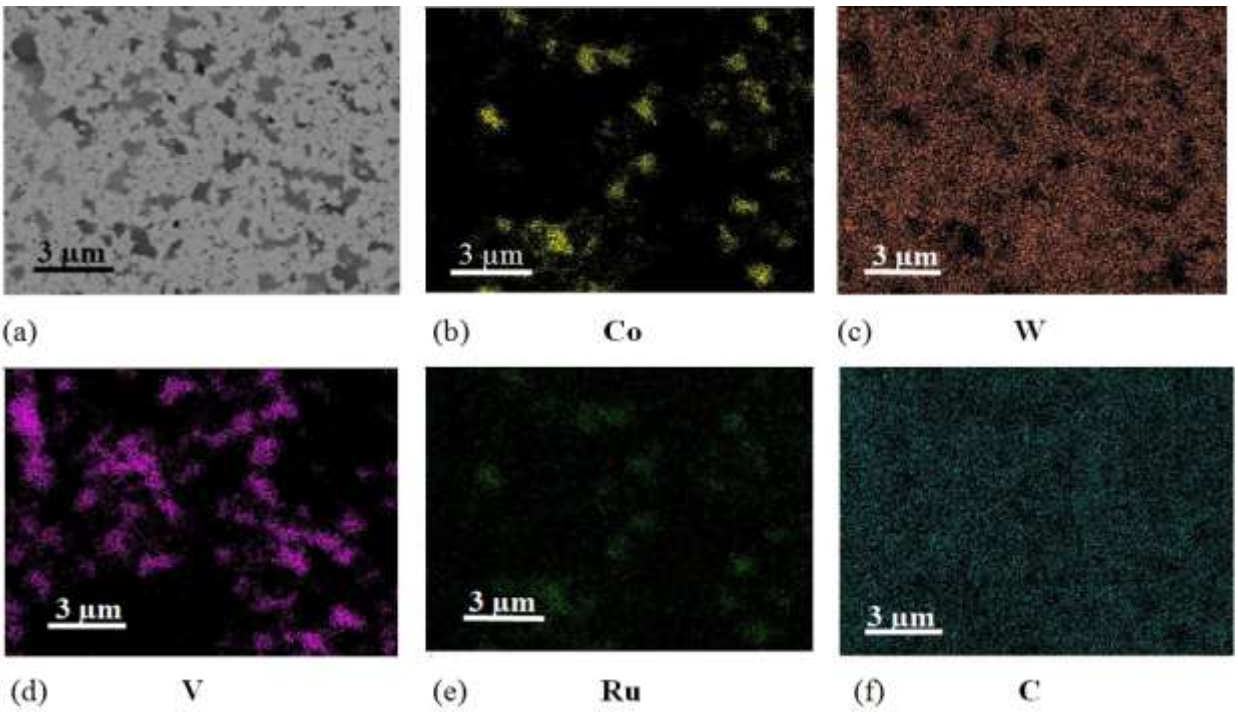

Figure B5. SEM-BSE EDS maps for the (a) 80WC-10VC-8.0Co-2.0Ru (wt%) alloy, showing the distribution of: b) Co, c) W, d) V, e) Ru and f) C.

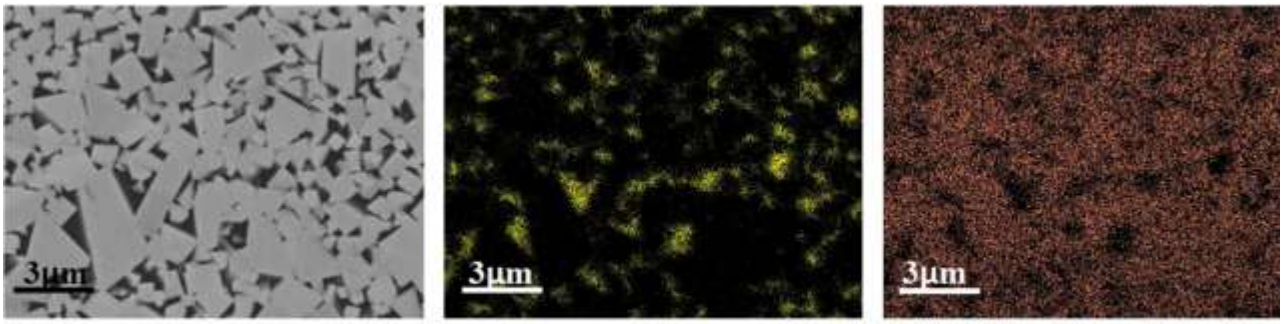

Figure B6. SEM-BSE EDS maps for the (a) 89.6WC-0.4VC-10Co (wt%) alloy, showing the distribution of: b) Co, and c) W.

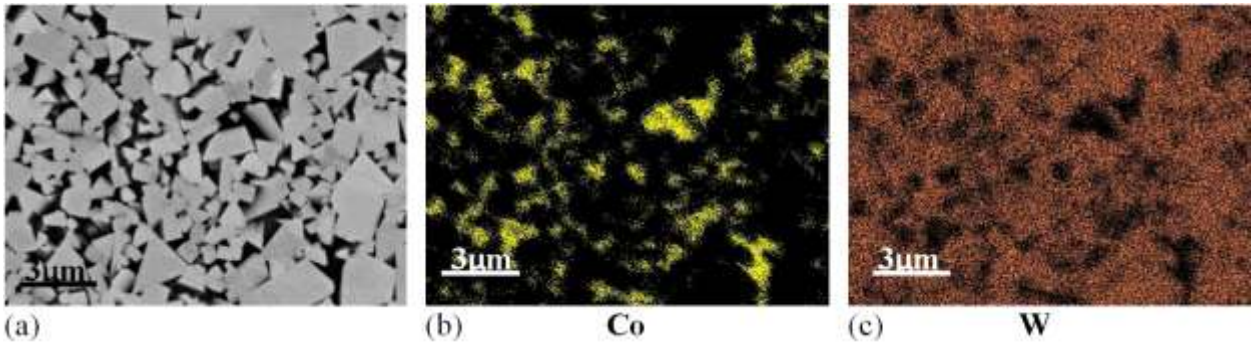

Figure B7. SEM-BSE EDS maps for the (a) 89.2WC-0.4VC-10Co-0.4Ru (wt%) alloy, showing the distribution of: b) Co, and c) W.

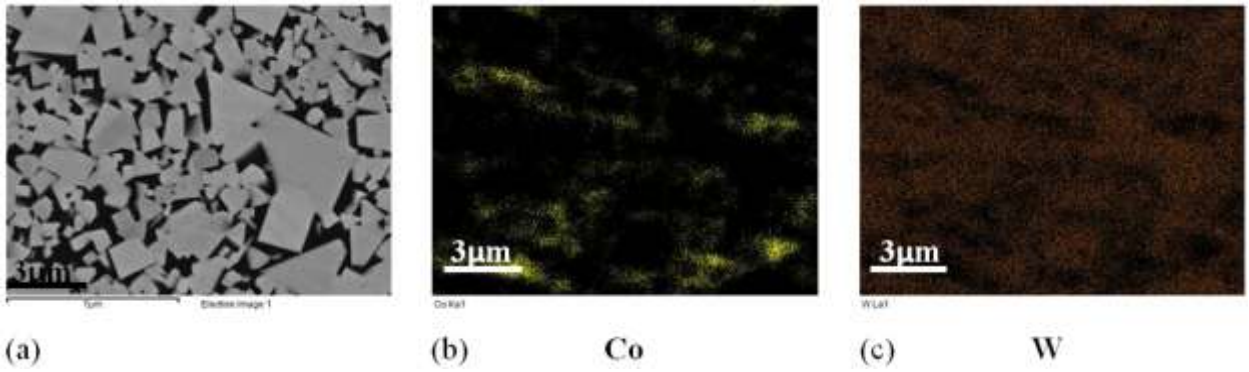

Figure B8. SEM-BSE EDS maps for the (a) 87.6WC-0.4VC-10Co-2.0Ru (wt%) alloy, showing the distribution of: b) Co, and c) W.

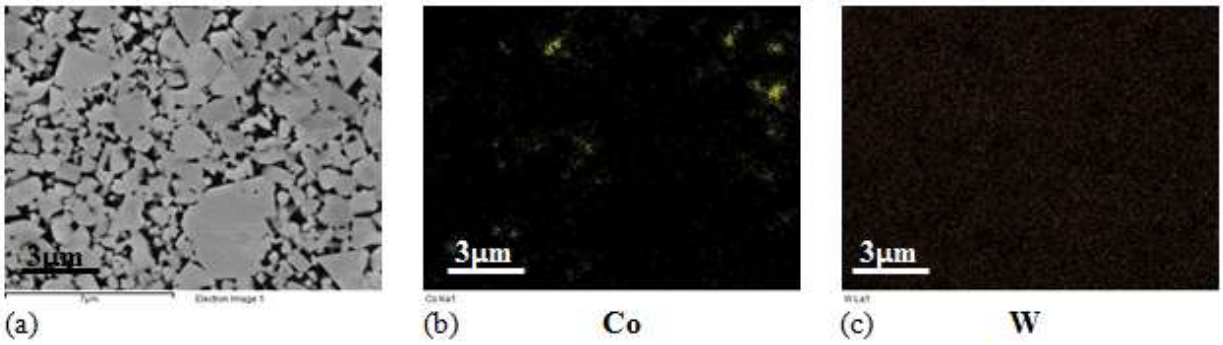

Figure B9. SEM-BSE EDS maps for the (a) 89.2WC-0.8VC-10Co (wt%) alloy, showing the distribution of: b) Co, and c) W.

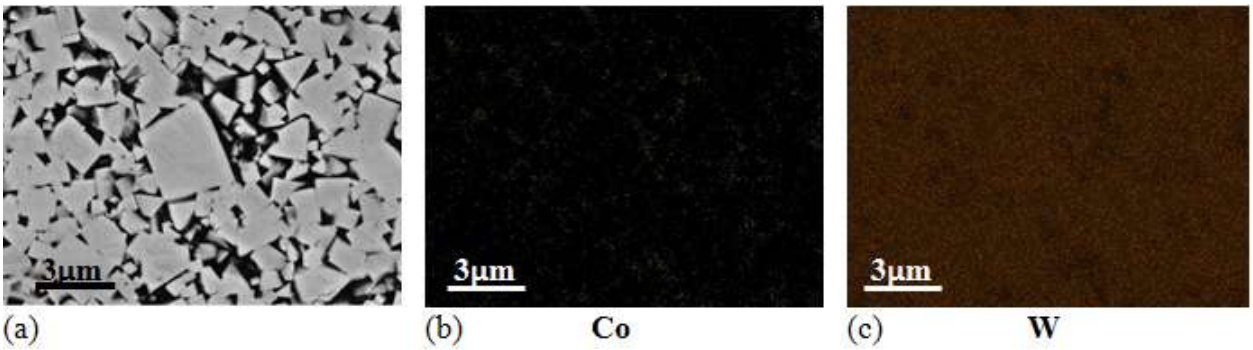

Figure B11. SEM-BSE EDS maps for the (a) 88.8WC-0.8VC-10Co-0.4Ru (wt%) alloy, showing the distribution of: b) Co, and c) W.

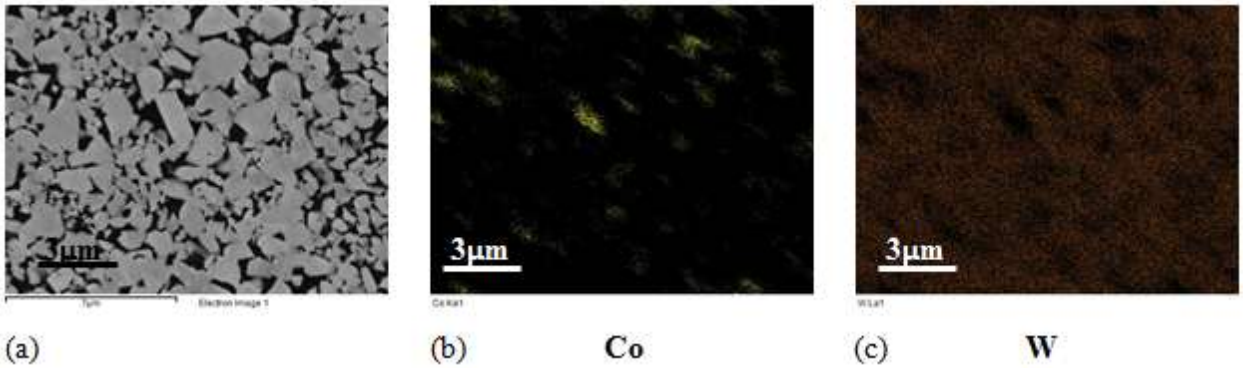

Figure B12. SEM-BSE EDS maps for the (a) 87.2WC-0.8VC-10Co-2.0Ru (wt%) alloy, showing the distribution of: b) Co, and c) W.

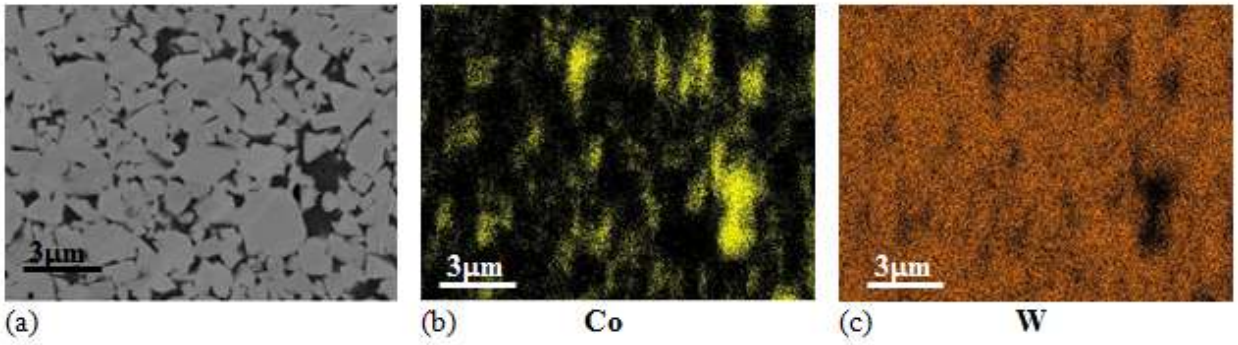

Figure B13. SEM-BSE EDS maps for the (a) 89.6WC-0.4VC-8.5Co-1.5Ru (wt%) alloy, showing the distribution of: b) Co, and c) W.

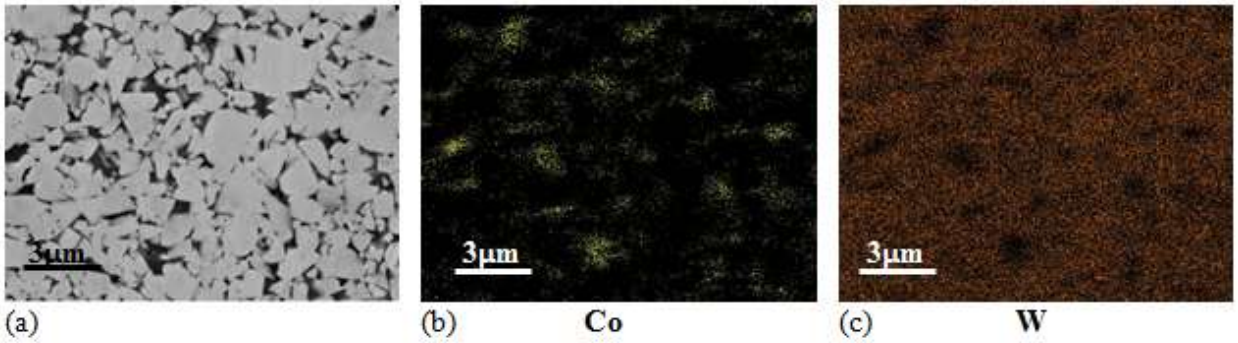

Figure B14. SEM-BSE EDS maps for the (a) 89.6WC-0.4VC-7.0Co-3.0Ru (wt%) alloy, showing

the distribution of: b) Co, and c) W.

Appendix C – XRD Patterns for Corroded Alloys with no Corrosion Products Identified by Raman Spectroscopy

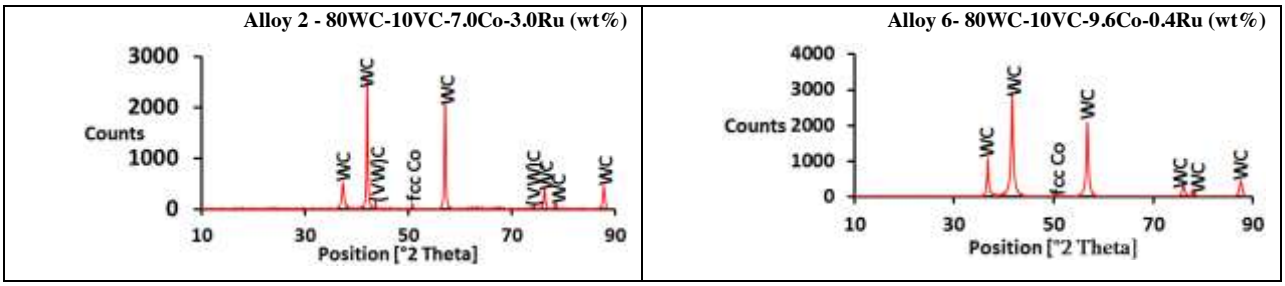

Figure C1. XRD patterns for the 80WC-10VC-(10-x)Co-xRu (wt%) alloys which had no detected corrosion products after exposure to 1 M H_2SO_4 .

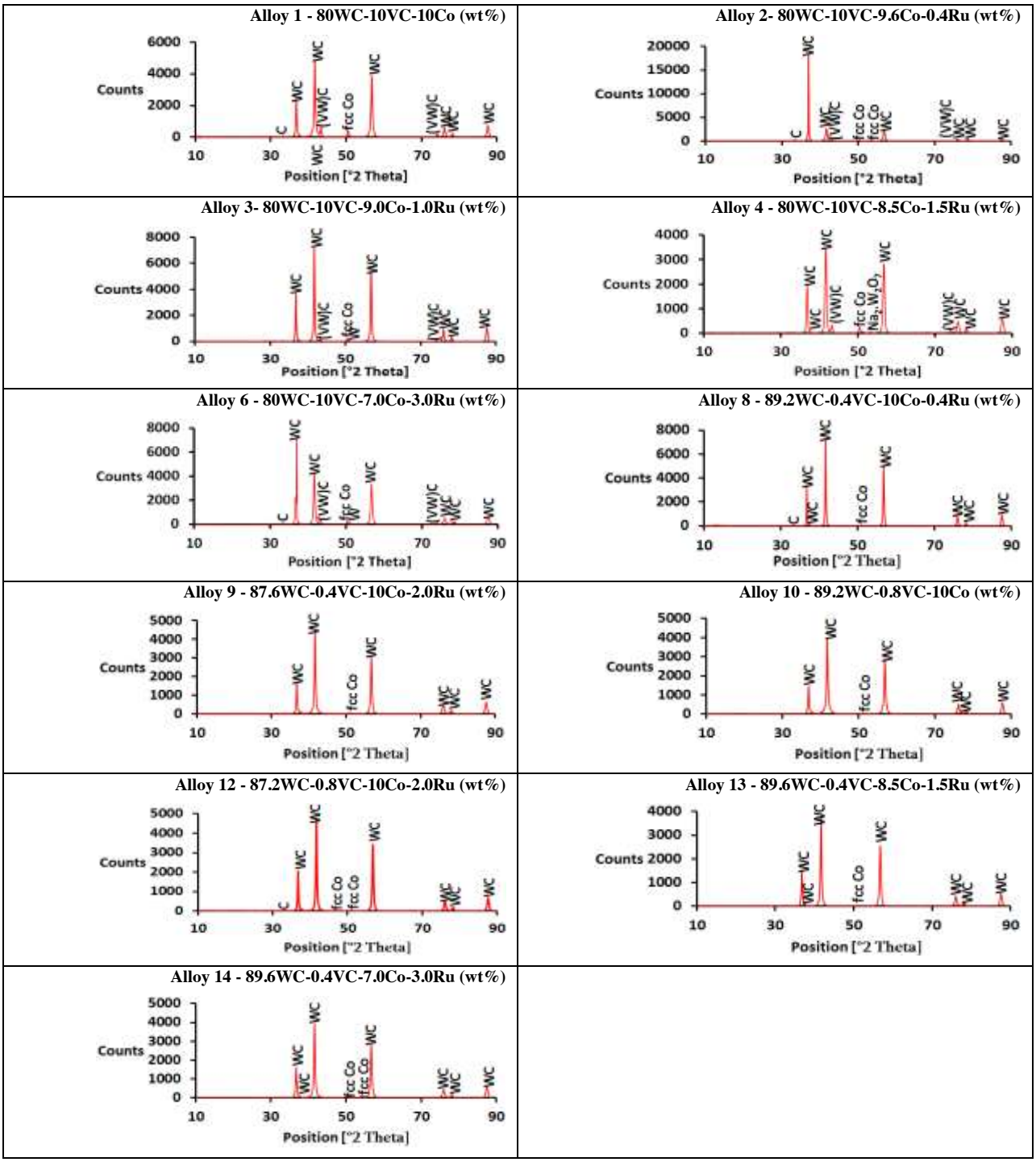

Figure C2. XRD patterns for the 80WC-10VC-(10-x)Co-xRu, (89.6-x)WC-0.4VC-10Co-xRu, (89.2-x)WC-0.8VC-10Co-xRu and 89.6WC-0.4VC-(10-x)Co-xRu (wt%) alloys which had no detected corrosion products after exposure to 1 M NaCl.

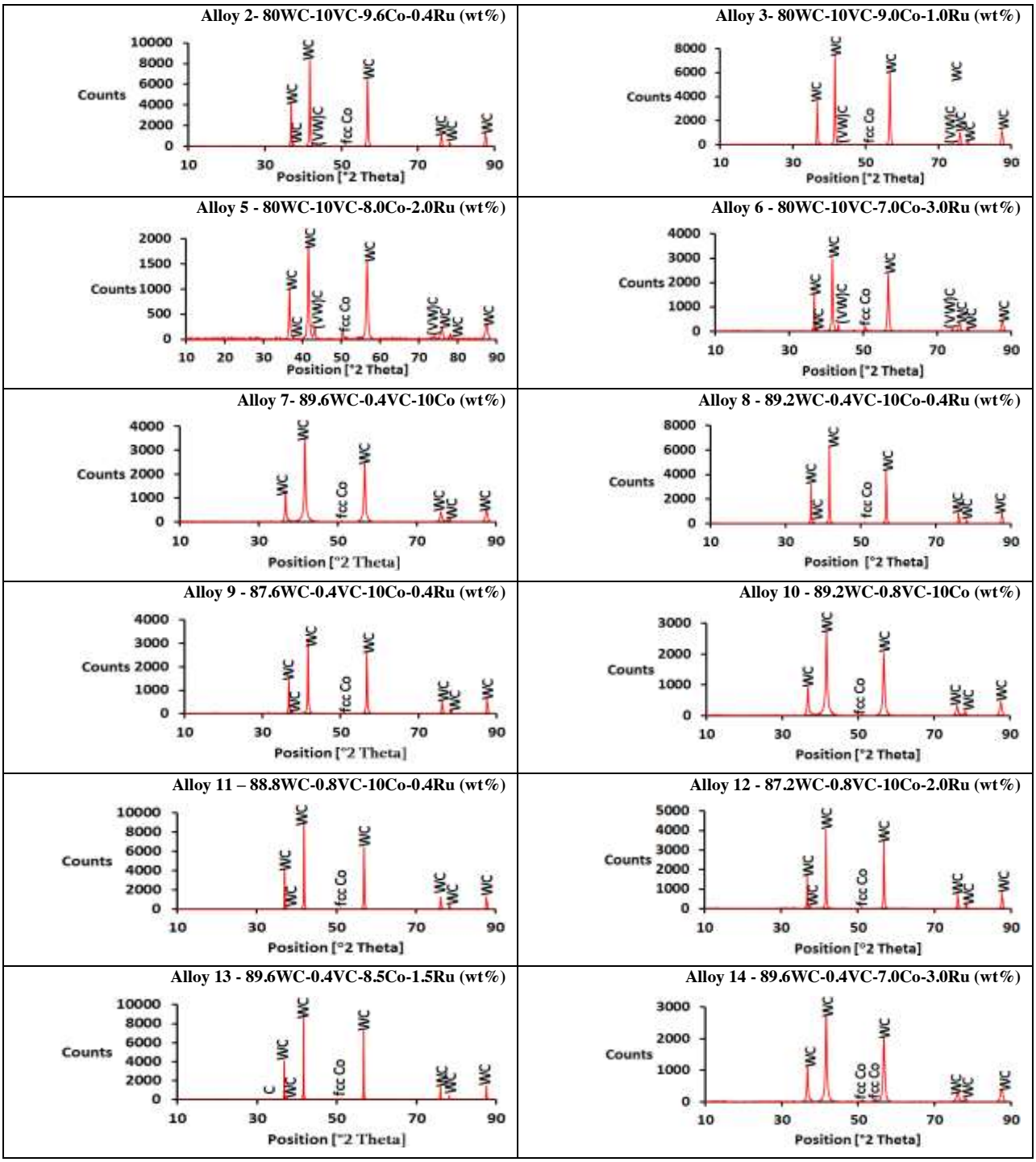

Figure C3. XRD patterns for the 80WC-10VC-(10-x)Co-xRu, (89.6-x)WC-0.4VC-10Co-xRu, (89.2-x)WC-0.8VC-10Co-xRu and 89.6WC-0.4VC-(10-x)Co-xRu (wt%) alloys which had no detected corrosion products after exposure to synthetic mine water.

Appendix D – Raman Peaks for As-Sintered Alloys 1 to 14

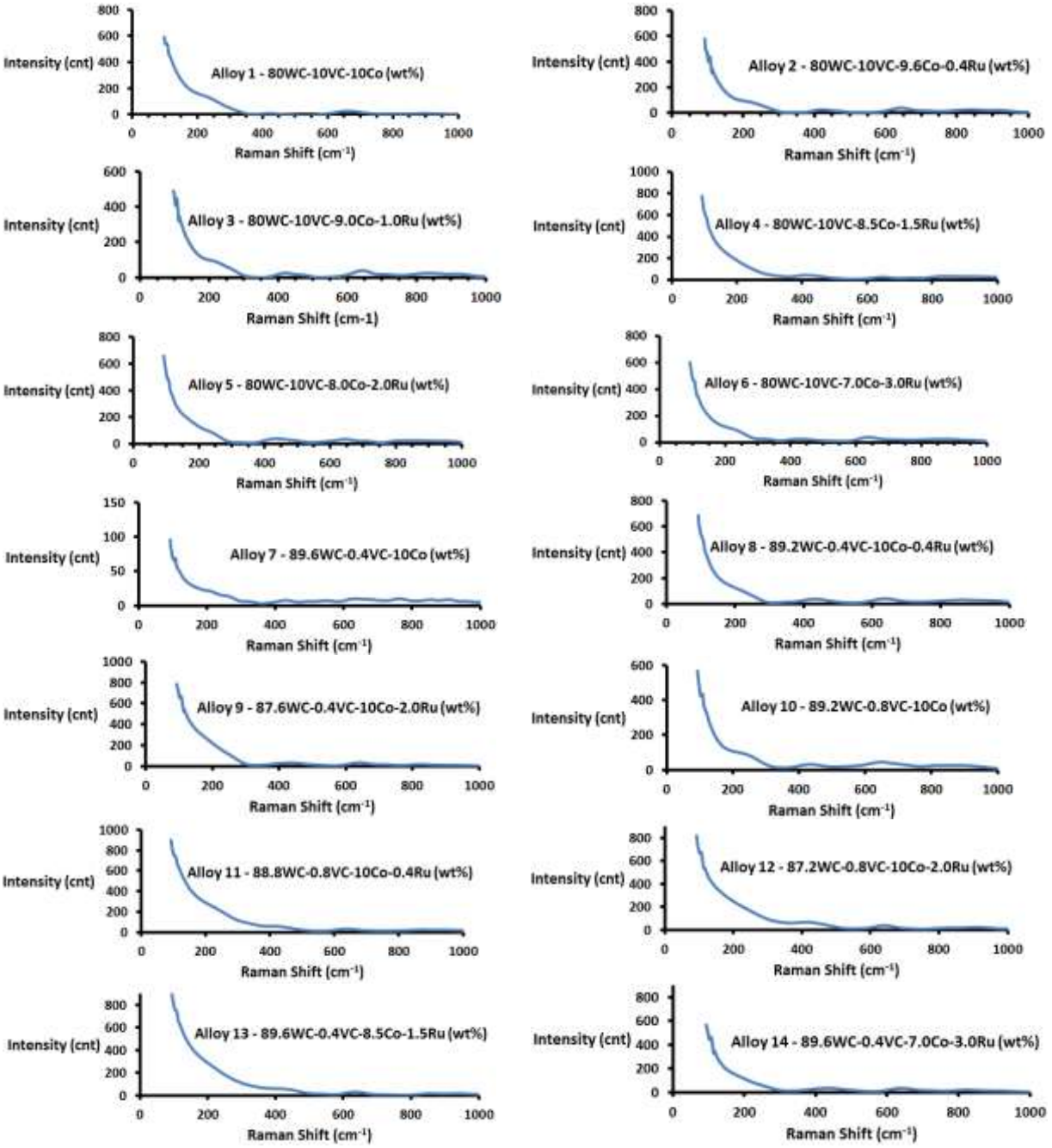

Figure D1. Raman patterns for 80WC-10VC-(10-x)Co-xRu, (89.6-x)WC-0.4VC-10Co-xRu, (89.2-x)WC-0.8VC-10Co-xRu and 89.6WC-0.4VC-(10-x)Co-xRu (wt%) alloys with some peaks that were probably due to the air environment and were too small to identify.

Appendix E – Miscellenous Results

Table E1. EDS analyses for light particles in Alloy 11, 88.8WC-0.8VC-10Co-0.4Ru (wt%) (Figure 4.105) after exposure to 1 M H_2SO_4.

Element	Amount (Atomic %)
C	6.6±1.2
O	3.3±1.1
W	90.1±2.6

Table E2. EDS analyses for light particles in Alloy 13, 89.6WC-0.4VC-8.5Co-1.5 Ru (wt%) (Figure 4.105) after exposure to 1 M H_2SO_4.

Element	Amount (Atomic %)
C	9.7 ±1.5
O	1.2±0.0
W	88.1±3.3

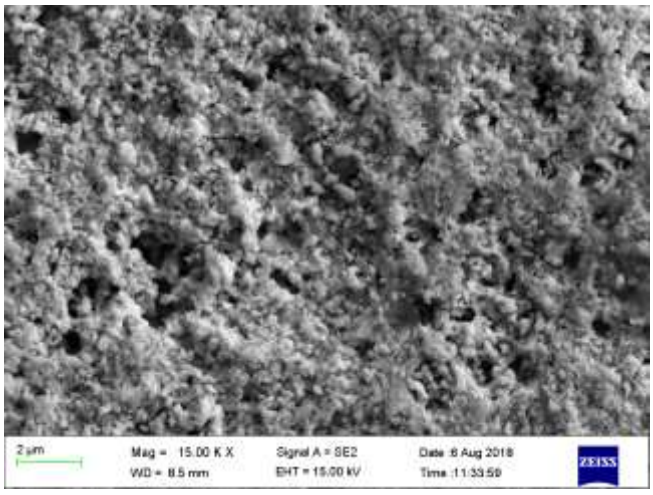

Figure E1. SEM-SE image of Alloy 3 (80WC-10VC-9.0Co-1.0Ru (wt%)) showing pores after exposure to 1 M NaCl.

Table E3. EDS analyses for light areas in Alloy 5, 80WC-10VC-8.0Co-2.0Ru (wt%) (Figure 4.117) after exposure to 1 M NaCl.

Element	Amount (Atomic %)
C	14.3±0.4
O	4.7±0.0
W	73.5±1.0
Na	0.6±0.0
Cl	0.6±0.2
V	4.3±1.7
Co	2.0±0.2

Table E4. EDS analyses for light contrast particles in Alloy 11, 88.8WC-0.8VC-10Co-0.4Ru (wt%) (Figure 4.117) after exposure to 1 M NaCl.

Element	Amount (Atomic %)
C	6.6±1.3
O	1.8±0.4
W	85.4±3.0
Na	2.6±0.9
Cl	3.6±1.0

Table E4. EDS analyses for light particles in Alloy 8, 89.2WC-0.4VC-10Co-0.4Ru (wt%) (Figure 4.130) after exposure to synthetic mine water.

Element	Amount (tomic %)
C	7.6±1.3
O	9.7±2.3
W	82.2±3.6
Ca	0.5±0.3

Table E5. EDS analyses for dark particles in Alloy 8, 89.2WC-0.4VC-10Co-0.4Ru (wt%) (Figure 4.130) after exposure to synthetic mine water.

Element	Amount (Atomic %)

C	14.8±2.1
O	24.8±2.1
W	52.6±2.5
S	0.3±0.1
Ca	4.2±1.2
Co	2.0±0.8
Ru	1.3±0.3

Table E6. EDS analysis for dark 'plate-like' phases in Alloy 13, 89.6WC-0.4VC-8.5Co-1.5Ru (wt%) (Figure 4.129) after exposure to synthetic mine water.

Element	**Amount (Atomic %)**
C	8.7±2.0
O	22.7±2.4
W	67.8±0.5
Na	0.5±0.1
Ca	0.3±0.0

OUTPUTS FROM THIS WORK

Conference Abstracts

1. L. Chipise, P.K. Jain and L.A. Cornish, Quantitative Microstructural Characterisation of WC-VC-Co-Ru Alloys, Proceedings of the Microscopy Society of Southern Africa (MSSA), ISBN 978-0-620-73767-8, 46 (2016) 55.
2. L. Chipise, P.K. Jain and L.A. Cornish, Characterisation of WC, VC, Co and Ru Powders, 3rd AMSEN Workshop, 2015, Johannesburg, South Africa.
3. L. Chipise, P.K. Jain and L.A. Cornish, Influence of Ru Additions on the Hardness and Densification of WC-VC-Co Alloys - 8th AMRS Conference, 2015, Accra, Ghana.

Conference Presentations

1. L. Chipise, P.K. Jain and L.A. Cornish, Cutting Potential Evaluation of WC-VC-Co-Ru Alloys - Poster, 4th AMSEN Workshop, 2017, Accra, Ghana.

Review Papers

1. Chipise, L.; Cornish, L.; Jain, P.; Mwabora, J., "Co-Pd Binary Phase Diagram Evaluation", in MSI Eureka, Effenberg, G. (Ed.), MSI, Materials Science International, Stuttgart (2017), Document ID: 20.32756.1.8 (Crys. Structure, Phase Diagram, Phase Relations, Assessment, 109).

Research papers

1. L. Chipise, P.K. Jain and L.A. Cornish, Magnetic and Microstructural Aspects of WC-VC-Co-Ru Alloys, International Journal for Refractory Metals and Hard Materials, 76 (2018) 49-56.
2. L. Chipise, P.K. Jain and L.A. Cornish, Influence of Ru on the Hardness and Fracture Toughness of WC-VC-Co alloys, International Journal for Refractory Metals and Hard Materials, 77 (2018) 54-60.

Awards

1. DST-NRF Centre of Excellence in Strong Materials, Best Poster Presentation (2017).
2. School of Chemical and Metallurgical Engineering, University of the Witwatersrand, 1st Runner Up, Postgraduate Poster Presentations (2015).
3. LASEC Prize – Best Experimental Design Award (2015).